QUANTUM SYNCHRONIZATION: INSIGHTS AND APPLICATIONS TO QUANTUM INFORMATION PROCESSING

SHEN YUAN

SCHOOL OF ELECTRIC & ELECTRICAL ENGINEERING

A THESIS SUBMITTED TO THE NANYANG TECHNOLOGICAL UNIVERSITY IN PARTIAL FULFILMENT OF THE REQUIREMENT FOR THE DEGREE OF DOCTOR OF PHILOSOPHY

2024

Statement of Originality

I hereby certify that the work embodied in this thesis is the result of original research, is free of plagiarised materials, and has not been submitted for a higher degree to any other University or Institution.

08/05/2024

. . . . Shen Yuan. . . . . .

Date

Supervisor Declaration Statement

I have reviewed the content and presentation style of this thesis and declare it is free of plagiarism and of sufficient grammatical clarity to be examined. To the best of my knowledge, the research and writing are those of the candidate except as acknowledged in the Author Attribution Statement. I confirm that the investigations were conducted in accord with the ethics policies and integrity standards of Nanyang Technological University and that the research data are presented honestly and without prejudice.

08/05/2024

. . . . . .

Date

. . . . . Fan Weijun . . . . . .

Authorship Attribution Statement

This thesis contains material from 4 paper(s) published in the following peer-reviewed journal(s) / from papers accepted at conferences in which I am listed as an author.

Chapter 3 is published as Y. Shen; H.Y. Soh; L.C. Kwek; W. Fan. Fisher information as general metrics of quantum synchronization. Entropy 2023, 25(8), 1116.

The contributions of the co-authors are as follows:

- A/Prof L.C. Kwek provided the initial project direction.
- H.Y. Soh and I prepared the manuscript drafts. The manuscript was revised by all authors.
- I coded the simulation software and performed simulations, followed by analyzing the data.
- A/Prof W. Fan provided general guidance and financial support.

Chapter 4 is published as Y. Shen; W.K. Mok; C. Noh; A.Q. Liu; L.C. Kwek; W. Fan; A. Chia. Quantum synchronization effects induced by strong nonlinearities. Phys. Rev. A 2023, 107, 053713.

The contributions of the co-authors are as follows:

- A/Prof L.C. Kwek and Dr A. Chia provided the initial project direction.
- I prepared the manuscript drafts. The manuscript was revised by all authors.
- I coded the simulation software and performed simulations, followed by analyzing the data.
- W.K. Mok performed analytical studies.
- A/Prof C. Noh, Prof A.Q. Liu and A/Prof W. Fan provided general guidance and financial support.

Chapter 5 is published as Y. Shen; H.Y. Soh; W. Fan; L.C. Kwek. Quantum synchronization enhanced by homodyne detection, noise and squeezing. Phys. Rev. E 108, 024204.

The contributions of the co-authors are as follows:

- A/Prof L.C. Kwek provided the initial project direction.
- H.Y. Soh and I prepared the manuscript drafts. The manuscript was revised by all authors.
- I coded the simulation software and performed simulations, followed by analyzing the data.
- A/Prof W. Fan provided general guidance and financial support.

Chapter 7 is published as Y. Shen, G. Marchegiani, G. Catelani, L. Amico, A. Q. Liu, W. Fan, and L. C. Kwek, GHZ-like states in the qubit-qudit Rabi model, SciPost Phys. 11, 099 (2021).

The contributions of the co-authors are as follows:

- A/Prof L.C. Kwek and I provided the initial project direction.
- I prepared the manuscript drafts. The manuscript was revised by all authors.
- I coded the simulation software and performed simulations, followed by analyzing the data.
- Dr G. Marchegiani and I performed analytical calculations.
- Dr G. Catelani provided guidance on the analysis and methodology.
- Prof L. Amico, Prof A.Q. Liu and A/Prof W. Fan provided general guidance and financial support.

08/05/2023

. . . . . .

Date

. . . . . Shen Yuan . . . . . .

Acknowledgments

I owe my deepest gratitude and appreciation to all those who have helped me in my journey to pursue this doctorate degree. Without their support, guidance, and encouragement, this work would not have been possible.

First of all, I am sincerely grateful to my supervisor Prof Fan Weijun and co-supervisor Prof Kwek Leong Chuan, for their invaluable advice, expertise and constant support throughout this research journey. Their unwavering dedication, insightful feedback and encouragement helped shape and improve this thesis. I am grateful to the members of my thesis committee, Prof Liu Ai-Qun, Prof Wei Lei, and Dr Cai Hong, for their valuable time and constructive feedback.

I extend my heartfelt appreciation to all my collaborators: Andy Chia and Mok Wai-Keong in CQT, Prof Changsuk Noh from Kyungpook National University, Soh Hongyi in NIE, Giampiero Marchegiani, Prof Gianluigi Catelani and Prof Luigi Amico from TII Quantum Labs, UAE, whose knowledge, mentoring, and intellectual discussions have enriched my academic experience and broadened my understanding in the field of quantum physics.

I have been fortunate enough to work closely with my colleagues and fellow researchers: Cao Lin, Luo Wei, Zhang Gong, Wan Lingxiao, Zhang Hui, Zhu Huihui, Yan Rudai in NTU for their enjoyable company during this research endeavor. Their support and guidance, especially during the beginning days of the journey have been invaluable. And I will cherish our friendship for many years to come.

Finally, I would like to express my deep appreciation to my family and my fiancée Wen Yuanyuan for their unconditional love, encouragement, and unwavering support throughout my academic journey. Their belief in me and their constant encouragement have been a source of inspiration and strength. My special thanks to my dog, Bronya, for being a good girl at home.

I have been blessed with these amazing people around me. And I am immensely grateful to everyone who has helped me along the way.

Abstract

This thesis explores various aspects of quantum synchronization, presenting novel perspectives and methodologies for studying nonlinear systems. By exploring different nonlinear oscillators, we study the interplay of nonlinear phenomena, like amplitude death and quantum synchronization, with information theoretic measures like Fisher information and quantum entanglement. We look at some some possible applications in superconducting circuit quantum electrodynamics (cQED) platform. Building on a robust theoretical framework encompassing appropriate quantum master equations, quantum stochastic differential equations, and quantum trajectory techniques, this research uncovers genuine quantum phenomena in synchronization, particularly in highly nonlinear quantum oscillators. Innovative entanglement generation techniques and new measures to capture quantum synchronization are proposed and analyzed, shedding light on their potential applications in the field of quantum information technologies. Moreover, this thesis examines counter-intuitive behaviors in coupled quantum oscillators, which are vital for understanding quantum nonlinear dynamics. These findings substantially contribute to our knowledge and utilization of quantum synchronization phenomena. It also paves the way for practical applications in quantum technologies using superconducting circuit QED.

Contents

List of Figures xi
List of Tables xix

1 Introduction **1**
1.1 The Field of Study 1
1.1.1 Quantum Nonlinear Dynamics 1
1.1.2 Circuit Quantum Electrodynamics(cQED) 1
1.2 A brief historical context 2
1.2.1 Classical synchronization 2
1.2.2 Cavity QED 4
1.3 Outline and reading guide 5

2 Theoretical framework **7**
2.1 Open quantum system and measurement 7
2.1.1 Von Neumann measurement and POVM 8
2.1.2 Quantum master equation 8
2.1.3 Quantum evolution under measurement 13
2.2 Classical synchronization 18
2.2.1 Self-sustained oscillations 18
2.2.2 Phase portraits and limit cycles 20
2.2.3 Synchronization by external force 21
2.2.4 Synchronization between two and more oscillators 22
2.3 Quantum Synchronization 24
2.3.1 Quantum synchronization by external force 25
2.3.2 Quantum synchronization between two oscillators 25
2.4 Theory of cQED 27
2.4.1 Quantum theory of light-matter interaction 34
2.4.2 Qubit-resonator Coupling Schemes 35
2.5 Quantum Fisher information 38

3 Fisher information as general metrics of quantum synchronization **41**
3.1 Oscillator model and synchronization measures 41

3.2 1-to-1 Synchronization 45
3.3 Squeezing enhances 2-to-1 synchronization 48
3.4 Effects of noise 50
3.5 Correlations between measures 52
3.6 Asymmetrical synchronization 54
3.7 Conclusion 55

4 Quantum synchronization effects induced by strong nonlinearities 57
4.1 Exact quantum model 58
4.2 An alternative quantum oscillator model 59
4.2.1 Poincaré–Lindstedt method 59
4.2.2 Krylov–Bogoliubov averaging 61
4.2.3 Quantum Duffing-vdP model 62
4.3 Nonlinearity-enhanced synchronization 63
4.3.1 Classical synchronization analysis 63
4.3.2 Quantum synchronization analysis 66
4.4 Nonlinearity-induced effects in disspatively coupled oscillators 68
4.4.1 Classical case 68
4.4.2 Quantum case 74
4.5 Nonlinearity-induced correlations in reactively coupled oscillators 79
4.5.1 Classical case 79
4.5.2 Quantum case 81
4.6 Conclusion 82

5 Quantum synchronization enhanced by homodyne detection,noise and squeezing 83
5.1 Homodyne-monitored quantum oscillator model 83
5.2 Synchronization in quantum regime 85
5.3 Noise-induced synchronization enhancement 89
5.4 Squeezing further improves synchronization 91
5.5 Conclusion 92

6 Mixing oscillations: Two Oscillators of the Same or Different Kinds. 95
6.1 Oscillator models 96
6.2 Pearson correlation of coupled homogeneous oscillators 97
6.3 Joint-probability distributions of coupled heterogeneous oscillators 99
6.3.1 Admixture of Quantum Rayleigh and Stuart-Landau oscillators 100
6.3.2 Admixture of Quantum vdP and Stuart-Landau oscillators 101

6.3.3 Admixture of Quantum Rayleigh and vdP oscillators 102
6.3.4 Admixture of Quantum Stuart-Landau and Ditzinger oscillators 104
6.4 Amplitude death 105
6.4.1 Two SL oscillators 105
6.4.2 Reactive coupling 107
6.4.3 Two vdP oscillators 109
6.5 Conclusion 109

7 GHZ-like states in the Qubit-Qudit Rabi Model 111
7.1 The qubit-qudit Rabi model 112
7.2 Negativity of entanglement 117
7.3 Dynamics 120
7.3.1 Quench dynamics 120
7.3.2 Adiabatic state preparation 122
7.4 Conclusion 124

8 A survey on synchronization in cQED platform 127
8.1 Quantum Stuart-Landau in superconducting cavities 128
8.2 Synchronization of spin-1 on IBM-Q 129
8.3 Simulation of driven QHO on IBM-Q 130

9 Outlook 133

A Quantum computing 137
A.1 NISQ hardwares 137
A.2 NISQ algorithms 141

References 150

List of Figures

2.1 (a) A person on a swing represents an example of a self-sustained oscillator. (b) Mechanical swing whose length changes according to a prescribed function of time is a forced system. Phase is free for a self-sustained system (a) and not free for a forced one (b). Therefore, if the two self-sustained system (a) are fixed to a common support, i.e., are weakly coupled, then they can synchronize if their parameters are close. By contrast, the forced system (b) do not synchronize. Figure taken from [PRK01]. 20

2.2 The phase portrait of a van der Pol equation, integrate with $\mu = 1.5$ and initial condition $(x, \dot{x}) = (1, 0)$. The limit cycle is not a circle and the stable waveform is not a sinusoidal form. 21

2.3 Simulation of an Arnold tongue of a quantum Stuart-Landau oscillator in Eq. 2.65 with $\gamma_2/\gamma_1 = 10$, where ω_0 is the natural frequency of the oscillator and $\tilde{\omega}$ denotes the observed frequency of the oscillator, after the external force is applied. The frequency and amplitude of the force is denoted by Ω and F respectively. For a fixed value of the force amplitude F, $\Omega - \tilde{\omega}$ is exactly zero near the frequency of the autonomous oscillator ω_0. This is called frequency locking. The $\Omega - \tilde{\omega}$ vs. $\Omega - \omega_0$ and driving amplitudes F and determined the domain where the frequency of the driven oscillator $\tilde{\omega}$ is equal to the drive Ω. This blue area is known as the Arnold tongue. 22

2.4 Quasi-probability distributions (Wigner functions) and the corresponding phase distributions $P(\phi)$, for (a)-(b) undriven and (c)-(d) driven quantum Stuart-Landau model. 26

2.5 Circuit diagram of a Cooper-pair box qubit 29

2.6 Frequency difference $\omega_j - \omega_0$ for the first three energy levels of the transmon Hamiltonian obtained from numerical diagonalization of Eqn. 2.85 expressed in the charge basis $|n\rangle$ for different E_j/E_c ratios. For large values of E_j/E_c the energy levels become insensitive to the offset charge. 31

2.7 Circuit schematics of a Transmon qubit 32

2.8 Circuit schematics of a tunable Transmon qubit 33

3.1 An example of a squeezed steady-state (a) Wigner function and its corresponding (b) phase distribution $P(\Phi)$. Squeezed Wigner function and phase distribution have two distinct peaks, which we refer to as 2-to-1 synchronization. Parameters in this example: $\Delta = 0, E = \eta = 0.5, \varphi = \pi/2, \gamma_1 = \gamma_2 = 1, \gamma_3 = 0$. 44

3.2 Phase coherence vs. FI-based measures. It is interesting to see FI-based measures is more sensitive(larger gradient) for highly synchronized states, as shown by the dotted reference line indicating $\nabla_{gradient} = 2$. Sample data simulated with: $\Delta = 0, E = 0.5, \eta = 0, \varphi = \pi/2, \gamma_1 = 1, \gamma_2 \in [1, 10], \gamma_3 = 0$. 45

3.3 Phase distribution $P(\phi)$ and synchronization measures plotted against driving amplitude E. Fixed parameters: $\Delta = 0, \gamma_1 = 1, \gamma_3 = 0$. In these cases of 1-to-1 synchronization, the driven oscillator has only one preferred phase to synchronize to. Unbounded and bounded measures are plotted separately. 46

3.4 Numerical results vs. analytical results. The oscillator is assumed in deep quantum regime ($\gamma_2 = 300$). Fixed parameters: $\Delta = 0, \eta = 0, \gamma_1 = 1, \gamma_3 = 0$.Analytical results are accurate only when $E \ll 1$. 49

3.5 Phase distribution $P(\phi)$ and synchronization measures plotted against squeezing amplitude η. Fixed parameters: $\Delta = 0, \varphi = \pi/2, \gamma_1 = 1, \gamma_3 = 0$. In these cases of 2-to-1 synchronization, the driven oscillator has two distinct phase to synchronize to. Unbounded and bounded measures are plotted separately. 50

3.6 Effects of single-photon dissipation noise in 1-to-1 synchronization, in the absence of squeezing ($\eta = 0$), with fixed parameters: $\Delta = 0, \gamma_1 = 1, \gamma_2 = 10, p = 0$. All measures exhibit an noise-induced boost where the dissipation is small, which is consistent with the previous works [MKH20, SSFK23]. 51

3.7 Effects of single-photon dissipation noise in 2-to-1 synchronization, without driving ($E = 0$), with fixed parameters: $\Delta = 0, \gamma_1 = 1, \gamma_2 = 10, p = 0$. As discussed above, $MRL^{(1)}$ and phase coherence are identically zero in these cases. 52

3.8 Effects of white noise in 1-to-1 synchronization, in the absence of squeezing ($\eta = 0$), with fixed parameters: $\Delta = 0, \gamma_1 = 1, \gamma_2 = 10, \gamma_3 = 0$. 53

3.9 Effects of white noise in 2-to-1 synchronization, without driving ($E = 0$), with fixed parameters: $\Delta = 0, \gamma_1 = 1, \gamma_2 = 10, \gamma_3 = 0$. $MRL^{(1)}$ and phase coherence are 0 in this case for the same reason as above. 54

3.10 Correlation between different measures on (a)1-to-1 synchronization. Calculations are performed on the same data as Fig. 3.3 left column. (b)2-to-1 synchronization. Calculations are performed on the same data as Fig. 3.5 right column. 55

3.11 Asymmetrical phase distribution and synchronization measures plotted against squeezing η. Fixed parameters: $\Delta = 0, \gamma_1 = 1, \gamma_2 = 10, \gamma_3 = 0$. 56

4.1 Dynamics of the undriven vdP oscillator. Results from an exact numerical simulation are shown as a blue solid line, while results from (4.9) are plotted as an orange dashed curve. (a) Long-time limit of $x(t)$ for $\lambda = 0.5$ (transient dynamics have been discarded). (b) Observed frequency ω. The Poincaré–Lindstedt method remains to be a good approximation up till about $\lambda \approx 1$. Copyright 2023, Phys. Rev. A, no permission needed for thesis purpose. 61

4.2 (a) Synchronization bandwidth against driving force F for $\lambda = 0.5$. Adding β enhances the synchronization bandwidth for weak to moderate forcing (compared to λ). The analytical predictions given by the dashed lines) are accurate up to $F \sim \lambda$. (b) Enhancement factor defined as the ratio between the bandwidth and its baseline value $F/2$. A value greater than one indicates enhancement of the bandwidth. $\lambda = 0.5, F = 0.2$, and the predicted minimum β for enhancement is $1/9$. Copyright 2023, Phys. Rev. A, no permission needed for thesis purpose. 66

4.3 Contour plot of the synchronization bandwidth for the quantum DvdP oscillator as a function of $\bar{\beta} \equiv \beta r^2$ (vertical axis) and F/r (horizontal axis) with unit limit-cycle radius, i.e. $r = 1$. In this case $\bar{\beta} = \beta$ and $\bar{\lambda} = \lambda$. The axes are also indicated in subplot (b). (a) Illustration of synchronization enhancement for $\bar{\lambda} = 0.1$. Above a critical value of $\bar{\beta}$, indicated by a red dashed line (obtained numerically), the synchronization bandwidth is enlarged as the Duffing nonlinearity is increased. (b) Synchronization enhancement disappears if we increase the vdP nonlinearity from $\bar{\lambda} = 0.1$ to $\bar{\lambda} = 0.5$, demonstrating the finite range of $\bar{\lambda}$ over which the enhancement is effective. Copyright 2023, Phys. Rev. A, no permission needed for thesis purpose. 68

4.4 Synchronization boundaries for different values of λ in (a)classical; (b)quantum simulations. The synchronization region lies below the curve in the all cases. The synchronization bandwidth is enlarged as λ is increased for a fixed η. Comparing (b) with Fig. 4.5(b), we see that the additional Kerr nonlinearity $\beta = 0.2$ does not change the synchronization boundary. Copyright 2023, Phys. Rev. A, no permission needed for thesis purpose. 73

4.5 Regions of frequency locking and amplitude death (as defined in the text by the power spectrum and Wigner function) for two dissipatively coupled vdP oscillators [subplots (a)–(d)] along with contours of Σ [subplots (a) and (c)]. All subplots have Δ on the vertical axis, and η on horizontal axis which we also indicate in subplot (c). (a) Large r (semiclassical regime). Note the region on the left does not correspond to any identifiable effect and is demarcated using a solid line while the boundary between frequency locking and amplitude death is a Hopf bifurcation, which we denote by a dash-dotted line. As r is increased, the classical boundary is recovered. (b) Effect of varying λ on synchronization for $r = 1$. Boundaries of the frequency-locking region and its corresponding λ are shown (i.e. the frequency-locking region is the area underneath each curve). Increasing λ can enlarge the synchronization bandwidth and induce frequency locking from a state of amplitude death. (c) Small r (deep quantum regime). At small r, amplitude death occurs even at zero initial detuning, which is a quantum effect. Note that $\bar{\lambda}$ in (a) and (c) are approximately equal, leaving the differences between the two plots only as a result of quantum effects. (d) Shifts in amplitude-death boundary as $\bar{\lambda}$ is increased (quantum-to-semiclassical transition). Copyright 2023, Phys. Rev. A, no permission needed for thesis purpose. 75

4.6 Positional correlation (4.55) for two reactively coupled vdP oscillators. (a) Contour of Σ as a function of λ and g for $r = 0.3$ and $\Delta = 0.05$. The bottom gap of zero correlation agrees with the SL limit. (b) Correlations along the three vertical dashed lines at $g = 0.2$, 0.4, and 0.8 in subplot (a). Copyright 2023, Phys. Rev. A, no permission needed for thesis purpose. 79

4.7 Correlation coefficient of two reactively-coupled vdP oscillators for $\Delta = 0.1, r = 1$. Copyright 2023, Phys. Rev. A, no permission needed for thesis purpose. 81

5.1 Phase coherence with/without homodyne detection (Top) and enhancement factor $\mathcal{F}$ (Bottom) plotted against nonlinear damping rate $\gamma_2 \in [0.5, 3]$, under different driving amplitude E. Fixed parameters: $\Delta = 0, \gamma_3 = 0.1, \theta = \pi/2$ (optimized for the highest enhancement factor). Take note that the fluctuations in the curves are consequences of a finite number of trajectories averaged in the simulations. The same applies for other plots below. 85

5.2 Enhancement factor at different measurement angle θ. (a) Zero detuning. (b) Non-vanishing detuning $\Delta = 0.05$. The curves are smoothed using polynomial interpolation. 86

5.3 Standard deviation in the enhancement factor $\mathcal{F}$ of Fig. 5.1. 88

5.4 Enhancement in purity of steady-state due to homodyne measurement is always present, but decays with increasing γ_2. (inset) Purity scales approximately with $\gamma_2^{1/3}$. Fixed parameters:$\Delta = 0, \gamma_3 = 0.1, \theta = \pi/2$ 88

5.5 Effect of γ_2 on enhancement factor $\mathcal{F}$ at different single-photon dissipation γ_3, with fixed parameters $\Delta = 0, \theta = \pi/2$. When single-photon dissipation γ_3 is small, the enhancement factor $\mathcal{F}$ drops after reaching the maximum. However, the enhancement factor starts to rise even in the quantum regime when a large single-photon dissipation is present. 89

5.6 Phase coherence in general vanishes with increasing γ_2. However, in the quantum regime, the presence of single-photon dissipation γ_3 can boost phase coherence. Homodyne measurement greatly amplifies this boost in the quantum regime. 90

5.7 Contour plot of enhancement factor $\mathcal{F}$ against γ_2 and γ_3 with (a)$\eta = 0$ and (b)$\eta = 0.1$; (c) differences between enhancement factor $\mathcal{F}$ of (a) and (b). 91

5.8 (a)The convergence of optimal γ_2 with increasing squeezing η. (b)Top-down view of the optimal γ_2 positions in the transition from Fig.5(a)-(b). 91

6.1 Pearson correlation coefficient of mutually coupled homogeneous oscillators, i.e. two Rayleigh or two van der Pol oscillators, plotted with increasing nonlinearity μ and limi cycle radius q_0. 98

6.2 A Rayleigh oscillator ($\mu_1 = 0.1, q_0^{(1)} = 1.5$) and a Rayleigh oscillator in Stuart-Landau limit($\mu_1 = 0.01, q_0^{(2)} = 1.5$) coupled by dissipative interaction. (left column) Wigner function of first oscillator, (middle column) Wigner function of second oscillator, (right column) joint-probability distribution $P(x_1, x_2)$. Different rows corresponding to coupling strengths $V = 0, 0.1, 10$. 100

6.3 A vdP oscillator ($\mu_1 = 0.1, q_0^{(1)} = 1.5$) and a vdP oscillator in Stuart-Landau limit($\mu_1 = 0.01, q_0^{(1)} = 1.5$) coupled by dissipative interaction. (left column) Wigner function of first oscillator, (middle column) Wigner function of second oscillator, (right column) joint-probability distribution $P(x_1, x_2)$. Different rows corresponding to coupling strengths $V = 0, 0.1, 10$. 101

6.4 Inter-species coupling between a quantum Rayleigh oscillator ($\mu = 0.1, q_0 = 1.5$) and a quantum vdP oscillator ($\mu = 0.01, q_0 = 1.5$). Different rows corresponding to coupling strengths $V = 0, 0.1, 10$. 102

6.5 Inter-species coupling between a quantum Rayleigh oscillator ($\mu = 0.1, q_0 = 1.1$) and a quantum vdP oscillator ($\mu = 0.1, q_0 = 1.5$). Different rows corresponding to coupling strengths $V = 0, 0.1, 10$. 103

6.6 Inter-species coupling between a quantum Stuart-Landau ($\gamma_2/\gamma_1 = 100$) and quantum Ditzinger oscillator with a limit cycle($b = 200, r_0 = 1$), with increasing coupling strengths $V = 0, 1, 10$ respectively. 104

6.7 Limit cycle radius of two dissipatively coupled Stuart Landau oscillators. (d) dashed line: $\Delta = \sqrt{\frac{27-15V^2-4V^3}{(V-1)(V+3)}}$ 107

6.8 Limit cycle radius of two Stuart-Landau under reactive coupling $V(a_1 a_2^\dagger + a_1^\dagger a_2)$. The transition from quantum to classical regime is unusual compared to dissipatively coupled case. 108

6.9 Limit cycle radius of two coupled identical vdP oscillators ($\mu_1 = \mu_2 = 0.1$) under increasing dissipative coupling. Tuning down q_0 from $2 \to 1.3$ results in a similar behaviour to two coupled SL case. 109

7.1 Model schematics. The system is composed of a qubit with level spacing Ω_1, an harmonic oscillator (resonator) with characteristic frequency ω, and a d-level quantum system (qudit) with level spacing Ω_2. The qubit and the qudit are coupled to the resonator through the coupling constants $g_{1,2}$. Copyright 2021, SciPost Phys., OA, no permission needed for thesis purpose. 113

7.2 Hamiltonian energy spectrum with qudit dimensions $d = 2, 3, 4$. (a)-(f) Low energy spectrum vs coupling strength g obtained through numerical diagonalization of the full Hamiltonian Eq. (7.1) (solid). The numerical results are compared to the low coupling approximations (black dotted-dashed) of Eq. (7.9) , and d-order perturbation approximation Eq. (7.11) in the ultrastrong coupling regime (red dashed), for $g_1 = g_2 = g$ and (top panels) $\Omega_1 = 0.15\omega, \Omega_2 = 0.1\omega$, (bottom panels) $\Omega_1 = 0.55\omega, \Omega_2 = 0.5\omega$. Copyright 2021, SciPost Phys., OA, no permission needed for thesis purpose. 115

7.3 Ground state vs GHZ state for $g_1 = g_2$ and different qudit sizes $d = 2, 3, 4$ (top to bottom at $g_1 = 0$). Fidelity between the Hamiltonian ground state (obtained through numerical diagonalization) and the GHZ state Eq. (7.13) as a function of the coupling strength for (a) $\Omega_1 = 0.15\omega, \Omega_2 = 0.1\omega$, (b) $\Omega_1 = 0.55\omega, \Omega_2 = 0.5\omega$. Copyright 2021, SciPost Phys., OA, no permission needed for thesis purpose. 118

7.4 Coupling dependence of the groundstate negativity between the qubit and the qudit. (a)-(c) Density plot of the groundstate negativity as a function of g_1 and g_2 for the (a) qubit-qubit, (b) qubit-qutrit, (c) qubit-ququart cases. The plots are obtained by numerical calculations for $\Omega_1 = \Omega_2 = 0.1\omega$. (d) Cuts of the density plots for $g_2 = 0.2\omega$, indicated by the dashed lines in panels (a)-(c). The results obtained through numerical calculations (solid) are compared with the approximate expression of the negativity Eq. (7.16) (dashed), obtained in the ultrastrong coupling regime. Copyright 2021, SciPost Phys., OA, no permission needed for thesis purpose. 118

7.5 Dynamics after quenching the interaction strength. a)-b)-c) Fidelity between the initial state of the system and the instantaneous state for qubit (a), qutrit (b) and ququart (c) cases. The initial state is the ground state of the uncoupled system. The numerical expressions (solid) are compared to approximations (dashed) derived in the main text Eq. (7.18). d)-e) -f) Dynamics of the expectation value of d) the qubit population, e) qudit population and f) mean photon number. The dashed lines in panel f) are given by Eq. (7.19) Parameters are $\Omega_1 = 0.12\omega, \Omega_2 = 0.1\omega$, and $g_1 = g_2 = 0.3\omega$. Copyright 2021, SciPost Phys., OA, no permission needed for thesis purpose. 120

7.6 Adiabatic state preparation of the GHZ state in the qubit, qutrit, and ququart cases. (a) Time evolution of the fidelity between the instantaneous state and the hybrid GHZ state in Eq.(7.13). The coupling terms g_1, g_2 are adiabatically switched on at $t = 0$ and linearly increased to 0.5ω, as shown in the inset. (b) State fidelity with the GHZ state vs time in the adiabatic process where the atoms frequencies are linearly reduced from the initial value $\Omega_1, \Omega_2 = 2\omega$ to 0.1ω, as displayed in the inset. Copyright 2021, SciPost Phys., OA, no permission needed for thesis purpose. 123

8.1 Experimental realization of the quantum van der Pol oscillator (or more accurately, the quantum Stuart Landau oscillator). Figure adapted from [LTP+15]. 128

List of Tables

2.1 Summary of capacitive coupling 35
2.2 Summary of galvanic coupling 36

Chapter 1

Introduction

1.1 The Field of Study

1.1.1 Quantum Nonlinear Dynamics

Dynamics has long been the central dogma of physics, from Isaac Newton and his discovery of laws of motion, to the chaos-induced Butterfly effect. Back in the 1600s, physicists were already capable of solving fairly complicating dynamical systems analytically with simple differential equations. Since then generations of mathematicians and physicists have tackled the challenge of applying Newton's differential equations to something even more complicated – e.g. the three-body problem (like the motion of sun, earth, and moon). Despite decades of effort, the three-body problem was eventually realized to be unsolvable, in the sense that obtaining analytical formulas for the motions of the three bodies is impossible. The three-body problem remains and will always be a road block, but a more interesting phenomena rampant in Nature arises: it is the new branch of study called nonlinear dynamics. Nonlinear systems are inherently more difficult. Yet, they comprise the vast majority of mathematical equations in Nature. Most nonlinear systems are thereforre difficult to solve, with the exception of some easy-to-solve quasi-linear systems.

Just as nonlinear dynamics plays an important role in classical physics, quantum nonlinear dynamics is becoming an active field of study. Many generic nonlinear effects, such as amplification, bifurcation, synchronization and chaos, find analogous effects in the quantum regime and often add new insights to their classical counterparts.

1.1.2 Circuit Quantum Electrodynamics(cQED)

With many interesting features lurking in the field of nonlinear quantum theory, it is undoubtedly significant to mimic and realize and observe such intricate phenomena in

the lab. And the best candidate for this task is no other than the superconducting circuit quantum electrodynamics (cQED) – an enabling experimental platform and arguably the Swiss-army knife for quantum technologies.

Quantum electrodynamics (QED) was originally a branch of study dedicated to the interactions between photons and atoms. It then becomes a key part in a broader field of quantum optics. In the experiments led by Serge Haroche, the 2012 Noble Prize for Physics laureate, the team uses individual atoms as a probe to observe the behavior of the light field. The interaction between a single atom and a beam of light is generally very weak. This makes it very hard to observe the effects that arise at the single-particle level. The solution demonstrated by the team, later known as the cavity QED, is to isolate an atom in a cavity with highly reflecting boundaries. Under carefully engineered settings, the electromagnetic field inside the cavity is quantized as a set of quantum harmonic oscillators, one of them being resonant with a transition between two energy levels of the atom treated as a spin-1/2. The photons will bounce back and forth inside the cavity, which means a single photon can interact with an atom multiple times before decaying away, hence amplifying the effects of the interactions. The fundamental ideas behind this are simple, but implementing them in the laboratory has never been easy. The physics of the cavity QED can be naturally studied in electrical circuits, opening up the new field of circuit QED. Circuit QED (cQED) refers to the technique of using superconducting electrical circuits to implement and manipulate qubits and quantized electromagnetic fields, replacing the atom and photons. It stemmed from atomic physics and quantum optics, and is now mainstream in this area. Circuit QED has led to advances in the fundamental study of quantum theory and quantum information technologies. At the same time, cQED makes it possible to study hybrid quantum systems, which are more interesting, such as quantum dots, magnons, Rydberg atoms, surface acoustic waves, and mechanical systems, interacting with microwave photons. This huge arsenal of experiment possibilities makes cQED the perfect test bed for quantum nonlinear effects.

1.2 A brief historical context

1.2.1 Classical synchronization

Synchronization is a relative newcomer to the study of nonlinear effects in quantum systems [RP03]. In its most elementary form, the system consists of applying a sinusoidal force, with amplitude f, and frequency Ω_{d}, to a self-sustained oscillator. Synchronization is then the modification of the oscillator frequency to Ω_{d}. This

phenomenon has been observed and studied for centuries. The first recorded observation of classical synchronization dates back to 1665, when Dutch scientist Christiaan Huygens observed that two pendulum clocks hanging on the same wall tended to synchronize their swings. Huygens attributed this synchronization to interactions between clocks transmitted by the wall. This discovery marked the beginning of a scientific investigation of synchronization.

The understanding of classical synchronization took a significant leap forward with the introduction of mathematical models. In the 20th century, Appleton, van der Pol, Rayleigh and others [vdP17, vdP22, App22, Stu60] contributed extensively to classical synchronization. This concept was further developed and popularized by American mathematician and physicist Arthur Winfree and Yoshiki Kuramoto in their respective studies of biological and chemical oscillators [Win80, Win67, Kur75].

The study of synchronization in complex systems has further enriched our understanding of classical synchronization. Researchers such as Steven Strogatz and Duncan Watts have explored the behavior of synchronization in networks of oscillators, revealing fascinating insights into the collective dynamics of these systems. Their work has expanded the application of classical synchronization to diverse fields such as neuroscience, power grids, and social networks.

From its early observations in the 17th century to the development of sophisticated mathematical models and the exploration of complex systems, the study of classical synchronization has indeed come a long way. It has not only illuminated our understanding of nonlinear phenomena, it has also been crucial for the understanding of chaos and other collective behaviors.

Van der Pol oscillator

In classical nonlinear theory, the van der Pol oscillator is an archetypical self-sustained oscillator which has a stable limit cycle and can exhibit synchronization. It was first introduced by the Dutch physicist Balthasar Van der Pol in 1920 [VdP20]. Its discovery and its subsequent study marked an important milestone in the field of nonlinear dynamics.

During the early 20th century, there was a growing interest among physicists and engineers to understand the behavior of electrical circuits, particularly those involving vacuum tubes. These circuits exhibited complex and sometimes unpredictable behaviors, which were not well explained by the existing linear models. Balthasar Van der Pol, who was working at the Philips Research Labs in Netherlands, was

investigating the phenomenon of self-oscillations in vacuum tube circuits. He aimed to develop a better understanding of the behavior of a circuit containing a vacuum tube with a nonlinear resistor. He discovered that under certain conditions, the system exhibited self-sustained oscillations with unique characteristics. His key insight was that the nonlinear resistor introduced a damping mechanism that depended on the amplitude of the oscillations. This damping, now known as "van der Pol damping" resulted in an interesting phenomenon: the amplitude of the oscillations would exhibit a limit cycle behavior. In other words, the oscillations would settle into a stable, repetitive pattern rather than growing or decaying indefinitely.

The van der Pol oscillator has since found applications in various fields, including physics, engineering, biology, and even economics. Its mathematical representation, known as the van der Pol equation, has become a standard model for studying nonlinear systems and understanding the emergence of complex behavior. The complete dynamics of a driven van der Pol oscillator are governed by the following equation

$$\frac{d^2x}{dt^2} - \mu(1 - x^2)\frac{dx}{dt} + \omega_0^2 x = F\cos(\omega_d t) \tag{1.1}$$

where μ is a scalar parameter representing the damping of the oscillator, ω_0 is the natural frequency of the oscillator, and ω_d is the driving frequency with strength F. Interested readers can find more details in a later section 2.2.

1.2.2 Cavity QED

The groundwork for cavity QED was laid by the pioneers of quantum mechanics and quantum electrodynamics in the early 20th century. Scientists such as Albert Einstein, Niels Bohr, and Werner Heisenberg established the fundamental principles of quantum mechanics, while Paul Dirac, Julian Schwinger, and Richard Feynman formulated the foundations of quantum electrodynamics. These developments provided the necessary framework to explore the quantum interactions between light and matter. Cavity QED has played a significant role in advancing our understanding of quantum phenomena such as spontaneous emission, the Purcell effect, and the development of quantum gates.

Cavity QED emerged in the 1970s, spurred by advances in laser technology and the development of high-quality optical cavities. Researchers such as Herbert Walther, Serge Haroche, and Daniel Kleppner were among the first to demonstrate that atoms could be trapped within an optical cavity, enabling the study of strong coupling between atoms and photons. This marked the beginning of cavity QED as a distinct

field of study.

In the 1980s and 1990s, a series of groundbreaking experiments solidified the importance of cavity QED in understanding quantum phenomena. These experiments include:

The observation of the Purcell effect, where the spontaneous emission rate of an atom is modified by its environment in the cavity. The demonstration of the vacuum Rabi oscillations, which show the coherent exchange of energy between an atom and a cavity photon. The realization of the micro-maser, a device that uses cavity QED principles to generate and amplify single photons. These experiments provided crucial insights into the behavior of atoms and photons in confined electromagnetic environments, paving the way for further advances in quantum science.

1.3 Outline and reading guide

This thesis explores the possibilities of simulating quantum nonlinear effects in a context of circuit quantum electrodynamics. The organization of this report follows: Chapter 2 provides a pedagogical review of the topics on quantum nonlinear dynamics and circuit QED as well as other topics on quantum information theory, including light-matter interaction, open quantum system and measurement, and quantum Fisher information. In Chapter 3, new measures of quantum phase synchronization are proposed and analyzed, with special focus on 2-to-1 synchronization. This study demonstrates Fisher information as a more advantageous indicator for quantum phase synchronization, in certain situations where all other established measures are unable to yield reliable results. In Chapter 4, quantum synchronization induced by strong nonlinearities with no classical analog is studied, and with it, an alternative model is proposed that approximates the van der Pol oscillator with finitely large nonlinearities while remaining numerically tractable. This allows the uncovering of interesting phenomena in the deep-quantum strongly-nonlinear regime with no classical analog. In Chapter 5, the study aims to show that quantum synchronization can be enhanced by various techniques, such as homodyne detection, single-photon dissipation noise and squeezing. The capability of enhancing quantum synchronization using experimentally feasible techniques can be useful in implementing synchronization into quantum information processing tasks. Chapter 6 presents a study on mixed oscillations in homogeneous and heterogeneous oscillators, which is important in bridging the gap between classical and quantum mutual synchronization. Chapter 7 presents a Rabi type Hamiltonian system, in the context of circuit-QED, in which a qubit and a d-level quantum system (qudit) are coupled through a common resonator, and the entanglement generation

method is discussed in such a system. This toy model demonstrates that circuit-QED is a powerful and versatile platform for quantum information processing. Chapter 8 reviews the current progress on quantum synchronization implemented on circuit QED platform, and provides insights towards practical synchronization-based quantum technologies. Chapter 9 concludes the thesis with a perspective on the state of the field and insights for possible future research directions.

Chapter 2

Theoretical framework

2.1 Open quantum system and measurement

In order to understand the general evolution of quantum systems, one needs to consider coupling them with a second quantum system. If the second system is much larger than the first, it is often called a bath, a reservoir or an environment, and the first system is called an open system.

In open quantum systems, or for mixed states in general, the system is described by a density matrix. The density matrix represents the state of a quantum system in a more general way than the state vector, and equivalently represents an observer's state of knowledge of a system. When a quantum state can be represented by a state vector $|\psi\rangle$, its density matrix is defined as the product

$$\rho = |\psi\rangle\langle\psi|. \tag{2.1}$$

A state of the form in Eq. 2.1 is considered to be pure. On the other hand, one that cannot be represented in this form is a mixed state. Instead, it is written in the following form:

$$\rho = \sum_{\alpha} p_\alpha |\psi_\alpha\rangle\langle\psi_\alpha|. \tag{2.2}$$

In a closed system, the equation of motion for a density matrix under unitary evolution is referred to as the *Schrodinger-von Neumann equation*:

$$\dot{\rho} = -\frac{i}{\hbar}[H, \rho], \tag{2.3}$$

2.1.1 Von Neumann measurement and POVM

A von Neumann measurement can be described by a set of projectors $\{P_n = |n\rangle\langle n|\}$. This type of measurement represents only a special class of all possible measurements that can be implemented in quantum states. However, all possible measurements can be derived from von Neumann measurement. Each of the von Neumann projectors corresponds to one of the possible measurement outcomes: if the initial state is $\rho_0 = |\psi_0\rangle\langle\psi_0|$, then the nth possible outcome of the final state is

$$\rho_f = |n\rangle\langle n| = \frac{P_n \rho_0 P_n}{\mathrm{Tr}[P_n \rho_0 P_n]}, \tag{2.4}$$

with probability

$$P(n) = \mathrm{Tr}[P_n \rho_0 P_n]. \tag{2.5}$$

This formalism can be generalized to arbitrary set of measurement operators Ω_m, as long as the set of operators satisfy the following condition:

$$\sum_m \Omega_m^\dagger \Omega_m = \hat{I}, \tag{2.6}$$

with $\hat{I}$ being the identity operator. Then all possible measurement outcomes can be described by

$$\rho_f = \frac{\Omega_m \rho_0 \Omega_m^\dagger}{\mathrm{Tr}[\Omega_m \rho_0 \Omega_m^\dagger]}, \tag{2.7}$$

with probability

$$P(m) = \mathrm{Tr}[\Omega_m \rho_0 \Omega_m^\dagger]. \tag{2.8}$$

These generalized measurement operators are referred to as the "positive operator-valued measure" (POVM). All POVMs can be implemented by performing a unitary transformation on the system together with an auxiliary system, and then performing a von Neumann measurement (projection) on the auxiliary system.

2.1.2 Quantum master equation

Here, the derivation of the master equation in the subsequent sections follows closely the steps in Ref. [WM09]. Consider a quantum state described by a time dependent

density matrix $\rho(t)$. The most general quantum evolution is a completely positive, trace preserving map $\hat{\Lambda}$ so that after time t the state evolved as

$$\rho(t) = \hat{\Lambda}[\rho(0)], \tag{2.9}$$

where $\rho(0)$ describes the state density matrix at initial time reference.

It is known [Lin76] that any smooth, time-homogeneous, complete positive, trace-preserving quantum channel $\hat{\Lambda}[\rho]$ which obeys the natural semi-group property $\hat{\Lambda}_p \cdot \hat{\Lambda}_q = \hat{\Lambda}_{p+q}$ can be expressed as

$$\hat{\Lambda}[\rho] = e^{t\hat{\mathcal{L}}}[\rho], \tag{2.10}$$

and thus

$$\frac{d}{dt}\rho = \hat{\mathcal{L}}[\rho]. \tag{2.11}$$

Here $\hat{\mathcal{L}}$ is a quantum Liouvillian of the Gorini–Kossakowski–Sudarshan–Lindblad form

$$\hat{\mathcal{L}}[\rho] = -i[H, \rho] + \sum_{\mu} \Big(2L_\mu \rho L_\mu^\dagger - \{L_\mu^\dagger L_\mu, \rho\} \Big), \tag{2.12}$$

where H is the system Hamiltonian and L_μ are referred to as the Lindblad jump operators. Such operators may, for example, be particle creation/annihilation operators to describe random particle gain/loss, or number operators to describe dephasing.

General form of Born-Markov equation

Under Born and Markov approximations, which means that the system couples very weakly to a very large environment, the dynamics of the state ρ_{tot} of the system and the environment is given in the Schrodinger picture by

$$\dot{\rho}_{tot}(t) = -i[\hat{H}_S + \hat{H}_E + \hat{V}, \rho_{tot}(t)]. \tag{2.13}$$

Here $\hat{H}_S$ is the Hamiltonian for the system, $\hat{H}_E$ is the Hamiltonian for the environment, and $\hat{V}$ described the coupling between the two.

Next, it is convenient to move into an interaction frame with free Hamiltonian $\hat{H}_0 = \hat{H}_S + \hat{H}_E$ and the interaction term becomes $\hat{V}_{int}(t) = e^{i\hat{H}_0 t}\hat{V}e^{-i\hat{H}_0 t}$. In this frame, equation (2.13) becomes

$$\dot{\rho}_{tot;int}(t) = -i[\hat{V}_{int}(t), \rho_{tot;int}(t)]. \tag{2.14}$$

For the sake of simplicity, we will drop the *int* subscripts in the following derivation. Since the interaction is assumed to be weak, equation (2.14) can be expanded implicitly:

$$\rho_{tot}(t) = \rho_{tot}(0) - i \int_0^t dt' [\hat{V}(t'), \rho_{tot}(t')]. \tag{2.15}$$

We then substitute this solution back into (2.14) to get

$$\dot{\rho}_{tot}(t) = -i[\hat{V}(t), \rho_{tot}(0)] - \int_0^t dt' [\hat{V}(t), [\hat{V}(t'), \rho_{tot}(t')]]. \tag{2.16}$$

Since we are interested here only in the evolution of the system $\rho_S(t) = \mathrm{Tr}_E[\rho_{tot}(t)]$, which is traced over the environment:

$$\begin{aligned} \dot{\rho}_S(t) = &- i\,\mathrm{Tr}_E\left([\hat{V}(t), \rho_{tot}(0)]\right) \\ &- \int_0^{t'} dt'\,\mathrm{Tr}_E\left([\hat{V}(t), [\hat{V}(t'), \rho_{tot}(t')]]\right). \end{aligned} \tag{2.17}$$

We now make a very important assumption, namely that the system only weakly affects the bath so that the last term in (2.17) can be replaced. This is known as the Born approximation. With this assumption, (2.17) becomes

$$\begin{aligned} \dot{\rho}(t) = &- i[\hat{V}_S(t), \rho(t)] \\ &- \int_0^t dt'\,\mathrm{Tr}_E\left([\hat{V}_{SE}(t), [\hat{V}_{SE}(t'), \rho(t') \otimes \rho_E(0)]]\right). \end{aligned} \tag{2.18}$$

Note that we have split $\hat{V}$ into two parts: $\hat{V}(t) = \hat{V}_S(t) + \hat{V}_{SE}(t)$, where $\hat{V}_S$ acting on the system is traced out, such that only $\hat{V}_{SE}$ acting on both system and environment remains. Next we apply the Markov approximation, replacing $\rho(t')$ by $\rho(t)$, the above equation becomes what is referred to as the Born-Markov master equation:

$$\begin{aligned} \dot{\rho}(t) = &- i[\hat{V}_S(t), \rho(t)] \\ &- \int_{-\infty}^t dt'\,\mathrm{Tr}_E\left([\hat{V}(t), [\hat{V}(t'), \rho(t) \otimes \rho_E(0)]]\right). \end{aligned} \tag{2.19}$$

We require the bath to have a continuum spectrum of energies.

Derivation of GKSL equation from microscopic dynamics

From the general form of Born-Markov master equation, the path I would follow to derive the commonly adopted GKSL form of master equation, is to use the example of

a single mode cavity dissipatively damped by the bath.

The free Hamiltonian for a mode of the electromagnetic field is that of a harmonic oscillator. The total Hamiltonian for the bath is thus

$$\hat{H}_E = \sum_k \omega_k \hat{b}_k^\dagger \hat{b}_k, \tag{2.20}$$

where the integer k codes all of the information specifying the mode. The total Hamiltonian for system plus environment is

$$\hat{H} = \omega_c \hat{a}^\dagger \hat{a} + \sum_k \omega_k \hat{b}_k^\dagger \hat{b}_k + \sum_k g_k (\hat{a} + \hat{a}^\dagger)(\hat{b}_k + \hat{b}_k^\dagger), \tag{2.21}$$

where the first term represents the free energy of the cavity mode of interest, the second is for the free energy of the many-mode field outside the cavity, and the last term represents the coupling of the two for optical frequencies. The coefficient g_k which can be assumed real without loss of generality is proportional to the dipole matrix element for the transition and depends on the structure of mode k.

Given that the coupling term is much smaller compared to the rest of (2.21), we can apply Born approximation and RWA, by casting the coupling term in the interaction frame:

$$\hat{V}_{int} = \sum_k g_k (\hat{a}^\dagger \hat{b}_k e^{-i(\omega_k - \omega_c)t} + \hat{a} \hat{b}_k^\dagger e^{i(\omega_k - \omega_c)t}). \tag{2.22}$$

Now substitute (2.22) into the general form of Born-Markov master equation to obtain a differential equation for the system density matrix. Before expanding the equation, we need to take the initial state of the bath to be the vacuum state. By doing so, the first term in (2.19) is exactly zero. Then, the equation for $\rho(t)$ becomes

$$\dot{\rho} = -\int_0^t dt' \{\Gamma(t - t')[\hat{a}^\dagger \hat{a} \rho(t') - \hat{a} \rho(t') \hat{a}^\dagger] + H.c.\}, \tag{2.23}$$

where H.c. stands for the Hermitian conjugate term, and

$$\Gamma(\tau) = \sum_k g_k^2 e^{-i((\omega_k - \omega_c)\tau}. \tag{2.24}$$

Next, we wish to make the Markov approximation. For an atom in free space, there is an infinite number of modes, each of which is infinite in volume, so the modulus squared of the coupling coefficients is infinitesimal. Thus we can justify replacing the

sum in (2.24) by an integral:

$$\Gamma(\tau) = \int_0^\infty d\omega \rho(\omega) g(\omega)^2 e^{i(\omega_c - \omega)\tau} \propto \delta(\tau), \tag{2.25}$$

which means that the reservoir correlation function $\Gamma(\tau)$ is sharply peaked at $\tau = 0$. Then simplifying (2.23) we arrive at the GKSL form in the interaction picture:

$$\dot{\rho} = \gamma \mathcal{D}[\hat{a}]\rho \tag{2.26}$$

where the superoperator

$$\mathcal{D}[\hat{A}]\rho = \hat{A}\rho\hat{A}^\dagger - \frac{1}{2}(\hat{A}^\dagger\hat{A}\rho + \rho\hat{A}^\dagger\hat{A}). \tag{2.27}$$

Converting back to Schrodinger picture we obtain

$$\dot{\rho} = -i[\hat{H}, \rho] + \gamma \mathcal{D}[\hat{a}]\rho. \tag{2.28}$$

Derivation of GKSL equation from quantum jump

Following [WM09], the GKSL master equation can also be derived from the quantum jump approach in a way that is more insightful. We start by examining the Markovian evolution of an isolated quantum system in the absence of measurement:

$$|\psi(t+T)\rangle = \hat{U}(T)|\psi(t)\rangle = \exp(-i\hat{H}T)|\psi(t)\rangle, \tag{2.29}$$

which leads to a finite differerntial

$$\lim_{\tau \to 0} \frac{|\psi(t+\tau)\rangle - |\psi(t)\rangle}{\tau} = -i\hat{H}(t)|\psi(t)\rangle, \tag{2.30}$$

and hence the evolution is continuous.

The continuous evolution of a density matrix is then

$$\lim_{\tau \to 0} \frac{\rho(t+\tau) - \rho(t)}{\tau} = \dot{\rho}(t). \tag{2.31}$$

We start monitoring the system at time t, then the state density matrix at time $t + dt$, an infinitesimally small time step, averaging over all possible measurement outcomes, is

$$\rho(t+dt) = \sum_r \hat{M}_r(dt)\rho(t)\hat{M}_r^\dagger. \tag{2.32}$$

where $\hat{M}_r$ is the measurement operator corresponding to certain outcome r, and each term in the sum is referred to as a quantum jump. Now let's assume the simplest scenario, considering only two outcomes, i.e. $r = 0$ and 1. Then the two measurement operators take the following form:

$$\hat{M}_0(dt) = \hat{I} - (\hat{c}^\dagger \hat{c}/2 + i\hat{H})dt, \tag{2.33}$$

$$\hat{M}_1(dt) = \sqrt{dt}\hat{c} \tag{2.34}$$

such that

$$\hat{M}_0^\dagger(dt)\hat{M}_0(dt) + \hat{M}_1^\dagger(dt)\hat{M}_1(dt) = \hat{I}. \tag{2.35}$$

This leads to the non-selective evolution

$$\rho(t + dt) = [\hat{I} - (\hat{c}^\dagger \hat{c}/2 + i\hat{H})dt]\rho(t)[\hat{I} - (\hat{c}^\dagger \hat{c}/2 - i\hat{H})dt] + dt\hat{c}\rho\hat{c}^\dagger, \tag{2.36}$$

which, by expanding and collecting the terms, gives the familar differential form

$$\dot{\rho} = -i[\hat{H}, \rho] + \mathcal{D}[\hat{c}]\rho. \tag{2.37}$$

2.1.3 Quantum evolution under measurement

Quantum trajectory

Let us consider the evolution monitored by the two measurement operators in (2.33) and (2.34). The probability of detecting the outcome $r = 1$ is

$$P_1(dt) = \mathrm{Tr}[\hat{M}_1(dt)\rho\hat{M}_1^\dagger(dt)] = dt\,\mathrm{Tr}[\hat{c}^\dagger\hat{c}\rho]. \tag{2.38}$$

Such detection would occur randomly at rate $P_1(dt)/dt$. When a detection occurs, the system undergoes a finite evolution induced by the measurement operator $\hat{M}_1(dt)$.

Denote the number of detections during a period of time from 0 to t by $N(t)$, and assume a pure state $|\psi(t)\rangle$ at time t. Then the stochastic increment $dN(t)$ obeys Itô point process:

$$dN(t)^2 = dN(t), \tag{2.39}$$

$$E[dN(t)] = \langle \hat{M}_1^\dagger(dt)\hat{M}_1(dt)\rangle = dt\langle\psi(t)|\hat{c}^\dagger\hat{c}|\psi(t)\rangle, \tag{2.40}$$

where $E[\cdot]$ denotes the classical expectation value and $\langle\cdot\rangle$ denotes the quantum ensemble average. Eq. 2.40 gives the mean of dN, which is identical to the probability of detecting

a photon in Eq. 2.38.

When a detection occurs $dN(t) = 1$, the state vector evolves to

$$|\psi_1(t+dt)\rangle = \frac{\hat{M}_1(dt)|\psi(t)\rangle}{\sqrt{\langle \hat{M}_1^\dagger(dt)\hat{M}_1(dt)\rangle(t)}} = \frac{\hat{c}|\psi(t)\rangle}{\sqrt{\langle \hat{c}^\dagger\hat{c}\rangle(t)}}. \tag{2.41}$$

When there is no detection $dN(t) = 0$,

$$\begin{aligned} |\psi_0(t+dt)\rangle &= \frac{\hat{M}_0(dt)|\psi(t)\rangle}{\sqrt{\langle \hat{M}_0^\dagger(dt)\hat{M}_0(dt)\rangle(t)}} \\ &= \{\hat{I} - dt[i\hat{H} + \frac{1}{2}\hat{c}^\dagger\hat{c} - \frac{1}{2}\langle \hat{c}^\dagger\hat{c}\rangle(t)]\}|\psi(t)\rangle. \end{aligned} \tag{2.42}$$

Combining Eq. 2.41 and 2.42, one can easily verify that the resulting stochastic evolution can be written explicitly as a nonlinear stochastic Schrodinger equation (SSE):

$$d|\psi(t)\rangle = \big[dN(t)\big(\frac{\hat{c}}{\sqrt{\langle \hat{c}^\dagger\hat{c}\rangle(t)}} - \hat{1}\big) + [1 - dN(t)]dt\big(\frac{\langle \hat{c}^\dagger\hat{c}\rangle(t)}{2} - \frac{\hat{c}^\dagger\hat{c}}{2} - i\hat{H}\big)\big]|\psi(t)\rangle. \tag{2.43}$$

A solution to this equation is referred to as a quantum trajectory for the system. We can simplify the SSE using $dN(t)dt = o(dt)$ to yield

$$d|\psi(t)\rangle = \big[dN(t)\big(\frac{\hat{c}}{\sqrt{\langle \hat{c}^\dagger\hat{c}\rangle(t)}} - \hat{1}\big) + dt\big(\frac{\langle \hat{c}^\dagger\hat{c}\rangle(t)}{2} - \frac{\hat{c}^\dagger\hat{c}}{2} - i\hat{H}\big)\big]|\psi(t)\rangle. \tag{2.44}$$

Now to construct a master equation we first define a projector

$$\hat{\pi}(t) = |\psi(t)\rangle\langle\psi(t)|. \tag{2.45}$$

such that $\rho(t) = E[\hat{\pi}(t)]$. Therefore the equation of motion for each of these projector, also known as the quantum trajectory, gives

$$\begin{aligned} d\hat{\pi}(t) &= |d\psi(t)\rangle\langle\psi(t)| + |\psi(t)\rangle\langle d\psi(t)| + |d\psi(t)\rangle\langle d\psi(t)| \\ &= \{dN(t)\mathcal{G}[\hat{c}] - dt\mathcal{H}[i\hat{H} + \frac{1}{2}\hat{c}^\dagger\hat{c}]\}\hat{\pi}(t), \end{aligned} \tag{2.46}$$

where the superoperator are defined by

$$\mathcal{G}[\hat{r}]\rho = \frac{\hat{r}\rho\hat{r}^\dagger}{\mathrm{Tr}[\hat{r}\rho\hat{r}^\dagger]} - \rho, \tag{2.47}$$

$$\mathcal{H}[\hat{r}]\rho = \hat{r}\rho + \rho\hat{r} - \mathrm{Tr}[\hat{r}\rho + \rho\hat{r}^\dagger]\rho. \tag{2.48}$$

Master equation under homodyne detection

The GKSL master equation (2.37) is invariant under the transformation

$$\hat{c} \to \hat{c} + \gamma; \tag{2.49}$$

$$\hat{H} \to \hat{H} - i\frac{1}{2}(\gamma^*\hat{c} - \gamma\hat{c}^\dagger), \tag{2.50}$$

where γ is an arbitrary complex number. Under this transformation, the measurement operators change accordingly:

$$\hat{M}_1(dt) = \sqrt{dt}(\hat{c} + \gamma), \tag{2.51}$$

$$\hat{M}_0(dt) = \hat{1} - dt[i\hat{H} + \frac{1}{2}(\hat{c}\gamma^* - \hat{c}^\dagger\gamma) + \frac{1}{2}(\hat{c}^\dagger + \gamma^*)(\hat{c} + \gamma)]. \tag{2.52}$$

This implies a rather important property of quantum master equation, that the unravelling of a deterministic master equation into a set of stochastic quantum trajectories is not unique. Physically, the above transformation can be achieved by a homodyne detection, which is a common technique in quantum optics. The homodyne detection scheme describes an input field passing through a beam-splitter with transmittance η. The input field $\hat{c}$ entering one port of the beam-splitter comes out as

$$\hat{c} \to \sqrt{\eta}\hat{c} + \sqrt{1-\eta}\hat{o}, \tag{2.53}$$

where $\hat{o}$ is the operator for the other input field into the other port. In the case of homodyne detection , this other input field is known as the local oscillator with the same frequency as the system dipole, which can be modeled as $\hat{o} = \gamma/\sqrt{1-\eta} + \hat{\nu}$. With η close to unity, (2.53) gives $\hat{c} \to \hat{c} + \gamma$, which is desired for the master equation to remain invariant.

Homodyne detection measures the quadrature of an input field, defined by $\hat{x} = \hat{c} + \hat{c}^\dagger; \hat{y} = -i(\hat{c} - \hat{c}^\dagger)$, depending on the phase difference between the input and local oscillator. For simplicity, we set the coherent field γ to be real, so that the homodyne detection leads to a measurement of the x quadrature of the system. Now the average

rate of detection is

$$E[dN(dt)/dt] = \mathrm{Tr}[(\gamma^2 + \gamma\hat{x} + \hat{c}^\dagger\hat{c})\rho(t)]. \tag{2.54}$$

As we expect, the photodetection rate is the sum of the individual photodetection rates for the local oscillator and the atomic radiation, plus an interference term. Here lies the advantage of homodyne detection: the atomic signal due to the interference terms is boosted by the local oscillator by a factor of $|\gamma|$. This is an enormous advantage if the detector suffers from a low level of background noise (shot noise or dark currents), since the homodyne scheme can raise the signal to a level much larger than background noise.

In the limit that γ is much larger than $\langle\hat{c}^\dagger\hat{c}\rangle$, the stochastic master equation for the conditioned density matrix is

$$d\rho(t) = \{dN(t)\mathcal{G}[\hat{c} + \gamma] - dt\mathcal{H}[i\hat{H} + \gamma\hat{c} + \frac{1}{2}\hat{c}^\dagger\hat{c}]\}\rho(t). \tag{2.55}$$

This also shows that the master equation (2.37) can be unravelled in a completely different manner from the usual quantum trajectory.

In the optimal scenario of homodyne detection, we will consider the local oscillator's amplitude approaches infinity, so the photodetection rate increases infinitely. However, the impact of each detection on the system diminishes to zero because most of the detected photons come from the local oscillator. Consequently, it becomes feasible to approximate the photocurrent as a continuous function of time and derive a smooth evolution equation for the system. The number of detection δN is effectively Gaussian with a mean

$$\mu = [\gamma^2 + \gamma\langle\hat{x}\rangle(t) + O(\gamma^{1/2})]\delta t, \tag{2.56}$$

and variance

$$\sigma^2 = [\gamma^2 + O(\gamma^{3/2})]\delta t. \tag{2.57}$$

Thus, δN can be written as

$$\delta N = \gamma^2\delta t[1 + \langle\hat{x}\rangle/\gamma] + \gamma\delta W, \tag{2.58}$$

where δW is a Wiener increment that satisfies the following

$$E[\delta W] = 0, \tag{2.59}$$

$$E[(\delta W)^2] = \delta t. \tag{2.60}$$

Expanding (2.55) to the powers of γ^{-1}:

$$\delta\rho(t) = \Big\{\delta N(t)\Big(\frac{\mathcal{H}[\hat{c}]}{\gamma} + \frac{\langle\hat{c}^\dagger\hat{c}\rangle(t)\mathcal{G}[\hat{c}] - \langle\hat{x}\rangle(t)\mathcal{H}[\hat{c}]}{\gamma^2} + O(\gamma^{-3})\Big) - \delta t\mathcal{H}[i\hat{H} + \gamma\hat{c} + \frac{1}{2}\hat{c}^\dagger\hat{c}]\Big\}\rho(t), \quad (2.61)$$

where $\mathcal{G}$ and $\mathcal{H}$ are defines as in (2.47) and (2.48). Substitute (2.58) of δN as a Gaussian random variable into (2.61), and keep terms up to $\gamma^{-1/2}$ and let $\delta t \to dt$ yields the stochastic master equation for homodyne detection:

$$d\rho(t) = \{-i[\hat{H}, \rho(t)] + \mathcal{D}[\hat{c}]\rho(t)\}dt + dW\mathcal{H}[\hat{c}]\rho(t), \quad (2.62)$$

where dW is the Wiener process defined previously.

2.2 Classical synchronization

In our everyday life, we are surrounded, consciously or unconsciously, by oscillators. Electrical equipment, fireflies emitting sequences of light pulses, a pacemaker cell that controls the contraction of the human heart – all these and many other systems have one thing in common: they produce rhythms. Most of the time, these systems are not isolated from the environment, but interact with the surroundings and even with each other. This interaction would cause the connected systems to converge to the same rhythm. This phenomenon is called synchronization. Initially, this effect was discovered and studied in different artificial devices, first in pendulum clocks that hang on the same wall and later in musical instruments, electronic circuits, and lasers. It finds various practical implementations in electrical and mechanical fields [DIA12, DUM+12]. What lies in the center of synchronization theory is the class of systems that demostrate self-sustained oscillations [AVK66].

2.2.1 Self-sustained oscillations

Self-oscillations form a special, but rather broad class of all oscillating processes and are characterized by the following features [BJPS09]: 1) the periodic motion of these systems do not damp; 2) these systems do not require external power source/drive to maintain the oscillation; 3) the shape, amplitude, and time scale of these oscillations are determined by the oscillating system alone, and external factors cannot easily change them.

For self-oscillations to occur, the oscillating system must be designed in a special way. The following three features of the self-oscillating systems are most essential: they must be nonlinear systems, there must be dissipation in them, and there must be a source of power to compensate for the dissipation.

First of all, let me explain what are non-linear systems. It is surprisingly true that the vast majority of mathematical equations and natural phenomena are non-linear, with linearity being the exceptional case. While the superposition principle states that any two solutions of a linear equation can be summed to get a new solution, two solutions of a nonlinear equation cannot. It is therefore not surprising that no general analytic approach exists for solving typical nonlinear equations. For instance, when water flows through a pipe at low velocity, its motion is laminar and is characteristic of linear behavior: regular, predictable, and describable in simple analytic mathematical terms. However, when the velocity exceeds a critical value, the motion becomes turbulent, with localized eddies moving in a complicated, irregular, and erratic way that typifies

nonlinear behavior. By reflecting on this and other examples, we can isolate at least three characteristics that distinguish linear and nonlinear physical phenomena:

1. the dynamics itself is qualitatively different. Linear systems typically exhibit smooth and regular motion in space and time, which can be described as well-behaved functions. However, non-linear systems often exhibit a transition from smooth motions to chaotic, erratic, or even apparently random behaviors. Quantitative descriptions of chaos are one of the triumphs of non-linear theory.

2. linear systems usually respond instantly to external stimulation or changes in parameters in direct proportion to the stimulation, as the nature of linearity implies. However, for nonlinear systems, small changes in parameters can lead to enormous qualitative changes in motion. Moreover, the response to external stimulation can differ from that of the stimulation itself, for example, periodic nonlinear systems may exhibit oscillations about half, quarter, or twice the period of stimulation.

3. a localized "lump" or pulse in a linear system is usually decaying and spreading over time. This phenomenon known as dispersion causes waves in linear systems to lose identity and fade out. In contrast, nonlinear systems can have highly coherent, stable localized structures - such as eddies in turbulent flows - that persist either long-term or in some idealized mathematical models at all time.

Dissipation is a mechanism through which energy is lost by the system while it changes its state. It has to be said that most macroscopic systems are dissipative anyway, since there is always some sort of friction in it. The oscillations in such systems are usually associated with the motion of either very small (microscopic) particles like electrons in an atom, or of very large (megascopic) objects like stars and planets. They do oscillate (rotate around their centers) eternally, but just because the energy of their oscillations is not wasted on friction.

Last but not least, self-sustained oscillation is not to be confused with forced oscillations, which they both are represented by closed curves in the phase portraits. Nevertheless, they have an essential difference: the phase on a limit cycle is free, but the phase on a stable closed curve of the forced system is unambiguously related to the phase of the external force.

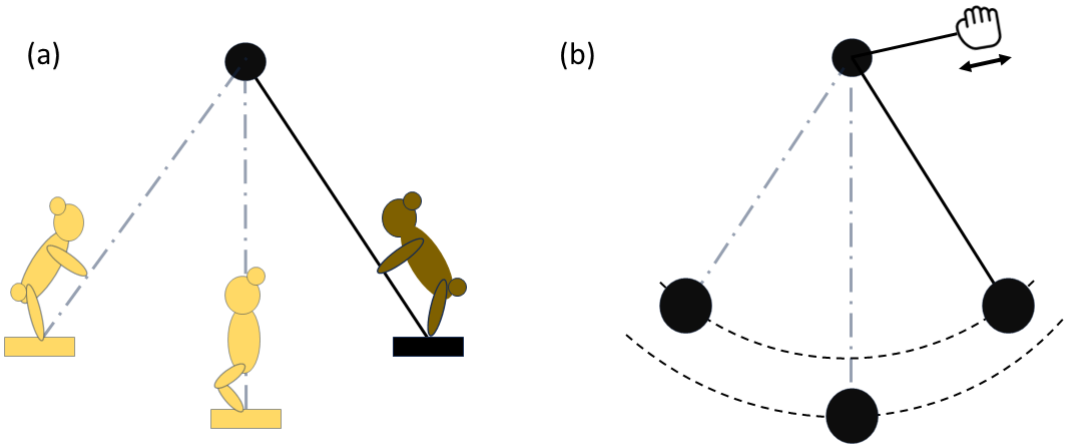

Figure 2.1: (a) A person on a swing represents an example of a self-sustained oscillator. (b) Mechanical swing whose length changes according to a prescribed function of time is a forced system. Phase is free for a self-sustained system (a) and not free for a forced one (b). Therefore, if the two self-sustained system (a) are fixed to a common support, i.e., are weakly coupled, then they can synchronize if their parameters are close. By contrast, the forced system (b) do not synchronize. Figure taken from [PRK01].

2.2.2 Phase portraits and limit cycles

When studying the dynamics of a nonlinear system, it is often convenient to look at the phase portraits. The general form of a vector field on the phase plane is given by

$$\begin{aligned} \dot{x}_1 &= f_1(x_1, x_2) \\ \dot{x}_2 &= f_2(x_1, x_2) \end{aligned} \tag{2.63}$$

where f_1 and f_2 are general functions of the coordinates x_1 and x_2. By flowing along the vector field, a phase point traces out a solution $x(t)$, corresponding to a trajectory winding through the phase plane. For nonlinear systems, there's typically no hope of finding the trajectories analytically. Even when explicit formulas are available, they are often too complicated to provide much insight. Instead we will try to determine the qualitative behavior of the solutions. Our goal is to find the system's phase portrait directly from the properties of $f(x)$.

In the following section, I will use the classical van der Pol equation as an example. The van der Pol equation is an important paradigm in nonlinear theory, which is given

by

$$\ddot{x} + \mu(x^2 - 1)\dot{x} + x = 0 \tag{2.64}$$

where $\mu \geq 0$ controls the nonlinearity. This equation resembles a simple harmonic oscillator, but with a nonlinear damping term $\mu(x^2 - 1)\dot{x}$. This term acts like ordinary positive damping for $|x| > 1$ but like negative damping for $|x| < 1$. In other words, it causes large-amplitude oscillations to decay, but it pumps them back up if they become too small. This leads to a pivotal concept in nonlinear science – limit cycle, an isolated closed trajectory, where the neighboring trajectories either spiral towards or away from it. Stable limit cycles are very important scientifically, and are key to systems that exhibit self-sustained oscillations. These systems oscillate even without external periodic forcing. If the system is slightly disturbed, the system always returns to the normal cycle. Limit cycles are inherently nonlinear phenomena, therefore they can't occur in linear systems. In the van der Pol equation, each μ defines a unique limit cycle. The oscillator provides a universal model to describe the dynamics in the vicinity of a supercritical Hopf bifurcations [GMK12, PVS+18].

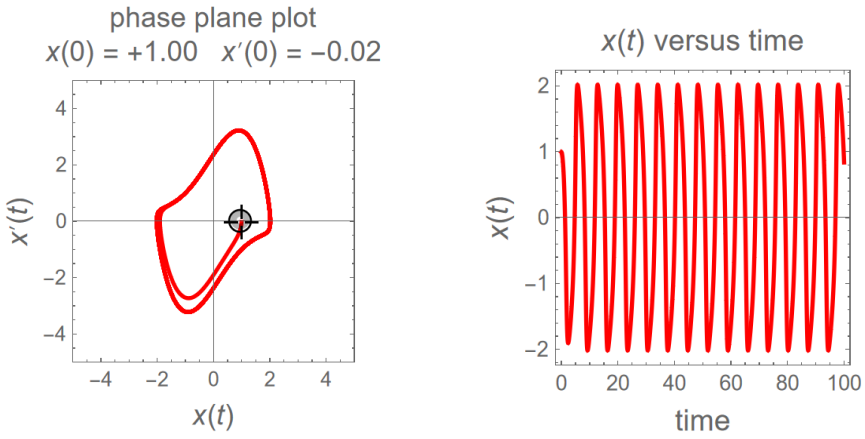

Figure 2.2: The phase portrait of a van der Pol equation, integrate with $\mu = 1.5$ and initial condition $(x, \dot{x}) = (1, 0)$. The limit cycle is not a circle and the stable waveform is not a sinusoidal form.

2.2.3 Synchronization by external force

For sufficiently small detuning, the external force entrains the oscillator, so that the frequency of the driven oscillator becomes equal to the frequency of the force. For detuning exceeding a certain critical value, this equality breaks down. This critical value has been designated as the synchronization region, also known as the Arnold tongue, see Fig. 2.3.

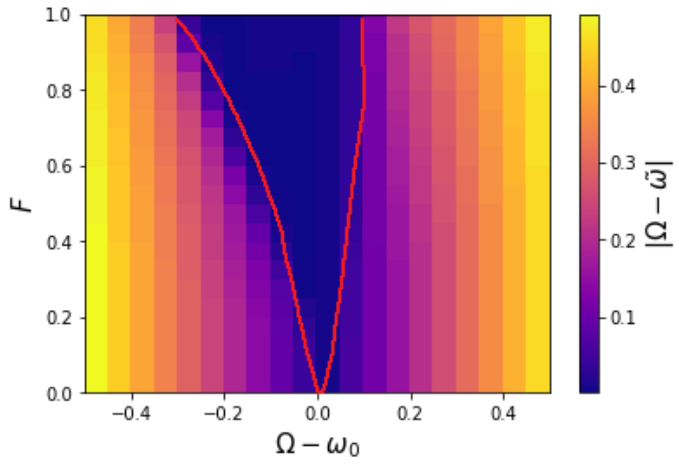

Figure 2.3: Simulation of an Arnold tongue of a quantum Stuart-Landau oscillator in Eq. 2.65 with $\gamma_2/\gamma_1 = 10$, where ω_0 is the natural frequency of the oscillator and $\tilde{\omega}$ denotes the observed frequency of the oscillator, after the external force is applied. The frequency and amplitude of the force is denoted by Ω and F respectively. For a fixed value of the force amplitude F, $\Omega - \tilde{\omega}$ is exactly zero near the frequency of the autonomous oscillator ω_0. This is called frequency locking. The $\Omega - \tilde{\omega}$ vs. $\Omega - \omega_0$ and driving amplitudes F and determined the domain where the frequency of the driven oscillator $\tilde{\omega}$ is equal to the drive Ω. This blue area is known as the Arnold tongue.

2.2.4 Synchronization between two and more oscillators

It was in two mutually coupled oscillators that the synchronization phenomenon was first discovered, by the observation of two pendulum clocks on the same wall.

Frequency locking occurs when the two system interacting are nonsymmetrical. Let us denote the frequencies of the two systems as ω_1 and ω_2 respectively, and assume $\omega_1 > \omega_2$. The observed frequencies of the interacting oscillators are $\Omega_{1,2}$. If the interaction is sufficiently strong, frequency locking occurs as $\omega_1 > \Omega_1 = \Omega_2 > \omega_2$.

Another synchronization setting is phase locking. Consider two nearly identical, symmetrically coupled oscillators. If the interaction is weak, then, in full analogy to the case of external forcing, we can assume that it influences only the phases, shifting the points along the limit cycles, but not the amplitudes. The interaction depends in some way on the two phases, and the two simplest cases are when coupling either brings the phases together. Clearly, the phase-attractive interaction leads to in-phase synchronization, whereas the phase-repulsive one results in anti-phase (out-of-phase) synchronization.

Amplitude death

Along with synchronization, another important emerging phenomenon is the complete suppression of oscillations, officially referred to as amplitude death (AD). This is the total suppression of oscillations. Oscillations throughout the system stop as a result of the interaction and lead to stationary behavior. When oscillations stop, AD has two possibilities. When the coupled systems have exactly the same equilibrium, the occurrence of an amplitude death implies that this equilibrium becomes asymptotically stable. However, coupled systems can have more than one stationary state, and then a new fixed point that is not stable (or may not even exist) in the uncoupled system can be stabilized.

Amplitude death in coupled oscillators has important implications for a variety of disciplines. In physics, it provides insights into the stability and dynamics of complex networks and helps to identify critical coupling strengths for synchronization suppression. In biology, amplitude death in neural networks has been observed in brains, which may influence neuronal firing coordination and contribute to information processing and pattern formation. Additionally, amplitude death has implications for engineering applications, such as secure communication and the design of electronic circuits with controlled oscillation dynamics.

2.3 Quantum Synchronization

As we have mentioned, the notion of synchronization in classical oscillatory systems has a long history and is a cornerstone in the field of nonlinear dynamics. The subject was later extended to quantum systems, and has received much interest since then.

In particular, the current paradigm for continuous-variable quantum synchronization is the so-called quantum van der Pol oscillator [WNB14, LS13, WNB15], described by the master equation,

$$\dot{\rho} = -i[\omega_0 a^\dagger a, \rho] + \gamma_1 \mathcal{D}[a^\dagger]\rho + \gamma_2 \mathcal{D}[a^2]\rho, \tag{2.65}$$

where $\mathcal{D}[\mathcal{O}]\rho = \mathcal{O}\rho\mathcal{O}^\dagger - \frac{1}{2}(\mathcal{O}^\dagger\mathcal{O}\rho - \rho\mathcal{O}^\dagger\mathcal{O})$. The steady state of which is rotationally symmetric in phase space (a circular limit cycle). Its analytical solutions have also been obtained in the deep quantum limit. This makes the Stuart-Landau oscillator much simpler to analyze, and has thus served as a starting point in the literature on quantum synchronization for continuous-variable systems, e.g. Refs. [LS13, WNB14, SHM+18, MKH20, LCW14, BOZ+15, WWM17, WNB15, MH15, IK17, AKLB18, BKBB20, BKB21, KYN19, KN20, BB21]. Despite the success in the current literature, it is really a quantum analogue of the Stuart-Landau oscillator [ZSZK21] which is an approximation of the van der Pol oscillator to first order. The trade-off of course, is that effects taking place at large nonlinearities are excluded. A prominent example is relaxation oscillations in the undriven van der Pol oscillator. To observe relaxation oscillations in quantum theory one needs to quantize the exact van der Pol model, and it is only relatively recently that such efforts have been made [SCVC15, CKN20, BACL21]. More effects start to appear if driving is included, such as quasi-periodicity and chaos [BT11, LR12, Moo08], both of which are absent in the driven Stuart-Landau oscillator. However, due to its nature of infinite-dimensional Hilbert space, numerical explorations are limited to single externally driven oscillator. Only recently, the model was modified to allow numerical simulations of a pair of mutually coupled oscillators [SMN+23].

Another approach to explore quantum synchronization beyond numerics is to look at spin systems. In [RB18], the single spin 1, with a Hilbert space dimension of 3, has been identified as the smallest system that can develop a limit cycle. From there, several analytical frameworks have been developed [KR19, BBJ22]. In this thesis, I will mainly focus on the oscillator model of synchronization.

2.3.1 Quantum synchronization by external force

In this section, let us consider the harmonically driven quantum van der Pol oscillator, for which the master equation reads:

$$\dot{\rho} = -i[-\Delta\hat{a}^\dagger\hat{a} + i\Omega(\hat{a} - \hat{a}^\dagger), \rho] + \gamma_1\mathcal{D}[\hat{a}^\dagger]\rho + \gamma_2\mathcal{D}[\hat{a}^2]\rho, \tag{2.66}$$

where Δ is the frequency detuning between the drive and the undriven oscillator, Ω is the driving amplitude. Similar to the phase portrait in classical theory, we can visualize the steady-state dynamics by using quasi-probability distributions, such as the Wigner function in Fig. 2.4. These distributions capture the characteristic of the classical model, hence proven useful to study phase locking in a driven oscillator. The inconvenient difference is that in the quantum models, quantum noise caused by uncertainty in the phase space is inevitable. The corresponding phase distribution is defined based on the Susskind-Glogower formalism [SG64]:

$$P(\Phi) = \frac{1}{2\pi}\langle\Phi|\rho|\Phi\rangle \tag{2.67}$$

where $|\Phi\rangle = \sum_{n=0}^{\infty} e^{in\Phi}|n\rangle$ represent sum over all Fock state $|n\rangle$. For a undriven van der Pol oscillator, the steady-state Wigner function figures a rotionally symmetric limit cycle, hence its phase distribution is a constant of $1/2\pi$. A driven oscillator, however, develops a preferred "region" of phases in the steady-state, as shown by the peaked phase distribution.

Another aspect of synchronization is frequency entrainment (locking). This is usually done finding the peak in the oscillator's power spectrum:

$$S(\omega) = \int_{-\infty}^{\infty} dt\, e^{i\omega t}\langle\hat{a}^\dagger(t)\hat{a}(0)\rangle, \tag{2.68}$$

where $\langle\cdot\rangle$ denotes the average with respect to the full steady-state density matrix.

2.3.2 Quantum synchronization between two oscillators

It is known that two classical van der Pol oscillator coupled together would spontaneously lock their phase. In the quantum regime, there are various schemes to couple two quantum oscillators, two of the popular choices are dissipative and reactive coupling.

Reactive coupling between two quantum van der Pol oscillator was first explored in

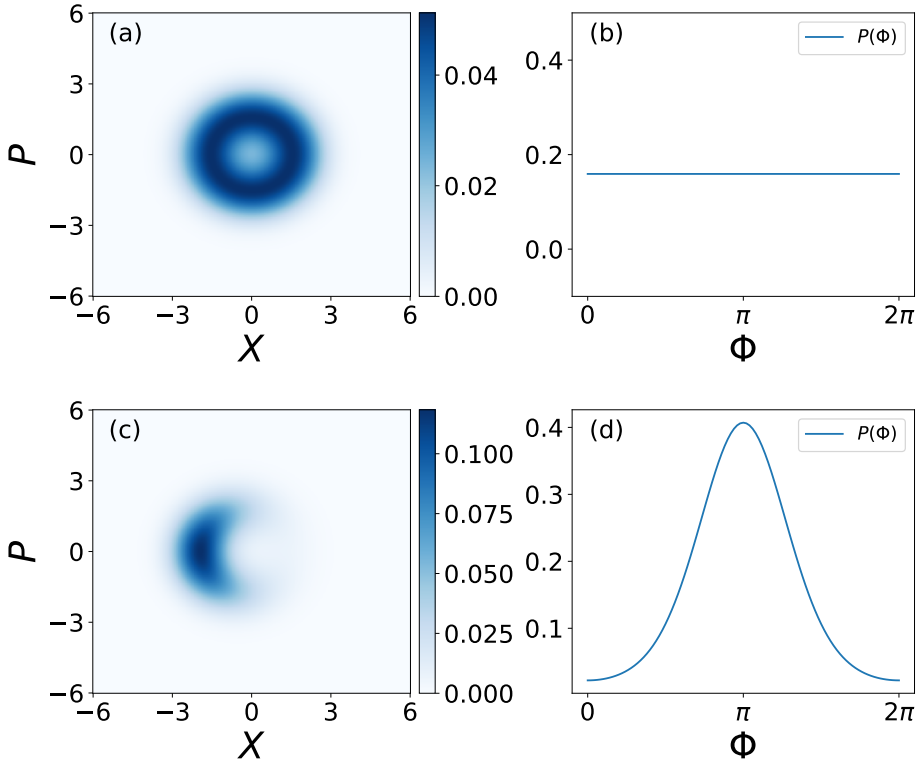

Figure 2.4: Quasi-probability distributions (Wigner functions) and the corresponding phase distributions $P(\phi)$, for (a)-(b) undriven and (c)-(d) driven quantum Stuart-Landau model.

[LS13], with a coherent coupling Hamiltonian

$$\hat{H} = V(\hat{a}_1^\dagger \hat{a}_2 + \hat{a}_1 \hat{a}_2^\dagger), \tag{2.69}$$

where V denoted the coupling strength and $a_{1,2}$ the bosonic operators of the two quantum oscillators respectively.

Dissipative coupling, on the other hand, introduces a dissipator term in the master equation:

$$\dot{\rho} = \mathcal{L}_0 \rho + \eta \mathcal{D}[\hat{a}_1 \pm \hat{a}_2]\rho \tag{2.70}$$

with η the coupling strength, while the term in the dissipator can represent different configurations – "-" for phase synchronization and "+" for anti-phase synchronization. More details on the interplay between different oscillators and coupling schemes will be given in Chapter. 6.

2.4 Theory of cQED

Since the first observation of coherent quantum behaviour in a superconducting qubit more than 20 years ago [MNAU02], there have been substantial advancements in the field of superconducting quantum circuits. One such development is the introduction of circuit QED, which borrows concepts from cavity QED to superconducting circuits [BGW+07, BGGW21]. This approach realizes in a single architecture the essential requirements for quantum computation, and has already been used to run simple quantum algorithms by controlling tens of superconducting qubits simultaneously [BCLK+22]. The superconducting qubits are controlled and manipulated using microwave pulses, which can perform various single-qubit and multi-qubit operations. The qubits can be coupled together to create entanglement, a crucial resource for quantum computing. The coupling between qubits is typically achieved using resonator circuits through capacitive or inductive coupling, enabling the transfer of quantum information between qubits. Over the years, this exploration has grown and given rise to experiments in which controls of the quantum state of single particles are now possible, as well as providing exquisitely precise tools to probe the counter-intuitive nature of quantum physics [HWA+08, HWA+09].

What lies at the heart of cQED is the electric LC circuit. In classical circuit theory, a simple LC oscillator consists of a capacitor C in parallel with an inductor L, which behaves like a classical harmonic oscillator. The capacitor stores electrical energy of $\frac{1}{2}CV^2$ and the inductor stores magnetic energy of $\frac{1}{2}LI^2$. Using the simple relation of $Q = CV$ and $\Phi = IL$, the total energy stored in the circuit is given by:

$$E_{tot} = \frac{1}{2L}\Phi^2 + \frac{1}{2C}Q^2. \tag{2.71}$$

This gives the classical Hamiltonian for the circuit.

The quantization of the classical description of electrical circuit to its quantum analog is straightforward within the Hamiltonian framework. Moving into quantum regime, the classical variables are replaced by the corresponding operators:

$$\Phi \to \hat{\Phi},$$
$$Q \to \hat{Q},$$

thus we get the quantum Hamiltonian:

$$\hat{H} = \frac{\hat{\Phi}}{2L} + \frac{\hat{Q}^2}{2C}. \tag{2.72}$$

The pairs of operators $\hat{\Phi}$ and $\hat{Q}$ correspond to conjugate variables P and X in quantum harmonic oscillators, which have to satisfy the commutation relation:

$$[\hat{\Phi}, \hat{Q}] = i\hbar. \tag{2.73}$$

This relation arises from the quantization of the electromagnetic field and corresponds to the fundamental commutator for conjugate variables.

The LC oscillator can now be treated quantum mechanically. Introducing the usual annihilation and creation operators with $[a, a^\dagger] = 1$, we have

$$\hat{\Phi} = \Phi_{ZPF}(a + a^\dagger), \tag{2.74}$$

$$\hat{Q} = \frac{1}{i} Q_{ZPF}(a - a^\dagger), \tag{2.75}$$

such that Eqn.2.72 becomes

$$\hat{H} = \frac{\hbar\omega_0}{2}(a^\dagger a + a a^\dagger) = \hbar\omega_0(a^\dagger a + \frac{1}{2}), \tag{2.76}$$

where

$$\omega_0 = \sqrt{\frac{1}{LC}}, \tag{2.77}$$

$$Z_0 = \sqrt{\frac{L}{C}}, \tag{2.78}$$

$$\Phi_{ZPF} = \sqrt{\frac{\hbar Z_0}{2}}, \tag{2.79}$$

$$Q_{ZPF} = \sqrt{\frac{\hbar}{2Z_0}}, \tag{2.80}$$

Φ_{ZPF} and Q_{ZPF} represent the zero point fluctuations (standard deviations) of the flux and charge of the ground state.

Although the linear LC oscillator is simple to build, it is challenging to perform any coherent control or measurement with such linear systems, let along encoding and manipulating quantum information in these systems. Fortunately, there is a device that would allow to introduce nonlinearity in quantum circuits. In particular, the Josephson

junction (an insulating barrier sandwiched by two superconducting electrodes) is a nonlinear circuit element that is perfect for the job – it is compatible with modern wafer fabrication process, has very low loss and injects a right amount of nonlinearity to the circuit.

A Josephson junction allows a dissipation-less current, a supercurrent, to flow between the two superconducting electrodes, and the supercurrent is given by the first Josephson relation $I = I_c \sin\phi$, where I_c is the critical current and ϕ the phase difference between the two superconducting condensates across the junction. The critical current is the maximal current that can be supported before Cooper pairs break free. When the supercurrent exceeds the critical value, dissipation will kick in and a finite voltage develops across the junction with a resistive current. The phase difference ϕ across the junction has a time dependence to the voltage across it, according to $d\phi/dt = 2\pi V/\Phi_0$ (second Josephson relation), where $\Phi_0 = h/2e$ is the flux quantum. Using the two Josephson relations, the Josephson inductance can be defined as

$$L_j(\Phi) = \left(\frac{\partial I}{\partial \Phi}\right)^{-1} = \frac{\Phi_0}{2\pi I_c} \frac{1}{\cos 2\pi\Phi/\Phi_0}. \tag{2.81}$$

As a result, when operating below the critical current, the Josephson junction can be thought of as a nonlinear inductor.

Cooper-pair box

Replacing the linear inductor in a common LC oscillator by a Josephson junction makes a nonlinear LC oscillator known as the Cooper-pair box, see Fig.2.5. In this case the energy levels of the circuit are no longer equally spaced. If the nonlinearity

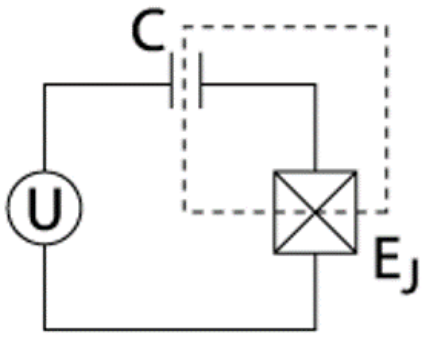

Figure 2.5: Circuit diagram of a Cooper-pair box qubit

and the quality factor of the junction are large enough, the energy spectrum resembles that of an atom, with well-resolved spectral lines. Therefore such type of circuit is refered to as an artificial atom.

Now let's see how the Hamiltonian of the circuit is modified by the presence of the nonlinear Josephson element. The energy stored in a linear inductor is given by $E = \int dtV(t)I(t) = \int dt(d\Phi/dt)I = \Phi^2/2L$, the energy of the nonlinear inductance takes the form

$$E = I_c \int dt(\frac{d\Phi}{dt}) \sin(\frac{2\pi}{\Phi_0}\Phi) = -E_j \cos(\frac{2\pi}{\Phi_0}\Phi), \tag{2.82}$$

with $E_j = \Phi_0 I_c/2\pi$ the Josephson energy. Adding up the capacitive energy stored in the linear capacitor, the total Hamiltonian of this circuit reads

$$\hat{H} = \frac{Q^2}{2C_J} - E_j \cos(\frac{2\pi}{\Phi_0}\Phi). \tag{2.83}$$

We can also re-express this Hamiltonian in a completely equivalent form using the alternative number and phase variables, defined by $Q = 2e\hat{N}$ and $\Phi = \phi_0\hat{\phi}$:

$$\hat{H} = E_c\hat{N}^2 - E_j \cos\hat{\phi}. \tag{2.84}$$

where $\hat{N}$ and $\hat{\phi}$ obey the commutation relation: $[\hat{\phi}, \hat{N}] = i$.

Next we consider applying a gate voltage to bias the electrode potential of the cooper-pair box, as a method of controlling the qubit. The gate voltage induces a gate charge Q_g on the electrode of the gate capacitor which is attached to the island. As a result, the cooper-pair box charging energy is lowered to $Q - Q_g$. The Hamiltonian under the gate voltage is therefore:

$$\begin{aligned} \hat{H} &= \frac{(Q-Q_g)^2}{2C_\Sigma} - E_j \cos(\frac{2\pi}{\Phi_0}\Phi) \\ &= E_C(\hat{N} - N_g)^2 - E_J \cos\hat{\phi}, \end{aligned} \tag{2.85}$$

where $C_\Sigma = C_g + C_J$ is the total capacitance and $N_g = Q_g/2e$ is the number of cooper pairs on the electrode, including the junction's capacitance C_J and the shunt capacitance C_g.

Transmon qubit

Fig. 2.6 shows the energy difference $\omega_j - \omega_0$ for the three lowest energy levels for different ratios E_J/E_C as obtained by numerical diagonalization of Eq. 2.85. Different ratios

of E_J/E_C correspond to different types of superconducting qubits [CW08, BGGW21]. Regardless of the parameter regime, one can always express the Hamiltonian in the diagonal form $\hat{H} = \sum_j \hbar\omega_j |j\rangle\langle j|$ in terms of its frequencies ω_j and eigenstates $|j\rangle$.

In the regime where the charging energy dominates($E_J/E_C < 1$), the eigenstates of the Hamiltonian is approximately given by eigenstates of the charge operator, $|j\rangle \simeq |n\rangle$, with $\hat{n}|n\rangle = n|n\rangle$. In this situation, a change in gate charge n_g has a large impact on the transition frequency of the device. As a result, unavoidable charge fluctuations in the circuit's environment lead to corresponding fluctuations in the qubit transition frequency and consequently causing dephasing.

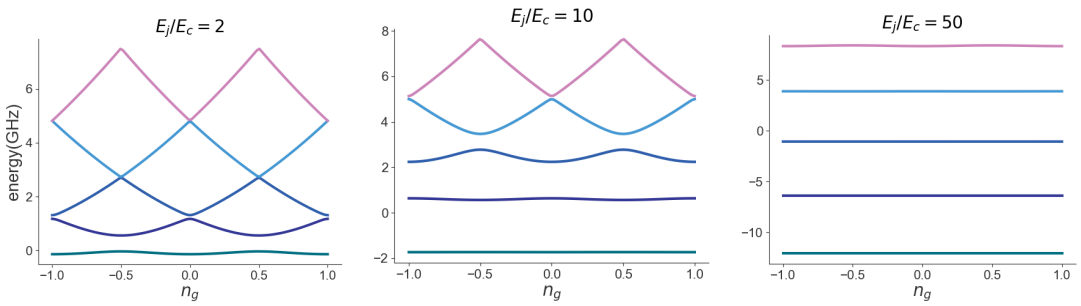

(a) **(b)** **(c)**

Figure 2.6: Frequency difference $\omega_j - \omega_0$ for the first three energy levels of the transmon Hamiltonian obtained from numerical diagonalization of Eqn. 2.85 expressed in the charge basis $|n\rangle$ for different E_j/E_c ratios. For large values of E_j/E_c the energy levels become insensitive to the offset charge.

To mitigate this problem, a solution is to work in the transmon regime where the ratio E_J/E_C is large (typically 20 - 80) [KYG+07]. In this situation, the charge degree of freedom is highly delocalized due to the large Josephson energy. Because of this, the first energy levels of the device become essentially independent of the gate charge. It can in fact be shown that the charge dispersion, which describes the variation of the energy levels with gate charge, decreases exponentially with E_J/E_C in the transmon regime [KYG+07]. The net result is that the coherence time of the device is much larger than at small E_J/E_C. However, the price to pay for this improvement in the coherence time is the reduced anharmonicity of the transmon qubit. Anharmonicity is required to control the qubit without exciting unwanted transitions.

For $E_j/E_c \gg 1$, the nonlinear correction of the Josephson junction to its harmonic potential can be truncated to first order, by Taylor expanding Eq. 2.85:

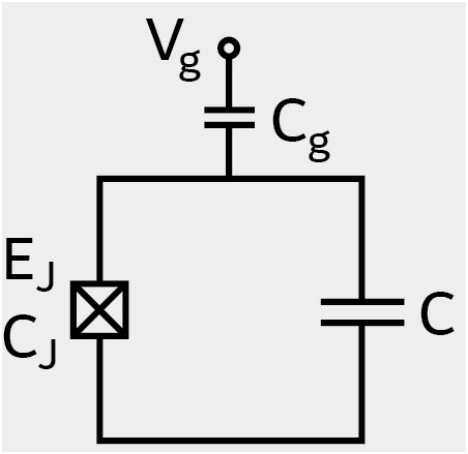

Figure 2.7: Circuit schematics of a Transmon qubit

$$\hat{H} = 4E_C\hat{n}^2 + \frac{1}{2}E_j\hat{\varphi}^2 - \frac{1}{4!}E_J\hat{\varphi}^4. \tag{2.86}$$

As expected from the above discussion, the transmon is thus a weakly anharmonic oscillator. It is then instructive to introduce creation and annihilation operators $b^\dagger$ and b that diagonalize the first two terms of Eq. 2.86:

$$\hat{\varphi} = (\frac{2E_C}{E_J})^{1/4}(b^\dagger + b), \tag{2.87}$$

$$\hat{n} = \frac{i}{2}(\frac{E_j}{2E_C})^{1/4}(b^\dagger - b). \tag{2.88}$$

Using these expressions in Eq. 2.86 leads to:

$$\hat{H} = \sqrt{8E_CE_J}b^\dagger b - \frac{E_C}{12}(b^\dagger + b)^4 \tag{2.89}$$

$$\approx \hbar\omega_q b^\dagger b - \frac{E_C}{2}b^\dagger b^\dagger bb, \tag{2.90}$$

where $\hbar\omega_q = \sqrt{8E_CE_J} - E_C$.

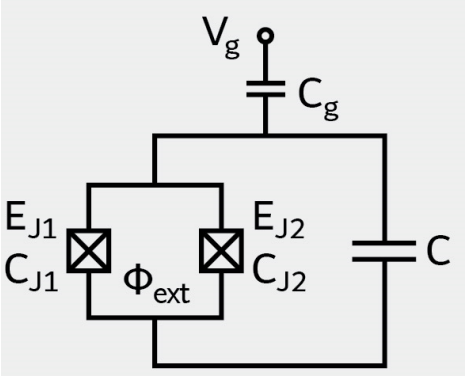

Figure 2.8: Circuit schematics of a tunable Transmon qubit

Tunable-transmon qubit

A useful variation of the transmon qubit is the flux-tunable transmon, which consists of two parallel Josephson junctions forming a SQUID shunted by a large capacitor, see Fig. 2.8. The Hamiltonian reads

$$\hat{H}_{tr} = 4E_c\hat{n}^2 - E_{j1}\cos\hat{\varphi}_1 - E_{j2}\cos\hat{\varphi}_2 \tag{2.91}$$

where E_{ji} is the Josephson energy of two junctions and $\hat{\varphi}_i$ are the phase differences across the junctions. In the presence of an external flux Φ_{tr}, the last two terms can be combined into $E_j(\Phi_{tr})\cos(\hat{\varphi})$ where [KYG+07, BGGW21]

$$E_j(\Phi_{tr}) = E_\Sigma \cos(\frac{\pi\Phi_{tr}}{\Phi_0})\sqrt{1 + d^2\tan^2(\frac{\pi\Phi_{tr}}{\Phi_0})}\,, \tag{2.92}$$

with $E_\Sigma = E_{j1}+E_{j2}$, $d = (E_{j1}-E_{j2})/E_\Sigma$ and average phase difference $\hat{\varphi} = (\hat{\varphi}_1+\hat{\varphi}_2)/2$. In the transmon regime we introduce the quantization of the operators

$$\hat{\varphi} = \Phi_0\left(\frac{2E_c}{E_j(\Phi_{tr})}\right)^{1/4}(b^\dagger + b)\,, \tag{2.93}$$

$$\hat{n} = i\left(\frac{E_j(\Phi_{tr})}{32E_c}\right)^{1/4}(b^\dagger - b)\,, \tag{2.94}$$

the Hamiltonian can be approximated as

$$\hat{H}_{tr} = \omega_{tr}b^\dagger b - \frac{E_c}{2}b^\dagger b^\dagger bb, \tag{2.95}$$

with frequency $\omega_{tr} = \sqrt{8E_cE_j(\Phi_{tr})} - E_c$.

2.4.1 Quantum theory of light-matter interaction

Recent progress has demonstrated the interactions in circuit QED experiments can reach the regimes of strong, ultrastrong and even deep-strong, characterized by the increasing coupling strengths between the qubit (i.e. atom) and resonator (i.e. field) [NDH+10, YFA+17, KML+19, FDLR+19, HBR20, BGO20]. The system is considered in strong coupling regime when the coupling strength exceeds the system loss. Whereas ultrastrong coupling regime is achieved when the coupling strength becomes comparable to the system bare frequencies and exceeds the system frequencies in the deep-strong regime [NC11, PFDSGR10, RVBSS17]. In the strong coupling regime, the interactions can be treated as perturbations to the free energy system Hamiltonian. And the system is governed by the renowned Jaynes-Cummings model [JC63], which can be easily diagonalized thanks to its continuous $U(1)$ symmetry and conservation of total number of excitations. However, Jaynes-Cummings model fails once the system enters ultrastrong coupling regime. Instead the system is modeled by the quantum Rabi Hamiltonian, where parity, rather than the number, of excitations is conserved. The ground state of quantum Rabi model (QRM) has no closed-form solutions and consists of non-classical highly entangled states of interacting atoms and fields [Bra11, BMS+17]. The ultrastrong coupling regime of circuit QED is now an active field of research, from which novel physics and potential applications are rapidly emerging [RBW+12, KFR+15, SCN20].

2.4.2 Qubit-resonator Coupling Schemes

Superconducting qubits are generally classified into two types: flux type and charge type. The qubit-resonator interaction can be of inductive (which includes galvanic coupling) or capacitive nature. Generally speaking, the capacitive interaction is determined by the mutual capacitance between the two coupled circuits. Similarly, geometric inductive couplings are given by the mutual qubit-resonator inductance. Galvanic couplings are given by the superconducting phase drop that is developed across the shared mutual inductance between the two circuits. Detailed formulations of these two types of coupling are summarized in Table. 2.1 & 2.2. It is possible to reach ultrastrong couplings with both capacitive and galvanic interactions, with quite different fundamental limits imposed for each type.

Capacitive coupling

Capacitive Coupling

Figure	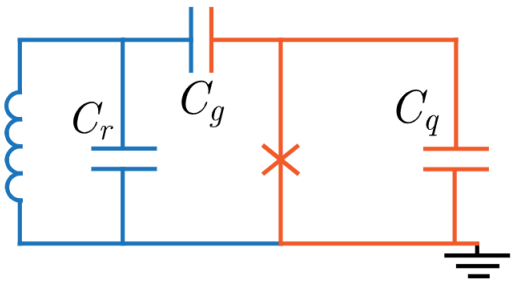	
Qubit	CPB	Transmon
Hamiltonian	$\hat{H}_{int} = 2e\frac{C_g}{C_g+C_q}V_{rms}\sigma_x(a+a^\dagger)$	$\hat{H}_{int} = e\frac{C_g}{C_g+C_q}\left(\frac{E_j}{2E_c}\right)^{\frac{1}{4}}V_{rms}\sigma_x(a+a^\dagger)$
Coupling ratio	$\frac{g^{CPB}}{\omega_r} = \frac{C_g}{C_g+C_q}\sqrt{\frac{2}{\pi^3}}\sqrt{\frac{Z_r}{Z_{vac}}}\alpha^{1/2}$	$\frac{g^{Tr}}{\omega_r} = \frac{C_g}{C_g+C_q}\sqrt{\frac{1}{\pi^3}}\left(\frac{E_j}{8E_c}\right)^{\frac{1}{4}}\sqrt{\frac{Z_r}{Z_{vac}}}\alpha^{1/2}$
Coupling limit	$\frac{g^{CPB}}{\omega_r} = \frac{2C_g}{\sqrt{C_r(C_q+C_g)+C_g(C_g+C_q)}}\sqrt{\frac{E_c}{E_j}}$ $< 2\sqrt{\frac{E_c}{E_j}}$	$\frac{g^{Tr}}{\omega_r} = \frac{0.2C_g}{\sqrt{C_r(C_q+C_g)+C_g(C_g+C_q)}} < 0.2$ for $\frac{E_j}{E_c} = 50$

Table 2.1: Summary of capacitive coupling

Capacitive coupling has been the most widely used coupling scheme with all types of superconducting qubits. This type of coupling is proportional to the root mean square (rms) voltage $\hat{V}$ in the ground state of the resonator mode with frequency ω_r

and capacitance C_r :

$$V_{rms} = \langle 0|\hat{V}^2|0\rangle^{1/2} = \sqrt{\frac{\hbar\omega_r}{2C_r}} = \omega_r\sqrt{\frac{\hbar Z}{2}}, \tag{2.96}$$

which scales as $\sqrt{Z}$, where Z is the impedance of the resonator mode coupled to the qubit [Gir11]. This scaling already points to high-impedance resonators to reach the USC regime.

The general interaction Hamiltonian for capacitive coupling is expressed as:

$$\hat{H}_{int} = -2e\hat{N}\frac{C_g}{C_\Sigma}V_{rms}(a^\dagger + a), \tag{2.97}$$

which is general and applies to all types of charge-based qubits, such as the CPB and the transmon. The factor $2e\hat{N}$ plays the role of the qubit dipole moment. One can picture this dipole moment as a charge $2e$ moving between the two plates of the capacitor where an external voltage $\hat{V}_{ext}$ has been induced by the external circuit [DGS07].

Galvanic coupling

Galvanic coupling

Type	External (Inductive)	Internal (Embeded)	
	Flux qubit	Flux qubit	Charge qubit
Figure	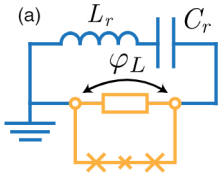	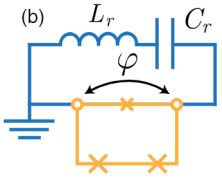	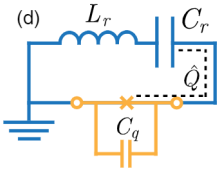
Hamiltonian	$\hat{H}_{int} = LI_pI_{rms}\sigma_x(a + a^\dagger)$ $= \hbar g\left(\frac{\epsilon}{\omega_q}\sigma_z - \frac{\Delta}{\omega_q}\sigma_x\right)(a + a^\dagger)$		$\hat{H}_{int} = -2e\hat{N}V_{rms}(a + a^\dagger)$
Coupling ratio	$\frac{g}{\omega_r} = \frac{1}{8}\langle 0\|\hat{\phi}\|1\rangle\sqrt{\frac{Z_{vac}}{\pi Z_r}}\alpha^{-1/2}$		$\frac{g}{\omega_r} = \frac{C_r}{C_q+C_r}\frac{\langle 0\|\hat{Q}\|1\rangle}{e}\sqrt{2\pi\frac{Z_r}{Z_{vac}}}\alpha^{1/2}$

Table 2.2: Summary of galvanic coupling

Two systems are galvanically coupled when they share a portion of their respective circuits. Here we distinguish two types of galvanic couplings based on the amount of circuit shared: (a) sharing a linear inductance (inductive) and (b) embedding the

qubit directly into the resonator circuit (embeded). The general picture is that the qubit and resonator share a circuit element, the latter case being the entire qubit itself. In both situations, the qubit-resonator coupling is then given by the superconducting phase drop across the shared circuit element $\hat{\varphi}$, which itself is a new degree of freedom of the circuit.

Coupling to the phase $\hat{\varphi}$ involves the rms current $\hat{I}$ in the ground state of the resonator mode with frequency ω and inductance L_r:

$$I_{rms} = \langle 0|\hat{I}^2|0\rangle^{1/2} = \sqrt{\frac{\hbar\omega_r}{2L_r}} = \omega_r\sqrt{\frac{\hbar}{2Z}}. \tag{2.98}$$

The interaction Hamiltonian in this case is written as:

$$\hat{H}_{int} = LI_pI_{rms}\sigma_x(a^\dagger + a), \tag{2.99}$$

where $I_p = \langle 0|\hat{I}|1\rangle$ is the persistent current in the qubit loop.

2.5 Quantum Fisher information

Fisher information has been used as a measure of the ability to estimate an unknown parameter or as a measure of the state of disorder of a system [Fri90, Fri04]. The quantum Fisher information (QFI) serves as a crucial measure in quantum parameter estimation, providing insights into the precision with which a quantum system can estimate an unknown parameter. In this section, we review the key concepts and properties of QFI, highlighting its significance and applications in quantum information science.

QFI quantifies the amount of information that a quantum system carries about an unknown parameter. It quantifies the ultimate precision achievable in estimating the parameter by exploiting the quantum resources encoded in the system. QFI is defined as the variance of the derivative of the quantum state with respect to the parameter, weighted by the inverse of the probability distribution. Mathematically, QFI can be expressed as the expectation value of the squared symmetric logarithmic derivative (SLD) operator L_λ squared [Par09]:

$$F(\lambda) = \mathrm{Tr}[\rho_\lambda L_\lambda^2], \tag{2.100}$$

with SLD L_λ as the self-adjoint operator satisfying the equation

$$\frac{L_\lambda \rho_\lambda + \rho_\lambda L_\lambda}{2} = \frac{\partial \rho_\lambda}{\partial \lambda}. \tag{2.101}$$

Another definition that is useful in numerical simulation gives

$$F[\rho, \hat{A}] = 2 \sum_{k,l} \frac{(\lambda_k - \lambda_l)^2}{(\lambda_k + \lambda_l)} |\langle k|\hat{A}|l\rangle|^2, \tag{2.102}$$

where $\lambda_{k,l}$ and $|k, l\rangle$ are the eigenvalues and eigenvectors of the density matrix ρ, and $\hat{A}$ is the observable for the system to estimate.

QFI is closely related to the quantum Cramér-Rao bound (QCRB), which establishes a lower bound on the uncertainty in estimating the parameter. The QCRB states that the variance of any unbiased estimator of the parameter cannot be smaller than the inverse of the QFI. Therefore, QFI sets the fundamental limit on the precision of parameter estimation in quantum systems.

QFI also has a geometric interpretation [SK20]. It corresponds to the curvature of the quantum state manifold induced by the parameter variation. The distance between

quantum states within this manifold can be related to the distinguishability of different parameter values. Higher values of QFI imply a more curved and informative manifold, enabling more precise estimation of the parameter.

QFI finds applications in various areas of quantum information science. In quantum sensing, QFI provides a measure of the sensitivity of a quantum sensor to external perturbations, enabling the development of high-precision measurement devices. QFI is also relevant in many-body entanglement [HQGY21, DPBE23], and quantum error correction [LYO15, HPJ22], where accurate estimation of parameters is essential.

Chapter 3

Fisher information as general metrics of quantum synchronization

Quantum synchronization has emerged as a crucial phenomenon in quantum nonlinear dynamics with potential applications in quantum information processing. Multiple measures for quantifying quantum synchronization exist. However, there is currently no widely agreed metric that is universally adopted. This chapter presents a proposal of using classical and quantum Fisher information (FI) as alternative metrics to detect and measure quantum synchronization. We establish the connection between FI and quantum synchronization, demonstrating that both classical and quantum FI can be deployed as more general indicators of quantum phase synchronization, in some regimes where all other existing measures fail to provide reliable results. We show advantages in FI-based measures, especially in 2-to-1 synchronization. Furthermore, we analyze the impact of noise on the synchronization measures, revealing the robustness and susceptibility of each method in the presence of dissipation and decoherence. Our results offer valuable insights for understanding and exploiting quantum synchronization.

3.1 Oscillator model and synchronization measures

We study the quantum van der Pol oscillator (also known as the quantum Stuart-Landau oscillator [SMN+23]) subjected to both single photon drive and two photon squeezing drive. The master equation in the rotating frame of the drive gives (with

This chapter is published substantially as "Fisher Information as General Metrics of Quantum Synchronization" in Entropy 2023, 25(8), 1116.(No written permission from MDPI is necessary for thesis purposes.)

$\hbar = 1$):

$$\begin{aligned}\dot{\rho} =& -i[\hat{H}, \rho] + \gamma_1 \mathcal{D}[a^\dagger]\rho + \gamma_2 \mathcal{D}[a^2]\rho + \gamma_3 \mathcal{D}[a]\rho \\ \hat{H} =& \Delta a^\dagger a + iE(a - a^\dagger) + i\eta(a^{\dagger 2} e^{2i\varphi} - a^2 e^{-2i\varphi}),\end{aligned} \tag{3.1}$$

where $\mathcal{D}[L]\rho = L\rho L^\dagger - \frac{1}{2}(L^\dagger L\rho + \rho L^\dagger L)$, γ represents the rate of decay, with γ_1, γ_2 and γ_3 corresponding to negative damping, nonlinear damping and linear damping respectively. $\Delta = \omega_0 - \omega_d$ is the amount of detuning between the frequency of the drive, ω_d, and the frequency of the oscillator, ω_0. E is the amplitude of the harmonic drive, with a and $a^\dagger$ being the annihilation and creation operators. η is the squeezing parameter, with φ representing the phase of squeezing.

In this section, we focus on the measures of quantum phase synchronization in an externally driven oscillator. As a measure of phase synchronization, the phase coherence is frequently used in the literature and, defined as [WKM16, LANB16, BBA05, SSFK23]

$$S_{pcoh} = \frac{\mathrm{Tr}[a\rho]}{\sqrt{\mathrm{Tr}[a^\dagger a\rho]}}, \tag{3.2}$$

where $|S|$ measures the degree of phase coherence with a range of $0 \leq |S| \leq 1$. Another appropriate simple measure is based on the relative phase distribution [HLG+15, LNN+17]:

$$S_{peak} = 2\pi \max[P(\Phi)] - 1, \tag{3.3}$$

where the phase distribution is defined by $P(\Phi) = (1/2\pi)\langle\Phi|\rho|\Phi\rangle$ with $|\Phi\rangle = \sum_{n=0}^{\infty} e^{in\Phi}|n\rangle$. S_{peak} represents the maximum value of $P(\Phi)$ compared to a uniform distribution. This measure is valuable for detecting synchronization because it is exclusively nonzero when $P(\Phi)$ deviates from a flat distribution.

It is well known that the phase operator is not well-defined in quantum theory. However, most quantum harmonic oscillators are populated up to some finite levels, and we can resort to the Pegg-Barnett phase operator. In Ref. [MKH20], the mean resultant length (MRL), which incorporates the Pegg-Barnett operator, has been proposed as a measure of synchronization. It arises from the study of circular statistics [PNR13] and is initially developed for 1-to-1 synchronization. However, it can be generalized to measure n-to-1 synchronization. The n-th order mean resultant length ($MRL^{(n)}$) of a circular distribution is given by

$$MRL^{(n)} = \sqrt{\langle \sin n\phi\rangle^2 + \langle \cos n\phi\rangle^2} = |\langle e^{in\phi}\rangle|. \tag{3.4}$$

This measure is capable of capturing n-to-1 synchronization, which exhibits multiple peaks in the phase distribution $P(\Phi)$ and fixed-points in the quasi-probability phase-space distribution, e.g. Wigner function.

Fisher information proves to be an important tool for determining classical synchronization in a system of Kuramoto oscillators [KZP18, dSVL21]. It has been mooted as a good measure for phase drift in clock synchronization, both classical and quantum [YZF15, ZZMF13, JADW00, CL10]. It is also a useful measure in classical signal processing [Ste93], being intimately related to the Cramer-Rao bound. Motivated by these works, we propose the quantum Fisher information (QFI) as a measure for quantum phase synchronization:

$$QFI = \mathcal{F}_Q[\rho, A] = 2\sum_{k,l} \frac{(\lambda_k - \lambda_l)^2}{(\lambda_k + \lambda_l)} |\langle k|A|l\rangle|^2, \tag{3.5}$$

where $\lambda_{k,l}$ and $|k, l\rangle$ are the eigenvalues and eigenvectors of the steady-state $\rho = \rho_{ss}$. We use $A = a^\dagger a$ to measure the phase uncertainty in the steady-state.

Phase synchronization is closely related to the phase distribution $P(\Phi)$, which is a classical probability distribution. Therefore, it make sense to directly inspect this classical distribution to obtain information about synchronization. We propose another measure of phase synchronization using classical Fisher information (CFI). This new measure is defined by the classical Fisher information of the phase distribution $P(\Phi)$:

$$CFI = E\left[\left(\frac{\partial}{\partial\Phi}\log P(\Phi)\right)^2\right], \tag{3.6}$$

It is important to note that this CFI is different from the conventional Fisher information, which is directly calculated from the density matrix as: $F(\hat{X}|\theta) = \sum_x \frac{1}{p(x|\theta)}(\frac{\partial p(x|\theta)}{\partial\theta})^2$, where $p(x|\theta)$ is the probability of observing outcome x when measuring observable $\hat{X}$ [Par09]. When dealing with phase distributions with multiple symmetrical peaks, the Fisher information is invariant whether one measures the single-peak portion or the whole distribution, due to taking expectation over the whole distribution in Eq. 3.6. However, for asymmetric peaks the result produced by this measure is not optimal. For more details on asymmetric peaks, see Section 3.6.

Classical and quantum Fisher information and S_{peak} reads 0 for unsynchronized states, but is unbounded for highly synchronized states, whereas phase coherence and $MRL^{(n)}$ is bounded between 0 and 1.

Two advantages of FI-based measures over phase coherence can be observed by

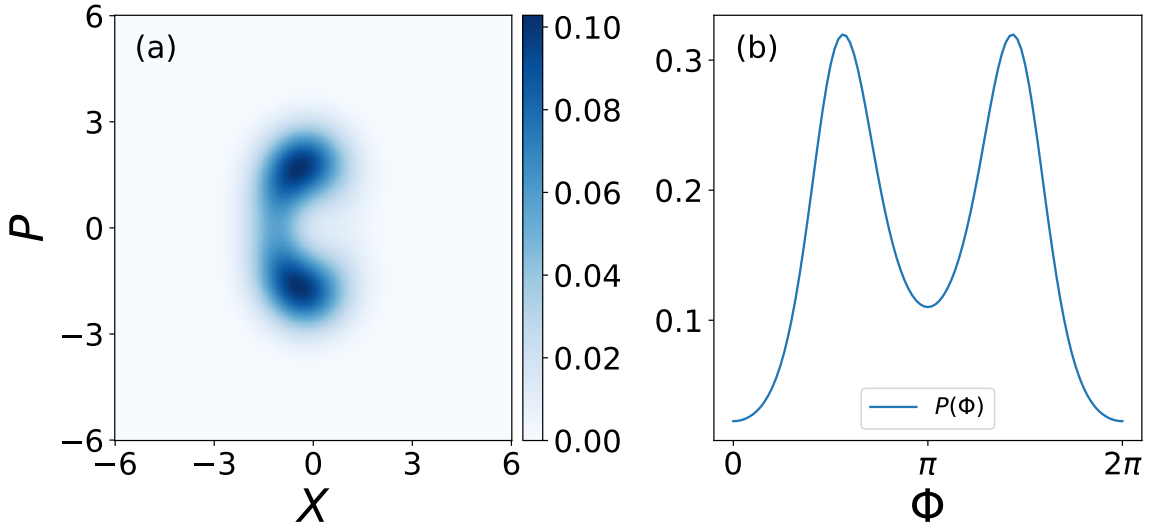

Figure 3.1: An example of a squeezed steady-state (a) Wigner function and its corresponding (b) phase distribution $P(\Phi)$. Squeezed Wigner function and phase distribution have two distinct peaks, which we refer to as 2-to-1 synchronization. Parameters in this example: $\Delta = 0, E = \eta = 0.5, \varphi = \pi/2, \gamma_1 = \gamma_2 = 1, \gamma_3 = 0$.

plotting phase coherence against FI-based measure, as shown in Fig. 3.2: Firstly, Fisher information appears to be more sensitive to highly synchronized states, while exhibiting less sensitivity at the other extreme. However, in most cases, our primary interest lies in the highly synchronized states. Secondly, FI-based measures are more general metrics of synchronization. Measures such as phase coherence face limitations in detecting synchronization of squeezed states or, more generally, Wigner functions with multiple peaks— n-to-1 synchronization, see Fig. 3.1 as an example. In contrast, FI-based measures are capable of detecting synchronization in such instances. As a measure of synchronization, we find that FI-based measures are not only comparable to existing measures for normal cases of 1-to-1 synchronization, it is also more appropriate for the measurement of 2-to-1 synchronization. Measuring QFI in experiments can be challenging due to its reliance on the full quantum state of the system. However, there are various strategies that have been developed to estimate QFI experimentally, such as randomized measurement [RBMV21, FSD16, YLW+21].

Recently there has been some work [DBK23] to relate quantum synchronization to quantum geometric phase [TSKO04]. In this work, they showed that the geometric phase for the quantum Stuart-Landau oscillator under driven pump exhibits an Arnold tongue-like structure, somewhat similar to the Arnold tongue in quantum synchronization as measured by the shifted phase distribution of the Q function. Also,

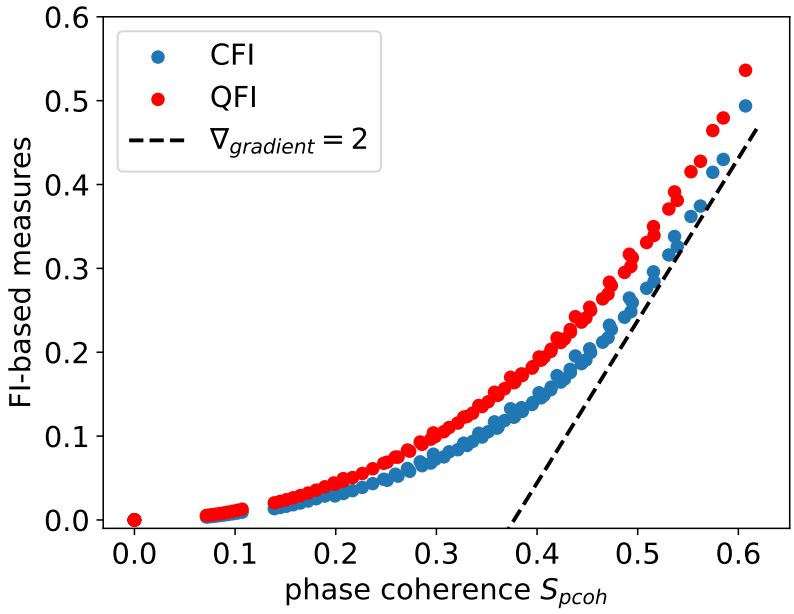

Figure 3.2: Phase coherence vs. FI-based measures. It is interesting to see FI-based measures is more sensitive(larger gradient) for highly synchronized states, as shown by the dotted reference line indicating $\nabla_{gradient} = 2$. Sample data simulated with: $\Delta = 0, E = 0.5, \eta = 0, \varphi = \pi/2, \gamma_1 = 1, \gamma_2 \in [1, 10], \gamma_3 = 0$.

for two oscillators, it is sometimes useful to measure the quantum mutual information [AEAM+15, JHS+20, ERCL+19].

3.2 1-to-1 Synchronization

We first study the scenario of a coherently driven oscillator without squeezing drive(by simply set $\eta = 0$). When only the coherent driving is present, there will be only one preferred phase (namely 'fixed point') to synchronize to and the phase distribution $P(\Phi)$ has only one peak, as shown by the first row in Fig. 3.3, whose position indicates the relative phase between the oscillator and drive. With increasing amplitude of the driving, the quantum phase synchronization between the oscillator and drive improves, and so does the values of the synchronization measures. This indicates a monotonic behavior in the measure. We show that all measures qualitatively agree in Fig. 3.3 where synchronization measures are plotted against coherent driving amplitude E. Therefore, these are all valid measures to capture 1-to-1 quantum phase synchronization, and their correlations are close to unity, as shown in the later section. Take note that in Fig. 3.3 the unbounded and bounded measures are plotted separately.

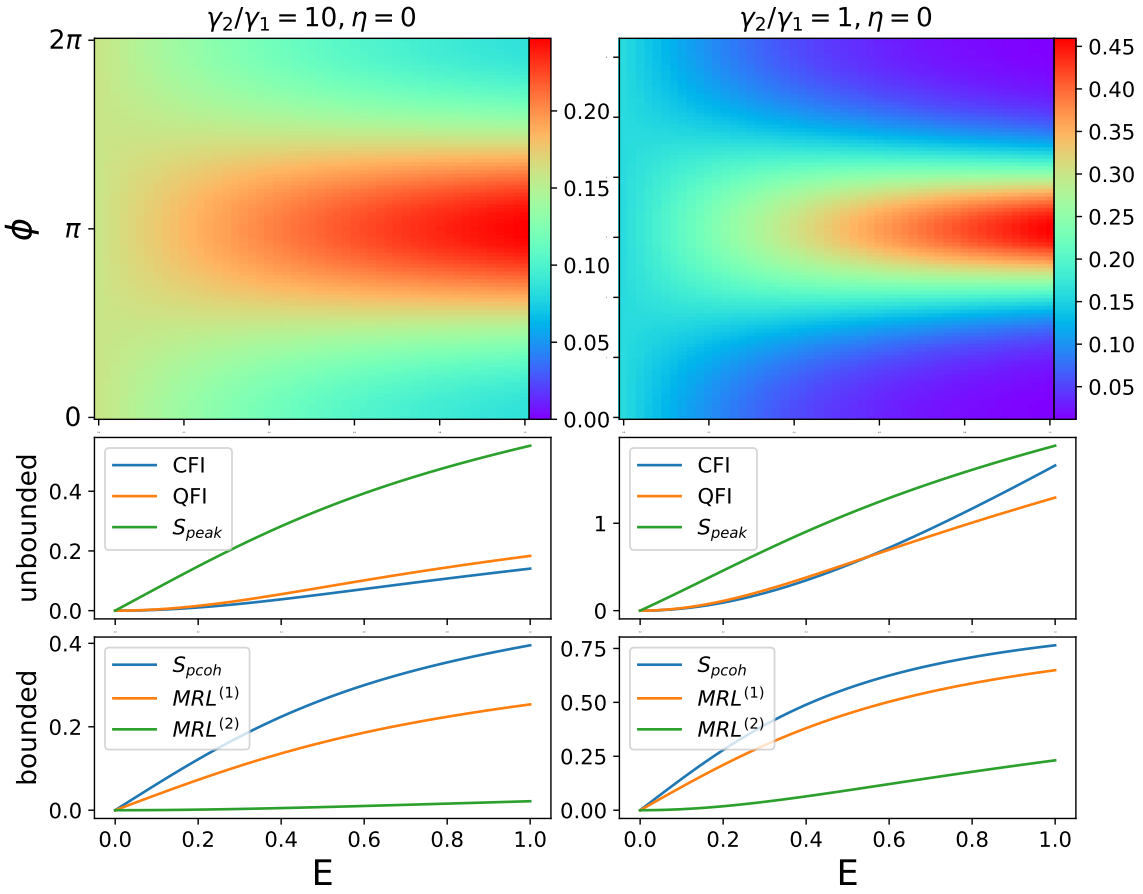

Figure 3.3: Phase distribution $P(\phi)$ and synchronization measures plotted against driving amplitude E. Fixed parameters: $\Delta = 0, \gamma_1 = 1, \gamma_3 = 0$. In these cases of 1-to-1 synchronization, the driven oscillator has only one preferred phase to synchronize to. Unbounded and bounded measures are plotted separately.

In Fig. 3.3, the synchronization measures are compared across different nonlinear damping ratios γ_2/γ_1, where this ratio directly controls the radius of the limit cycle and mean photon number in the oscillator. Conventionally, the oscillator is regarded in 'semi-classical' regime when $\gamma_2/\gamma_1 \approx 1$, and 'quantum' regime when $\gamma_2/\gamma_1 \gg 1$. We can see that these measures remain valid for different regimes. A driven oscillator with a smaller radius (i.e. larger γ_2/γ_1) is more prone to lose synchronization by phase diffusion and quantum noise [LANB16, LS13, WNB14]. Comparing two columns of Fig. 3.3, the values of a synchronization measure are higher in the classical regime, as expected. Note that in Fig. 3.3 right column, the value of CFI surpass QFI at certain driving amplitude E. As we have explained previously, the CFI we proposed in this paper is not the direct classical analog of QFI. Therefore, this is not a violation of the property that QFI should be the supremum of the CFI over all observables.

More insights can be developed in deep quantum regime ($\gamma_2 \to \infty$), where the analytical solutions to all these measures can be obtained. The 3×3 density matrix ansatz in noiseless limit ($\gamma_3 = 0$) is given in the Fock basis [MKH20]:

$$\rho = \begin{pmatrix} \rho_{00} & \rho_{01} & 0 \\ \rho_{10} & \rho_{11} & 0 \\ 0 & 0 & \rho_{22} \end{pmatrix}, \tag{3.7}$$

with

$$\rho_{00} = \frac{\gamma_2(12E^2+18)}{12E^2+9+3\gamma_2(9+8E^2)}, \tag{3.8}$$

$$\rho_{11} = \frac{\gamma_2(12E^2+9)}{12E^2+9+3\gamma_2(9+8E^2)}, \tag{3.9}$$

$$\rho_{22} = \frac{12E^2+9}{12E^2+9+3\gamma_2(9+8E^2)}, \tag{3.10}$$

$$\rho_{01} = \rho_{10}^* = \frac{6i\gamma_2 E}{12E^2+9+3\gamma_2(9+8E^2)}. \tag{3.11}$$

This amounts to restricting the number of excitations to 2, and neglecting all coherences involving the state $|2\rangle$. The higher order coherences are dropped on the grounds that they can be seen to be small in exact numerical simulations, and dropping them makes analytical calculations much easier and more insightful.

The analytical equation for $MRL^{(1)}$, QFI and phase coherence S_{pcoh} are obtained as (with $\Delta = 0, \gamma_1 = 1, \gamma_3 = 0$):

$$\lim_{\gamma_2 \to \infty} MRL^{(1)} = \frac{2E}{9+8E^2}, \tag{3.12}$$

$$\lim_{\gamma_2 \to \infty} QFI = 4\left|\frac{2E}{9+8E^2}\right|^2, \tag{3.13}$$

$$\lim_{\gamma_2 \to \infty} S_{pcoh} = \frac{2E}{\sqrt{(8E^2+9)(4E^2+3)}}. \tag{3.14}$$

Subsequently, the phase distribution $P(\Phi)$ can be obtained:

$$\lim_{\gamma_2\to\infty} P(\Phi) = \frac{1}{2\pi}[1 - \frac{4E}{9+8E^2}\cos(\Phi)] \tag{3.15}$$

After deriving the phase distribution $P(\Phi)$, the peak of phase distribution S_{peak} and CFI can be easily obtained as

$$\lim_{\gamma_2\to\infty} S_{peak} = \frac{4E}{9+8E^2}, \tag{3.16}$$

$$\lim_{\gamma_2\to\infty} CFI = 4\frac{A_0 + A_1E^2 + A_2E^4 + A_3E^6 + A_4E^8}{\lambda(9+8E^2)(\lambda-9-8E^2)^2}, \tag{3.17}$$

where

$$\begin{aligned} A_0 &= 729(\lambda-9),\\ A_1 &= 108(17\lambda-201),\\ A_2 &= 544(3\lambda-52),\\ A_3 &= 256(2\lambda-67),\\ A_4 &= -4096,\\ \lambda &= \sqrt{(9+4E+8E^2)(9-4E+8E^2)}. \end{aligned} \tag{3.18}$$

In Fig. 3.4 we compare the analytical solutions to the numerical simulation, revealing that the validity of the solutions lies in the range when coherent driving is small ($E \ll 1$). With larger driving E, the oscillator will be excited to higher levels beyond the assumption of the 3×3 ansatz.

3.3 Squeezing enhances 2-to-1 synchronization

In this section, we show squeezing drive can create and enhance quantum 2-to-1 synchronization, i.e. synchronization with two distinct fixed points in phase space, and the phase distribution $P(\Phi)$ has two distinct peaks. However, as mentioned previously, some synchronization measures are not suitable for measuring such type of synchronization.

As shown in Fig. 3.5 left column, increasing squeezing sharpens the two peaks in the phase distribution and thus improves mixed synchronization. Here, we need to consider

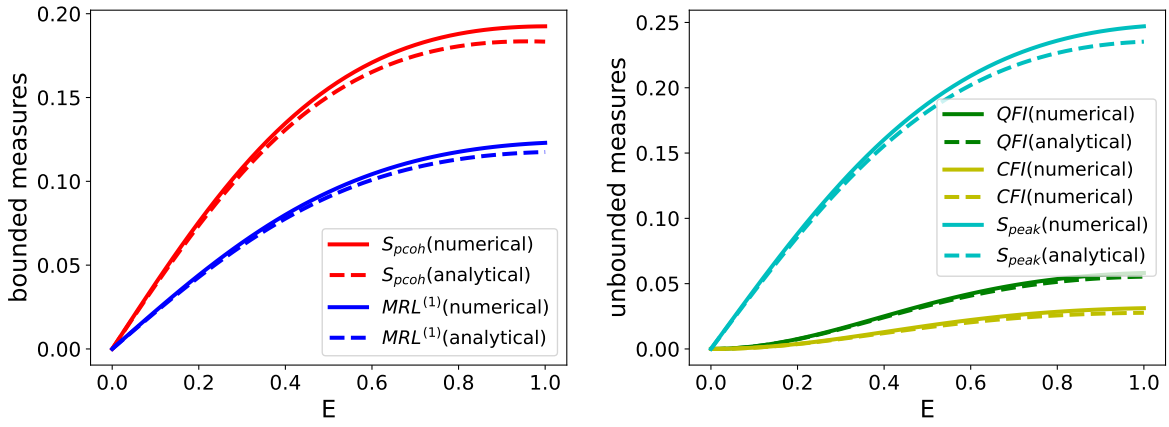

(a) **(b)**

Figure 3.4: Numerical results vs. analytical results. The oscillator is assumed in deep quantum regime ($\gamma_2 = 300$). Fixed parameters: $\Delta = 0, \eta = 0, \gamma_1 = 1, \gamma_3 = 0$.Analytical results are accurate only when $E \ll 1$.

the following question: Does $E = 0$. i.e. no drive, makes sense for synchronization? We can always regard the squeezing term as a drive. When squeezing is present without coherent drive, the synchronization can be regarded as between the oscillator and the squeezing drive. This is also considered in Ref. [SHM+18] where they did for frequency entrainment (the frequencies of the oscillator and external drive converge). Note that phase coherence S_{pcoh} and $MRL^{(1)}$ is zero when only squeezing is present, which is expected, as these measures reflect the first off-diagonal elements in the density matrix. On the other hand, S_{peak} and $MRL^{(2)}$ scale almost linearly with squeezing.

2-to-1 synchronization can be created out of 1-to-1 synchronization. This is shown in the right column of Fig. 3.5, where in addition to squeezing, a coherent drive with amplitude $E = 0.5$ is present. This coherent drive creates a single peak when squeezing is off or small. When the squeezing is tuned up, the single peak splits into two under pitchfork bifurcation, so does the corresponding Wigner functions [SHM+18]. In this scenario, the two measures (phase coherence S_{pcoh} and $MRL^{(1)}$) which are only capable of measuring 1-to-1 synchronization decrease and appears to change almost linearly with increasing squeezing parameter. $MRL^{(2)}$ is a measure dedicated to 2-to-1 synchronization, therefore it is unsurprising that it only provides partial information when single peak is present. This explains why $MRL^{(2)}$ drops to zero at small η and increases linearly afterwards. The measurement of S_{peak} lacks the ability to differentiate between two types of synchronization. Consequently, only the

classical and quantum Fisher information measures exhibit a monotonic relationship with respect to squeezing.

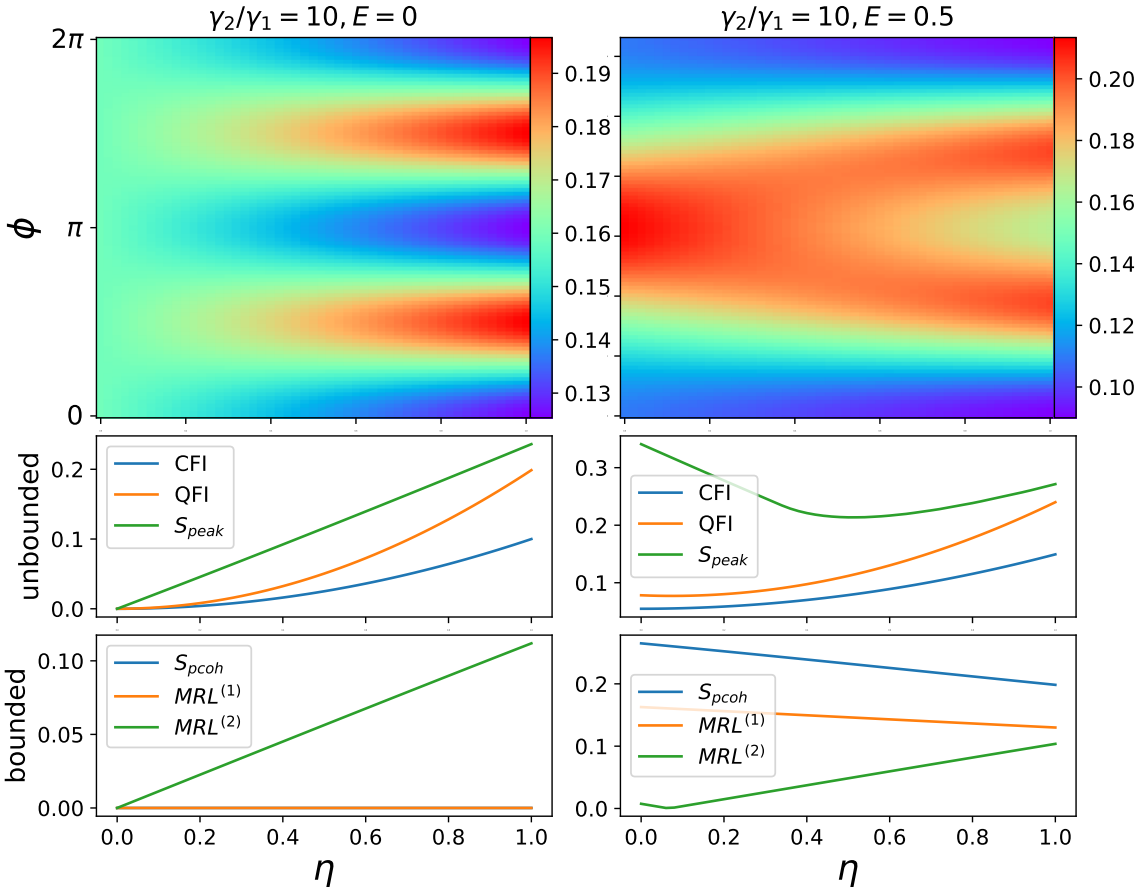

Figure 3.5: Phase distribution $P(\phi)$ and synchronization measures plotted against squeezing amplitude η. Fixed parameters: $\Delta = 0, \varphi = \pi/2, \gamma_1 = 1, \gamma_3 = 0$. In these cases of 2-to-1 synchronization, the driven oscillator has two distinct phase to synchronize to. Unbounded and bounded measures are plotted separately.

3.4 Effects of noise

In this section, we investigate and compare the effect of different noise across these measures. We consider two types of noise, namely single photon dissipation and white noise.

The single photon dissipation process is implemented by the Lindblad dissipator proportional to γ_3 in the master equation (3.1). In Fig. 3.6, all six measures are captured in the surface plots with respect to the single photon dissipation γ_3 and coherent driving amplitude E. It is known that single photon dissipation can be beneficial for 1-to-1 synchronization in coherently driven oscillators [MKH20, SSFK23],

which is reflected in Fig. 3.6 among all measures consistently. Surprisingly, this noise-induced synchronization boost is absent in 2-to-1 synchronization, as shown in Fig. 3.7, in which the squeezing η is increasing instead of driving amplitude E. Again, the phase coherence and $MRL^{(1)}$ remain 0 for the same reason explained in the previous section.

To introduce white noise into the density matrix, we define noise parameter $p \in [0, 1]$, thus the noisy steady-state density matrix is defined as:

$$\rho_{noisy} = (1 - p)\rho_{ss} + p\hat{I}/N_{dim}, \tag{3.19}$$

where ρ_{ss} is the noise-less steady-state density matrix and $\hat{I}$ is the identity matrix with dimension N_{dim}.

After introducing white noise, it is expected for all measures to degrade with increasing p. Interestingly, phase coherence turns out to be most sensitive to white noise, as shown in Fig. 3.8, where there is a bigger drop in the measure as a function of noise p compared to other measures.

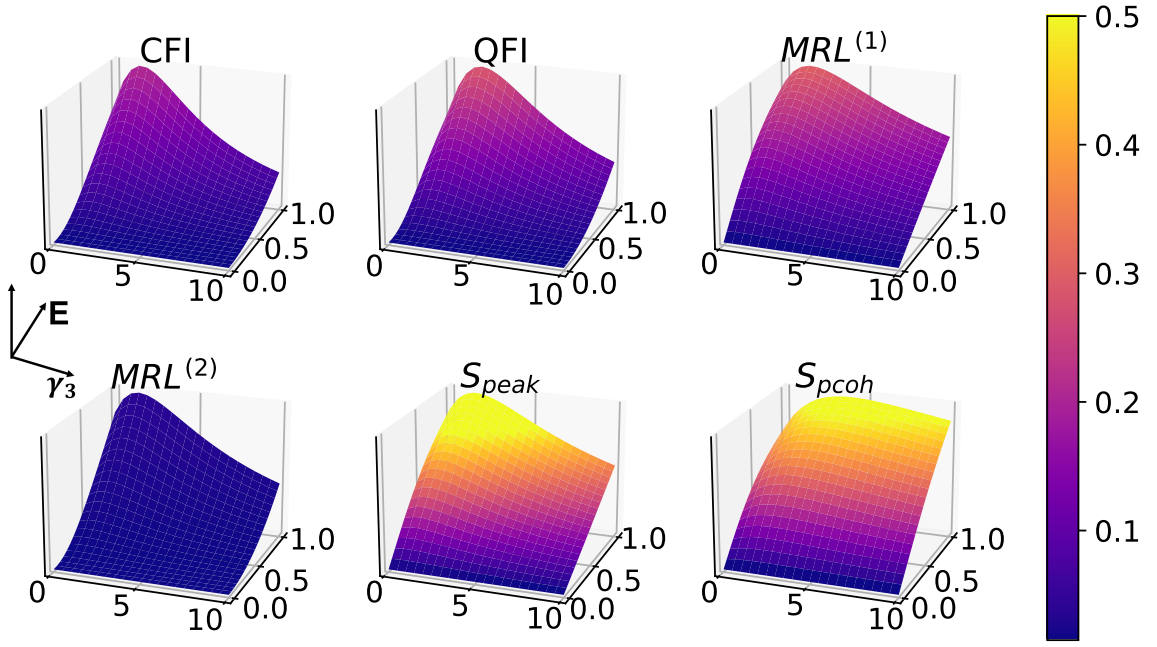

Figure 3.6: Effects of single-photon dissipation noise in 1-to-1 synchronization, in the absence of squeezing ($\eta = 0$), with fixed parameters: $\Delta = 0, \gamma_1 = 1, \gamma_2 = 10, p = 0$. All measures exhibit an noise-induced boost where the dissipation is small, which is consistent with the previous works [MKH20, SSFK23].

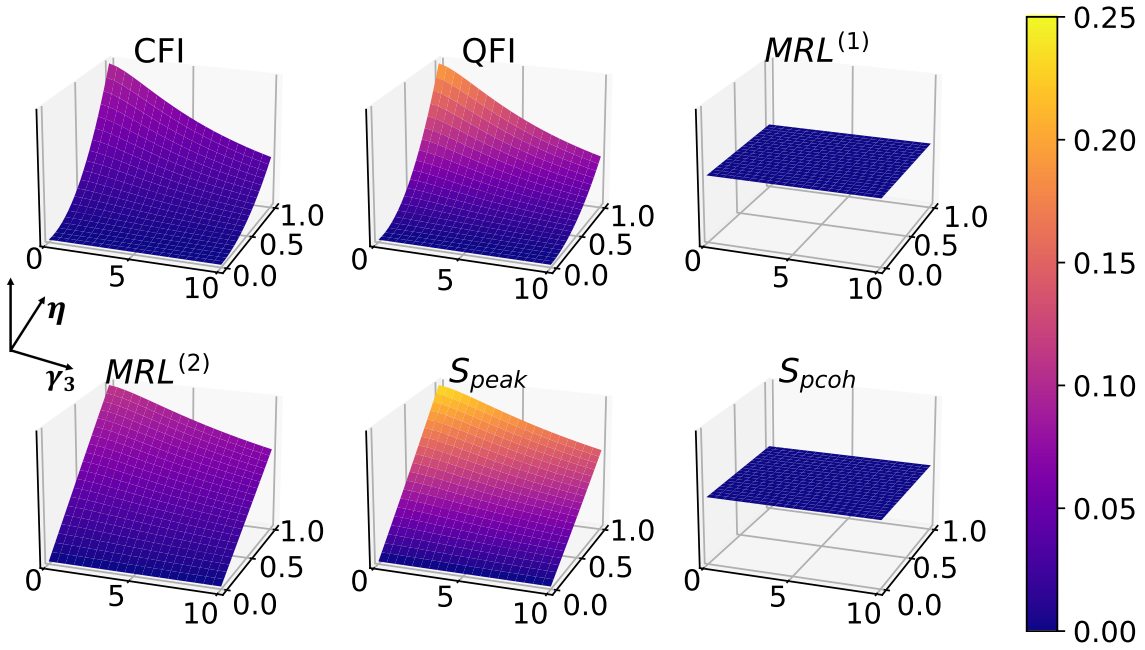

Figure 3.7: Effects of single-photon dissipation noise in 2-to-1 synchronization, without driving ($E = 0$), with fixed parameters: $\Delta = 0, \gamma_1 = 1, \gamma_2 = 10, p = 0$. As discussed above, $MRL^{(1)}$ and phase coherence are identically zero in these cases.

3.5 Correlations between measures

In this section, a correlation analysis was performed to investigate to what extent the different measures of quantum synchronization carry independent and non-redundant information. We calculate the Pearson correlation between the values of different measures, defined as

$$\mathcal{C} = \frac{\mathrm{cov}(X, Y)}{\sigma_X \sigma_Y}, \tag{3.20}$$

with $\mathrm{cov}(X, Y)$ being the covariance between two synchronization measures and σ the standard deviation. In the case of 1-to-1 synchronization, i.e. single peak, high Pearson correlations are observed across all the measures, as shown in Fig. 3.10(a). Whereas in the case of 2-to-1 synchronization, it is obvious that phase coherence S_{pcoh}, S_{peak} and $MRL^{(1)}$ are ill-suited measures, as they are negatively related to the other three proper measures.

From both plots of Fig. 3.10, we can tell the connections between these measures: CFI, QFI and $MRL^{(2)}$ are highly correlated in their response to the driving. On the other hand, phase coherence S_{pcoh} and $MRL^{(1)}$ exhibit a strong connection, as they

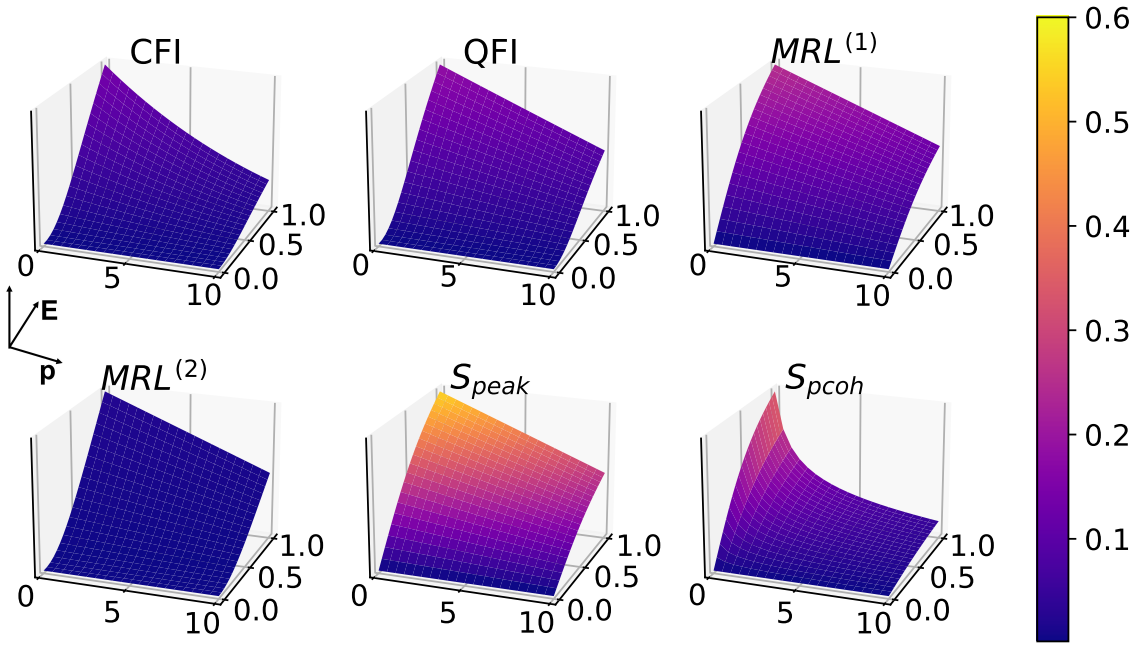

Figure 3.8: Effects of white noise in 1-to-1 synchronization, in the absence of squeezing ($\eta = 0$), with fixed parameters: $\Delta = 0, \gamma_1 = 1, \gamma_2 = 10, \gamma_3 = 0$.

are both related to the first off-diagonal coherences.

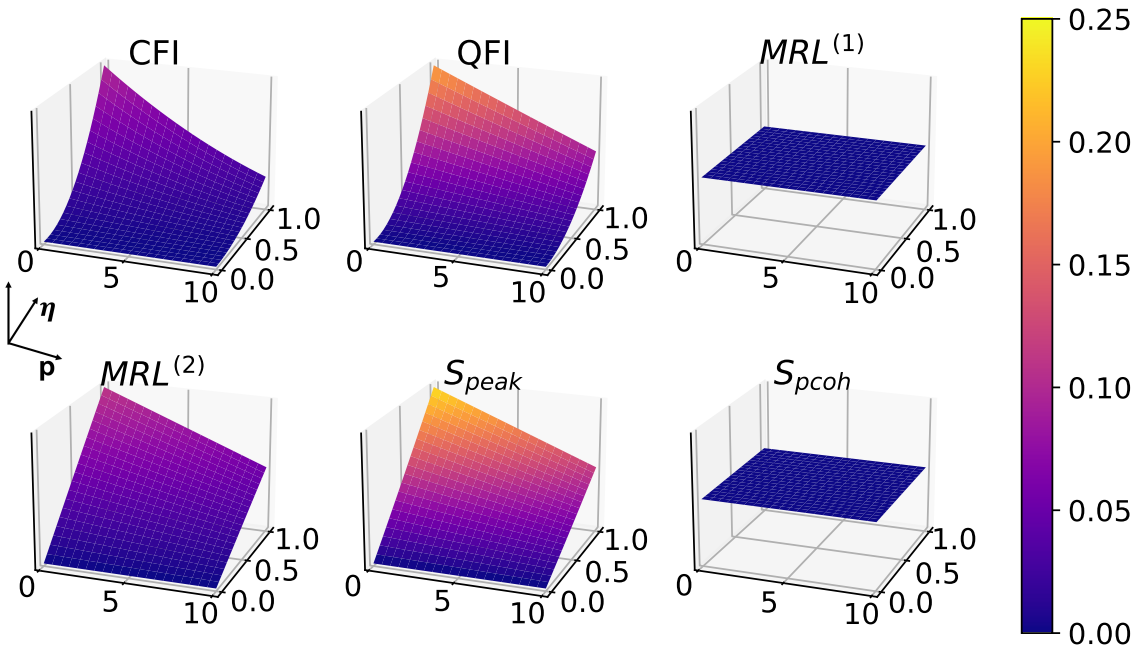

Figure 3.9: Effects of white noise in 2-to-1 synchronization, without driving ($E = 0$), with fixed parameters: $\Delta = 0, \gamma_1 = 1, \gamma_2 = 10, \gamma_3 = 0$. $MRL^{(1)}$ and phase coherence are 0 in this case for the same reason as above.

3.6 Asymmetrical synchronization

So far we have discussed cases when the two peaks in phase distribution are symmetrical (i.e. the peaks have identical amplitude). To complete the whole picture, in this section we discuss the situation when the two peaks are distorted and asymmetrical. This asymmetrical phase distribution can be observed when both coherent drive and squeezing are present with a difference of phase, as shown in Fig. 3.11.

Interestingly, both FI-based measures are shown to be insensitive to the change of symmetry, by varying the phase of squeezing φ in Fig.3.11. Meanwhile, all the other measures have great dependence on the phase of squeezing φ. This is another convenient trait of FI-based measures of being tolerant to phase mismatch. As the phase of squeezing is usually determined by the specific experiment setups, such as the properties of cavity in cQED platform [LTP+15] and nonlinear crystals in optical platform [DLM+15, Sch17].

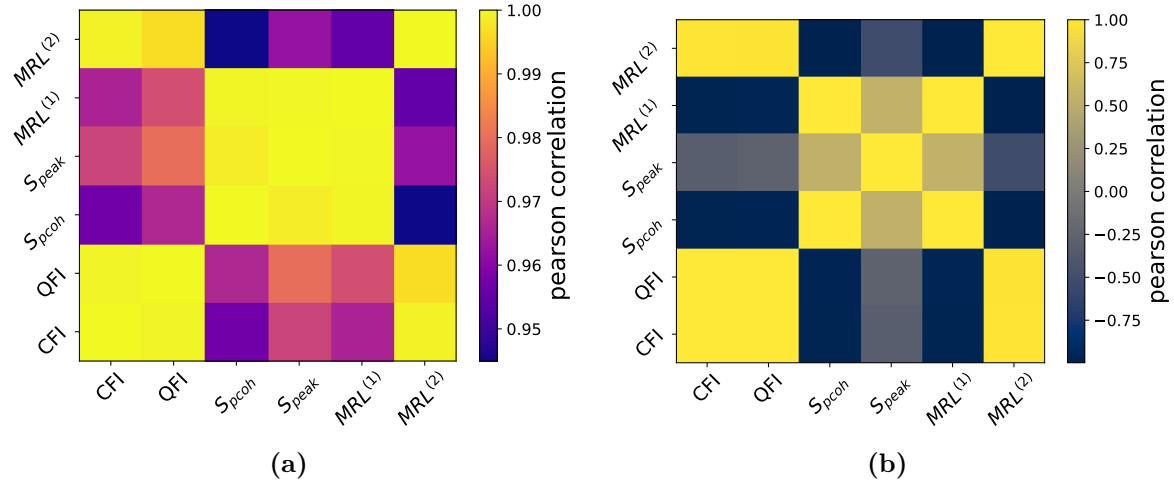

(a) (b)

Figure 3.10: Correlation between different measures on (a)1-to-1 synchronization. Calculations are performed on the same data as Fig. 3.3 left column. (b)2-to-1 synchronization. Calculations are performed on the same data as Fig. 3.5 right column.

3.7 Conclusion

In conclusion, this research provides a comprehensive analysis of quantum phase synchronization measures. Our work proposes a novel approach to measure the degree of synchronization by deploying classical and quantum Fisher information. Significantly, both measures demonstrate success in characterizing both the 1-to-1 and 2-to-1 synchronization regimes, where other existing methods fail to yield reliable results in one or another.

Our comparative study of the classical and quantum Fisher information measures with existing measures highlights the advantages and limitations of each method. Our study offers valuable guidance for future investigations and practical implementations. Our analysis of the impact of noise on the synchronization measures reveals the robustness and susceptibility of each method in the presence of decoherence. Furthermore, the correlations between these measures provide insight into the similarities and differences between different measures of quantum synchronization.

Our findings contribute significantly to the characterization of quantum phase synchronization, particularly in the 2-to-1 synchronization regime. These results pave the way for further research in the field, such as the development of more efficient and robust quantum communication and computing protocols. Future work could explore other synchronization regimes, investigate the impact of various types of noise, and

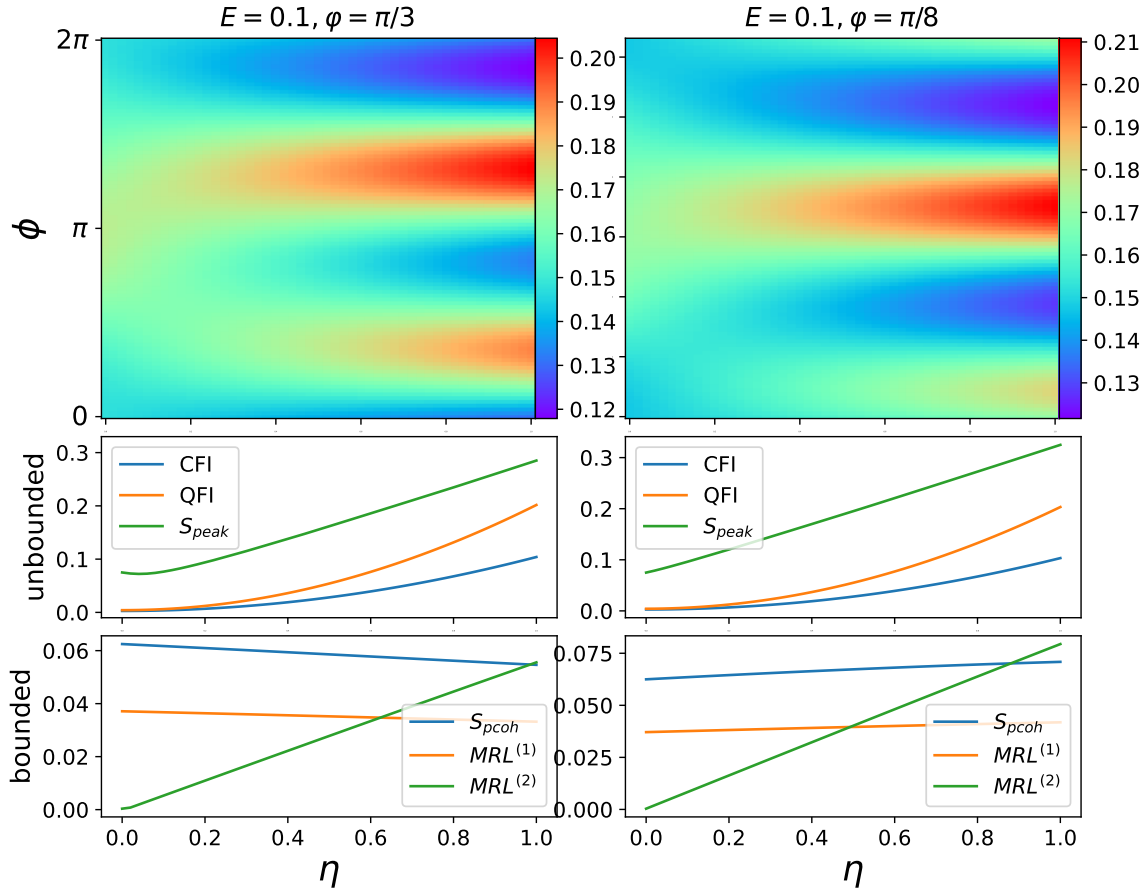

Figure 3.11: Asymmetrical phase distribution and synchronization measures plotted against squeezing η. Fixed parameters: $\Delta = 0, \gamma_1 = 1, \gamma_2 = 10, \gamma_3 = 0$.

assess potential applications of our proposed measures in real-world quantum systems.

Chapter 4

Quantum synchronization effects induced by strong nonlinearities

Mathematical modeling has shown us how the immense variety and beauty of nature can be governed by nonlinear differential equations [May19, EK05, JS07, Deb12]. Such equations, owing to their nonlinearity, are difficult to analyze and their application to physical processes has come to be known as nonlinear science [Cam87, Sco06]. In physics, interest in nonlinear phenomena has spread to quantum-mechanical systems. Effects such as chaos [Stö00, Haa91, Wal12, Wim14], stochastic resonance [GHJM98, WSB03, Lud19, WTB+19], and coherence resonance [WSB03, KN21b], are some of the better known examples. Besides fundamental research, there are also several promising applications of nonlinear dissipation, e.g. stabilizing bosonic qubits for fault-tolerant quantum computing [MLA+14, LTP+15, CNAA+22], and enhancing the sensitivity of quantum sensors [DC19, SMnFS21].

In this chapter, we investigate the effects of nonlinearity in quantum oscillators by considering a more general model based on the classical Duffing–van der Pol (DvdP) oscillator. This adds $\zeta\, x^3$ to y' where ζ is another nonlinearity parameter. To overcome the inadequacy of the SL model we propose a quantum DvdP oscillator in which the vdP and Duffing nonlinearities (respectively μ and ζ) are nonvanishing, but also not arbitrarily large. Our model is accurate up to order $(\mu/\omega_0)^2$, at which the distinct signatures of strong nonlinearity appear, such as relaxation oscillations [CKN20]. Our approach has the benefit of capturing novel nonlinear effects while evading the large computational cost of simulating quantum systems with very strong nonlinear dissipations.

This chapter is published substantially as "Quantum synchronization effects induced by strong nonlinearities" in Phys. Rev. A 2023, 107, 053713.(No written permission from APS is necessary for thesis purposes.)

We show that for a single oscillator with periodic forcing there exists a critical Duffing nonlinearity, above which further increases in ζ enlarges the synchronization bandwidth (the amount of detuning the forcing can tolerate from the oscillator and still entrain it). This result is similar to the synchronization enhancement from the classical literature [ACG+15], but now generalized to quantum oscillators.[1] In contrast, the vdP nonlinearity activates genuine quantum effects. Coupling two vdP oscillators dissipatively may lead to either amplitude death (the cessation of oscillations), or mutual synchronization. Classically, amplitude death occurs only when the two oscillators are sufficiently detuned [SPR12]. Interestingly, we find this need not be the case for quantum oscillators. We show that two quantum vdP oscillators possessing relatively small limit cycles and nonvanishing nonlinearities can exhibit amplitude death even with zero detuning. Larger limit cycles on the other hand can mutually synchronize from a state of amplitude death if their nonlinearity is increased.

We also consider reactively coupled oscillators. Two such SL oscillators cannot develop positional correlations, and hence do not synchronize. This is true regardless of whether the oscillators are classical or quantum. We show here that at finitely large nonlinearity, position correlations behave rather differently between the classical and quantum oscillators: Two reactively coupled quantum vdP oscillators can undergo nonlinearity-induced correlations whereby their position correlation increases as they become more nonlinear. In contrast, we find that making the analogous classical oscillators more nonlinear monotonically reduces their position correlation. The nonlinearity-induced correlations in the quantum vdP oscillators are thus a consequence of both their quantum nature and strong nonlinearity.

4.1 Exact quantum model

Here, we describe how the quantum master equation for the exact Duffing-van der Pol model is obtained, following the approach in [CKN20]. For simplicity we consider here a dimensionless DvdP model in terms of the nonlinearity parameters $\lambda \equiv \mu q^2/\omega_0 r^2$ and $\beta \equiv \zeta q^2/\omega_0^2 r^2$ in which r is a dimensionless scale parameter:

$$\tilde{x}' = \tilde{y}\,, \quad \tilde{y}' = F\cos(\omega_{\rm d}\tilde{t}\,) - \tilde{x} - \lambda(\tilde{x} - r^2)\tilde{x}' - \beta\,\tilde{x}^3. \tag{4.1}$$

[1] It is also worth mentioning that nonlinear oscillators are of interest to quantum information too, when they are coupled to qubits. In this context the Duffing nonlinearity has been shown to both increase and stabilize the oscillator-qubit entanglement [MFB14].

Note that $\tilde{x} \equiv xr/q$ is now a function of $\tilde{t} = \omega_0 t$, and we have also included a dimensionless external force parameterized by $F = fr/\omega_0^2 q$ and $\omega_\mathrm{d} = \Omega_\mathrm{d}/\omega_0$.

By defining the complex amplitude $\alpha = (\tilde{x} + i\tilde{y})/2$, we get the equation of motion

$$\alpha' = i\,\frac{F}{2}\cos(\omega_\mathrm{d} t) - i\,\alpha - i\,\frac{\beta}{2}(\alpha+\alpha^*)^3 - \frac{\lambda}{2}(\alpha^3 + |\alpha|^2\alpha - |\alpha|^2\alpha^* - \alpha^{*3} - r^2\alpha + r^2\alpha^*)\,. \quad (4.2)$$

Quantum theory defines the state of a dynamical system by a density operator ρ satisfying $\rho' = \mathcal{L}\rho$, where $\mathcal{L}$ is a linear superoperator. By regarding $(\hat{a}, \hat{a}^\dagger)$ as the analog of (α, α^*), where $[\hat{a}, \hat{a}^\dagger] = \hat{1}$, we can quantize a system prescribed by $\alpha' = h(\alpha, \alpha^*)$ by searching for an $\mathcal{L}$ such that in the Schrödinger picture, $\langle \hat{a} \rangle' = \mathrm{Tr}[\hat{a}\,\mathcal{L}\rho] = \langle :h(\hat{a}, \hat{a}^\dagger): \rangle$. Note that we have chosen to normally order $h(\hat{a}, \hat{a}^\dagger)$, denoted by colons [e.g. if $h(\hat{a}, \hat{a}^\dagger) = \hat{a}\hat{a}^\dagger$, then $:h(\hat{a}, \hat{a}^\dagger): = \hat{a}^\dagger\hat{a}$]. Such an $\mathcal{L}$ corresponding to (4.2) can be found in Lindblad form [Lin76, GKS76, BP02], and which we refer to as a Lindbladian:

$$\mathcal{L} = -i\,[\hat{H}, \cdot] + \lambda\mathcal{D}[\hat{a}^\dagger\hat{a} - \hat{a}^{\dagger 2}/2] + \lambda r^2 \mathcal{D}[\hat{a}^\dagger] + \frac{3\lambda}{4}\mathcal{D}[\hat{a}^2]\,,$$

where

$$\begin{aligned}\hat{H} = {} & \hat{a}^\dagger\hat{a} - \frac{F}{2}\cos(\omega_\mathrm{d} t)(\hat{a} + \hat{a}^\dagger) + \frac{3\beta}{4}\hat{a}^{\dagger 2}\hat{a}^2 + \frac{\beta}{2}(\hat{a}^\dagger\hat{a}^3 + \hat{a}^{\dagger 3}\hat{a}) + \frac{\beta}{8}(\hat{a}^4 + \hat{a}^{\dagger 4}) \\ & - i\frac{\lambda}{2}(\hat{a}^2 - \hat{a}^{\dagger 2}) - i\frac{\lambda}{4}(\hat{a}^\dagger\hat{a}^3 - \hat{a}^{\dagger 3}\hat{a}) - i\frac{\lambda}{8}(\hat{a}^4 - \hat{a}^{\dagger 4})\,. \end{aligned} \quad (4.3)$$

We remark that the choice of the master equation is not unique, since we only demand that the classical equation of motion is recovered in the mean-field limit. Different choices of the master equation will in general lead to different quantum noise effects, which are most pronounced at low excitations (sometimes referred to as the deep quantum limit [MKH20]).

4.2 An alternative quantum oscillator model

4.2.1 Poincaré–Lindstedt method

The Poincaré–Lindstedt method is a perturbative technique to find approximate periodic solutions [Str18]. Regular perturbation theory fails at long time due to the existence secular terms. Taking λ to be the perturbative parameter, such secular terms in the van der Pol (vdP) oscillator are of the form $t\cos t$, which are unbounded in t. The Poincaré–Lindstedt method overcomes this problem by removing secular terms

explicitly.

Let us consider the undriven vdP oscillator (setting $F = 0$). Defining a rescaled time $\tau \equiv \omega t$ where ω is the oscillation frequency, we have the equation

$$\omega^2 \, x''(\tau) + \lambda(x^2 - 1)\, \omega \, x'(\tau) + x(\tau) = 0 \; . \tag{4.4}$$

where a prime denotes differentiation with respect to the argument. Now, we perform the perturbative expansions

$$x(\tau) = \breve{x}_0(\tau) + \lambda \, \breve{x}_1(\tau) + \lambda^2 \, \breve{x}_2(\tau) + \mathrm{O}(\lambda^3) \; , \quad \omega = 1 + \lambda \, \breve{\omega}_1 + \lambda^2 \, \breve{\omega}_2 + \mathrm{O}(\lambda^3) \; . \tag{4.5}$$

Collecting terms of the same order in λ, the zeroth-order equation reads

$$\breve{x}_0'' + \breve{x}_0 = 0 \; , \tag{4.6}$$

which just describes simple harmonic oscillations given by $\breve{x}_0(\tau) = a \cos\tau$, where $a = \breve{x}_0(0)$. The first-order equation reads

$$\begin{aligned} \breve{x}_1'' + \breve{x}_1 = & \; - 2\, \breve{\omega}_1 \breve{x}_0'' - (\breve{x}_0^2 - 1)\breve{x}_0'' \\ = & \underbrace{2\, \breve{\omega}_1 a \cos\tau - a \left(1 - \frac{a^2}{4}\right) \sin\tau}_{\text{resonant forcing}} + \frac{a^3}{4} \, \sin(3\tau) \; . \end{aligned} \tag{4.7}$$

The resonant forcing gives rise to secular terms such as $\tau\cos\tau$ and $\tau\sin\tau$ which are unwanted. Hence, setting the resonant forcing to zero yields $\breve{\omega}_1 = 0, a = 2$ which gives $\breve{x}_0(\tau) = 2\cos\tau$, $\omega = 1 + \mathrm{O}(\lambda^2)$. This is the Stuart–Landau (SL), i.e. weakly nonlinear limit of the vdP which describes quasiharmonic oscillations. Solving the resulting first-order equation, we get the leading-order correction for $x(\tau)$: $x_1(\tau) = \sin^3\tau$. To obtain the leading-order correction for ω, we look at the second-order equation

$$\begin{aligned} \breve{x}_2'' + \breve{x}_2 &= -(\breve{\omega}_1^2 + 2\, \breve{\omega}_2)\, \breve{x}_0'' - 2\, \breve{\omega}_1 \, \breve{x}_1'' - (\breve{x}_0^2 - 1)\, (\breve{x}_1' + \breve{\omega}_1 \, \breve{x}_0') - 2\, \breve{x}_0 \, \breve{x}_1 \, \breve{x}_0' \\ &= \left(4\, \breve{\omega}_2 + \frac{1}{4}\right) \cos\tau + \text{higher harmonics} \; . \end{aligned} \tag{4.8}$$

Again, eliminating the resonant forcing, we get $\breve{\omega}_2 = -1/16$. In terms of t, we then have

$$x(t) = 2\cos(\omega t) + \lambda \sin^3(\omega t) + \mathrm{O}(\lambda^2) \; , \quad \omega = 1 - \frac{\lambda^2}{16} + \mathrm{O}(\lambda^3) \; . \tag{4.9}$$

Thus, the effect of small nonlinearity on the limit cycle is a decrease in frequency

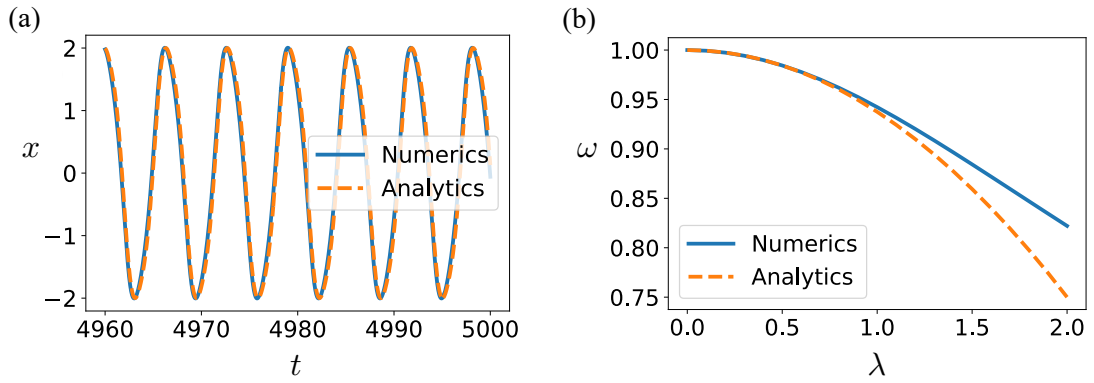

Figure 4.1: Dynamics of the undriven vdP oscillator. Results from an exact numerical simulation are shown as a blue solid line, while results from (4.9) are plotted as an orange dashed curve. (a) Long-time limit of $x(t)$ for $\lambda = 0.5$ (transient dynamics have been discarded). (b) Observed frequency ω. The Poincaré–Lindstedt method remains to be a good approximation up till about $\lambda \approx 1$. Copyright 2023, Phys. Rev. A, no permission needed for thesis purpose.

and a distortion without a change in the limit cycle amplitude (from the first-order approximation of $x(t)$ we can see that for $\lambda < 4/3$ the amplitude of the oscillation is constant at 2. Hence, the amplitude is unchanged to order λ.) A numerical simulation of $x(t)$ and observed frequency ω as given by (4.9) are plotted in Fig. 4.1. Good agreement between the analytic and numeric simulation can be seen for $\lambda < 1$.

From the approximate analysis of (4.9), the leading contribution to the oscillator frequency is quadratic in λ, and linear in β, given by $\omega \approx 1 + r^2(3\beta/2 - \lambda^2 r^2/16)$. This motivates a Bogoliubov–Krylov time-average of the equations of motion up to these orders [SVM07].

4.2.2 Krylov–Bogoliubov averaging

The Krylov–Bogoliubov averaging method essentially assumes that the amplitude is slowly varying and can be treated as a constant when averaging the dynamics over one period, which produced the time-averaged equations of motion. Introducing the complex amplitude,

$$\alpha(t) = \frac{1}{2}\left[\, x(t) + i\, y(t) \,\right], \tag{4.10}$$

where $y = x'$, we can rewrite the vdP equation as a complex equation of motion

$$\alpha' = -i\,\alpha + i\,\frac{F}{2}\cos(\omega_{\rm d}t) - \frac{\lambda}{2}\left(\alpha^3 - \alpha^{*3} + |\alpha|^2\alpha - |\alpha|^2\alpha^* - \alpha + \alpha^*\right). \tag{4.11}$$

Performing the Krylov–Bogoliubov time averaging to first-order in λ, we obtain

$$\alpha' = -i\,\alpha + \frac{\lambda}{2}\left(1 - |\alpha|^2\right)\alpha\,, \tag{4.12}$$

which is the well-known SL equation representing the normal form of a supercritical Hopf bifurcation. The stable oscillations are described by $\alpha(t) = \exp(-it)$. This gives $x(t) = 2\cos t$ which is consistent with the Poincaré–Lindstedt method up to zeroth order in λ.

The second-order averaging yields [SVM07]

$$\alpha' = -i\,\alpha + \frac{\lambda}{2}(1 - |\alpha|^2)\,\alpha + i\,\frac{\lambda^2}{8}\left(1 - 6\,|\alpha|^2 + \frac{11}{2}\,|\alpha|^4\right)\alpha\,, \tag{4.13}$$

which predicts a limit cycle amplitude of $\breve{x}_0 = 2|\alpha| = 2$ and frequency $\omega = 1 - \lambda^2/16$, again consistent with the zeroth-order Poincaré–Lindstedt method.

4.2.3 Quantum Duffing-vdP model

From (4.13), a periodic driving term can be added to obtain

$$\begin{aligned}\alpha' = i\,\frac{F}{2}\cos(\omega_{\rm d}t) - i\,\alpha - i\frac{3\beta}{2}|\alpha|^2\alpha + \frac{\lambda}{2}(r^2 - |\alpha|^2)\alpha \\ + i\frac{\lambda^2}{8}\left(r^4 - 6r^2|\alpha|^2 + \frac{11}{2}|\alpha|^4\right)\alpha,\end{aligned} \tag{4.14}$$

where $\alpha = (\tilde{x} + i\,\tilde{y})/2$. For $F = 0$, (4.14) predicts a limit-cycle amplitude of $2|\alpha| = 2r$ with the expected frequency shifts due to λ and β. Additionally, note the first-order averaging in λ for $\beta = 0$ yields the SL equation. Our approximate model captures the effects of strong vdP nonlinearity of order λ^2. We seek a quantum master equation $\rho' = \mathcal{L}\rho$ such that $\langle\hat{a}\rangle' = \mathrm{Tr}[\hat{a}\,\mathcal{L}\rho]$ (with $[\hat{a}, \hat{a}^\dagger] = \hat{1}$) agrees with (4.14) in the mean-field limit [CKN20]. It can then be shown that this is satisfied by the Lindbladian [Lin76, GKS76, BP02]

$$\mathcal{L} = -i\,[\hat{H}, \cdot] + \lambda r^2\mathcal{D}[\hat{a}^\dagger] + \frac{\lambda}{2}\,\mathcal{D}[\hat{a}^2]\,, \tag{4.15}$$

where

$$\hat{H} = \left(1 - \frac{\lambda^2 r^4}{8}\right)\hat{a}^\dagger\hat{a} + \frac{3\lambda^2 r^2}{8}\,\hat{a}^{\dagger 2}\hat{a}^2 - \frac{11\lambda^2}{48}\,\hat{a}^{\dagger 3}\hat{a}^3 + \frac{3\beta}{4}\,\hat{a}^{\dagger 2}\hat{a}^2 - \frac{F}{2}\cos(\omega_{\mathrm{d}}t)(\hat{a} + \hat{a}^\dagger)\,. \tag{4.16}$$

We have also defined $\mathcal{D}[\hat{c}] \equiv \hat{c}\,\cdot\,\hat{c}^\dagger - (\hat{c}^\dagger\hat{c}\,\cdot + \cdot\,\hat{c}^\dagger\hat{c})/2$ for any $\hat{c}$, and a dot denotes the position of ρ when acted upon by a superoperator. We remark that both the higher-order Kerr terms and the nonlinear two-photon dissipation in our proposed model can be implemented in circuit QED [HQ22, LTP+15]. The tunability of the limit cycle radius r allows us to access different parameter regimes of the quantum oscillator, in particular the quantum ($r \ll 1$), and semiclassical ($r \approx 1$) regimes. We have included the second-order contributions in λ in our model for its nonlinearity-tuning capability, since the terms linear in λ neither affect the limit-cycle amplitude nor phase dynamics. The Duffing nonlinearity translates to a Kerr term in $\mathcal{L}$. This model can be considered as an alternative to the quantum SL oscillator, but with flexibility in tuning the nonlinearity. All our numerical results for a given parameter set are obtained with a sufficiently large truncation of the Hilbert space by ensuring the corresponding steady-state power spectrum converge.

4.3 Nonlinearity-enhanced synchronization

4.3.1 Classical synchronization analysis

Here, we use the harmonic-balance method to analyze the synchronization behavior for the Duffing–van der Pol (DvdP) equation in non-dimensionalized form, given by

$$x'' + \lambda\,(x^2 - r^2)x' + x + \beta x^3 = F\cos(\omega_{\mathrm{d}}t)\,. \tag{4.17}$$

Note that for ease of writing we have omitted tildes for x and all dimensionless parameters (e.g. time). We then assume a synchronized solution of the form $x(t) = A\cos(\omega_{\mathrm{d}}t - \phi)$, where A is the amplitude of the motion and ϕ is a constant phase shift from the driving force. Substituting the ansatz for x into (4.17), we get

$$-\omega_{\mathrm{d}}^2 A\cos(\omega_{\mathrm{d}}t - \phi) - \lambda\,\omega_{\mathrm{d}}A^3\cos^2(\omega_{\mathrm{d}}t - \phi)\sin(\omega_{\mathrm{d}}t - \phi) + \lambda\,\omega_{\mathrm{d}}r^2 A\sin(\omega_{\mathrm{d}}t - \phi) + A\cos(\omega_{\mathrm{d}}t - \phi) + \beta A^3\cos^3(\omega_{\mathrm{d}}t - \phi) = F\cos(\omega_{\mathrm{d}}t)\,. \tag{4.18}$$

The second term on the left-hand side may be written as

$$\cos^2(\omega_{\rm d}t-\phi)\sin(\omega_{\rm d}t-\phi)=\frac{1}{4}\sin(\omega_{\rm d}t-\phi)+\text{higher harmonics}\,. \tag{4.19}$$

Neglecting the higher harmonics and then collecting the coefficients of $\cos(\omega_{\rm d}t)$ and $\sin(\omega_{\rm d}t)$, we obtain

$$\begin{aligned}(1-\omega_{\rm d}^2)A\cos\phi+\frac{1}{4}\lambda\,\omega_{\rm d}A^3\sin\phi-\lambda\,\omega_{\rm d}Ar^2\sin\phi+\frac{3}{4}\beta A^3\cos\phi=F\,,\\ (1-\omega_{\rm d}^2)A\sin\phi-\frac{1}{4}\lambda\,\omega_{\rm d}A^3\cos\phi+\lambda\,\omega_{\rm d}Ar^2\cos\phi+\frac{3}{4}\beta A^3\sin\phi=0\,.\end{aligned} \tag{4.20}$$

These may be expressed compactly as a single complex equation as

$$\left(1-\omega_{\rm d}^2\right)A-i\lambda\,\omega_{\rm d}A\left(\frac{A^2}{4}-r^2\right)+\frac{3}{4}\,\beta A^3=Fe^{-i\phi}\,. \tag{4.21}$$

$$A=A_\star+p\,\delta A\,,\quad \omega_{\rm d}=\omega_\star+p\,\delta\omega\,. \tag{4.22}$$

Substituting (4.22) into (4.21) then gives the first-order equation in p,

$$\delta A\left(6\beta r^2-2i\sqrt{1+3\beta r^2}\,\lambda r^2\right)-4r\sqrt{1+3\beta r^2}\,\delta\omega=\lambda\,e^{-i\phi}\,. \tag{4.23}$$

The modulus of the left-hand side must be λ, hence we have

$$\left(6\beta r^2\delta A-4r\sqrt{1+3\beta r^2}\,\delta\omega\right)^2+\left(2\lambda r^2\sqrt{1+3\beta r^2}\,\delta A\right)^2=\lambda^2\,. \tag{4.24}$$

This can be solved to obtain the relationship between δA and $\delta\omega$. In order to derive the synchronization frequency range, we first notice that (4.24) is a quadratic equation in δA. For synchronization to exist, δA must be real, hence the discriminant must be non-negative, i.e.,

$$\left(48\beta r^3\sqrt{1+3\beta r^2}\,\delta\omega\right)^2-4\left\{4r^4\left[9\beta^2+\lambda^2(1+3\beta r^2)\right]\right\}\left[16\,r^2(1+3\beta r^2)\,\delta\omega^2-\lambda^2\right]\geq 0\,, \tag{4.25}$$

which yields

$$\delta\omega^2\leq\frac{9\beta^2+\lambda^2(1+3\beta r^2)}{16r^2(1+3\beta r^2)^2}\equiv\omega_{\rm c}^2\,. \tag{4.26}$$

Hence, the vdP oscillator is synchronized if the driving frequency is within the critical interval

$$\omega_0-\frac{F}{\lambda}\omega_{\rm c}\leq\omega_{\rm d}\leq\omega_0+\frac{F}{\lambda}\omega_{\rm c}\,. \tag{4.27}$$

The synchronization bandwidth is thus

$$\frac{2F}{\lambda}\,\omega_{\mathrm{c}} = \frac{(F/r)}{2\lambda r^2(1+3\beta r^2)}\sqrt{(\lambda r^2)^2(1+3\beta r^2)+9(\beta r^2)^2}\,. \tag{4.28}$$

Evidently, by fixing F/r, λr^2, and βr^2, the synchronization bandwidth becomes independent of the scale parameter r. As shown in the main text, this does not hold true in the quantum case due to quantum noise. Defining

$$\bar{F} = F/r\,, \quad \bar{\lambda} = \lambda r^2\,, \quad \bar{\beta} = \beta r^2\,, \tag{4.29}$$

the bandwidth can be rewritten as

$$\frac{2\bar{F}}{\bar{\lambda}}\omega_c = \frac{\bar{F}}{2\bar{\lambda}(1+3\bar{\beta})}\sqrt{\bar{\lambda}^2(1+3\bar{\beta})+9\bar{\beta}^2} \approx \begin{cases} \bar{F}/2\bar{\lambda}\,, & \bar{\beta}\longrightarrow\infty \\ \bar{F}/2\,, & \bar{\beta}\longrightarrow 0 \end{cases} \tag{4.30}$$

where in the last step we have taken the limit of large and small $\bar{\beta}$. For the usual vdP oscillator ($\bar{\beta}=0$), the synchronization bandwidth reduces to $\bar{F}/2$ which is independent of λ. In order to obtain nonlinearity-induced enhancement in the bandwidth, we require

$$\frac{\bar{F}}{2\bar{\lambda}(1+3\bar{\beta})}\sqrt{\bar{\lambda}^2(1+3\bar{\beta})+9\bar{\beta}^2} > \frac{\bar{F}}{2}\,. \tag{4.31}$$

This results in the conditions

$$\bar{\beta} > \frac{\bar{\lambda}^2}{3(1-\bar{\lambda}^2)}\,, \quad 0<\bar{\lambda}<1\,. \tag{4.32}$$

Without loss of generality, we can set $r=1$ in the following discussion. In this case $\bar{\lambda}=\lambda$, $\bar{\beta}=\beta$, and $\bar{F}=F$. Interestingly, the nonlinearity-induced enhancement only acts for a finite range of λ and requires a minimum β. In the limit of large β, the bandwidth tends to $F/2\lambda$. However, the method of harmonic balance assumes λ and β to be weak. In this regime, we can interpret the existence of a minimum β as a competition between the effects of λ and β. Note that the oscillator frequency is $\omega \approx 1+3\beta/2-\lambda^2/16$ from our previous analysis. The threshold for synchronization enhancement occurs when these two opposite effects on the frequency are of the same scale, i.e. $\beta\sim\lambda^2$.

Figure 4.2 shows the effect of adding the Duffing nonlinearity on the synchronization bandwidth for $r=1$. Comparing $\beta=0$ and $\beta=1$ in Fig. 4.2(a), we can see that the synchronization bandwidth is enhanced for the $\beta=1$ case for weak to moderate

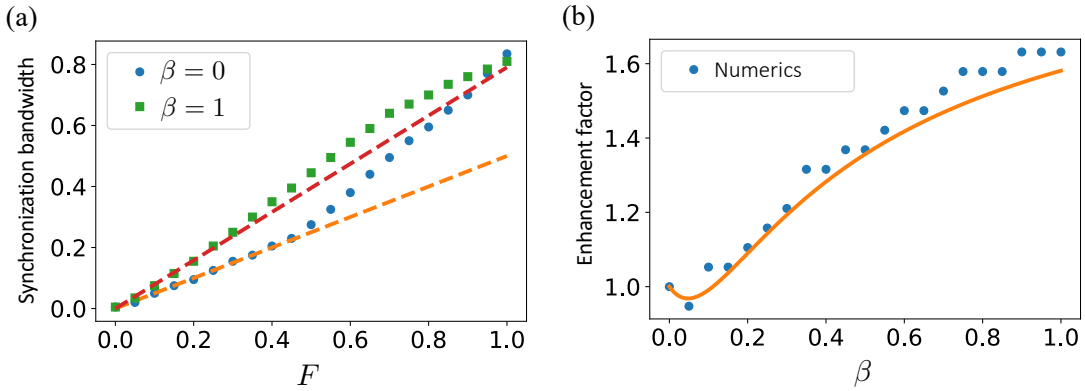

Figure 4.2: (a) Synchronization bandwidth against driving force F for $\lambda = 0.5$. Adding β enhances the synchronization bandwidth for weak to moderate forcing (compared to λ). The analytical predictions given by the dashed lines) are accurate up to $F \sim \lambda$. (b) Enhancement factor defined as the ratio between the bandwidth and its baseline value $F/2$. A value greater than one indicates enhancement of the bandwidth. $\lambda = 0.5, F = 0.2$, and the predicted minimum β for enhancement is $1/9$. Copyright 2023, Phys. Rev. A, no permission needed for thesis purpose.

forcing F (compared to λ). The analytical prediction of the bandwidth agrees with the numerical simulations up to $F \sim \lambda$, beyond which the numerical bandwidth exceeds the predicted value indicating the suppression of natural dynamics at strong forcing. Using $\lambda = 0.5$, we also predict that the synchronization enhancement occurs when $\beta > 1/9$. Indeed, by plotting in Fig. 4.2(b) the enhancement factor, defined as the ratio between the bandwidth and its baseline value $F/2$, we see a good agreement between the numerical results and the analytical calculations. Fluctuations in the numerics can be attributed to a few reasons, such as the time resolution dt in the simulation, the number of samples used for $x(t)$, the frequency resolution $d\omega$ used in determining the bandwidth, and the threshold observed detuning used to determine the frequency-locked regions (set to 0.001). The numerical results also appear to deviate slightly from the prediction at large β, which is likely due to the breakdown in making the ansatz $x(t) = A\cos(\omega_{\mathrm{d}}\, t - \phi)$ used in the derivation. Including higher harmonics in the ansatz might result in more accurate predictions at larger β.

4.3.2 Quantum synchronization analysis

We study first the frequency locking of the approximate quantum DvdP oscillator to a periodic force [(4.15) and (4.16)]. The synchronization bandwidth is the range of ω_{d} for which the oscillator frequency is locked to the driving frequency at steady state.

This is achieved when $|\omega_{\mathrm{d}} - \tilde{\omega}| = 0$, where $\tilde{\omega}$ the observed frequency of the driven oscillator, obtained from the peak of its spectrum averaged over one period of the drive [CKN20].

Here we find the Duffing nonlinearity to enhance quantum synchronization: For a range of λ and a fixed r, increasing β past a critical value widens the synchronization bandwidth linearly. This is illustrated in Fig. 4.3(a) where the synchronization bandwidth is plotted as a contour against $\bar{\beta} \equiv \beta r^2$ and F/r. The critical value of $\bar{\beta}$ is indicated by the red dashed line, where the bandwidth is equal to its corresponding value at $\bar{\beta} = 0$. However, this enhancement does not occur for all values of the vdP nonlinearity. In Fig. 4.3(b) we see that an increase of $\bar{\lambda} \equiv \lambda r^2$ from its value in Fig. 4.3(a) can ruin the gain in synchronization bandwidth due to $\bar{\beta}$. Noting that the dissipative terms in $\mathcal{L}$ are all proportional to λ, this effect can be qualitatively attributed to the phase diffusion due to quantum noise, which is known to inhibit synchronization [WNB14, LCW14, LS13]. We can develop some understanding of the quantum DvdP by examining its classical analog. Using the method of harmonic balance on x, we are able to derive the conditions for nonlinearity-enhanced synchronization analytically for the classical DvdP oscillator, given by

$$\bar{\beta} > \frac{\bar{\lambda}^2}{3(1-\bar{\lambda}^2)}\,, \quad 0 < \bar{\lambda} < 1\,. \tag{4.33}$$

This shows clearly the existence of a critical value of $\bar{\beta}$, and a finite interval of $\bar{\lambda}$ over which the synchronization enhancement occurs. These results are consistent with Fig. 4.3 except for the fact that quantum noise makes the range of λ for synchronization enhancement in the quantum DvdP oscillator smaller compared to the classical range as seen in Fig. 4.3(b).

It has also been shown in Fig that increasing the vdP nonlinearity in the quantum model can only reduce the synchronization bandwidth. One can thus be certain that the synchronization enhancement seen in our model is induced by the Duffing nonlinearity.

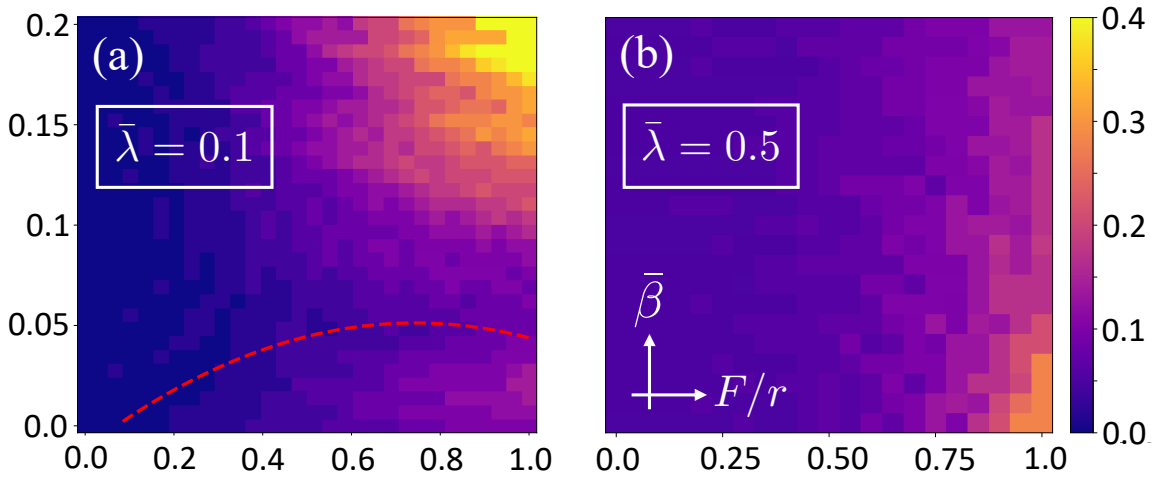

Figure 4.3: Contour plot of the synchronization bandwidth for the quantum DvdP oscillator as a function of $\bar{\beta} \equiv \beta r^2$ (vertical axis) and F/r (horizontal axis) with unit limit-cycle radius, i.e. $r = 1$. In this case $\bar{\beta} = \beta$ and $\bar{\lambda} = \lambda$. The axes are also indicated in subplot (b). (a) Illustration of synchronization enhancement for $\bar{\lambda} = 0.1$. Above a critical value of $\bar{\beta}$, indicated by a red dashed line (obtained numerically), the synchronization bandwidth is enlarged as the Duffing nonlinearity is increased. (b) Synchronization enhancement disappears if we increase the vdP nonlinearity from $\bar{\lambda} = 0.1$ to $\bar{\lambda} = 0.5$, demonstrating the finite range of $\bar{\lambda}$ over which the enhancement is effective. Copyright 2023, Phys. Rev. A, no permission needed for thesis purpose.

4.4 Nonlinearity-induced effects in disspatively coupled oscillators

4.4.1 Classical case

The equations of motion for two dissipatively coupled vdP oscillators are often written as

$$\begin{aligned} x_1'' + \lambda(x_1^2 - 1)\, x_1' + x_1 &= \frac{\eta}{2}\,(x_2' - x_1')\,, \\ x_2'' + \lambda(x_2^2 - 1)\, x_2' + (1 + \Delta)x_2 &= \frac{\eta}{2}\,(x_1' - x_2')\,, \end{aligned} \tag{4.34}$$

where η is the coupling strength and Δ is the detuning between the two oscillators. The system has four phase-space dimensions, two for each oscillator, given by $(x_1, y_1) = (x_1, x_1')$ and $(x_2, y_2) = (x_2, x_2')$. We can express the coupled system more simply using

complex amplitudes as we did in (4.10), except now

$$\alpha_k(t) = \frac{1}{2}\left[\, x_k(t) + i\, y_k(t) \,\right], \quad k = 1, 2\,. \tag{4.35}$$

We will analyze the following first-order averaged equations for the coupled system assuming the nonlinearity to be weak,

$$\begin{aligned} \alpha_1' &= -i\,\alpha_1 + \frac{\lambda}{2}\,(1 - |\alpha_1|^2)\alpha_1 + \frac{\eta}{2}\,(\alpha_2 - \alpha_1)\,, \\ \alpha_2' &= -i\,(1+\Delta)\alpha_2 + \frac{\lambda}{2}\,(1 - |\alpha_2|^2)\alpha_2 + \frac{\eta}{2}\,(\alpha_1 - \alpha_2)\,. \end{aligned} \tag{4.36}$$

Synchronization analysis

In fact, only three real variables are needed in polar coordinates. If we write

$$\alpha_k = R_k \exp\left(-i\phi_k\right), \quad k = 1, 2, \tag{4.37}$$

then we may express the coupled dynamics in terms of only R_1, R_2, and the phase difference $\varphi \equiv \phi_2 - \phi_1$:

$$\begin{aligned} R_1' &= \frac{\lambda}{2}\,R_1\,(1 - R_1^2) + \frac{\eta}{2}\,(R_2\cos\varphi - R_1)\,, \\ R_2' &= \frac{\lambda}{2}\,R_2\,(1 - R_2^2) + \frac{\eta}{2}\,(R_1\cos\varphi - R_2)\,, \\ \varphi' &= \Delta - \frac{\eta}{2}\left(\frac{R_1}{R_2} + \frac{R_2}{R_1}\right)\sin\varphi\,. \end{aligned} \tag{4.38}$$

By symmetry, if the two oscillators synchronize, we must have $R_1 = R_2 = R$. In this case the above equations simplify further to

$$\begin{aligned} R' &= \frac{\lambda}{2}\,R(1 - R^2) + \frac{\eta}{2}\,R(\cos\varphi - 1)\,, \\ \varphi' &= \Delta - \eta\sin\varphi\,. \end{aligned} \tag{4.39}$$

In the synchronized state, $R' = \varphi' = 0$. Solving the phase equation, we get two solutions, $\varphi_\star^{(1)} = \sin^{-1}(\Delta/\eta)$ and $\varphi_\star^{(2)} = \pi - \sin^{-1}(\Delta/\eta)$. To determine the stable phase, we use linear stability analysis. Substituting $\varphi(t) = \varphi_\star^{(k)} + \epsilon(t)$ $(k = 1, 2)$ into

the phase equation of motion and keeping only first-order terms in ϵ, we get

$$\epsilon' = \Delta - \eta \sin\left[\varphi_\star^{(k)} + \epsilon\right] = \Delta - \eta \sin\left[\sin^{-1}\left(\frac{\Delta}{\eta}\right) - (-1)^k \epsilon\right] \approx (-1)^k \epsilon\, \eta \sqrt{1 - \frac{\Delta^2}{\eta^2}}\ . \tag{4.40}$$

From this we see that $\varphi_\star^{(1)}$ is stable while $\varphi_\star^{(2)}$ is unstable. We also find that $|\Delta| < \eta$ to be a necessary condition for synchronization. Substituting $\varphi_\star^{(1)}$ into the radial equation $R' = 0$ then gives

$$\frac{\lambda}{2} R\,(1 - R^2) + \frac{\eta}{2} R \left(\sqrt{1 - \frac{\Delta^2}{\eta^2}} - 1\right) = 0\ . \tag{4.41}$$

This has the solution

$$R_\star^2 = 1 + \frac{\eta}{\lambda} \left(\sqrt{1 - \frac{\Delta^2}{\eta^2}} - 1\right)\ . \tag{4.42}$$

The zero-amplitude solution corresponds to the case of amplitude death and will be analyzed next. Performing linear stability analysis, we find that $r_\star$ is stable for $0 < |\Delta| \leq \lambda$ and $|\Delta| < \eta$, or when, $|\Delta| > \lambda$ and $|\Delta| < \sqrt{\lambda(2\eta - \lambda)}$. Combining the phase and amplitude solutions, the conditions for synchronization is then

$$|\Delta| < \eta\ , \quad \text{for } \eta \leq \lambda\ , \tag{4.43}$$

$$|\Delta| < \sqrt{\lambda(2\eta - \lambda)}\ , \quad \text{for } \eta > \lambda\ . \tag{4.44}$$

Amplitude death

It is possible for coupled oscillators to achieve amplitude death, where the limit cycle oscillations are suppressed due to the mutual coupling. To obtain the conditions for amplitude death, we require the solution $\alpha_1 = \alpha_2 = 0$ to be stable. Since the phase is undefined in this case, we will analyze in Cartesian coordinates instead. Denoting $\alpha_k = \Re[\epsilon_k] + i\,\Im[\epsilon_k]$ $(k = 1, 2)$ for small ϵ_k, we can linearize the coupled equations

around the origin, giving,

$$\begin{pmatrix} \Re[\epsilon_1] \\ \Im[\epsilon_1] \\ \Re[\epsilon_2] \\ \Im[\epsilon_2] \end{pmatrix}' = \begin{pmatrix} (\lambda-\eta)/2 & \omega_1 & \eta/2 & 0 \\ -\omega_1 & (\lambda-\eta)/2 & 0 & \eta/2 \\ \eta/2 & 0 & (\lambda-\eta)/2 & \omega_2 \\ 0 & \eta/2 & -\omega_2 & (\lambda-\eta)/2 \end{pmatrix} \begin{pmatrix} \Re[\epsilon_1] \\ \Im[\epsilon_1] \\ \Re[\epsilon_2] \\ \Im[\epsilon_2] \end{pmatrix} , \tag{4.45}$$

where $\omega_1 = 1$ and $\omega_2 = 1 + \Delta$. Let h be the eigenvalues of the stability matrix in (4.45), and $p = h - (\lambda - \eta)/2$. The characteristic polynomial for h then reads

$$p^4 + p^2 \left(\omega_1^2 + \omega_2^2 - \frac{\eta^2}{2}\right) + \left(\frac{\eta^2}{4} + \omega_1\,\omega_2\right)^2 = 0$$

$$\implies \quad \left[p^2 - \left(\frac{\eta^2}{4} + \omega_1\,\omega_2\right)\right]^2 = -(\omega_1+\omega_2)^2\,p^2 \,. \tag{4.46}$$

The eigenvalues h are therefore

$$h = \frac{1}{2}\left[\lambda - \eta \pm \sqrt{\eta^2 - \Delta^2}\right] \pm i\,\frac{(\omega_1+\omega_2)}{2} \,. \tag{4.47}$$

For $\alpha_1 = \alpha_2 = 0$ to be stable, the real part of h must be negative. This gives us the the following necessary and sufficient condition for amplitude death

$$\eta > \lambda \,, \quad |\Delta| > \sqrt{\lambda(2\eta - \lambda)} \,. \tag{4.48}$$

The curve $|\Delta| = \sqrt{\lambda\,(2\eta - \lambda)}$ thus separates the regions of synchronization and amplitude death, also known as the Hopf bifurcation curve.

Effect of the Duffing nonlinearity

Recall from (4.17) that a Duffing–van der Pol (DvdP) oscillator has a nonlinear frequency term βx^3 in its second-order equation of motion for x. If we were to define the DvdP by its equation of motion for its complex amplitude α, then this term amounts to adding $-i3\beta|\alpha|^2\alpha$ to α' under first-order time averaging with respect to the Duffing nonlinearity. We show here that such a modification due to the Duffing nonlinearity in two dissipatively coupled DvdP oscillators does not change their mutual synchronization from the $\beta = 0$ case. The classical time-averaged equations of motion

for two dissipatively-coupled DvdP oscillators are

$$\alpha_1' = -i\,\omega_1\,\alpha_1 + \frac{\lambda}{2}\,(r^2 - |\alpha_1|^2)\alpha_1 + i\frac{\lambda^2}{8}\left(r^4 - 6r^2|\alpha_1|^2 + \frac{11}{2}|\alpha_1|^4\right)\alpha_1 - i\frac{3\beta}{2}\,|\alpha_1|^2\alpha_1 + \frac{\eta}{2}\,(\alpha_2 - \alpha_1)\,, \tag{4.49}$$

$$\alpha_2' = -i\,\omega_2\,\alpha_2 + \frac{\lambda}{2}\,(r^2 - |\alpha_2|^2)\alpha_2 + i\frac{\lambda^2}{8}\left(r^4 - 6r^2|\alpha_2|^2 + \frac{11}{2}|\alpha_2|^4\right)\alpha_2 - i\frac{3\beta}{2}\,|\alpha_2|^2\alpha_2 + \frac{\eta}{2}(\alpha_1 - \alpha_2)\,, \tag{4.50}$$

where $\omega_1 = 1$ and $\omega_2 = 1 + \Delta$. Note these equations assume second-order time averaging with respect to the vdP nonlinearity [see (4.13)]. As in the case of $\beta = 0$ in Sec. 4.4.1, mutual synchronization is more easily analyzed using polar coordinates, where $\alpha_k = R_k \exp(-i\phi_k)$ $(k = 1, 2)$. Equations (4.49) and (4.50) are then equivalent to

$$\begin{aligned} R_1' &= \frac{\lambda}{2}\left(r - R_1^2\right)R_1 + \frac{\eta}{2}\left(R_2\cos\varphi - R_1\right)\,, \\ R_2' &= \frac{\lambda}{2}\left(r - R_2^2\right)R_2 + \frac{\eta}{2}\left(R_1\cos\varphi - R_2\right)\,, \\ \varphi' &= \Delta - \frac{\lambda^2}{8}\left[6r^2\left(R_1^2 - R_2^2\right) - \frac{11}{2}\left(R_1^4 - R_2^4\right)\right] - \frac{3\beta}{2}\left(R_1^2 - R_2^2\right) - \frac{\eta}{2}\left(\frac{R_1}{R_2} + \frac{R_2}{R_1}\right)\sin\varphi\,. \end{aligned} \tag{4.51}$$

Recall from Sec. 4.4.1 that we have defined $\varphi \equiv \phi_2 - \phi_1$. By symmetry, when the two oscillators synchronize, we have $R_1 = R_2$. Consequently, the equation of motion for the phase difference φ becomes independent of R_1 and R_2. Moreover, the β term vanishes, which suggests that the β nonlinearity has no effect on the mutual synchronization.

Synchronization bandwidth

For a fixed η, we define from Eq. (4.44) the synchronization bandwidth to be the range of initial detunings Δ for which the two oscillators synchronize. This is given by the piecewise function

$$\text{Bandwidth} = \begin{cases} 2\sqrt{\lambda(2\eta - \lambda)} & \lambda \le \eta \\ 2\,\eta & \lambda > \eta \end{cases} \tag{4.52}$$

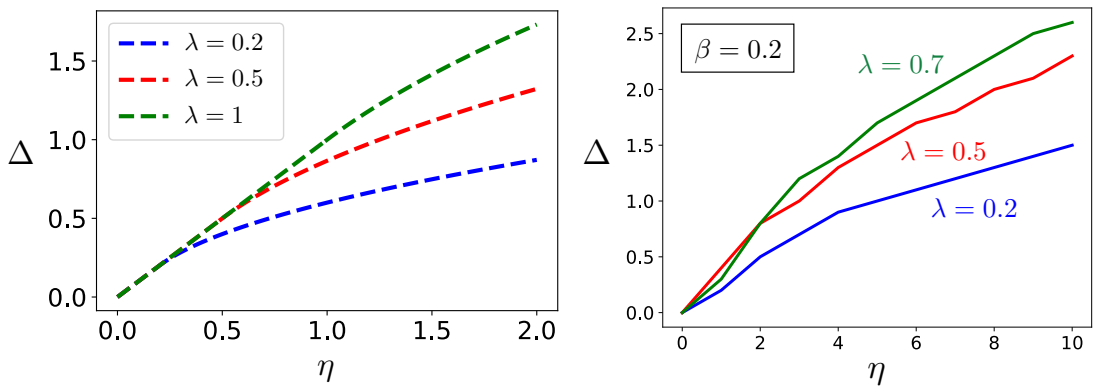

Figure 4.4: Synchronization boundaries for different values of λ in (a)classical; (b)quantum simulations. The synchronization region lies below the curve in the all cases. The synchronization bandwidth is enlarged as λ is increased for a fixed η. Comparing (b) with Fig. 4.5(b), we see that the additional Kerr nonlinearity $\beta = 0.2$ does not change the synchronization boundary. Copyright 2023, Phys. Rev. A, no permission needed for thesis purpose.

where the factor of 2 arises because Δ can be either positive or negative (or zero). Increasing λ from 0, we find that the bandwidth increases monotonically until $\lambda = \eta$, after which the bandwidth saturates at 2η. Thus, the vdP nonlinearity enlarges the synchronization bandwidth. This is shown by the synchronization boundaries in Fig. 4.4 for various values of λ, where synchronization regions lie below the boundary curves. Fixing η and increasing the nonlinearity parameter λ leads to a larger synchronization bandwidth. This also implies that fixing Δ and η while increasing λ can lead to *nonlinearity-induced* mutual synchronization whereby the two oscillators transition suddenly from amplitude death to synchronized oscillations.

As a measure for synchronization enhancement, we can calculate the 'total bandwidth' by integrating the synchronization bandwidth from $\eta = 0$ to some $\eta = \eta_{\max}$, which can then be evaluated asymptotically for large $\eta_{\max}$ (compared to λ). This gives (assuming $\eta_{\max} > \lambda$)

$$B(\lambda, \eta_{\max}) = \int_0^{\lambda} d\eta\, \eta + \int_{\lambda}^{\eta_{\max}} d\eta\, \sqrt{\lambda(2\eta - \lambda)} = \frac{1}{6}\lambda^2 + \frac{1}{3}\lambda^{1/2}\,(2\eta_{\max} - \lambda)^{3/2}$$
$$\approx \frac{2\sqrt{2}}{3}\,\lambda^{1/2}\,\eta_{\max}^{3/2}\,, \quad (4.53)$$

which increases as $\lambda^{1/2}$. Since B has the geometrical interpretation of the area covered

by the synchronization region in the parameter space (λ, η), this means that the synchronization region grows with the vdP nonlinearity λ.

4.4.2 Quantum case

Two dissipatively coupled vdP oscillators (i.e. no Duffing nonlinearity) can be described by the Lindbladian

$$\mathcal{L} = \mathcal{L}_1 + \mathcal{L}_2 - i\,\Delta[\hat{a}_2^\dagger \hat{a}_2, \cdot] + \eta\,\mathcal{D}[\hat{a}_1 - \hat{a}_2]\,, \tag{4.54}$$

where $\mathcal{L}_k$ $(k = 1, 2)$ is the Lindbladian for oscillator k, defined by setting $\hat{a}$ to $\hat{a}_k$ and $\beta = F = 0$ in (4.15) and (4.16). We have assumed the oscillators to be identical (i.e. same λ and r) except for an initial detuning of Δ, and denoted their coupling strength by η.

In this case, frequency locking occurs when the observed frequencies of the two oscillators become identical at steady state. As before, the observed frequency of oscillator k is given by the location at which its spectrum is peaked, i.e. where $S_k(\omega) = \int_{-\infty}^{\infty} dt\, \exp(i\omega t)\langle \hat{a}_k^\dagger(t)\hat{a}_k(0)\rangle$ is maximized, and where the two-oscillator steady state is to be used. For a fixed η, we define the synchronization bandwidth to be the range of Δ for which the two oscillators lock frequencies. It will also be interesting to look at position correlations in the two oscillators at steady state, defined by

$$\Sigma = \frac{\langle \hat{x}_1 \hat{x}_2 \rangle - \langle \hat{x}_1 \rangle \langle \hat{x}_2 \rangle}{\sqrt{\left[\, \langle \hat{x}_1^2 \rangle - \langle \hat{x}_1 \rangle^2 \,\right] \left[\, \langle \hat{x}_2^2 \rangle - \langle \hat{x}_2 \rangle^2 \,\right]}}\,, \tag{4.55}$$

where $\hat{x}_k = \hat{a}_k + \hat{a}_k^\dagger$. Note that frequency locking implies a nonzero Σ, but not vice versa.

In addition to frequency locking, dissipatively coupled oscillators can also cease to oscillate. If the oscillators are classical, then this may happen for a range of η provided that Δ is sufficiently large. And if both oscillators stabilize to the same phase-space point, which may be taken to be the origin without loss of generality, then the effect is termed amplitude death [SPR12, KVK13]. To define amplitude death in quantum oscillators we generalize the notion of P-bifurcations from classical stochastic systems to the steady-state Wigner function of a reduced state (see Ref. [CMNK22] and other references therein). In this case, amplitude death is said to occur if the single-oscillator Wigner functions peak at the origin in quantum phase space. This approach is

consistent with previous studies on amplitude death in coupled quantum oscillators [BKBB20, AKLB18, BKB21, IK17].

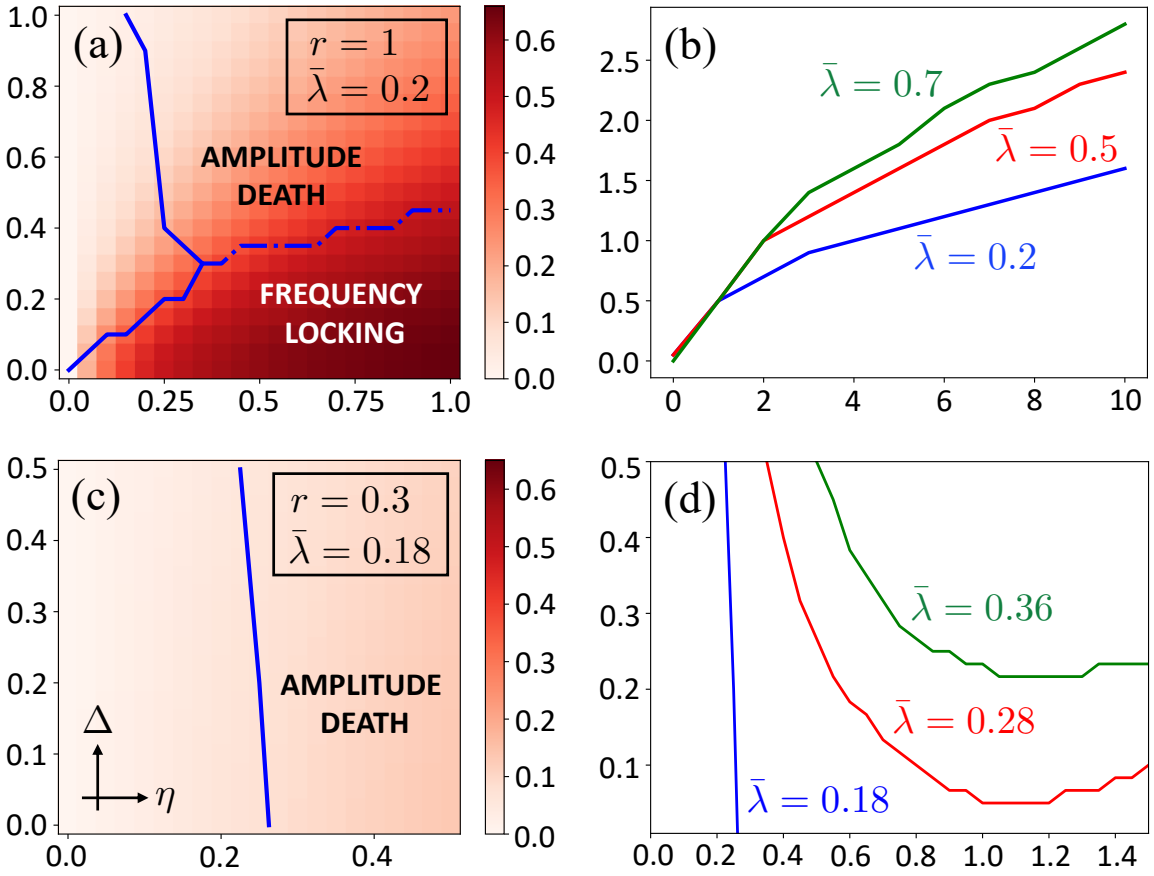

Figure 4.5: Regions of frequency locking and amplitude death (as defined in the text by the power spectrum and Wigner function) for two dissipatively coupled vdP oscillators [subplots (a)–(d)] along with contours of Σ [subplots (a) and (c)]. All subplots have Δ on the vertical axis, and η on horizontal axis which we also indicate in subplot (c). (a) Large r (semiclassical regime). Note the region on the left does not correspond to any identifiable effect and is demarcated using a solid line while the boundary between frequency locking and amplitude death is a Hopf bifurcation, which we denote by a dash-dotted line. As r is increased, the classical boundary is recovered. (b) Effect of varying λ on synchronization for $r = 1$. Boundaries of the frequency-locking region and its corresponding λ are shown (i.e. the frequency-locking region is the area underneath each curve). Increasing λ can enlarge the synchronization bandwidth and induce frequency locking from a state of amplitude death. (c) Small r (deep quantum regime). At small r, amplitude death occurs even at zero initial detuning, which is a quantum effect. Note that $\bar{\lambda}$ in (a) and (c) are approximately equal, leaving the differences between the two plots only as a result of quantum effects. (d) Shifts in amplitude-death boundary as $\bar{\lambda}$ is increased (quantum-to-semiclassical transition). Copyright 2023, Phys. Rev. A, no permission needed for thesis purpose.

In Fig. 4.5 we work out regions of frequency locking and amplitude death in the (η, Δ)

parameter space for (4.54), along with Σ, shown as a contour in Fig. 4.5(a) and (c). Two especially interesting scenarios are—when the limit cycles are relatively large compared to quantum noise [Fig. 4.5(a)]; and when they become small, being more susceptible to quantum noise [Fig. 4.5(c)].

In Fig. 4.5(a) we have indicated the boundary between frequency locking and amplitude death by a dash-dotted line, while no identifiable phenomenon occurs to the left of the solid line. Note the dash-dotted line is a Hopf-bifurcation curve because the transition from amplitude death to frequency locking is facilitated by a Hopf bifurcation. Clearly, Σ is larger inside the frequency-locking region. Especially significant here is the effect of the vdP nonlinearity on synchronization. Whereas in the single-oscillator case the vdP nonlinearity had only detrimental effects, it now has a constructive role by enlarging the (mutual) synchronization bandwidth. We illustrate this in Fig. 4.5(b) where additional frequency-locking boundaries for different values of vdP nonlinearity λ are plotted. It can be seen that increasing λ enlarges the frequency-locking region. This means that two oscillators in a state of amplitude death with an (η, Δ) lying above the Hopf-bifurcation curve in Fig. 4.5(a) will transit suddenly to a state of synchronized oscillations when λ is sufficiently increased. This may be appropriately called nonlinearity-induced mutual synchronization.

Turning now to the case of a small limit cycle ($r \ll 1$) in Fig. 4.5(c), we find frequency locking to be absent while position correlations become negligible. The blue solid line delineates the boundary of amplitude death. Most striking is the persistence of amplitude death at zero detuning (i.e. $\Delta = 0$). Classically, some frequency mismatch between the two oscillators must be present in order for amplitude death to occur [SPR12]. This signifies a clear distinction between classical and quantum dynamics. A loss of amplitude death at $\Delta = 0$ may then be expected if we increased either r or λ (while holding the other constant). This is indeed what we find, as illustrated in Fig. 4.5(d), where such a quantum-to-semiclassical transition is captured by increasing $\bar{\lambda} \equiv \lambda r^2$.

Since we have focused exclusively on the vdP nonlinearity here, we note that incorporating a Duffing nonlinearity into our model will not in fact change the frequency-locking boundary. We can understand this from the classical coupled equations of motion, where we see that β appears only in the phase dynamics of the oscillators, and that such terms vanish at steady state for identical oscillators (equal limit cycle radii) [AEK90].

Deep quantum limit

We derive here a sufficient condition for amplitude death in two dissipatively coupled SL oscillators in the deep quantum regime. The density operator for two dissipatively-coupled oscillators satisfies $\rho' = \mathcal{L}\rho$ where $\mathcal{L}$ given by

$$\mathcal{L} = -i\,\Delta\left[\hat{a}_1^\dagger \hat{a}_1, \bullet\right] + \kappa\left(\mathcal{D}[\hat{a}_1^\dagger] + \mathcal{D}[\hat{a}_2^\dagger]\right) + \gamma\left(\mathcal{D}[\hat{a}_1^2] + \mathcal{D}[\hat{a}_2^2]\right) + \eta\,\mathcal{D}[\hat{a}_1 - \hat{a}_2]\,, \quad (4.56)$$

where Δ is the detuning between the two oscillators and η is the dissipative coupling strength. Note that we have assumed equal single-photon amplification rates κ, and equal two-photon dissipation rates γ for the two oscillators. In the deep quantum limit, i.e. when $\gamma/\kappa \longrightarrow \infty$, the process of two-photon loss dominates and this confines each oscillator to the zero- and one-photon subspace. This allows us to treat each oscillator effectively as a two-level system. After adiabatically eliminating the higher excited states [LCW14]) we have

$$\bar{\mathcal{L}} = -i\,\bar{\Delta}\left[\hat{\sigma}_1^+\hat{\sigma}_1^-, \bullet\right] + \mathcal{D}[\hat{\sigma}_1^+] + \mathcal{D}[\hat{\sigma}_2^+] + 2\,\mathcal{D}[\hat{\sigma}_1^-] + 2\,\mathcal{D}[\hat{\sigma}_2^-] + \bar{\eta}\,\mathcal{D}[\hat{\sigma}_1 - \hat{\sigma}_2^-] \quad (4.57)$$

where $\bar{\Delta} \equiv \Delta/\kappa$ and $\bar{\eta} \equiv \eta/\kappa$. We have also denoted the creation and annihilation operators for the jth oscillator in the $\{|0\rangle, |1\rangle\}$ subspace by $\hat{\sigma}_j^+$ and $\hat{\sigma}_j^-$. With this simplification, we can solve for the steady-state density matrix exactly, defined by $\bar{\mathcal{L}}\varrho = 0$. In the basis $\{|00\rangle, |01\rangle, |10\rangle, |11\rangle\}$ we find

$$\varrho = \begin{pmatrix} \varrho_{11} & 0 & 0 & 0 \\ 0 & \varrho_{22} & \varrho_{23} & 0 \\ 0 & \varrho_{32} & \varrho_{33} & 0 \\ 0 & 0 & 0 & \varrho_{44} \end{pmatrix}. \quad (4.58)$$

The matrix elements are given explicitly by

$$\begin{aligned} \varrho_{11} &= \left[6\,\bar{\eta}^3 + (\bar{\eta}+2)^2\bar{\Delta}^2 + 34\,\bar{\eta}^2 + 60\,\bar{\eta} + 36\right]/\nu\,, \\ \varrho_{22} = \varrho_{33} &= \left[\bar{\eta}^3 + (\bar{\eta}+2)^2\,\bar{\Delta}^2 + 8\bar{\eta}^2 + 21\bar{\eta} + 18\right]/\nu\,, \\ \varrho_{44} &= \left[\bar{\eta}^2 + \bar{\Delta}^2 + 6\,\bar{\eta} + 9\right]/\nu\,, \\ \varrho_{23} = \varrho_{32}^* &= \left[\bar{\eta}(\bar{\eta}+1)(\bar{\eta}+3) + i\,\bar{\eta}(\bar{\eta}+1)\bar{\Delta}\right]/\nu\,, \end{aligned} \quad (4.59)$$

where for ease of writing we have introduced the factor

$$\nu = 8\,\bar{\eta}^3 + (\bar{\eta}+3)^2\bar{\Delta}^2 + 51\,\bar{\eta}^2 + 108\,\bar{\eta} + 81\ . \tag{4.60}$$

It is straightforward to evaluate the position correlation coefficient

$$\begin{aligned}\Sigma =& \frac{\langle \hat{x}_1\hat{x}_2\rangle - \langle \hat{x}_1\rangle\langle \hat{x}_2\rangle}{\sqrt{\left[\,\langle \hat{x}_1^2\rangle - \langle \hat{x}_1\rangle^2\,\right]\left[\,\langle \hat{x}_2^2\rangle - \langle \hat{x}_2\rangle^2\,\right]}} \\ =& \frac{\rho_{23}+\rho_{32}}{\mathrm{Tr}[\varrho]} = \frac{2\,\bar{\eta}\,(\bar{\eta}+1)}{8\,\bar{\eta}^2 + 27\,\bar{\eta} + (\bar{\eta}+3)\bar{\Delta}^2 + 27}\end{aligned} \tag{4.61}$$

where $\hat{x}_j = \hat{\sigma}_j^+ + \hat{\sigma}_j^-$ $(j=1,2)$. The maximum correlation $\Sigma \longrightarrow 1/4$ is achieved in the limit $\bar{\Delta} \longrightarrow 0$ and $\bar{\eta} \longrightarrow \infty$. To study amplitude death, we trace out the second oscillator, giving the single-oscillator density matrix

$$\varrho_1 = \mathrm{Tr}_2[\varrho] = \begin{pmatrix} \varrho_{11}+\varrho_{22} & 0 \\ 0 & \varrho_{33}+\varrho_{44} \end{pmatrix}. \tag{4.62}$$

Its Wigner distribution, taken as a function of the radial coordinate r, can then be calculated explicitly as

$$W_1(r) = (\varrho_{11}+\varrho_{22})\,e^{-r^2} + (\varrho_{33}+\varrho_{44})(2\,r^2-1)\,e^{-r^2}\ . \tag{4.63}$$

We define amplitude death to be the regime where the Wigner distribution possesses a single peak at the origin instead of being ring like. A sufficient and necessary condition for this is when $\varrho_{11}+\varrho_{22} \geq 3/4$, or equivalently,

$$\bar{\Delta}^2 \geq \frac{27 - 15\,\bar{\eta}^2 - 4\,\bar{\eta}^3}{(\bar{\eta}-1)(\bar{\eta}-2)}\ . \tag{4.64}$$

Interestingly, when the two oscillators are on resonance ($\bar{\Delta} = \Delta = 0$), amplitude death can still occur as long as $\bar{\eta} \gtrsim 1.17$. This is due to the quantum noise which is significant in the deep quantum limit, rather than coming from the frequency mismatch between the oscillators.

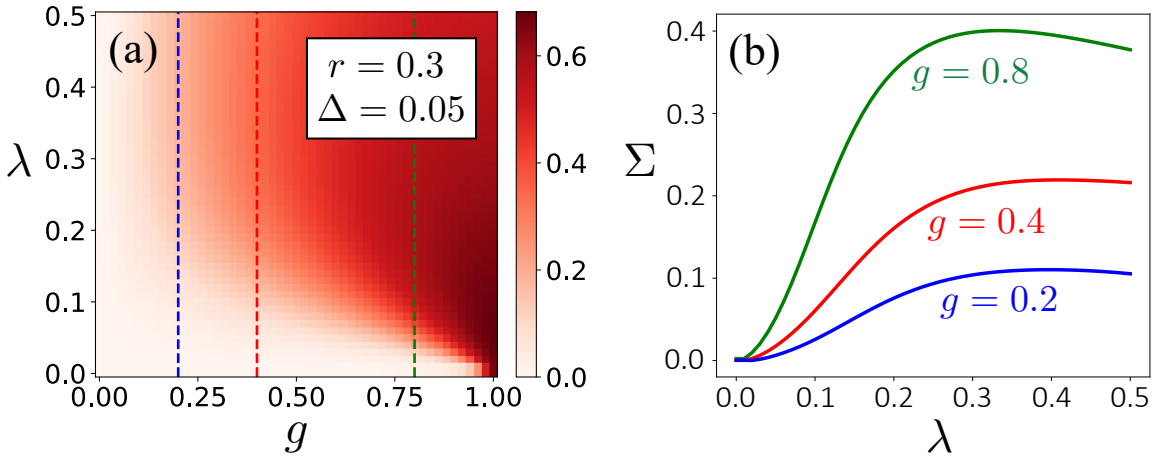

Figure 4.6: Positional correlation (4.55) for two reactively coupled vdP oscillators. (a) Contour of Σ as a function of λ and g for $r = 0.3$ and $\Delta = 0.05$. The bottom gap of zero correlation agrees with the SL limit. (b) Correlations along the three vertical dashed lines at $g = 0.2$, 0.4, and 0.8 in subplot (a). Copyright 2023, Phys. Rev. A, no permission needed for thesis purpose.

4.5 Nonlinearity-induced correlations in reactively coupled oscillators

4.5.1 Classical case

Let us first consider two classical SL oscillators which are reactively coupled with strength g. The coupled complex-amplitude equations are

$$\begin{aligned}\alpha_1' &= -i\,\alpha_1 + \frac{\lambda}{2}(1 - |\alpha_1|^2)\,\alpha_1 + i\,g(\alpha_2 - \alpha_1)\,,\\ \alpha_2' &= -i\,(1+\Delta)\,\alpha_2 + \frac{\lambda}{2}(1 - |\alpha_2|^2)\,\alpha_2 + i\,g(\alpha_1 - \alpha_2)\,.\end{aligned} \tag{4.65}$$

Similar to before, we work in polar coordinates, giving

$$\begin{aligned}R_1' &= \frac{\lambda}{2}\,R_1(1 - R_1^2) + g\,R_2\sin\varphi\,,\\ R_2' &= \frac{\lambda}{2}\,R_2(1 - R_2^2) - g\,R_1\sin\varphi\,,\\ \varphi' &= \Delta + g\left(\frac{R_2}{R_1} - \frac{R_1}{R_2}\right)\cos\varphi\,.\end{aligned} \tag{4.66}$$

At steady state, $R_1 = R_2$, and we see that $\varphi' = \Delta$. In other words, the rate at which the phase difference grows is exactly the detuning between the two oscillators.

Thus for reactive coupling, the two oscillators simply cannot synchronize. This result generalizes to the case two quantum SL oscillators.

What is particularly interesting in the case of reactive coupling is how the oscillators behave beyond the $\lambda \longrightarrow 0^+$ limit. In the main text we have shown that increasing the nonlinearity in two reactively coupled quantum vdP oscillators increases their position correlation before a plateau is reached. This result is particularly interesting because the analogous classical system fails to produce the same effect. Here we show this explicitly by computing the steady-state correlation coefficient for the positions of two classical vdP oscillators as a function of their nonlinearities (assumed identical, given by λ) and their coupling strength. The position correlation coefficient in this case is given by

$$\Sigma = \frac{\sum_{m=1}^{M} \left[x_1^{(m)} - \bar{x}_1\right]\left[x_2^{(m)} - \bar{x}_2\right]}{\sqrt{\sum_{m=1}^{M} \left[x_1^{(m)} - \bar{x}_1\right]^2}\sqrt{\sum_{m=1}^{M} \left[x_2^{(m)} - \bar{x}_2\right]^2}} \,, \tag{4.67}$$

where $\left\{\left(x_1^{(1)}, x_2^{(1)}\right), \left(x_1^{(2)}, x_2^{(2)}\right), \ldots, \left(x_1^{(M)}, x_2^{(M)}\right)\right\}$ are pairwise samples of $\left(x_1(t), x_2(t)\right)$. Note that since we are interested in how $x_1(t)$ and $x_2(t)$ are correlated in the long-time time limit, each pairwise sample must be taken from $x_1(t)$ and $x_2(t)$ after all transience has died out. We have also defined

$$\bar{x}_k = \frac{1}{M}\sum_{m=1}^{M} x_k^{(m)} \,. \tag{4.68}$$

For the two classical vdP oscillators we may simply take $\left(x_1^{(m)}, x_2^{(m)})\right) = \left(x_1(m\,\delta t), x_2(m\,\delta t)\right)$ where we have introduced a small time increment δt. For a sufficiently large sample size M, (4.67) measures how correlated $x_1(t)$ and $x_2(t)$ are in the long-time limit (or steady state). The result of such a computation is shown in Fig. 4.7 as a function of λ and g. As $\lambda \longrightarrow 0$, we can see that the correlation vanishes, as expected from the SL model. But more importantly, and omitting the degenerate $\lambda = 0$ case, we find that Σ appears to decrease monotonically with λ, and decreases sharply to zero when λ exceeds some critical value. It is simply impossible to increase Σ by increasing λ for two reactively-coupled classical vdP oscillators at a fixed g. This is in stark contrast to the same calculation performed for two such quantum vdP oscillators for which Σ can increase if λ is increased for a given g.

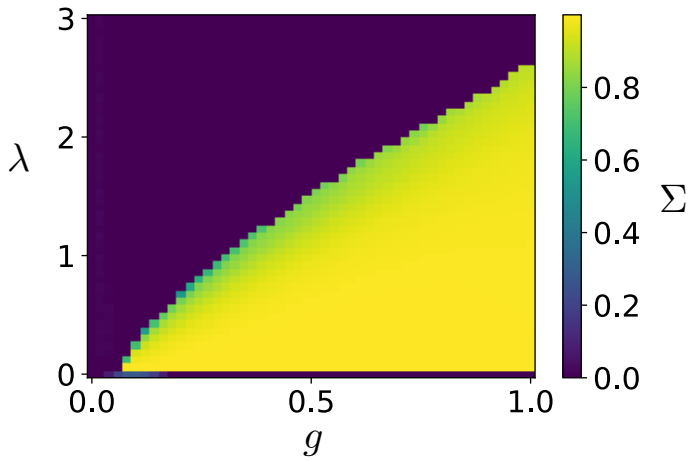

Figure 4.7: Correlation coefficient of two reactively-coupled vdP oscillators for $\Delta = 0.1, r = 1$. Copyright 2023, Phys. Rev. A, no permission needed for thesis purpose.

4.5.2 Quantum case

It is known that two reactively coupled SL oscillators cannot synchronize nor share position correlations. This is true even in the quantum case. However, we show here that positional correlations between two reactively coupled quantum vdP oscillators do develop. Here we must use the exact vdP Lindbladian [CKN20], because under reactive coupling, the approximate model does not produce any off-diagonal elements in the steady state, and hence cannot generate correlations in the two oscillators. As with the dissipatively coupled system, two reactively coupled vdP oscillators can be modelled by considering two uncoupled vdP oscillators with annihilation operators $\hat{a}_1$ and $\hat{a}_2$, coupled by the Hamiltonian $g(\hat{a}_1\hat{a}_2^\dagger + \hat{a}_1^\dagger\hat{a}_2)$, where g is the reactive coupling strength. As before, we assume that both oscillators have the same nonlinearity λ.

In Fig. 4.6(a), we generate a contour plot of Σ as a function of λ and g at $r = 0.3$ and $\Delta = 0.05$. From this we see that for a fixed g, increasing the oscillator nonlinearity beyond the SL regime leads to stronger correlations. We illustrate this more clearly in Fig. 4.6(b) by showing how Σ varies as a function of λ for $g = 0.2$, 0.4, and 0.8, which are marked in Fig. 4.6(a) by vertical dashed lines. Note this also shows the existence of an optimal λ which maximizes Σ. Such nonlinearity-induced correlations are absent in the corresponding classical model. At a given coupling strength, the position correlation in two reactively coupled classical vdP oscillators decreases monotonically as λ increases.

Deep quantum limit

We show here that two identical reactively-coupled quantum SL oscillators cannot share any position correlations. This permits calling the correlations observed in two similarly coupled vdP oscillators to be nonlinearity induced. For two reactively-coupled quantum SL oscillators, its Lindbladian (in units where $\kappa = 1$, $\Delta = 0$)

$$\mathcal{L} = -ig\left[\hat{a}_1^\dagger \hat{a}_2 + \hat{a}_2^\dagger \hat{a}_1, \bullet\right] + \mathcal{D}\left[\hat{a}_1^\dagger\right] + \mathcal{D}\left[\hat{a}_2^\dagger\right] + \gamma\left(\mathcal{D}\left[\hat{a}_1^2\right] + \mathcal{D}\left[\hat{a}_2^2\right]\right). \tag{4.69}$$

To order $1/\gamma$, we can truncate the Hilbert space of each oscillator to the first three levels, and solve for the steady-state density matrix ϱ (again defined by $\mathcal{L}\varrho = 0$),

$$\begin{aligned}\varrho = &\left[\frac{4}{9} + \frac{4(7g^2-6)}{81\gamma}\right]|00\rangle\langle 00| + \left[\frac{2}{9} - \frac{4(g^2+3)}{81\gamma}\right](|01\rangle\langle 01| + |10\rangle\langle 10|) + \frac{2}{9\gamma}|02\rangle\langle 02| \\ &+ \frac{2}{9\gamma}(|02\rangle\langle 02| + \langle 20|\langle 20|) + \left[\frac{1}{9} - \frac{2(10g^2+3)}{81\gamma}\right]|11\rangle\langle 11| + \frac{1}{9\gamma}\big(|12\rangle\langle 12| + |21\rangle\langle 21|\big) \\ &+ \frac{i\sqrt{2}g}{9\gamma}\big(|11\rangle\langle 20| + |11\rangle\langle 02| - |02\rangle\langle 11| - |20\rangle\langle 11|\big).\end{aligned} \tag{4.70}$$

It can then be checked explicitly from this expression for ϱ that Σ is always zero.

4.6 Conclusion

This work goes beyond the well-studied paradigm of weak nonlinearity in quantum synchronization, and provides the first systematic study of quantum synchronization effects for strong nonlinearity. We introduced a new quantum oscillator model which captures intriguing effects induced by two strong nonlinearities. We showed that a strong Duffing nonlinearity leads to a linear enhancement of the synchronization bandwidth in driven oscillators. We also reported genuine quantum synchronization effects exclusive to strong nonlinearity which are not observed previously: Increasing the vdP nonlinearity enhances the synchronization bandwidth, and revives synchronization between dissipatively-coupled oscillators in amplitude death. For reactively-coupled vdP oscillators on the other hand, we find that strong nonlinearity induces position correlations which are impossible in the weakly-nonlinear limit. This model provides a new paradigm for studying other strongly nonlinear effects such as chaos [Stö00, Str18, Haa00, Bra01].

Chapter 5

Quantum synchronization enhanced by homodyne detection,noise and squeezing

Despite the rapid development in the field of quantum synchronization, few researchers have studied how to efficiently boost synchronization. Homodyne measurement emerges as one of the successful candidates for this task, but existing work is confined to the semi-classical regime. In our work, we focus on the phase synchronization of a harmonic-driven quantum Stuart-Landau oscillator, and show that the enhancement induced by homodyne measurement persists into the quantum regime. Interestingly, optimal two-photon damping rates exist when the oscillator and driving are at resonance and with a small single-photon damping rate. We also report noise-induced enhancement in quantum synchronization when the single-photon damping rate is sufficiently large. Apart from these results, we discover that adding a squeezing Hamiltonian can further boost synchronization, especially in the semi-classical regime. Furthermore, the addition of squeezing affects the optimal two-photon pumping rates.

5.1 Homodyne-monitored quantum oscillator model

We study the quantum Stuart–Landau model (also widely accepted as the quantum van der Pol model in the existing literature) subjected to both harmonic drive and two photon squeezing drive, with continuous homodyne measurement at the output. The stochastic master equation of the system under homodyne measurement in the

This chapter is published substantially as "Enhancing quantum synchronization through homodyne measurement, noise, and squeezing" in Physical Review E 108 (2), 024204, 2023.(No written permission from APS is necessary for thesis purposes.)

rotating frame of the drive is given by(with $\hbar = 1$):

$$\begin{aligned} d\rho =& \{-i[\hat{H}, \rho] + \gamma_1 \mathcal{D}[a^\dagger]\rho + \gamma_2 \mathcal{D}[a^2]\rho \\ &+ \gamma_3 \mathcal{D}[a]\rho\} dt + \sqrt{\eta_d \gamma_3}\mathcal{H}[ae^{-i\theta}]\rho dW, \qquad (5.1) \\ \hat{H} =& \Delta a^\dagger a + iE(a - a^\dagger) + i\eta(a^{\dagger 2} e^{2i\phi} - a^2 e^{-2i\phi}), \qquad (5.2) \end{aligned}$$

where $\mathcal{D}[L]\rho = L\rho L^\dagger - \frac{1}{2}(L^\dagger L\rho + \rho L^\dagger L)$, $\mathcal{H}[L]\rho = L\rho + \rho L^\dagger - \mathrm{Tr}[(L+L^\dagger)\rho]\rho$, and $\mathcal{H}[ae^{-i\theta}]$ characterizes the measurement on the quadrature $ae^{-i\theta} + a^\dagger e^{i\theta}$, with γ_1, γ_2 and γ_3 corresponding to negative damping, nonlinear damping and linear damping respectively. Without loss of generality we assume a perfect detector and its detection efficiency is set to $\eta_d = 1$ throughout this paper. We denote $\Delta = \omega_0 - \omega_d$ as the amount of initial detuning between the frequency of the drive, ω_d, and the natural frequency of the oscillator, ω_0. E denotes the amplitude of the harmonic drive, with a the annihilation operator and $a^\dagger$ the creation operator. η is the squeezing parameter, and ϕ represents the phase of the squeezing. W represents the Wiener process where $\mathbb{E}[dW] = 0$ and $\mathbb{E}[dW^2] = dt$, and the measurement record $dY = \sqrt{\eta_d \gamma_3}\ \mathrm{Tr}[(ae^{-i\theta} + a^\dagger e^{i\theta})\rho]dt + dW$. For simplicity, we scale every parameter in the unit of $\gamma_1 = 1$.

As a measure of synchronization, the phase coherence is frequently used in the literature [LNN+17, KN21a], defined as

$$S = |S|e^{i\phi_{avg}} = \frac{\mathrm{Tr}[a\rho]}{\sqrt{\mathrm{Tr}[a^\dagger a\rho]}}, \qquad (5.3)$$

where $|S|$ measures the degree of phase coherence with a range of $0 \leq |S| \leq 1$. ϕ_{avg} represents the average phase of the oscillator. The phase coherence quantifies the statistic fluctuation in the phase distribution and therefore the tendency for quantum oscillator to lock phase with the external drive.

The enhancement of phase coherence through homodyne measurement is calculated as $\mathcal{F} = |S_{HD}|/|S_0|$, where S_{HD} is the average phase coherence over N_{traj} trajectories, defined by

$$S_{HD} = \frac{1}{N_{traj}} \Sigma_{k=1}^{N_{traj}} \frac{\mathrm{Tr}[a\rho_k]}{\sqrt{\mathrm{Tr}[a^\dagger a\rho_k]}}, \qquad (5.4)$$

and S_0 is the phase coherence obtained from unconditioned master equation without homodyne measurements. We will refer to $\mathcal{F}$ as the enhancement factor. In our simulations, we ensure the finite Hilbert space truncation by examining the fock-space distribution in the steady-states, and we fixed the number of trajectories at $N_{traj} = 300$. This allows us to efficiently simulate without utilizing too much computation resources,

and further increase the number of trajectories does not change the result qualitatively.

5.2 Synchronization in quantum regime

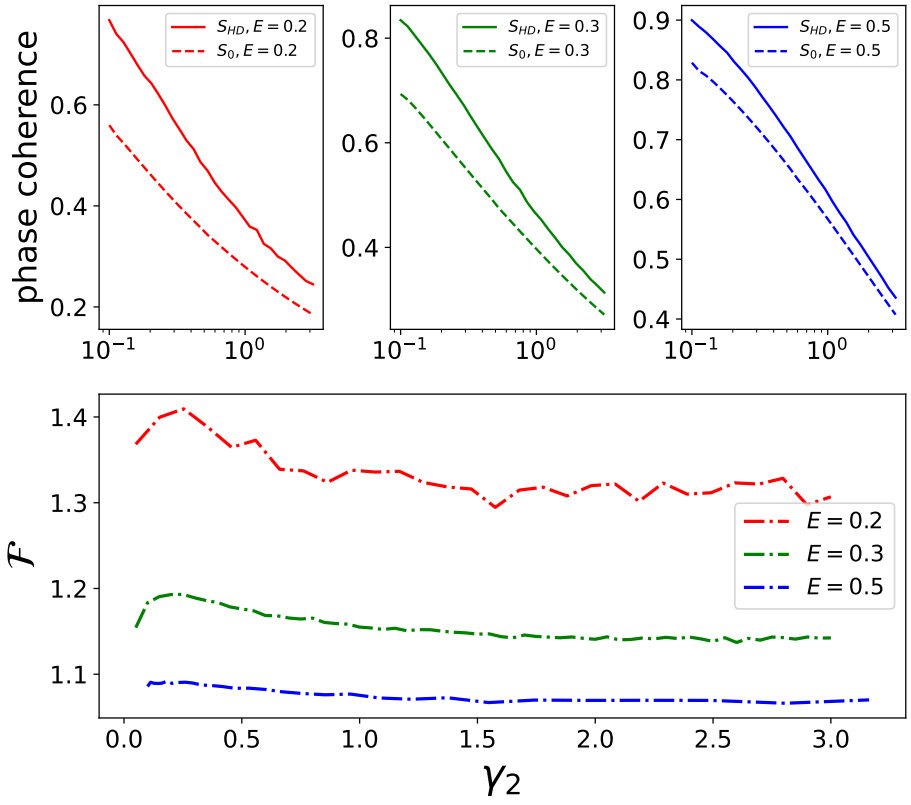

Figure 5.1: Phase coherence with/without homodyne detection (Top) and enhancement factor $\mathcal{F}$ (Bottom) plotted against nonlinear damping rate $\gamma_2 \in [0.5, 3]$, under different driving amplitude E. Fixed parameters: $\Delta = 0, \gamma_3 = 0.1, \theta = \pi/2$ (optimized for the highest enhancement factor). Take note that the fluctuations in the curves are consequences of a finite number of trajectories averaged in the simulations. The same applies for other plots below.

We first study the phase synchronization of a quantum Stuart–Landau oscillator with coherent drive but without squeezing Hamiltonian (by simply set $\eta = 0$). Quantum synchronization (i.e. phase locking) has been shown to improve when the system in semi-classical regime (the definition of different regimes will be provided later in the section) is continuously monitored by homodyne measurement [KN21a]. Here, we investigate the enhancing effect of homodyne measurement in a wider parameter regime and under different driving amplitude. In our simulations, we set zero initial detuning between the oscillator and drive, i.e. $\Delta = 0$. This might seem unusual in the context of classical synchronization, where two systems are definitely synchronized

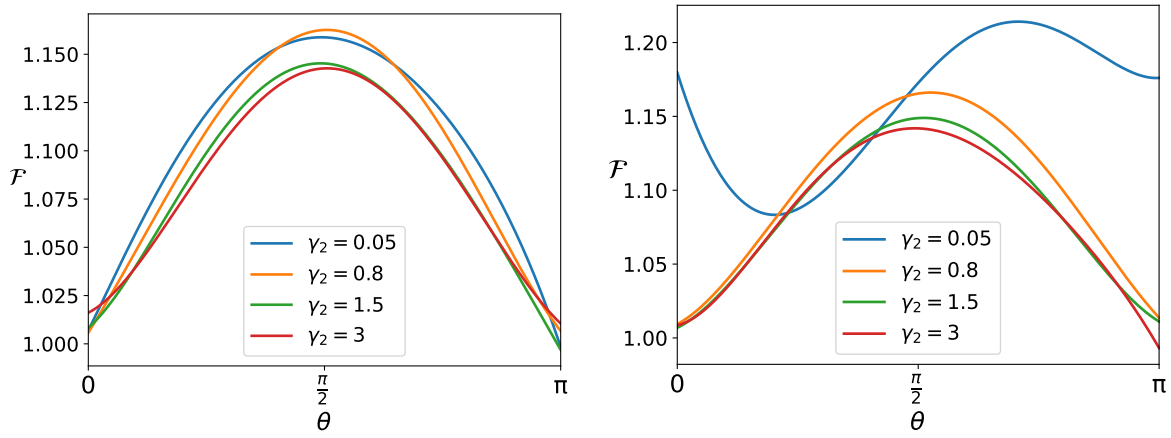

(a) $\Delta = 0$ **(b)** $\Delta = 0.05$

Figure 5.2: Enhancement factor at different measurement angle θ. (a) Zero detuning. (b) Non-vanishing detuning $\Delta = 0.05$. The curves are smoothed using polynomial interpolation.

without detuning. But here we are interested in the phase synchronization particularly, which is not guaranteed by zero initial detuning. This is due to the presence of quantum fluctuations which prevent the phase-space portrait of the steady-state from concentrating onto one fixed-point, and consequently cause diffusion around it. Another reason for choosing zero initial detuning is that, changing γ_2 also changes the optimal phase θ of the measurement when the detuning is non-zero. Whereas with zero detuning, $\theta = \pi/2$ is optimal for all values of γ_2. As shown in Fig. 5.2(a), with zero detuning, the optimal enhancement factors are obtained at $\theta = \pi/2$ and the corresponding measurement angle do not depend on γ_2. One can also see the optimal enhancement factors do not scale with γ_2 monotonically, i.e. the highest points of the curves rise and then drop, in the range of $\gamma_2 = 0.05$ to 3. In Fig. 5.2(b), with non-vanishing detuning, the optimal measurement angles shift away from $\pi/2$. Additionally, the highest enhancement factors are monotonically decreasing with respect to increasing γ_2.

In the limit of large mean photon number, the oscillator can be described statistically by a set of classical equations of motion [WNB14]. This limit is referred to as the semi-classical regime. On the other hand, in the regime with low mean photon number, where the classical model breaks down, the oscillator is considered in the quantum regime. In this regime, quantum noise comes into play and genuine quantum phenomena arise [MKH20, SMN+23]. Different synchronization regimes of quantum

Stuart–Landau oscillator can be characterized in terms of the nonlinear two-photon damping rate γ_2. By increasing this rate, the limit cycle of oscillator shrinks and its mean photon number decreases, signifying a transition from semi-classical regime ($\gamma_2 < 1$) to quantum regime ($\gamma_2 \gg 1$). In order to access different regimes, we assume the parameter γ_2 can be tuned freely. States in quantum regime will be more prone to diffusion through quantum fluctuations, causing them to lose phase synchronization with the driving force. This is shown in the top row panels of Fig. 5.1, where phase coherence drops with increasing γ_2, regardless of the driving amplitude.

In Fig. 5.1 we also show the enhancing effect of homodyne measurement on quantum synchronization, quantified by the enhancement factor $\mathcal{F}$. The presence of homodyne measurement always enhances the phase coherence even in the quantum regime, provided that the phase θ of the measurement is optimized. Larger enhancement is observed when driving amplitude E is small. Notice in Fig.1, for small γ_2, there is an optimal ratio for the enhancement factor to peak at, which only appears at zero initial detuning between the oscillator and driving force (see Appendix A for non-zero detuning cases). After that the enhancement factor drops with γ_2 until asymptotically reaching a ratio above unity. In addition, later in Section. 5.4, we will show that this optimal ratio is sensitive to the dissipative noise and squeezing. Additionally, we numerically simulated the error (standard deviation) in the data of Fig. 5.1, with 100 sample runs and number of trajectories $N_{traj} = 300$. According to quantum Monte-Carlo simulation method [CA86], the standard deviation is on the order of $N_{traj}^{-1/2}$.In Fig. 5.3, we show that the largest standard deviation is below 1% of the data in Fig. 5.1.

It has been shown that this enhancement F is a consequence of the increase in the purity of states, defined as $P = \mathrm{Tr}[\rho^2]$, as the effective phase space diffusion is inversely proportional to the purity of states. We note that, on average, homodyne measurement increases the purity. To this end, we look at the ratio of the purity of the steady state P_{HD} at $\eta_d = 1$, corresponding to homodyne measurement, to the purity P_0 at $\eta_d = 0$ where homodyne measurement is turned off, i.e. $\mathcal{F}_{purity} = |P_{HD}|/|P_0|$. Fig. 2 shows this ratio with γ_2. We see that this ratio is always greater than 1, indicating that homodyne measurement enhances the purity of states. However, with increasing γ_2, this ratio tends to unity, regardless of the amplitude E.

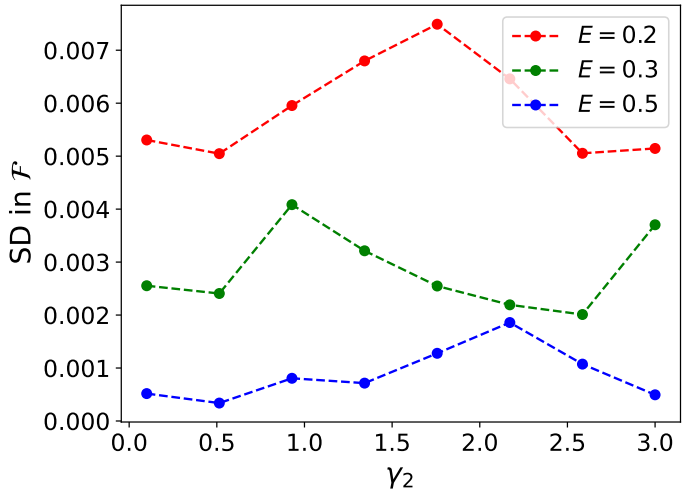

Figure 5.3: Standard deviation in the enhancement factor $\mathcal{F}$ of Fig. 5.1.

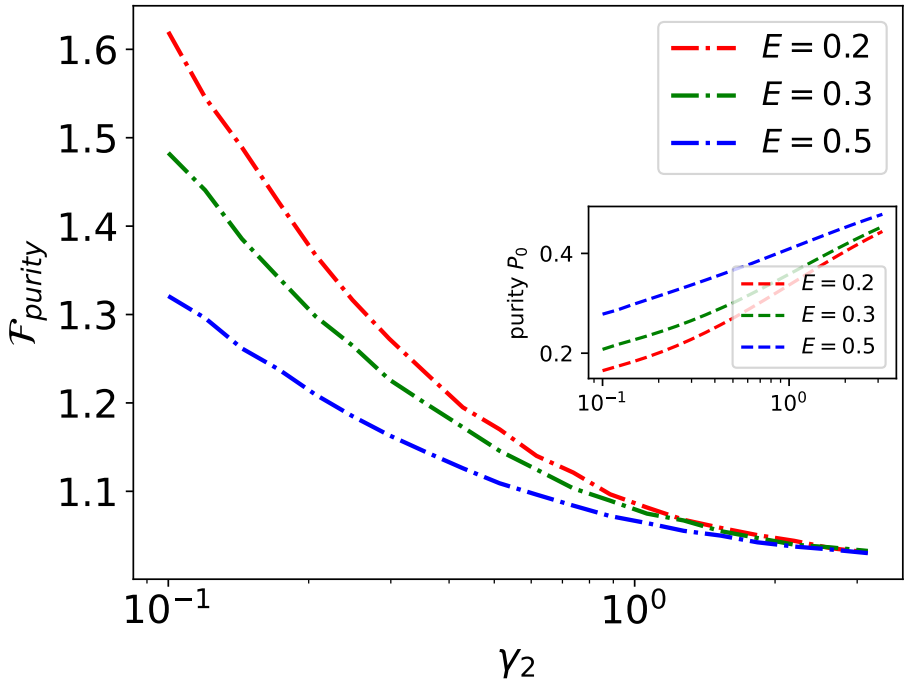

Figure 5.4: Enhancement in purity of steady-state due to homodyne measurement is always present, but decays with increasing γ_2. (inset) Purity scales approximately with $\gamma_2^{1/3}$. Fixed parameters:$\Delta = 0, \gamma_3 = 0.1, \theta = \pi/2$

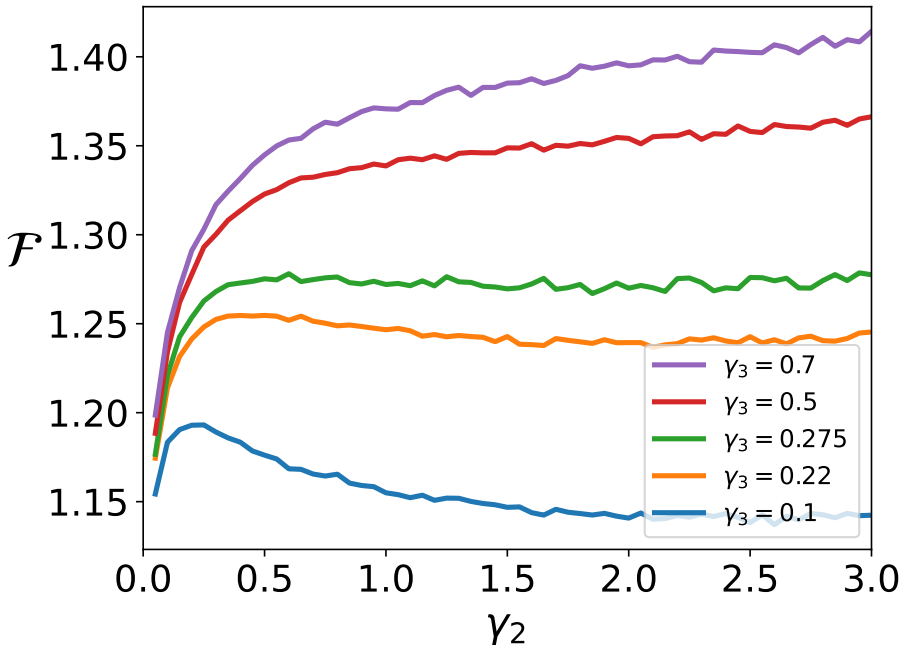

Figure 5.5: Effect of γ_2 on enhancement factor $\mathcal{F}$ at different single-photon dissipation γ_3, with fixed parameters $\Delta = 0, \theta = \pi/2$. When single-photon dissipation γ_3 is small, the enhancement factor $\mathcal{F}$ drops after reaching the maximum. However, the enhancement factor starts to rise even in the quantum regime when a large single-photon dissipation is present.

5.3 Noise-induced synchronization enhancement

It has been established that classically chaotic systems exhibit noise-induced synchronization in the presence of common Gaussian noise [ZK02, TMHGP01], and such synchronization can be enhanced, for instance, by additional dichotomic noise [RFNSG01]. In quantum domain, noise is also reported to boost quantum synchronization, such as inducing frequency entrainment in quantum Stuart–Landau oscillators [MKH20] and helping to develop correlation and entanglement between two ends of a quantum spin chain [SL22]. Here we show another example of such noise-induced phase synchronization of a driven quantum Stuart–Landau oscillator.

We show that more single photon damping can effectively raise the enhancement through homodyne measurement. In Eq. (5.1), γ_3 corresponds to the rate of single photon damping, acting as a dissipative noise for the oscillator. At the same time, it characterizes the coupling between the measurement device and the monitored system, since all dissipated photons will be captured by the detector ($\eta_d = 1$). The damping rate γ_3 also scales the back-action of homodyne detection (last term in Eq. (5.1)).

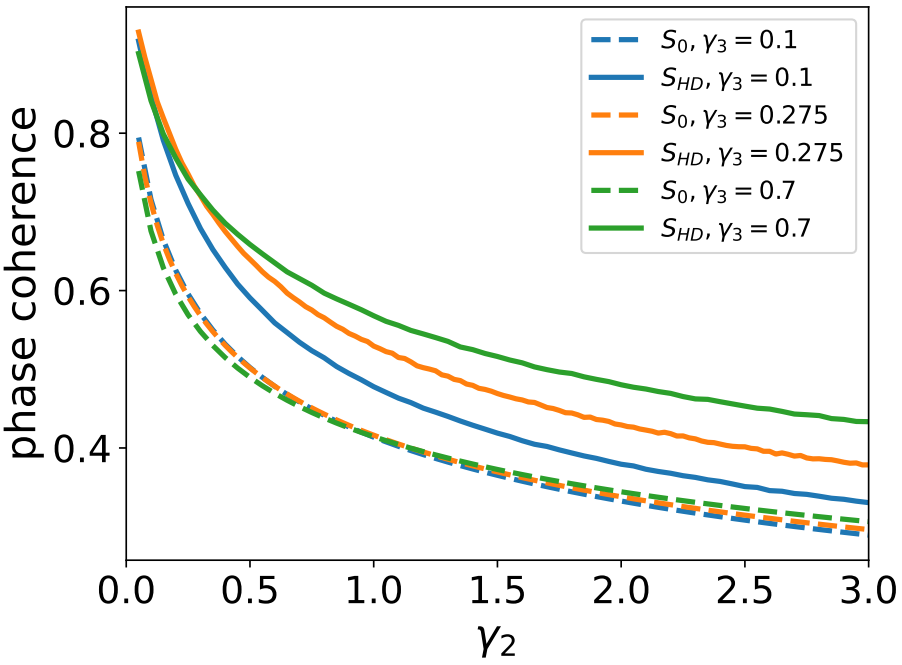

Figure 5.6: Phase coherence in general vanishes with increasing γ_2. However, in the quantum regime, the presence of single-photon dissipation γ_3 can boost phase coherence. Homodyne measurement greatly amplifies this boost in the quantum regime.

Therefore, it is not surprising that increasing γ_3 results in a more potent homodyne measurement and thereby improves the enhancement factor. This is shown in Fig. 5.5 where the enhancement factor is plotted against the non-linear damping rate γ_2 at different single photon damping γ_3. Dissipative noise increases the enhancement factor across all values of γ_2. Especially in the quantum regime where $\gamma_2 > 1$, the enhancement factor receives a greater boost compared to the semiclassical regime. As a consequence, the enhancement factor increases with non-linear damping rate γ_2, given a moderate single-photon damping ($\gamma_3 \approx 0.3$) is present. We refer to this as noise-induced synchronization enhancement through homodyne measurement. This is a significant result; compared to Fig. 5.1, we reverse the effect of increasing γ_2, from detrimental to enhancing. And this is achieved by simply adding linear damping.

It has also been reported that without any measurements, dissipative noise can produce an increase in the off-diagonal density matrix elements in deep quantum regime [MKH20], which contribute to a higher phase coherence. But such increase is marginal in amplitude as seen in our results in Fig. 5.6.

5.4 Squeezing further improves synchronization

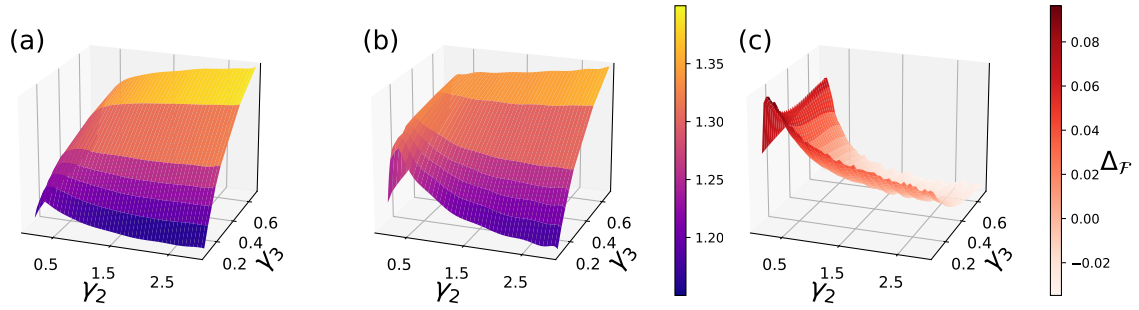

Figure 5.7: Contour plot of enhancement factor $\mathcal{F}$ against γ_2 and γ_3 with (a)$\eta = 0$ and (b)$\eta = 0.1$; (c) differences between enhancement factor $\mathcal{F}$ of (a) and (b).

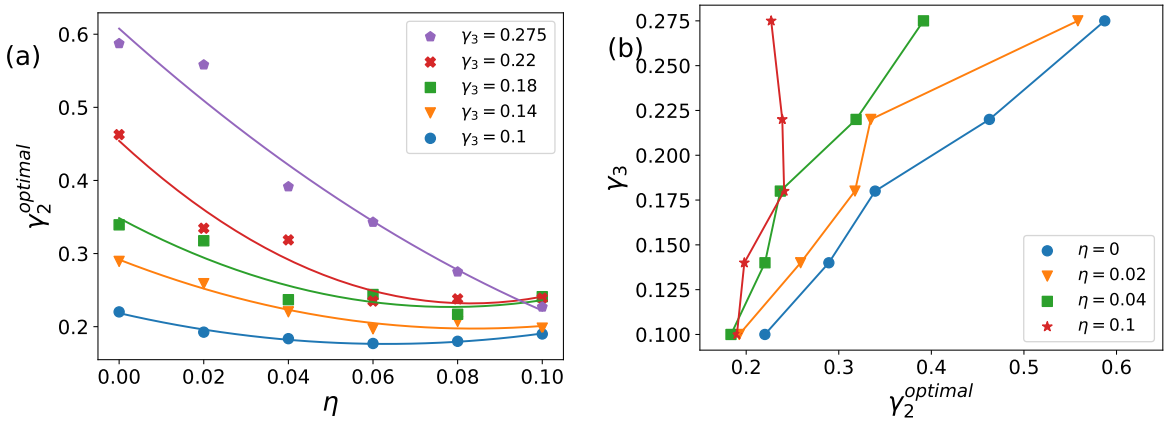

Figure 5.8: (a)The convergence of optimal γ_2 with increasing squeezing η. (b)Top-down view of the optimal γ_2 positions in the transition from Fig.5(a)-(b).

Another useful technique to boost quantum synchronization is squeezing [SHM+18]. However, the measure of phase coherence is no longer appropriate for capturing quantum phase synchronization when large squeezing is present. The calculation of phase coherence is valid when the density matrix has only first off-diagonal coherences [LNN+17]. Therefore, in order to study the effects of squeezing, we only applied a small amount of squeezing while ensuring the second and higher off-diagonal elements remain negligible. It is also known that under squeezing the Wigner function of such system will undergo a pitchfork bifurcation, i.e. the steady-state Wigner function has two peaks. In the presence of two peaks, the use of phase coherence as a measure is generally small due to some form of averaging. Such cases are beyond our scope for this study, therefore we limit the amplitude of squeezing below $\eta = 0.1$ in the $\phi = 0$ direction, so that the peak in the Wigner function is not split into two or more peaks.

Indeed, squeezing is shown to further improve quantum phase synchronization. In Fig. 5.7, we show that squeezing is more likely to boost synchronization in the semiclassical regime, while in the quantum regime, squeezing has negligible effects. The parameter region where squeezing offers the most observable benefits is when both (γ_2, γ_3) are small (bottom-left corner of the contour plots). Moving on to the large (γ_2, γ_3), the enhancing effect of squeezing vanishes, as illustrated in Fig. 5.7(c). Squeezing and nonlinear damping appear to be more closely related to each other, as they are two-photon processes. This is evident from the 3D plots in Fig. 5.7, where increasing squeezing parameter pushes the landscape along γ_2 rather than γ_3.

In addition to this additional enhancement caused by squeezing itself, adding squeezing also modifies the enhancement produced by homodyne measurement. Interestingly, the optimal values of γ_2 for the highest enhancement factor under various γ_3 converge to a narrow region around $\gamma_2 = 0.2$, with a small squeezing up to $\eta = 0.1$. This is shown in Fig. 5.8(a) where we numerically plot the optimal γ_2 as a function of the squeezing parameter η. Another interpretation of the effect is that additional squeezing makes the optimal point stronger against dissipative noise γ_3. As shown in Fig. 5.8(b), the optimal points γ_2 move closer to the left vertical axis when the pressure increases, and eventually become independent of γ_3 when $\eta = 0.1$. This effect is interesting as it provides some insights into possible stochastic resonance in the dynamics.

5.5 Conclusion

To conclude, our study has made the following observations in quantum synchronization: First, in the presence of homodyne measurement, enhancement in phase synchronization persists to the quantum regime. Next, optimal two-photon nonlinear damping rates (γ_2) exist in which the enhancement factors are maximum, with small single-photon damping rates (γ_3) when the oscillator is driven at resonance $(\Delta = 0)$. This phenomenon is unusual as it only appears with zero initial detuning. On the other hand, moderate single-photon damping rates (γ_3) allow higher enhancement factors to be achieved even in the quantum regime, despite acting as a source of dissipative noise. Additionally, adding a small amount of squeezing can further enhance quantum phase synchronization, especially in the semi-classical regime. More strikingly, with additional squeezing, the optimal nonlinear damping rates (γ_2) become insensitive to dissipative noise (γ_3).

In this study, we show several practical techniques that can be employed to enhance quantum synchronization and are readily achievable in experiments. Homodyne mea-

surement is a fundamental technique developed in quantum optics. Yet, it plays a pivotal role in quantum information and technology. Several continuous variable quantum key distribution protocols respond to homodyne detection to extract quadrature information encoded in the signal [GG02, GVAW+03], which have been demonstrated experimentally [JKJL+13, ZHC+19]. It has also been proposed to improve the sensitivity of quantum sensors [CLL+23]. The open quantum system monitored by homodyne measurement can be modeled by a master equation conditioned on the measurement record [WM93], also known as quantum trajectory theory [WM09, Car09]. It has also been shown that additional squeezing can produce stronger frequency entrainment than harmonic drive [SHM+18]. Recently, the well-studied field of classical noise-induced synchronization [ZK02, HSS03, RFNSG01, TMHGP01] has also been extended to quantum regime [SL22].

The Stuart-Landau model used in this work is implementable using the state-of-the-art superconducting circuits, where the two-photon dissipation and squeezing can be engineered using parametric conversion process in Josephson junctions [DDI06, LTP+15]. I will further discuss the implementation of such oscillator model in Chapter 8. As a future direction, it would be interesting to explore the effects of homodyne measurement and squeezing on a true van der Pol oscillator [CKN20], where a modified quantum Stuart–Landau oscillator provides a phase space plot that closely resembles the classical diamond-like phase space plot of a van der Pol oscillator.

Chapter 6

Mixing oscillations: Two Oscillators of the Same or Different Kinds.

Nonlinear oscillators play a fundamental role in various areas of physics, ranging from classical mechanics to quantum systems. These systems exhibit rich dynamics, often leading to complex and fascinating behaviors. In recent years, significant attention has been devoted to the understanding of the behavior of nonlinear oscillators that are mutually coupled, especially in the quantum domain. The study of such coupled systems has provided profound insights into the emergence of synchronization, collective phenomena like amplitude death and chaos, as well as the interplay between classical and quantum dynamics.

While the study of coupled oscillators has a long history in classical physics, the exploration into such self-sustained mutually coupled oscillators in the quantum settings remains relatively unexplored. The dynamics of nonlinear oscillators are greatly influenced by their mutual interactions, leading to a wide range of intriguing phenomena that have yet to be fully understood. The reader may refer to papers on coupled vdP and Duffing oscillators in [WCF96, VK08, KST09, RKT+22, CFWD01, KCK+12].

In classical systems, the study of coupled nonlinear oscillators has revealed a plethora of fascinating phenomena, such as synchronization, amplitude death, and chaos. However, the extension of these investigations to the quantum regime introduces entirely new challenges and possibilities. The quantum nature of the oscillators introduces novel features, including quantum entanglement. Understanding the dynamics and properties of these coupled oscillators in the quantum realm presents an exciting frontier for research, with potential applications in quantum information processing, quantum sensing, and quantum communication. Exploring the behavior of coupled quantum nonlinear oscillators provides valuable insights into the interplay between classical and quantum dynamics, shedding light on the boundaries between these two domains.

6.1 Oscillator models

In this chapter, some of these quantized nonlinear oscillator models, namely the quantum Stuart-Landau, Rayleigh, van der Pol and Ditzinger oscillators, are considered. The models are described in the form of Lindblad master equations with $\hbar = 1$.

For the quantum Stuart-Landau model [WNB14]:

$$\dot{\rho} = -i[H, \rho] + \gamma_1 \mathcal{D}[a^\dagger]\rho + \gamma_2 \mathcal{D}[a^2]\rho, \tag{6.1}$$

where $H = \omega a^\dagger a$ and the coefficients γ_1 and γ_2 describe negative and nonlinear damping of the oscillator.

The quantum Rayleigh and van der Pol model share the same formalism in terms of master equation and Hamiltonian [CKN20]:

$$\begin{aligned} \dot{\rho} &= -i[H, \rho] + \mu(q_0^2 - 1)\mathcal{D}[a^\dagger]\rho, \\ &\quad + \frac{3\mu}{4}\mathcal{D}[a^2]\rho + \mu\mathcal{D}[a^\dagger a - \frac{1}{2}a^{\dagger 2}]\rho \qquad (6.2) \\ H &= \omega a^\dagger a + i\zeta(a^\dagger a^3 - a^{\dagger 3}a) + i\beta(a^4 - a^{\dagger 4}) \\ &\quad - i\eta(a^2 - a^{\dagger 2}). \qquad (6.3) \end{aligned}$$

But the difference between these models lies with the nonlinear coefficients (6.3).

In the Rayleigh model,

$$\zeta = \frac{\mu}{12},\ \beta = \frac{\mu}{24},\ \eta = \frac{\mu(q_0^2 - 1)}{4}. \tag{6.4}$$

whereas in the Van der Pol model,

$$\zeta = -\frac{\mu}{4},\ \beta = -\frac{\mu}{8},\ \eta = -\frac{\mu(q_0^2 - 1)}{4}. \tag{6.5}$$

There is also another nonlinear oscillator called the quantum Ditzinger model. The Ditzinger model describes a self-sustained oscillator with a circular limit cycle, which unlike the Stuart-Landau oscillator, has a non-uniform phase flow around the limit

cycle. In polar coordinates (r, ϕ). The classical equations of motion are given by

$$\begin{aligned} \dot{r} &= r(r_0^2 - r^2) \\ \dot{\phi} &= b - r\cos\phi \end{aligned} \tag{6.6}$$

where r_0 is the radius of the limit cycle and b is the position of the vertical nullcline (in the usual Cartesian coordinates). The system exhibits a (non-uniform) limit cycle for $b > r_0$ and a stable fixed point for $b < r_0$. The Ditzinger model reduces to the Stuart-Landau oscillator in the limit $b \to \infty$.

Following a similar quantization procedure as in Ref. [CKN20] for the van der Pol and Rayleigh oscillators, we denote the complex amplitude $\alpha \equiv r\exp(i\phi)$ and write down the corresponding quantum equation of motion for $\alpha \to \langle a \rangle$ (normal ordering is assumed):

$$\frac{d}{dt}\langle a\rangle = r_0^2\langle a\rangle - \langle a^\dagger a^2\rangle - \frac{i}{2}\langle a^2\rangle - \frac{i}{2}\langle a^\dagger a\rangle + ib\langle a\rangle \tag{6.7}$$

The next step is to seek a master equation which produces the above quantum equation of motion. It is easy to check that the following master equation is a valid choice:

$$\begin{aligned} \dot{\rho} &= -i[H,\rho] + \sum_{k=1,2}(2r_0^{(k)2}+1)\mathcal{D}[a_k^\dagger]\rho + \mathcal{D}[a_k^2]\rho \\ &\quad + \frac{1}{2}\mathcal{D}[ia_k + a_k^\dagger a_k]\rho \end{aligned} \tag{6.8}$$

$$H = \sum_{k=1,2}\frac{1}{4}(a_k^\dagger a_k^2 + a_k^{\dagger 2}a_k) - b_k a_k^\dagger a_k, \tag{6.9}$$

6.2 Pearson correlation of coupled homogeneous oscillators

The system of dissipatively coupled quantum Rayleigh / van der Pol oscillators is governed by the master equation [CKN20]:

$$\begin{aligned} \dot{\rho} &= -i[H,\rho] + \sum_{k=1,2}\mu_k(q_0^{(k)2}-1)\mathcal{D}[a_k^\dagger]\rho \\ &\quad + \frac{3\mu_k}{4}\mathcal{D}[a_k^2]\rho + \mu_k\mathcal{D}[a_k^\dagger a_k - \frac{1}{2}a_k^{\dagger 2}]\rho + V\mathcal{D}[a_1 - a_2]\rho, \end{aligned} \tag{6.10}$$

$$\begin{aligned} H &= \sum_{k=1,2}\omega_k a_k^\dagger a_k + i\zeta_k(a_k^\dagger a_k^3 - a_k^{\dagger 3}a_k) + i\beta_k(a_k^4 - a_k^{\dagger 4}) \\ &\quad - i\eta_k(a_k^2 - a_k^{\dagger 2}), \end{aligned} \tag{6.11}$$

where the coefficients ζ_k, β_k, η_k are defined in (6.4)&(6.5).

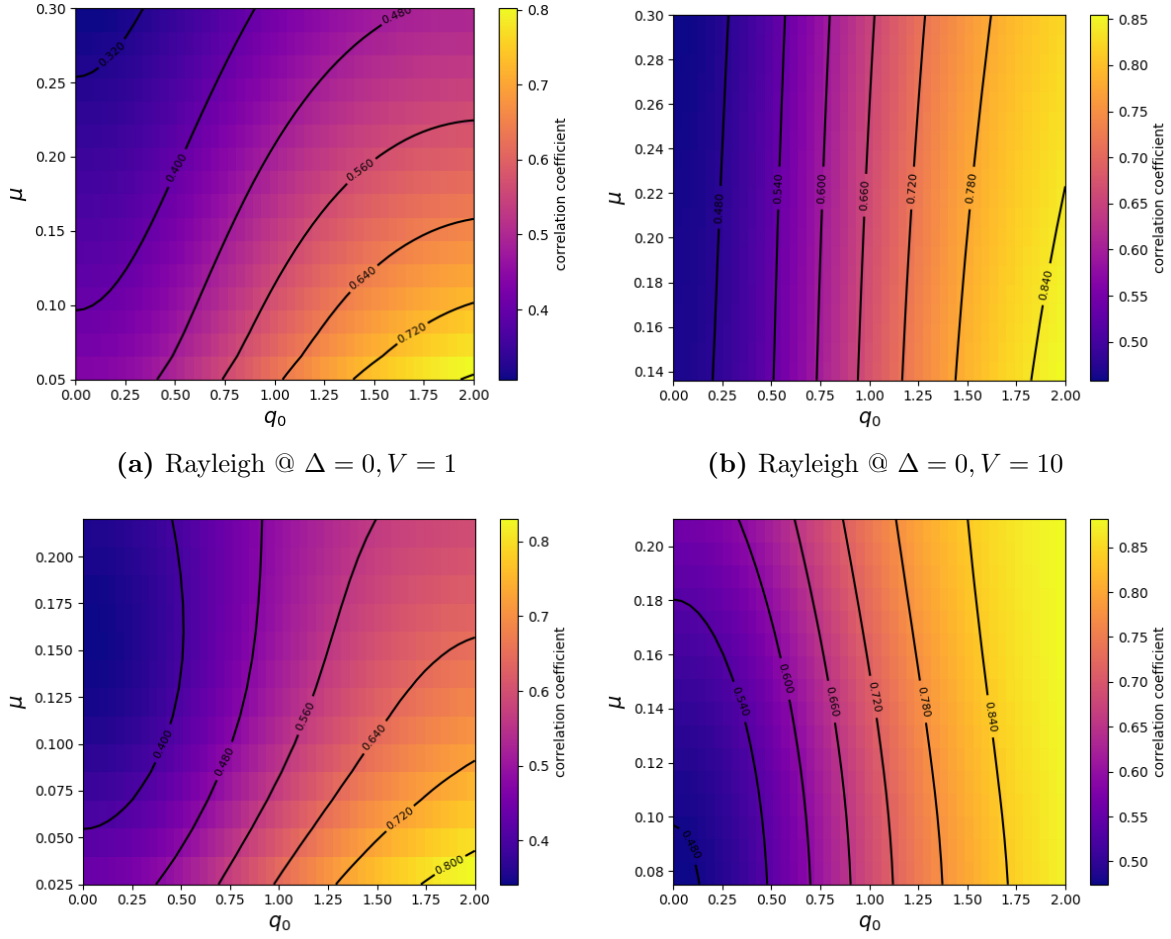

(a) Rayleigh @ $\Delta = 0, V = 1$

(b) Rayleigh @ $\Delta = 0, V = 10$

(c) vdP @ $\Delta = 0, V = 1$

(d) vdP @ $\Delta = 0, V = 10$

Figure 6.1: Pearson correlation coefficient of mutually coupled homogeneous oscillators, i.e. two Rayleigh or two van der Pol oscillators, plotted with increasing nonlinearity μ and limi cycle radius q_0.

To quantify the degree of synchronization between two oscillators, Pearson correlation emerges as a viable candidate. The Pearson correlation coefficient is primarily used to measure the linear relationship between two variables. While the Pearson correlation coefficient may exhibit some correlation when oscillators are synchronized, it does not provide a comprehensive measure of synchronization capturing the dynamics and temporal relationships essential for synchronization. Other measures such as mutual information and entanglement entropy can be exploited in the future works.

In Fig. 6.1, the Pearson correlations between two homogeneous oscillators. Two interesting phenomena can be observed: 1) for both types of nonlinear oscillators, increasing coupling strength reduces the effects of nonlinearity; 2) while the nonlinearities in

the Rayleigh model always weaken the correlation, the vdP model can actually take advantage of nonlinearity to enhance correlation, but only when coupling strength is high.

6.3 Joint-probability distributions of coupled heterogeneous oscillators

In this section, we investigate the steady-state properties of the coupled oscillator system, by calculating the Wigner functions $W(x_i, p_i)$ of each oscillator in steady state, and the joint-probability distribution $P(x_1, x_2)$ for the position basis of the oscillators. The joint-probability distribution $P(x_1, x_2)$ is defined by

$$P(x_1, x_2) = \langle x_1, x_2 | \rho | x_1, x_2 \rangle. \tag{6.12}$$

6.3.1 Admixture of Quantum Rayleigh and Stuart-Landau oscillators

We first consider a system of two coupled quantum Rayleigh oscillators, with one of the oscillators in 'Stuart Landau limit', by setting $\mu_1 = 0.1$, $\mu_2 = 0.01$ in the master equation given by (6.2).

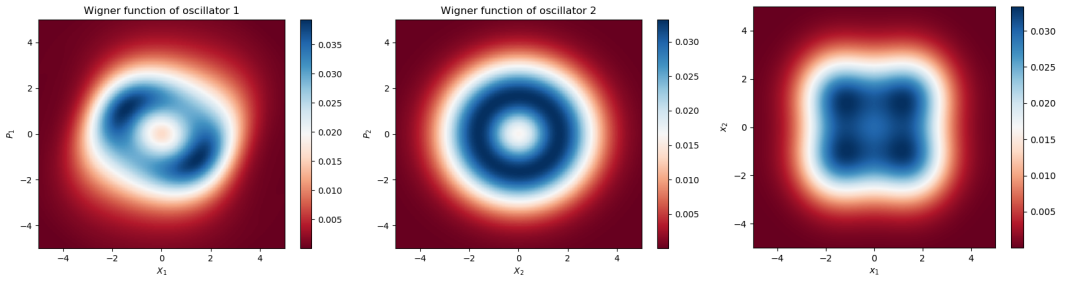

(a) $V = 0$

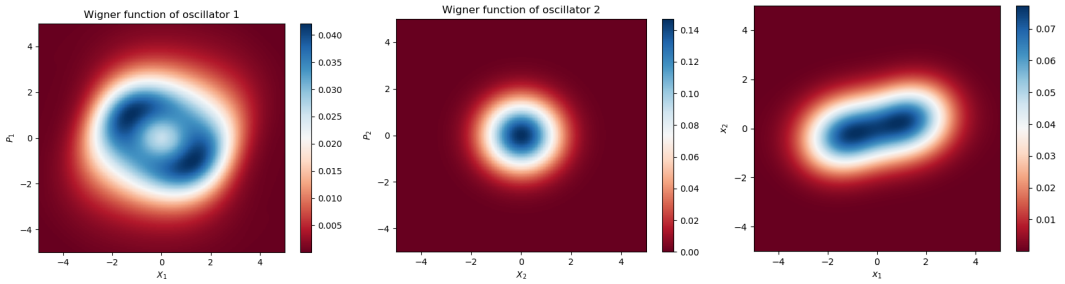

(b) $V = 0.1$

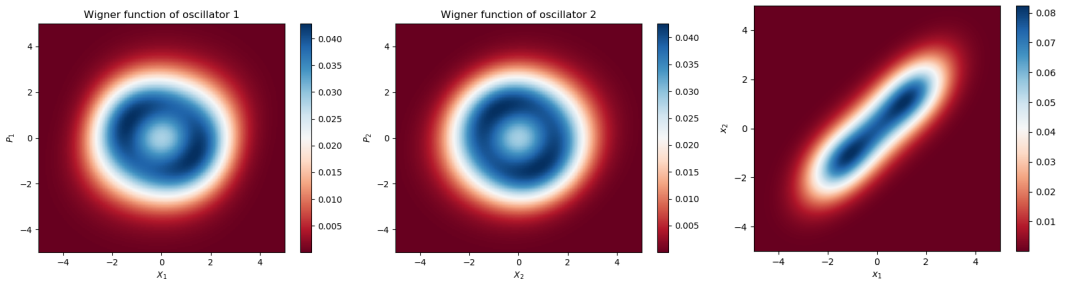

(c) $V = 10$

Figure 6.2: A Rayleigh oscillator ($\mu_1 = 0.1, q_0^{(1)} = 1.5$) and a Rayleigh oscillator in Stuart-Landau limit($\mu_1 = 0.01, q_0^{(2)} = 1.5$) coupled by dissipative interaction. (left column) Wigner function of first oscillator, (middle column) Wigner function of second oscillator, (right column) joint-probability distribution $P(x_1, x_2)$. Different rows corresponding to coupling strengths $V = 0, 0.1, 10$.

6.3.2 Admixture of Quantum vdP and Stuart-Landau oscillators

Likewise a quantum vdP oscillator is coupled to its "Stuart Landau limit" counterpart, with $\mu_1 = 0.1$, $\mu_2 = 0.01$ in the master equation given by (6.2).

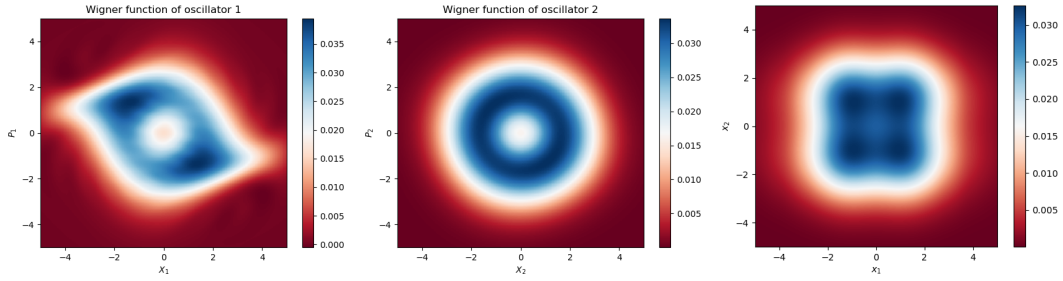

(a) $V = 0$

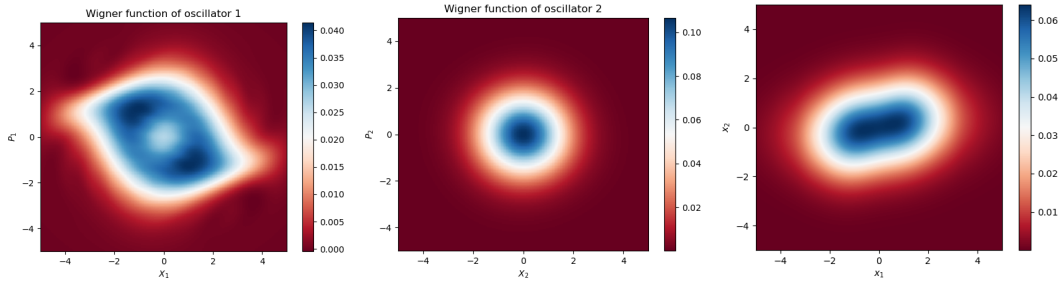

(b) $V = 0.1$

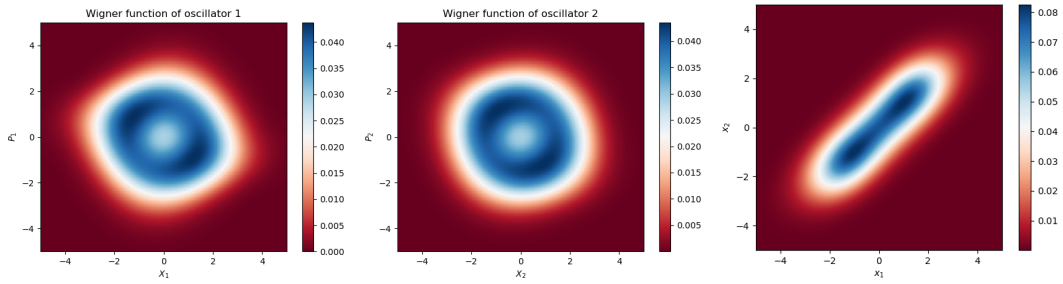

(c) $V = 10$

Figure 6.3: A vdP oscillator ($\mu_1 = 0.1, q_0^{(1)} = 1.5$) and a vdP oscillator in Stuart-Landau limit($\mu_1 = 0.01, q_0^{(1)} = 1.5$) coupled by dissipative interaction. (left column) Wigner function of first oscillator, (middle column) Wigner function of second oscillator, (right column) joint-probability distribution $P(x_1, x_2)$. Different rows corresponding to coupling strengths $V = 0, 0.1, 10$.

6.3.3 Admixture of Quantum Rayleigh and vdP oscillators

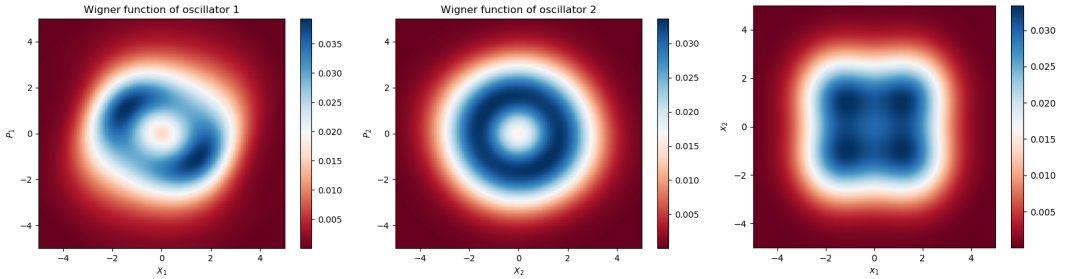

(a) $V = 0$

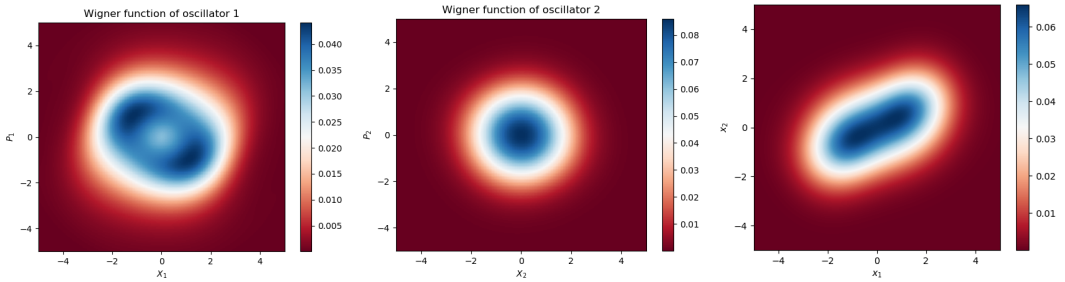

(b) $V = 0.1$

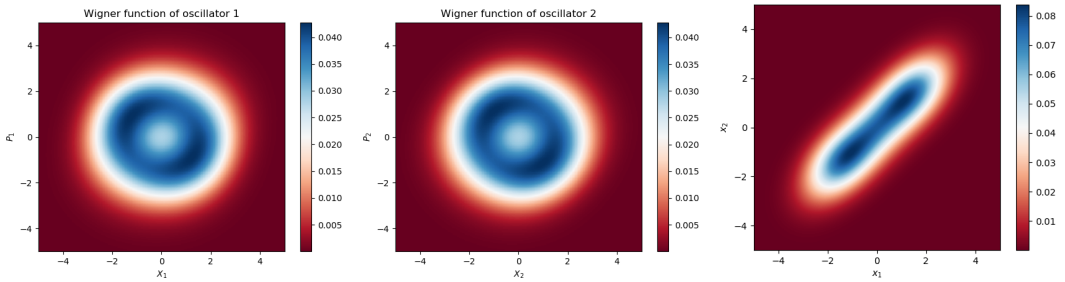

(c) $V = 10$

Figure 6.4: Inter-species coupling between a quantum Rayleigh oscillator ($\mu = 0.1, q_0 = 1.5$) and a quantum vdP oscillator ($\mu = 0.01, q_0 = 1.5$). Different rows corresponding to coupling strengths $V = 0, 0.1, 10$.

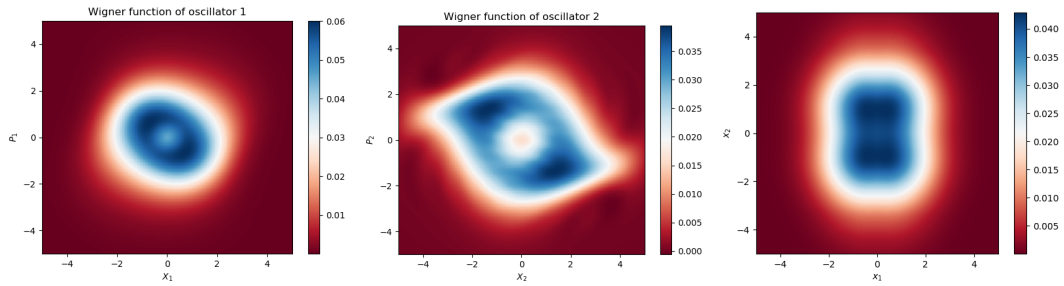

(a) $V = 0$

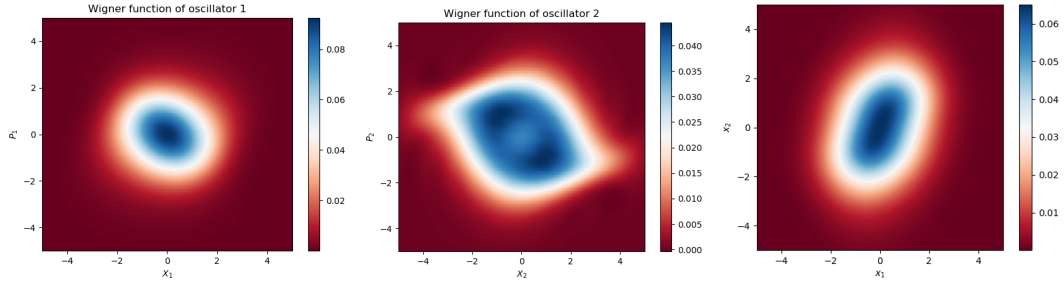

(b) $V = 0.1$

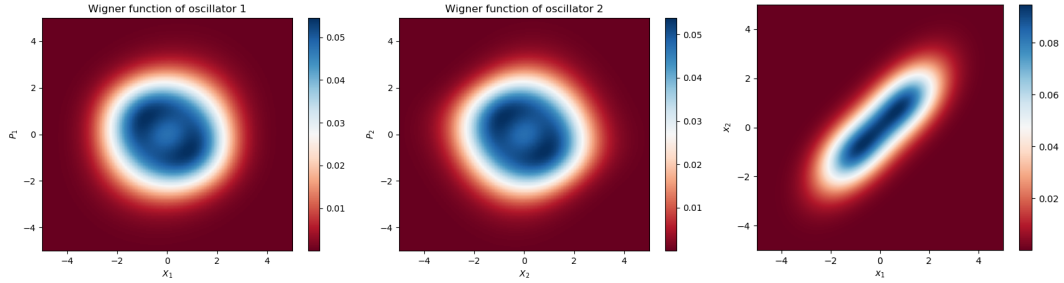

(c) $V = 10$

Figure 6.5: Inter-species coupling between a quantum Rayleigh oscillator ($\mu = 0.1, q_0 = 1.1$) and a quantum vdP oscillator ($\mu = 0.1, q_0 = 1.5$). Different rows corresponding to coupling strengths $V = 0, 0.1, 10$.

6.3.4 Admixture of Quantum Stuart-Landau and Ditzinger oscillators

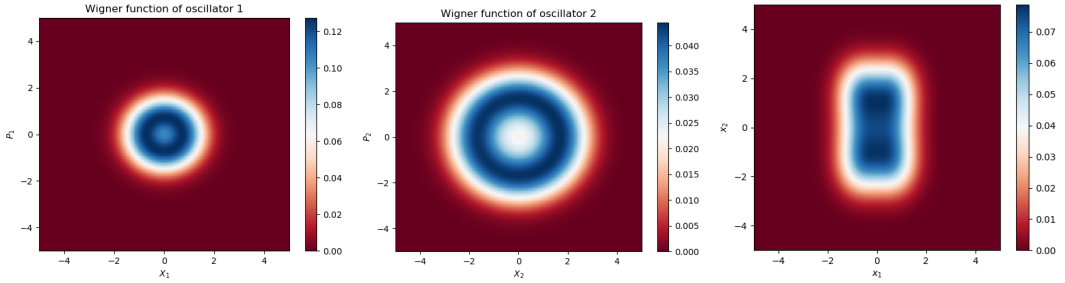

(a) $V = 0$

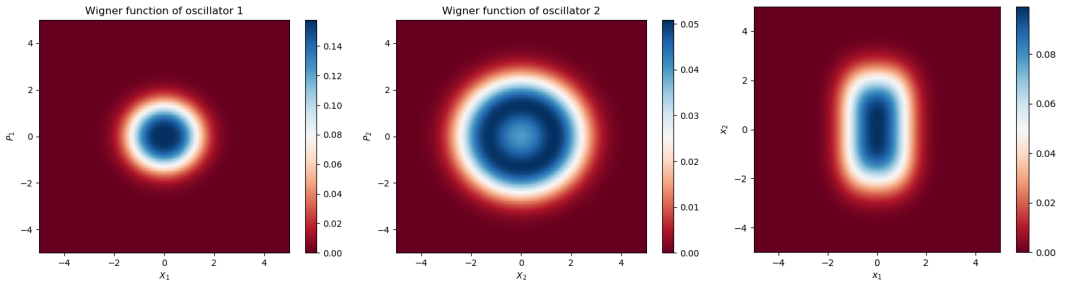

(b) $V = 1$

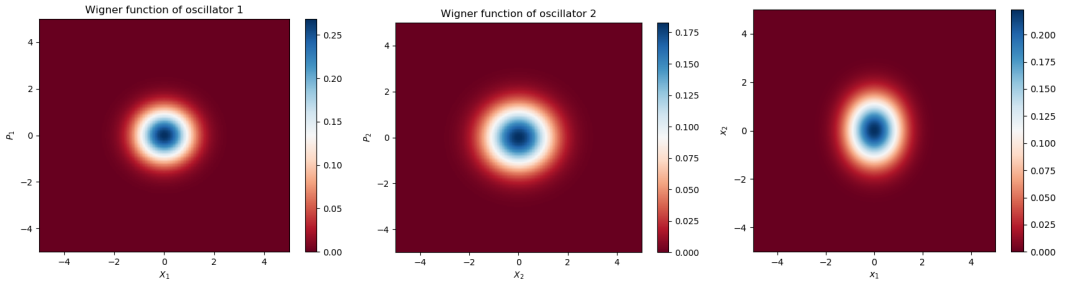

(c) $V = 10$

Figure 6.6: Inter-species coupling between a quantum Stuart-Landau ($\gamma_2/\gamma_1 = 100$) and quantum Ditzinger oscillator with a limit cycle($b = 200, r_0 = 1$), with increasing coupling strengths $V = 0, 1, 10$ respectively.

From all the cases above, we can conclude that, in the two coupled heterogeneous nonlinear oscillators, the 'dominant' oscillator would generally cause one of the oscillator to 'halt', and after that correlations would start to build up. The 'dominant' oscillator is the one with either larger nonlinearity μ or is more 'macroscopic' (larger oscillation amplitude q_0).

6.4 Amplitude death

Coupling two or more self-oscillating systems may stabilize their zero-amplitude rest state. This phenomenon is termed "amplitude death".

In this section, we study the amplitude death of coupled oscillator system by calculating the limit cycle radius of the oscillators, given by the highest point in the Wigner function. The occurrence of amplitude death is indicated by the limit cycle radius collapsing to 0, and the Wigner function becoming a blob centered at 0.

6.4.1 Two SL oscillators

For simplicity, let us consider the case of $\gamma_1^k = \gamma_2$, $\gamma_2^k = \gamma_2$. In the deep quantum limit where $\gamma_2/\gamma_1 \to \infty$, the states of both SL oscillators are confined within the subspace spanned by $|0\rangle$ and $|1\rangle$ [LCW14, MKH20]. Tracing out one of the SL oscillators, the density matrix of each SL is effectively given by $\rho_1 = \mathrm{diag}(p_0, p_1)$ with (setting $\gamma_1 = 1$)

$$\begin{aligned} p_0 &= \frac{1}{d}[7V^3 + (V+2)(V+3)\Delta^2 + 42V^2 + 81V + 54] \\ p_1 &= \frac{1}{d}[V^3 + 9V^2 + (V+3)\Delta^2 + 27V + 27] \\ d &= 8V^3 + (V+3)^2\Delta^2 + 51V^2 + 108V + 81 \end{aligned} \tag{6.13}$$

Since the density matrix is diagonal, the corresponding Wigner function must be rotationally symmetric. In polar coordinates, the Wigner function for the Fock state $|n\rangle$ is given by $W_n(r) = \frac{2}{\pi}(-1)^n L_n(4r^2)\exp(-2r^2)$, where $L_n(r)$ are the Laguerre polynomials. We define the onset of amplitude death to be the case where the radial Wigner function $W(r)$ transitions from being unimodally peaked at the origin $r = 0$ to being peaked at some $r > 0$. This is analogous to the notion of stochastic P-bifurcation. It is easy to show that amplitude death occurs when

$$4V^3 + (V-1)(V+3)\Delta^2 + 15V^2 - 27 > 0 \tag{6.14}$$

which gives us the Hopf bifurcation curve

$$\Delta = \sqrt{\frac{27 - 15V^2 - 4V^3}{(V-1)(V+3)}} \tag{6.15}$$

Interestingly, this result tells us that in the deep quantum limit, $V > 1$ is a necessary condition for amplitude death, which is also true for the classical case. What is

different however, is that the quantum SL allows for amplitude death even for zero detuning $\Delta = 0$, something that is impossible in the classical case.

We can also interpret the results from a quantum perspective. Assuming the entanglement between the two SL oscillators is weak, we can approximately factorize the density matrix for the two SLs $\rho \approx \rho_1 \otimes \rho_2$. Tracing out one of the oscillators as usual, the effective master equation for a single SL reads

$$\dot{\rho_1} = -i[H_{\text{eff}}, \rho_1] + V\mathcal{D}[a_1]\rho_1 \tag{6.16}$$

with the effective Hamiltonian $H_{\text{eff}} = \Delta a_1^\dagger a_1 + \frac{iV}{2}(\langle a_2 \rangle a_1^\dagger - \langle a_2^\dagger \rangle a_1)$ [MKH20]. Noting that $\langle a_2 \rangle \approx 0$ from the rotational symmetry of the uncoupled SL, we can thus interpret the effect of mutual coupling as an effective single-photon loss on the SL. When this effective single-photon loss rate exceeds a critical value, the population of the SL decreases below threshold which causes a qualitative change of the Wigner function. More quantitatively, in the deep quantum limit, we find that the effective single-photon loss rate κ_{eff} is given by

$$\kappa_{\text{eff}} = \frac{V(5V + 9 + \Delta^2)}{(V+3)^2 + \Delta^2} \tag{6.17}$$

This reduces to $\kappa_{\text{eff}} \approx V$ for small V or very large Δ, both of which are consistent with the aforementioned assumption of negligible entanglement.

In the deep quantum limit, the entanglement can be quantified by calculating the negativity analytically. The maximum negativity is attained in the limit of $\Delta \to 0$ and $V \to \infty$ which gives

$$N_{\text{max}} = \frac{\sqrt{10} - 3}{8} \approx 0.0203 \tag{6.18}$$

which justifies our assumption of weak entanglement. The boundary between entangled and separable oscillators in the $\Delta - V$ space is also distinct from that of the amplitude death boundary, which seems to suggest that there is no close connection between amplitude death and entanglement.

The joint probability distribution between two dissipatively coupled SL in the deep quantum limit can also be worked out (assuming resonant oscillators) to give

$$\lim_{V \to \infty} P(x_1, x_2) = \frac{1}{4\pi} e^{-(x_1^2 + x_2^2)}[3 + (x_1 + x_2)^2] \tag{6.19}$$

which gives a Pearson correlation coefficient of $r = 0.2$.

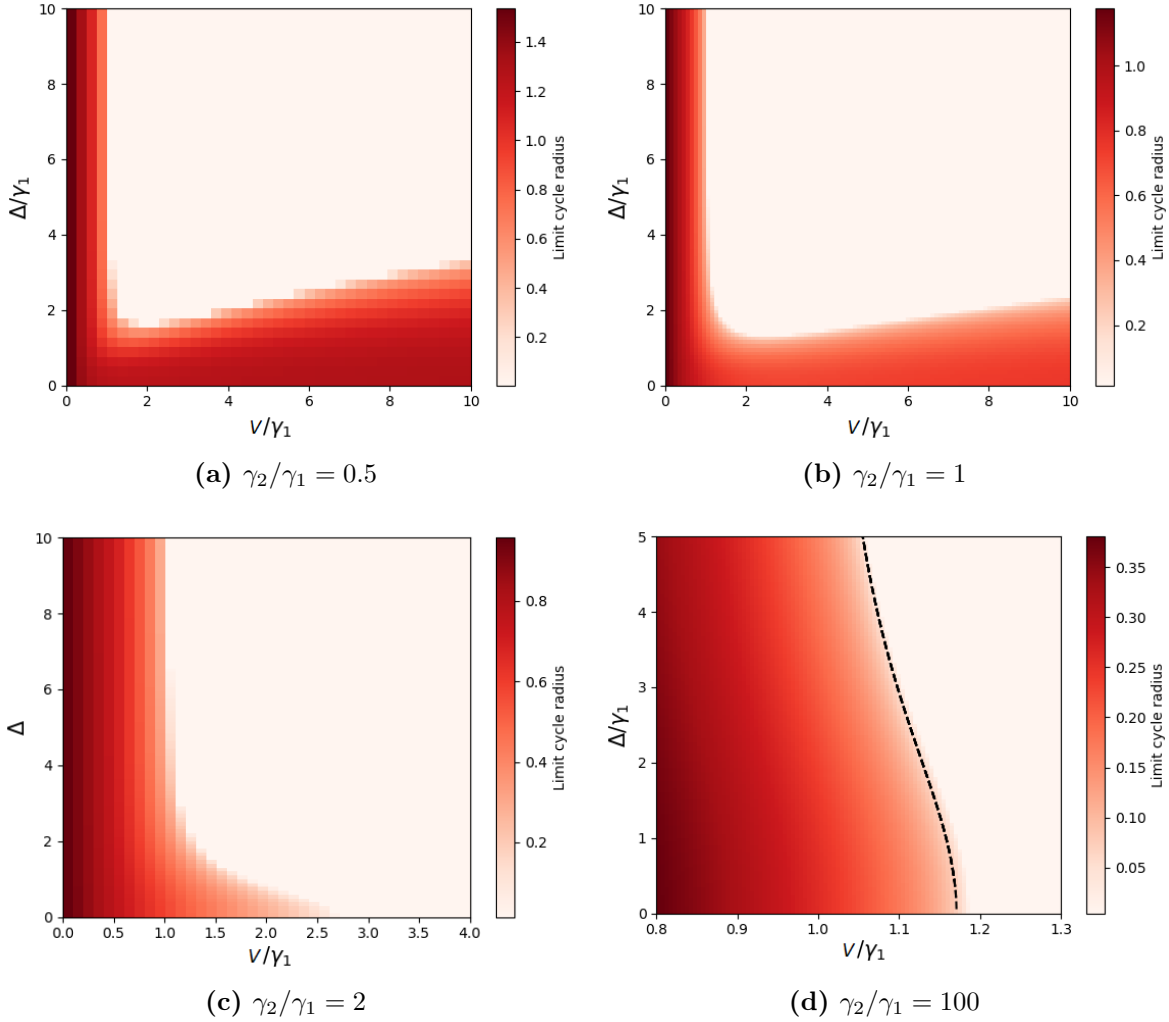

(a) $\gamma_2/\gamma_1 = 0.5$ **(b)** $\gamma_2/\gamma_1 = 1$

(c) $\gamma_2/\gamma_1 = 2$ **(d)** $\gamma_2/\gamma_1 = 100$

Figure 6.7: Limit cycle radius of two dissipatively coupled Stuart Landau oscillators. (d) dashed line: $\Delta = \sqrt{\frac{27-15V^2-4V^3}{(V-1)(V+3)}}$

6.4.2 Reactive coupling

Apart from the dissipative coupling between two oscillators, we also consider the reactive coupling. In the quantum case, this is realized by adding to the Hamiltonian a hopping interaction $g(a_1^\dagger a_2 + a_2^\dagger a_1)$ between the two SLs. Truncating the Hilbert space dimension of each oscillator to three dimensions (which is valid for large γ_2/γ_1, the steady-state density matrix can be solved exactly. Imposing the condition that $\partial^2 W(r=0)/\partial r^2 < 0$ for amplitude death, we can find the critical coupling g_c where amplitude death occurs. The exact expression is too complicated and not shown here,

but we can expand it in powers of $1/\gamma_2$ (setting $\gamma_1 = 1$ as usual) which gives:

$$g_c = \frac{\sqrt{3}}{2}\gamma_2^{1/2} - \frac{5}{4\sqrt{3}}\gamma_2^{-1/2} + \frac{9\Delta^2 - 271}{12\sqrt{3}}\gamma_2^{-3/2} + \mathcal{O}(\gamma_2^{-5/2}) \tag{6.20}$$

We can make some interesting remarks about this result: (i) In contrast with dissipative coupling, the AD for reactive coupling does not exist in the deep quantum limit where $\gamma_2/\gamma_1 \to \infty$, since $g_c \to \infty$ in this limit. (ii) For sufficiently small detuning Δ, the critical coupling g_c is almost independent of Δ, since it only appears in the second correction term to $g_c \approx \sqrt{3\gamma_2}/2$. (iii) Classically, it is known that reactive coupling of the SLs alone cannot lead to AD, hence this is a genuine quantum effect.

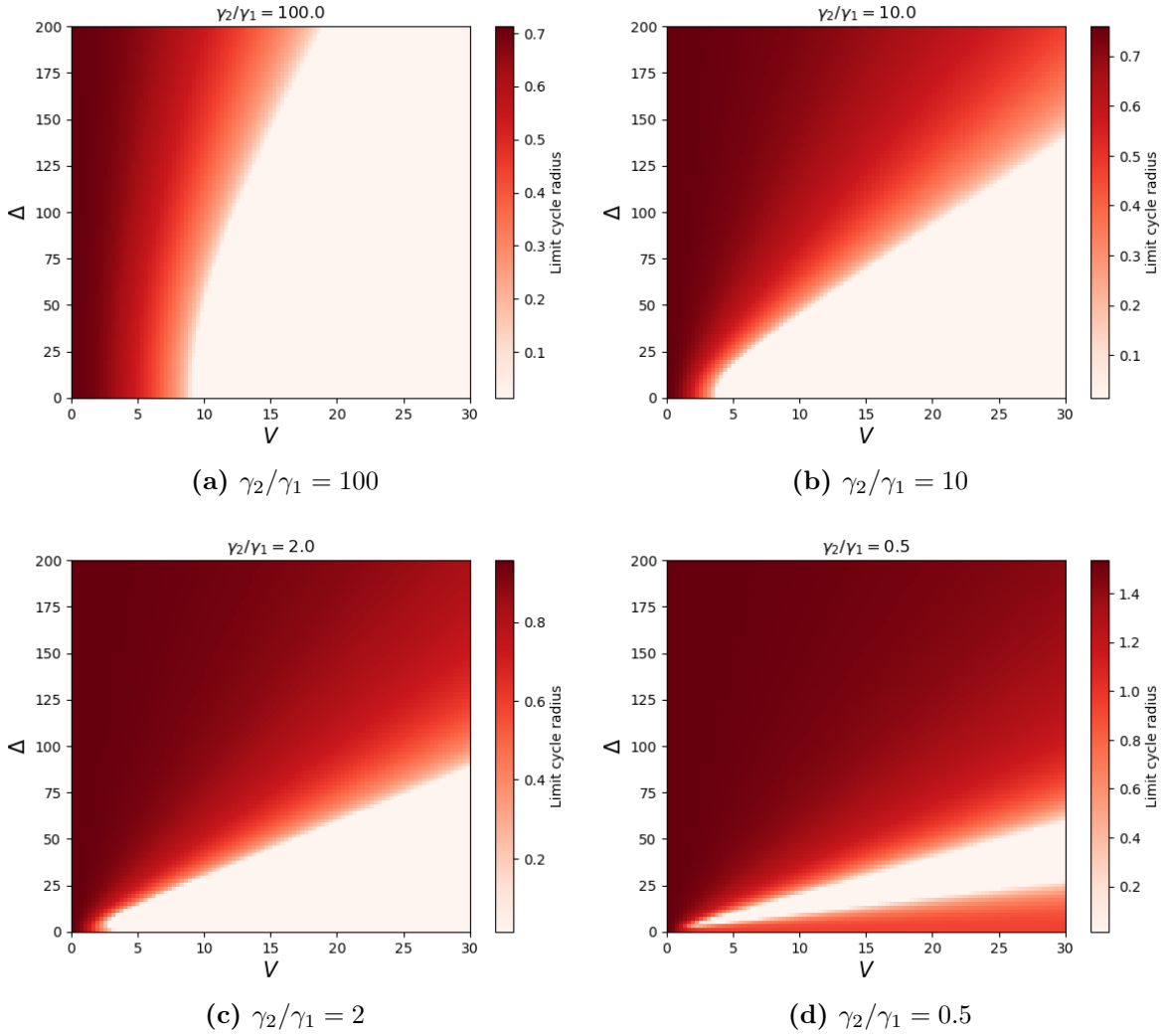

(a) $\gamma_2/\gamma_1 = 100$ **(b)** $\gamma_2/\gamma_1 = 10$

(c) $\gamma_2/\gamma_1 = 2$ **(d)** $\gamma_2/\gamma_1 = 0.5$

Figure 6.8: Limit cycle radius of two Stuart-Landau under reactive coupling $V(a_1 a_2^\dagger + a_1^\dagger a_2)$. The transition from quantum to classical regime is unusual compared to dissipatively coupled case.

6.4.3 Two vdP oscillators

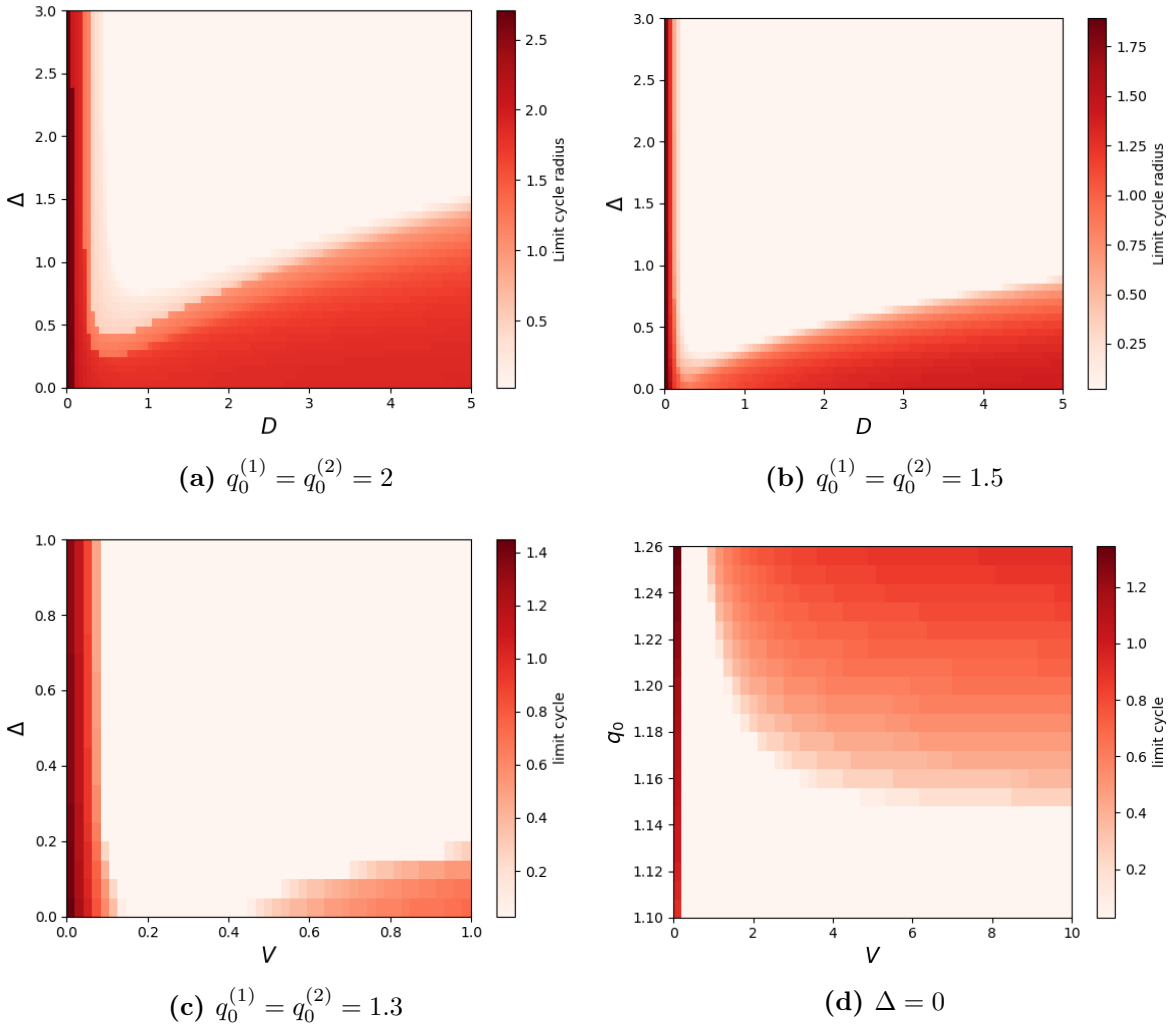

(a) $q_0^{(1)} = q_0^{(2)} = 2$ **(b)** $q_0^{(1)} = q_0^{(2)} = 1.5$

(c) $q_0^{(1)} = q_0^{(2)} = 1.3$ **(d)** $\Delta = 0$

Figure 6.9: Limit cycle radius of two coupled identical vdP oscillators ($\mu_1 = \mu_2 = 0.1$) under increasing dissipative coupling. Tuning down q_0 from $2 \to 1.3$ results in a similar behaviour to two coupled SL case.

In terms of amplitude death, the Stuart-Landau captures similar quantum-to-classical transition as the exact vdP. This transition is solely driven by the limit-cycle radius, not the nonlinearity. Hence this transition is a quantum phenomenon caused by quantum noise.

6.5 Conclusion

The study of coupling heterogeneous quantum oscillators, while being less explored, is of enormous importance and provides exciting possibilities for many applications in

quantum information and dynamics. The coupling of heterogeneous oscillators, each with unique properties and dynamics, enriches our understanding of complex quantum systems and allows the exploration of new phenomena and behaviors not achievable in homogeneous systems. In quantum information processing, the coupling of different oscillators can be used to enhance quantum communication, quantum sensing and quantum computation capabilities. In addition, research into coupled heterogeneous oscillators goes beyond the scope of quantum information processing. Synchronization phenomena are relevant to various scientific disciplines such as physics, biology and complex systems. Understanding and controlling synchronization in quantum systems has pave the way for advances in quantum metrology, quantum sensor, and collective behavior analysis in biological and neural networks.

Chapter 7

GHZ-like states in the Qubit-Qudit Rabi Model

In order to observe quantum synchronization in an experiment, e.g. on cQED platform, one needs to achieve large coupling strengths between the system components. In the current state-of-art cQED experiments, the light-matter interaction is described by the famous Jaynes-Cummings(JC) model, which is only valid when the coupling strength is weak. Whereas the more general quantum Rabi model can be used to describe larger coupling strengths, In this Chapter, a new model based on the quantum Rabi model is exploited and its dynamics studied.

The quantum Rabi model (QRM) describes the interaction between a two-level system and a single quantized harmonic oscillator mode. It is one of the most celebrated models in atomic physics for light-matter interaction [CTDRG98]. In quantum technology, Rabi-like models are widely employed to describe the effective physics emerging in a variety of different contexts ranging from spintronics [DD90, MSB01] to trapped ions [HJG+98], and from cQED [BGW+07] to atom-superconducting qubit hybrid schemes [XAYN13]. Despite its simple form, the Rabi model was solved exactly only recently [Bra11, BCBS16]. The ground state of the quantum Rabi model consists of a non-classical highly entangled state of two-level system and bosonic mode [Bra11, BMS+17]. In cQED, different regimes of interaction between the two-level system and the bosonic field can be explored. In particular, weak and strong coupling regimes are routinely exploited for read-out and coherent state transfer [BGGW21]. Recent research has demonstrated the possibility of reaching the ultrastrong and deep strong coupling regimes, too [NDH+10, YFA+17].

This chapter is published substantially as "GHZ-like states in the qubit-qudit Rabi model" in SciPost Phys. 11, 099 (2021). (No written permission from scipost.org is necessary for thesis purposes.)

Here, we formulate and study a Rabi-type minimal model describing qubit-qudit interaction mediated by a single mode quantum bosonic field. This type of models has emerged recently in several studies of specific systems where atoms, solid state devices (such as superconducting or quantum dot qubits) are assembled together to form hybrid quantum networks [XAYN13, YVH+16, YKAD17, YLV+16, YVH+16, YLK+18, YKAD18, FLB+12]. In this context, entangling quantum systems of heterogeneous nature is sought intensively [CZG+15, JZK+14, MPC+20], as such hybrid entangled states could become useful in converting quantum information between different encodings [ANNVLF15].

We shall see that the physics of our model is particularly interesting in the ultrastrong coupling regime [KFR+15, YKAD17, CIZGN+18, FDLR+19, SCN20]. In particular, the ground state of the system turns out to be defining a Greenberger-Horne-Zeilinger (GHZ) entangled state. GHZ states present great significance among all types of multipartite entanglement [GHSZ90]. These states exhibit maximal correlations between three or more quantum systems. GHZ states have been considered a key resource in fundamental physics since the early stages of quantum information. They have also been proven useful in various quantum technologies, including quantum error-correcting codes [Kni05] and quantum metrology beyond the Heisenberg limit [GLM11].

7.1 The qubit-qudit Rabi model

We investigate the physical system schematically pictured in Fig. 7.1. The scheme features a qubit (two-level quantum system) and a qudit (d-level quantum system) individually coupled to a common quantum resonator described by bosonic degrees of freedom. The Hamiltonian reads (here, and in the rest of this manuscript, we work in units $\hbar = 1$)

$$\hat{H} = \omega \hat{a}^\dagger \hat{a} - \frac{\Omega_1}{2}\hat{\sigma}_z + \Omega_2 \hat{J}_d^z + [g_1 \hat{\sigma}_x + g_2(\hat{J}_d^+ + \hat{J}_d^-)](\hat{a}^\dagger + \hat{a}). \tag{7.1}$$

Here, $\hat{\sigma}_{x,y,z}$ are the Pauli matrices for the qubit with transition frequency Ω_1, $\hat{J}_d^{z,\pm}$ are the spin $(d-1)/2$ operators with level spacing Ω_2, and $\hat{a}(\hat{a}^\dagger)$ is the annihilation (creation) operator for the bosonic field with frequency ω. The coupling strengths $g_{1,2}$ in Eq. (7.1) quantify the vacuum-Rabi splittings. Employing a jargon that is widely used in the literature, we will denote the qubit and the qudit as "artificial atoms". For $d = 2$, our model is equivalent (up to a sign convention) to the two-qubit quantum Rabi model [ARE12, CRL13, PRB+14, Don16]. In contrast to the single

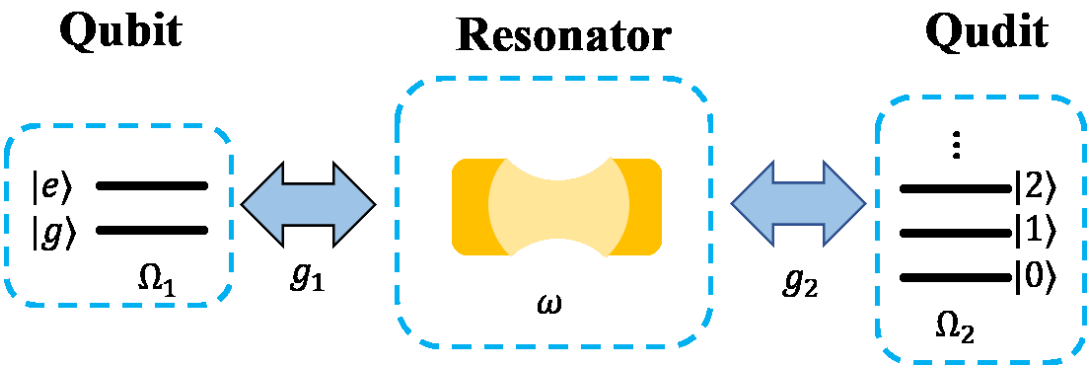

Figure 7.1: Model schematics. The system is composed of a qubit with level spacing Ω_1, an harmonic oscillator (resonator) with characteristic frequency ω, and a d-level quantum system (qudit) with level spacing Ω_2. The qubit and the qudit are coupled to the resonator through the coupling constants $g_{1,2}$. Copyright 2021, SciPost Phys., OA, no permission needed for thesis purpose.

qubit Rabi model, this generalized model is not integrable for general parameter values [CRL13, PRB+14].

The eigenvalues and eigenstates of $\hat{H}$ can be readily obtained numerically. Here, we devise analytical approximation schemes both in the weak-coupling and in the ultrastrong coupling regimes.

The weak coupling limit ($g_1, g_2 \ll \omega$), in the presence of strong qubit/qudit-resonator detuning ($\Omega_1, \Omega_2 \ll \omega$), can be treated by means of a Schrieffer-Wolff transformation [BGW+07, MCG+07]. In particular, we apply the following unitary transformation to the Hamiltonian Eq. (7.1):

$$\begin{aligned}\hat{V} &= \exp(\hat{S}) \\ &= \exp[\epsilon_1(\hat{a}^\dagger\hat{\sigma}_+ - \hat{a}\hat{\sigma}_-) + \xi_1(\hat{a}^\dagger\hat{\sigma}_- - \hat{a}\hat{\sigma}_+) \\ &\quad +\epsilon_2(\hat{a}^\dagger\hat{J}_d^+ - \hat{a}\hat{J}_d^-) + \xi_2(\hat{a}^\dagger\hat{J}_d^- - \hat{a}\hat{J}_d^+)]\end{aligned} \tag{7.2}$$

where we choose

$$\epsilon_i = \frac{g_i}{\omega - \Omega_i} = \frac{g_i}{\Delta_i}, \tag{7.3}$$

$$\xi_i = \frac{g_i}{\omega + \Omega_i} = \frac{g_i}{\Sigma_i}. \tag{7.4}$$

In the weak coupling limit considered here $\epsilon_i, \xi_i \ll 1$. In particular, at the lowest order

in the expansion, the effective Hamiltonian $\hat{H}_{\text{eff}} = \hat{V}\hat{H}\hat{V}^\dagger$ reads:

$$\begin{aligned}\hat{H}_{\text{eff}} &\simeq \hat{H}_0 - \frac{1}{2}\left[[g_1\hat{\sigma}_x + g_2(\hat{J}_d^+ + \hat{J}_d^-)](\hat{a}^\dagger + \hat{a}), \hat{S}\right] \\ &= \tilde{\omega}\hat{a}^\dagger\hat{a} - \frac{\tilde{\Omega}_1}{2}\hat{\sigma}_z + \tilde{\Omega}_2\hat{J}_d^z - g_{\text{eff}}\hat{\sigma}_x(\hat{J}_d^+ + \hat{J}_d^-) \\ &- \frac{1}{2}g_2(\epsilon_2 + \xi_2)\left[\frac{d^2-1}{2} - 2(\hat{J}_d^z)^2 + (\hat{J}_d^+)^2 + (\hat{J}_d^-)^2\right] \\ &- \frac{1}{2}g_1(\epsilon_1 + \xi_1) \end{aligned} \tag{7.5}$$

with renormalized frequencies [1]:

$$\tilde{\omega} = \omega + g_1(\epsilon_1 - \xi_1)\hat{\sigma}_z + 2g_2(\epsilon_2 - \xi_2)\hat{J}_d^z \tag{7.6}$$

$$\tilde{\Omega}_1 = \Omega_1 - g_1(\epsilon_1 - \xi_1) \tag{7.7}$$

$$\tilde{\Omega}_2 = \Omega_2 - g_2(\epsilon_2 - \xi_2) \tag{7.8}$$

and effective coupling $g_{\text{eff}} = [g_1(\epsilon_2 + \xi_2) + g_2(\epsilon_1 + \xi_1)]/2$. In Eq. (7.5), $\hat{H}_0 = \omega\hat{a}^\dagger\hat{a} - \frac{\Omega_1}{2}\hat{\sigma}_z + \Omega_2\hat{J}_d^z$ is the uncoupled Hamiltonian and $[..., ...]$ denotes the commutator. Within our approximation, the energy spectrum consists of different manifolds characterized by a fixed value of resonator photon number operator $\hat{N} = \hat{a}^\dagger\hat{a}$ (the interactions between different manifolds can be neglected due to the large resonator frequency compared to other energy scales). For the qubit ($d = 2$), we have $(\hat{J}_2^\pm)^2 = 0$, $(\hat{J}_2^z)^2 = 1/4$, and the spectrum of the Hamiltonian in Eq. (7.5) can be found by diagonalizing a 4×4 matrix consisting of two 2×2 blocks. In the lowest manifold ($N = 0$), the four eigen-energies are given by

$$E_{d=2} = \pm\sqrt{\frac{1}{4}(\tilde{\Omega}_1 \pm \tilde{\Omega}_2)^2 + g_{\text{eff}}^2} - \sum_{i=1,2}\frac{1}{2}g_i(\epsilon_i + \xi_i). \tag{7.9}$$

In the general qudit case ($d \geq 3$), the eigen-energies can be obtained by computing the roots of the product of two degree d characteristic polynomials of submatrices of dimension $2 \times d$. Simplified expression can be obtained by neglecting the $(\hat{J}_d^\pm)^2$ terms in Eq. (7.5), and performing an approximation similar to the standard rotating wave approximation $\hat{\sigma}_x(\hat{J}_d^+ + \hat{J}_d^-) \sim \hat{\sigma}_+\hat{J}_d^- + \hat{\sigma}_-\hat{J}_d^+$, valid for $\Omega_1 \sim \Omega_2$. The approximate results in the $N = 0$ subspace for the qutrit and the ququart are reported in [SMC+21].

In the ultrastrong coupling regime, the numerical results to be presented below are

[1] Here our notations is slightly abusive, since $\tilde{\omega}$ contains the operators $\hat{\sigma}_z, \hat{J}_d^z$. However, since we focus on the $N = 0$ subspace of the resonator degree of freedom, this notation simplifies the subsequent discussion.

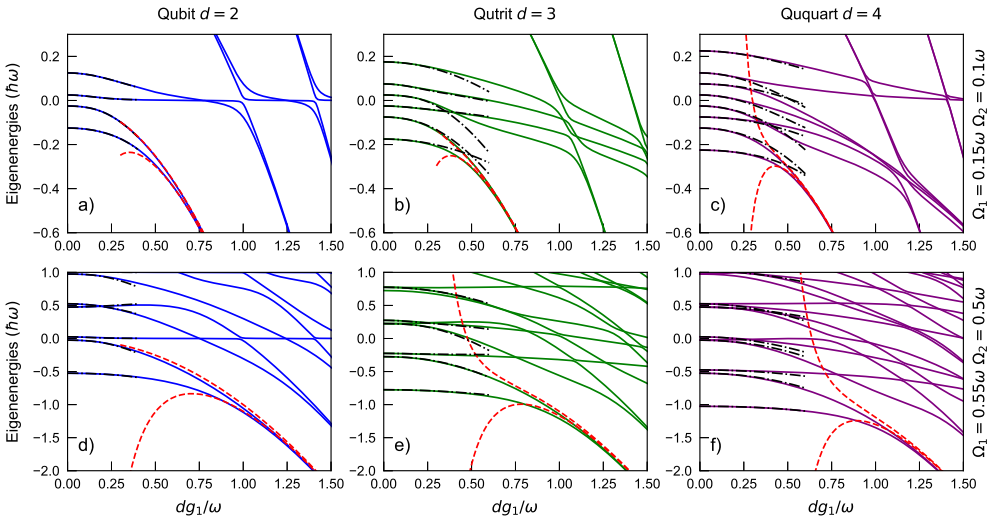

Figure 7.2: Hamiltonian energy spectrum with qudit dimensions $d = 2, 3, 4$. (a)-(f) Low energy spectrum vs coupling strength g obtained through numerical diagonalization of the full Hamiltonian Eq. (7.1) (solid). The numerical results are compared to the low coupling approximations (black dotted-dashed) of Eq. (7.9) , and d-order perturbation approximation Eq. (7.11) in the ultrastrong coupling regime (red dashed), for $g_1 = g_2 = g$ and (top panels) $\Omega_1 = 0.15\omega, \Omega_2 = 0.1\omega$, (bottom panels) $\Omega_1 = 0.55\omega, \Omega_2 = 0.5\omega$. Copyright 2021, SciPost Phys., OA, no permission needed for thesis purpose.

corroborated by an analytical approach combining the adiabatic approximation in the displaced oscillator basis [IGBMS05] and degenerate perturbation theory. More precisely, we first obtain the exact spectrum of the reduced Hamiltonian

$$\tilde{H} = \omega\hat{a}^\dagger\hat{a} + g_1\hat{\sigma}_x(\hat{a}^\dagger + \hat{a}) + g_2(\hat{J}_d^+ + \hat{J}_d^-)(\hat{a}^\dagger + \hat{a}), \tag{7.10}$$

neglecting the free Hamiltonian of the qubit and qudit in the limit where $\Omega_1, \Omega_2 \ll \omega$, and $g_1, g_2 \lesssim \omega$. Then, these terms are restored within a perturbative expansion. The eigenstates of $\tilde{H}$ are product states $|\sigma\ m\ N_{\sigma,m}\rangle = |\sigma\rangle \otimes |m\rangle \otimes |N_{\sigma,m}\rangle$. Here, $\sigma = \uparrow, \downarrow$ are the eigenstates of $\hat{\sigma}_x$ with eigenvalues ± 1, $|m = 0, 1, \ldots, d-1\rangle$ are the eigenstates of the qudit operator $(\hat{J}_d^+ + \hat{J}_d^-)$ with eigenvalues $\lambda_m = -(d-1) + 2m$, and $|N_{\sigma,m}\rangle$ are displaced Fock states [IGBMS05, ARE12, CRL13]. The system yields a two-fold degenerate ground state, obtained from a displacement of the vacuum state in the resonator $\{|\uparrow, +, 0_{\uparrow,+}\rangle, |\downarrow, -, 0_{\downarrow,-}\rangle\}$, with energy $E_0 = -[g_1 + (d-1)g_2]^2/\omega$, where $|+\rangle$ ($|-\rangle$) is the eigenstate of the operator $(\hat{J}_d^+ + \hat{J}_d^-)$ with the largest(lowest) eigenvalue, i.e., $d-1(-d+1)$. The corrections to the spectrum of $\tilde{H}$ are then evaluated through

perturbation theory in $\hat{H}' = -\frac{1}{2}\Omega_1\hat{\sigma}_z + \Omega_2\hat{J}_d^z$. The lowest (second) order corrections to the energy are obtained as:

$$\begin{aligned}\mathcal{E}_\pm = E_0 &- \frac{\omega}{16(d-1)g_1g_2}\Omega_1^2 e^{-4g_1^2/\omega^2} \\ &- \omega\frac{(d-1)}{16(d-2)g_2^2+16g_1g_2}\Omega_2^2 e^{-4g_2^2/\omega^2} \\ &\pm \delta_{d,2}\frac{\omega\Omega_1\Omega_2}{8(d-1)g_1g_2}e^{-2[g_1^2+(d-1)^2g_2^2]/\omega^2}\end{aligned} \tag{7.11}$$

where $\delta_{i,j}$ is the Kronecker delta [2]. Notably, the two-fold degeneration of ground state is only resolved at d-order perturbation theory in $\hat{H}'$, with a correction proportional to $\Omega_1\Omega_2^{d-1}$. The corresponding eigenstates read

$$\begin{aligned}|\Psi_\pm\rangle =&\frac{1}{\mathcal{C}}[|\uparrow,+,0_{\uparrow,+}\rangle \pm |\downarrow,-,0_{\downarrow,-}\rangle + \\ &\sum_{(\sigma,m)\neq(\uparrow,+),(\downarrow,-)} C_{\sigma,m}(g_1,g_2)\,|\sigma,m,0_{\sigma,m}\rangle]\end{aligned} \tag{7.12}$$

where $\mathcal{C}$ is the normalization factor, and the functions $C_{\sigma,m}(g_1,g_2) \propto e^{-g_1^2/\omega^2}$, $e^{-g_2^2/\omega^2}$ are exponentially suppressed with the coupling strengths. As discussed above, the analytical expression in Eqs. (7.11)-(7.12) are expected to hold in the regime where the free Hamiltonian terms of the atoms are treated as perturbations to the interacting system, *i.e.* $\Omega_1, \Omega_2 \ll \omega, g_1, g_2$.

In Fig. 7.2, we display the low-energy spectrum of the Hamiltonian in Eq. (7.1) as a function of the coupling strength (with $g_1 = g_2$) for $d = 2$ (panels a,d), $d = 3$ (panels b,e), and $d = 4$ (panels c,f). For visualization purposes, we plot the energy as a function of dg_1 (with d number of levels in the qudit), since the ground state energy for $g_1 = g_2$ scales as $E_0/\omega \sim -(dg_1/\omega)^2$ for large values of g_1. The analytical expressions obtained in the low-coupling limit (dotted-dashed) and through perturbation theory in the ultrastrong coupling regime (dashed) are compared with the solutions obtained through numerical diagonalization (solid). In the low coupling regime, the analytical expression of Eq. (7.9) gives a very accurate description of the spectrum for $dg_1 \lesssim 0.4\Omega$ (see Fig. 7.2a), and Fig. 7.2d)). For the general qudit case, the expressions obtained through RWA approximation reproduce the numerical results in a less satisfactory way. Still, they correctly reproduce the spectrum for $dg_1 \lesssim 0.3\Omega$.

[2]We have verified that for $d = 2$, when both equations (7.9) and (7.11) are applicable (that is, when taking g_i, $\Omega_i \to 0$) they agree at next to leading order.

For $\Omega_1 = 0.15\omega, \Omega_2 = 0.1\omega$ (top panels), an excellent agreement between the strong coupling regime approximations and numerical solutions arises for $dg_1, dg_2 \gtrsim 0.3\omega$. For higher Ω_1 and Ω_2 values ($\Omega_1 = 0.55\omega, \Omega_2 = 0.5\omega$, bottom panels), the adiabatic approximation breaks down below $dg_1, dg_2 \sim 0.75\omega$ (Fig. 7.2b).

With increasing coupling strength g_1, g_2, the higher order correction terms in Eq. (7.12) are suppressed exponentially, and the states $|\Psi_\pm\rangle$ approach the GHZ-type states. Note that the states $|0_{\uparrow,+}\rangle = D^\dagger(\frac{g_1+(d-1)g_2}{\omega})|0\rangle$ and $|0_{\downarrow,-}\rangle = D^\dagger(-\frac{g_1+(d-1)g_2}{\omega})|0\rangle$ are coherent states with opposite displacement in the phase space, which are asymptotically orthogonal in the limit $g_1, g_2 \to \infty$. As a result, the ground state under such large coupling assumption can be approximated as:

$$|\Psi_{GHZ}\rangle \quad = \quad \frac{1}{\sqrt{2}}(|\uparrow, +, 0_{\uparrow,+}\rangle \pm |\downarrow, -, 0_{\downarrow,-}\rangle). \tag{7.13}$$

The validity of this approximation is investigated in Fig. 7.3, where the fidelity between the GHZ state and the ground state of the Hamiltonian obtained through numerical diagonalization is plotted as a function of the coupling strength $g_1 = g_2$. In this manuscript, we define the fidelity between two pure states $|\phi\rangle, |\psi\rangle$ as $\mathcal{F} = |\langle\phi|\psi\rangle|$. In agreement with our perturbative calculation, the fidelity of the ground state with the GHZ state approaches the unit value in the limit $g_1 \gg \Omega_1, \Omega_2$.

7.2 Negativity of entanglement

In our scheme, it is interesting to investigate the bipartite entanglement between the qubit and qudit. We choose to compute negativity [VW02] as the measure of entanglement. For a bipartite pure state $|\varphi\rangle_{AB}$ in a $d \otimes d' (d \leq d')$ quantum system, the negativity is defined as

$$\mathcal{N}_{|\varphi\rangle_{AB}} = \frac{1}{2}(\||\varphi\rangle_{AB}\langle\varphi|^{T_B}\|_1 - 1) \tag{7.14}$$

where $|\varphi\rangle_{AB}\langle\varphi|^{T_B}$ is the partial transpose of $|\varphi\rangle_{AB}\langle\varphi|$ and $\|\cdot\|_1$ is the trace norm. To extract bipartite pair-wise entanglement in a tripartite system, we use the reduced density matrix of $|\varphi\rangle_{ABC}$ on subsystem $A \otimes B$ by tracing over subsystem C: $\rho_{AB} = \mathrm{Tr}_C |\varphi\rangle_{ABC}\langle\varphi|$.

Figure 7.4 displays the density plot of the negativity as a function of the coupling strengths g_1, g_2 in the qubit (Fig. 7.4a), qutrit (Fig. 7.4b), ququart (Fig. 7.4c) cases, for $\Omega_1 = \Omega_2 = 0.1\omega$. Note that the negativity is clearly symmetric under the exchange

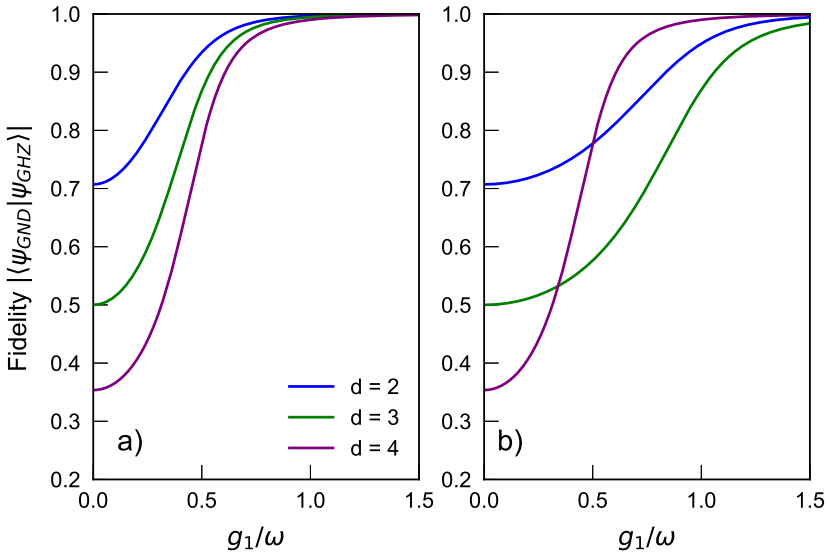

Figure 7.3: Ground state vs GHZ state for $g_1 = g_2$ and different qudit sizes $d = 2, 3, 4$ (top to bottom at $g_1 = 0$). Fidelity between the Hamiltonian ground state (obtained through numerical diagonalization) and the GHZ state Eq. (7.13) as a function of the coupling strength for (a) $\Omega_1 = 0.15\omega, \Omega_2 = 0.1\omega$, (b) $\Omega_1 = 0.55\omega, \Omega_2 = 0.5\omega$. Copyright 2021, SciPost Phys., OA, no permission needed for thesis purpose.

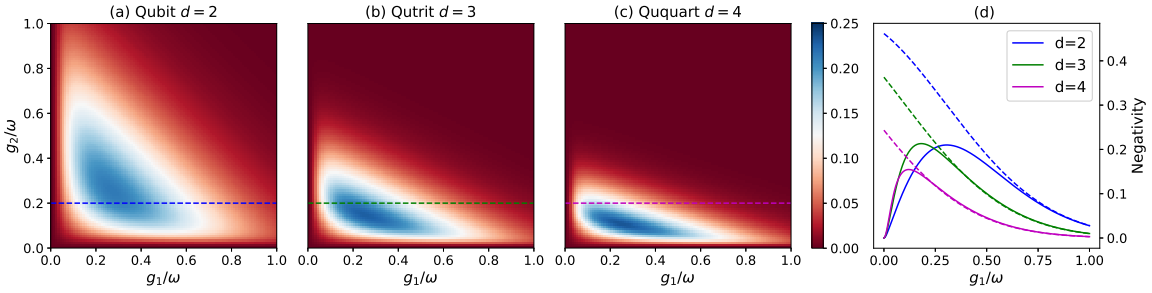

Figure 7.4: Coupling dependence of the groundstate negativity between the qubit and the qudit. (a)-(c) Density plot of the groundstate negativity as a function of g_1 and g_2 for the (a) qubit-qubit, (b) qubit-qutrit, (c) qubit-ququart cases. The plots are obtained by numerical calculations for $\Omega_1 = \Omega_2 = 0.1\omega$. (d) Cuts of the density plots for $g_2 = 0.2\omega$, indicated by the dashed lines in panels (a)-(c). The results obtained through numerical calculations (solid) are compared with the approximate expression of the negativity Eq. (7.16) (dashed), obtained in the ultrastrong coupling regime. Copyright 2021, SciPost Phys., OA, no permission needed for thesis purpose.

$g_1 \leftrightarrow g_2$ in the qubit case (since $\Omega_1 = \Omega_2$), and it becomes gradually more asymmetric by increasing the number of levels. The bipartite entanglement between the two

artificial atoms has a nontrivial response to the coupling strengths between subsystems. In particular the negativity is maximum for intermediate values of the couplings, and it is strongly suppressed at large couplings. The position of the maximum depends on the number of levels in the qudit and reads: $g_1 = g_2 \simeq 0.24\omega$ (qubit), $g_1 \simeq 0.21\omega$, $g_2 \simeq 0.17\omega$ (qutrit), $g_1 \simeq 0.21\omega$, $g_2 \simeq 0.14\omega$ (ququart).

For a better visualization, in Fig. 7.4d we consider cuts of Figs. 7.4a-c at a fixed value of $g_2 = 0.2\omega$. The negativity first rises to a maximum with increased coupling strength g_1, before decaying to zero exponentially (as we will discuss below). This phenomenon is reported in [LL13] where an approximate expression is derived to explain the curve at weaker coupling. Here, we obtain an analytical expression for the decaying curve. In addition, our approach demonstrates that the entanglement suppression is a consequence of the structure of the entanglement encoded in the ground state [see Eq. (7.13)]: the tripartite GHZ state at large coupling limit($g_1, g_2 \to \infty$), hinders the bipartite entanglement obtained after tracing out one of the subsystems, that asymptotically vanishes. This property of the GHZ states results in a counter-intuitive implication: the strong coupling can destroy entanglement between the two quantum systems connected by the resonator.

Now we show that the approximate expression of the ground state, i.e., the GHZ state of Eq. (7.13), leads to an accurate prediction for the entanglement at large coupling; we can easily calculate the negativity for those states. Indeed, the corresponding reduced density matrix ρ' with resonator degree-of-freedom traced out is a $(2d \times 2d)$ matrix and has only four non-zero matrix elements:

$$\rho' = \frac{1}{2}\begin{bmatrix} 1 & \dots & K \\ \vdots & \ddots & \vdots \\ K & \dots & 1 \end{bmatrix}, \tag{7.15}$$

with $K = \exp\{-2[g_1 + (d-1)g_2]^2/\omega^2\}$. Therefore the analytical expression for the negativity of the ground state in Eq. (7.13) is

$$\mathcal{N} = \frac{1}{2}|K| = \frac{1}{2}\exp\{-2[g_1 + (d-1)g_2]^2/\omega^2\} \tag{7.16}$$

These approximate expressions are displayed (dashed) in Fig. 7.4. Note that the approximation describes very accurately the exponential decay of the negativity at large coupling.

We close the section by noting that the negativity measure is not a sufficient test of entanglement for systems with dimensions beyond 2×3. Under such circumstances, a state with zero negativity could possibly be a PPT or "bound entangled" state, which is argued to be metrologically useful [TV18, T620, HLLMH18].

7.3 Dynamics

7.3.1 Quench dynamics

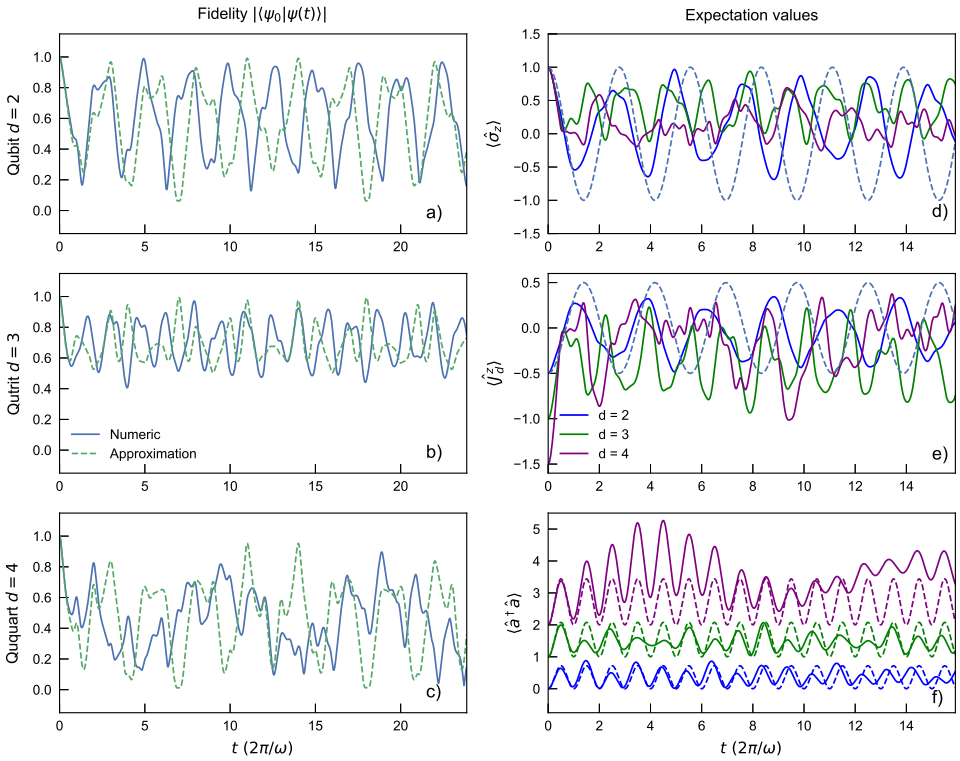

Figure 7.5: Dynamics after quenching the interaction strength. a)-b)-c) Fidelity between the initial state of the system and the instantaneous state for qubit (a), qutrit (b) and ququart (c) cases. The initial state is the ground state of the uncoupled system. The numerical expressions (solid) are compared to approximations (dashed) derived in the main text Eq. (7.18). d)-e) -f) Dynamics of the expectation value of d) the qubit population, e) qudit population and f) mean photon number. The dashed lines in panel f) are given by Eq. (7.19) Parameters are $\Omega_1 = 0.12\omega, \Omega_2 = 0.1\omega$, and $g_1 = g_2 = 0.3\omega$. Copyright 2021, SciPost Phys., OA, no permission needed for thesis purpose.

We start by discussing the dynamics of the system under non-adiabatic switching

of the interaction. We consider the system initially prepared in the ground state of the uncoupled Hamiltonian $\hat{H}_0$, *i.e.* $|\psi_0\rangle = |g\,0\,0\rangle$. For simplicity, we consider an instantaneous quench of the coupling constant to the final values $g_1 = g_2 = 0.3\omega$. In this case, the time-evolved state reads

$$|\psi(t)\rangle = e^{-i\hat{H}t}|\psi_0\rangle. \tag{7.17}$$

Due to the non-adiabatic control, the state of the system is different from the ground state of the interacting Hamiltonian after the quench, and evolves in time.

Figures 7.5(a)-(c) display the time evolution of the fidelity between the initial state $|\psi_0\rangle$ and the time evolved state $|\psi(t)\rangle = e^{-i\hat{H}t}\,|\psi_0\rangle$ in the qubit, qutrit, and ququart cases, respectively, for $\Omega_1 = 0.12\omega$ and $\Omega_2 = 0.1\omega$. We note that the dynamics of $|\psi_0\rangle$ involves multiple frequencies, and displays a clear dependence on the number of levels of the qudit. An approximate description of the evolution can be obtained by neglecting the free terms of the atoms in the Hamiltonian. Namely, we set $\Omega_{1,2} = 0$, and expand $|\psi_0\rangle$ in the eigenstates basis of $\tilde{H}$, *i.e.*, $|\psi_0\rangle = \sum_{\sigma m N} \langle \sigma\, m\, N_{\sigma m}|g\,0\,0\rangle\, |\sigma\, m\, N_{\sigma m}\rangle$. For the qubit case, we obtain

$$\mathcal{F}^{d=2} = \frac{1}{2}\left|\sum_{N=0}^{+\infty} e^{-iE_{\uparrow+}t}|\,\langle N_{\uparrow,+}|0\rangle\,|^2 + e^{-iE_{\uparrow-}t}|\,\langle N_{\uparrow,-}|0\rangle\,|^2\right| \tag{7.18}$$

where $E_{\uparrow\pm} = \omega(N - \alpha_\pm^2)$ and $|\,\langle N_{\uparrow,\pm}|0\rangle\,|^2 = e^{-\alpha_\pm^2}\alpha_\pm^{2N}/N!$, with $\alpha_\pm = (g_1 \pm g_2)/\omega$. For the qutrit and the ququart case the summation in Eq. (7.18) involves d terms. Such approximated dynamics is displayed [3] in Figs. 7.5(a),(b),(c). We note that the approximate expressions capture the initial decrease in fidelity and the amplitude of its oscillations, as well as the main frequency components of the evolution.

The right column of Fig. 7.5 displays the time evolution of the expectation values of $\hat{\sigma}_z$ (panel d), $\hat{J}_d^z$ (panel e), and the mean photon number $\hat{a}^\dagger\hat{a}$ (panel f) for the qubit, qutrit and ququart cases. Consider first the qubit population $\langle\hat{\sigma}_z(t)\rangle$: in all the three cases, the evolution is non-harmonic, and the number of relevant frequencies increases by increasing the number of levels in the qudit. In particular, for precise modeling of the dynamic in this regime different Fock number states must be included in the calculation and neglecting the off-diagonal terms in the basis of $\tilde{H}$ would provide a poor description of the physics (see the above discussion).

[3] In the infinite sum of Eq. (7.18), we retained terms up to $N_{\max} = 10$, since we verified that the convergence is quite rapid for our parameter values.

Consider for instance, the time evolution of $\hat{\sigma}_z$ in the qubit case (blue curve in Fig. 7.5d). We can work within the approximation exploited above for the strong coupling regime. Namely, we approximate $\hat{H} = \tilde{H}$, and we write $|\psi_0\rangle$ in the basis of $\tilde{H}$. By performing the calculation, it is possible to derive a simple expression for $\langle\hat{\sigma}_z\rangle$ when $g_1 = g_2$ (as in the plot of Fig. 7.5d), namely $\langle\hat{\sigma}_z(t)\rangle \sim \cos(4g_1g_2t/\omega)$. This approximate expression is displayed in Fig. 7.5a (dashed). Note that the approximate expression fails to reproduce correctly both the frequency and the amplitude of the time oscillation, which turns out smaller in the numerical calculation (solid blue). A similar analysis can be performed for the time evolution of the expectation value of $\langle\hat{J}_z\rangle$. For the qubit case, the approximation $\hat{H} \sim \tilde{H}$ predicts an evolution $\langle\hat{J}_z(t)\rangle \sim -\cos(4g_1g_2t/\omega)/2$. We note that this approximated analytical expression overestimates both the frequency and the amplitude of the oscillations.

Notably, the dynamics of the mean photon number $\langle\hat{a}^\dagger\hat{a}\rangle$ is much more regular, as displayed in Fig. 7.5; for visualization purposes, the various curves are offset by the quantity $d-1$. Note that the main frequency of the oscillations is independent of the number of levels in the qudit; the amplitude of the oscillations, instead, increases with d. These features can be discussed retaining the approximation $\hat{H} \sim \tilde{H}$. In particular, by applying the Baker-Hausdorff expansion to the operator $e^{i\tilde{H}t}\hat{a}^\dagger\hat{a}e^{-i\tilde{H}t}$, we derive

$$\langle\psi(t)|\hat{a}^\dagger\hat{a}|\psi(t)\rangle = 4[g_1^2 + (d-1)g_2^2]\sin^2(\omega t/2). \tag{7.19}$$

The validity of this approximation is investigated in Fig. 7.5(f) (dashed curves). While we find a good agreement for the qubit and the qutrit cases, the deviations are more relevant for the ququart. This feature indicates that the presence of additional levels is beneficial to inducing non-adiabatic photon generation in the ultrastrong coupling regime.

7.3.2 Adiabatic state preparation

In this section we demonstrate how the state in Eq. (7.13) can be prepared with high fidelity by adiabatic evolution:

$$\hat{H}(t) = [1-\mu(t)]\,\hat{H}_{\rm in} + \mu(t)\hat{H} \tag{7.20}$$

The initial state and the final state correspond to the ground state of the Hamiltonians $\hat{H}_{\rm in} = \hat{H}(t=0)$ and $\hat{H}$, respectively, and $\mu(t)$ is a function that goes from 0 to 1 when t goes from 0 to the final evolution time t_f; $\mu(t)$ is chosen to be a linear function in

our simulations. Here we propose two simple schemes to prepare the hybrid GHZ state: I. switch on the couplings at fixed frequencies; II. change the frequencies at fixed couplings. In both schemes, the final Hamiltonian $\hat{H}$ is set to be the Hamiltonian of the qubit-resonator-qudit system in Eq. (7.1).

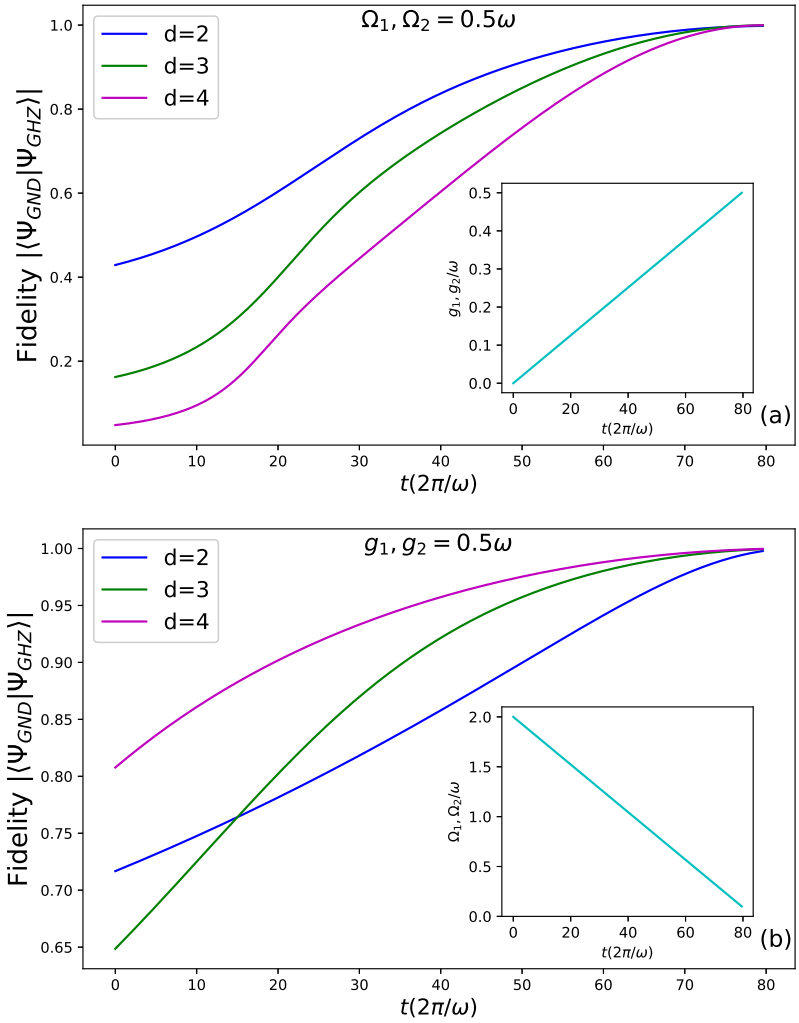

Figure 7.6: Adiabatic state preparation of the GHZ state in the qubit, qutrit, and ququart cases. (a) Time evolution of the fidelity between the instantaneous state and the hybrid GHZ state in Eq.(7.13). The coupling terms g_1, g_2 are adiabatically switched on at $t = 0$ and linearly increased to 0.5ω, as shown in the inset. (b) State fidelity with the GHZ state vs time in the adiabatic process where the atoms frequencies are linearly reduced from the initial value $\Omega_1, \Omega_2 = 2\omega$ to 0.1ω, as displayed in the inset. Copyright 2021, SciPost Phys., OA, no permission needed for thesis purpose.

I. In the first approach, the system is initialized without coupling terms $g_1(t = 0) = g_2(t = 0) = 0$, *i.e.*, $\hat{H}_{\rm in} = \hat{H}_0 = \omega\hat{a}^\dagger\hat{a} - \frac{\Omega_1}{2}\hat{\sigma}_z + \Omega_2\hat{J}_d^z$. During the adiabatic evolution, the coupling terms are gradually switched on to the final value $g_f = 0.5\omega$, reading $g_1(t) = g_2(t) = \mu(t)g_f$, see the inset in Fig. 7.6a. The main panel of Fig. 7.6a displays

the evolution of the fidelity between the instantaneous state of the system under the time-dependent Hamiltonian $\hat{H}(t)$ and the expected GHZ state at the final time, obtained by setting $g_1 = g_2 = 0.5\omega$ in Eq. (7.13). The different curves corresponds to the qubit, qutrit and ququart cases. In all the cases, the fidelity is minimum at $t = 0$ and grows monotonically with time, reaching the unit value (within numerical accuracy) for $t = t_f = 500/\omega$. Note that for a given time the fidelity is maximum in the qubit case, and typically decreases by increasing the number of levels in the qudit.

II. Here, we keep fixed the coupling terms g_1, g_2, while tuning the characteristic frequencies of the artificial atoms. Specifically, the system is initialized to $\hat{H}_0 = \omega\hat{a}^\dagger\hat{a} - \Omega_1'\hat{\sigma}_z/2 + \Omega_2'\hat{J}_d^z + g_1\hat{\sigma}_x(\hat{a}^\dagger + \hat{a}) + g_2(\hat{J}_d^+ + \hat{J}_d^-)(\hat{a}^\dagger + \hat{a})$, with the initial transition frequencies satisfying $\Omega_1' \gg \Omega_1$ and $\Omega_2' \gg \Omega_2$. In the adiabatic preparation, the artificial atoms frequencies $\Omega_1(t), \Omega_2(t)$, are linearly reduced to the final values $\Omega_1 = \Omega_2 = 0.1\omega$ (see the inset of Fig. 7.6(b)). The corresponding evolution of the fidelity with the final GHZ state is shown in Fig. 7.6(b). As in the previous case, the fidelity grows monotonically to 1 as time approaches t_f in all the cases. Notably, the presence of additional levels in the qudit is displayed to be beneficial to the process: for a given $t > t_f/2$, the fidelity is larger in the qutrit and ququart case with respect to the qubit case.

7.4 Conclusion

We formulated and studied a quantum Rabi type model describing the interaction between a two-level and a multi-level system mediated by a single mode bosonic field (in quantum technology such bosonic field is realized by a resonator). In the weak and in the strong coupling limits, we devised two different analytical schemes. In the weak-coupling limit, the effective Hamiltonian is obtained through a suitable Schrieffer-Wolff transformation. Assuming the qudit degenerating in a two-level system, the spectrum of the effective Hamiltonian has been obtained exactly. In the strong coupling limit, the ground state of the system is provided by a tripartite-entangled state of the GHZ type. A known feature of the GHZ states is that they do not allow bipartite entanglement between the three partners. As a result, qubit and qudit cannot be highly entangled, and the correlation between them drops exponentially with increasing coupling in the ultrastrong coupling regime. Such analysis is corroborated by the study of the negativity providing the sufficient condition for the qubit-qudit entanglement.

We analyzed the system dynamics both under quenching and adiabatic switching of the couplings between the atoms and the resonator. The non-adiabatic nature of

the quantum quench leads to the generations of photons in the resonator, with a magnified effect by increasing the number of levels in the qudit. By this procedure, the GHZ states can be adiabatically prepared with high fidelity. Both the analysis of the spectrum and the dynamics indicate that the interaction is effectively magnified by the number of the levels of the qudit. The study of the dynamics gives preliminary information on the qubit-qudit coherent state transfer. Our work provides relevant information for applications in quantum technology, particularly for hybrid quantum networks design [ANNVLF15, JZK+14, CZG+15, HLJM+19].

Chapter 8

A survey on synchronization in cQED platform

Circuit QED provides a well-controlled and scalable platform for studying the interaction between superconducting qubits and electromagnetic fields, making it suitable for investigating quantum synchronization phenomena.

In cQED systems, superconducting qubits can be coupled to one or multiple microwave resonators, which act as channels for mediating the interactions between qubits. These interactions can lead to the entanglement of qubits, allowing for the emergence of quantum synchronization. By carefully controlling the coupling strength between qubits and resonators, as well as the parameters of the qubits themselves.

Quantum synchronization in cQED systems has potential applications in quantum technologies, such as building robust quantum communication networks, improving the performance of quantum gates, and developing quantum error correction schemes. For example, synchronized qubits can be utilized to create highly sensitive detectors or more efficient quantum gates, and the synchronization phenomenon can be harnessed to improve the overall coherence and stability of a quantum system.

In this chapter, the most-recent attempts towards quantum synchronization in circuit QED are reviewed. A quantum Stuart-Landau oscillator is realizable in superconducting cavities thanks to the engineered nonlinear dissipation [LTP+15]. Another path to achieve quantum synchronization is digital simulation on a quantum computer. Current NISQ-era quantum hardware is already capable of simulating driven quantum harmonic oscillator [BKBP19] and demonstrating quantum synchronization using qubits [KBR20].

8.1 Quantum Stuart-Landau in superconducting cavities

In Ref. [LTP+15], the authors managed to confine the microwave mode in a superconducting cavity into a stablized manifold through carefully engineered two-photon loss. The setup comprised two superconducting microwave cavity coupled through a Josephson junction in a bridge transmon configuration as shown in Figure 8.1. Pump and drive microwave tones are applied to the readout cavity, creating the appropriate nonlinear interaction which generates a coherent superposition of steady states in the storage cavity. The dynamics of the storage cavity is governed by

$$\hat{H}_s = \epsilon(\hat{a}_s^2 + (\hat{a}_s^\dagger)^2) - \chi(\hat{a}_s^\dagger)^2\hat{a}_s^2, \tag{8.1}$$

with loss operators $\sqrt{\kappa_2}\hat{a}_s^2$ and $\sqrt{\kappa_s}\hat{a}_a$. Both squeezing and two-photon loss causes the steady-state in the storage cavity relaxes into a stable manifold. This steady-state resembles a quantum Stuart-Landau oscillator with squeezing drive, except for the thermal excitations which are inevitable in experiments.

In Ref. [CKN20], a truly nonlinear quantum van der Pol oscillator has been proposed. This oscillator has a Wigner function that resembles the classical phase space plot of a van der Pol oscillator. Yet, no attempt has been made to study this modified quantum oscillator as it is still challenging to construct experimentally.

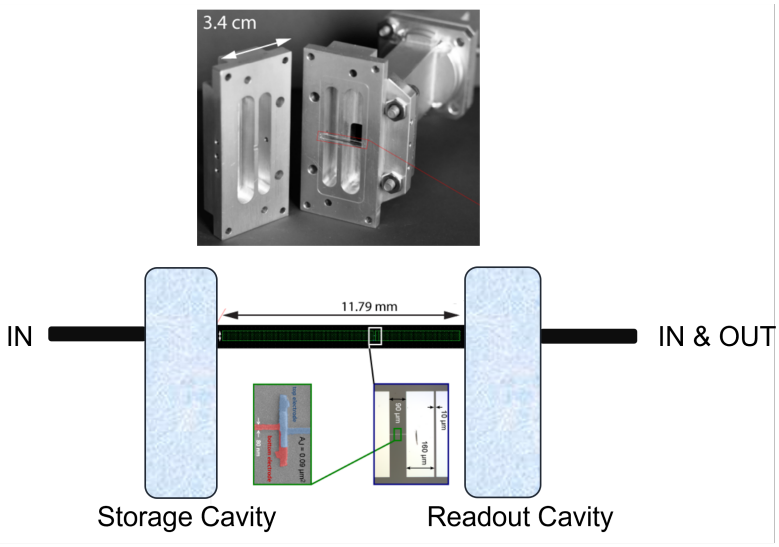

Figure 8.1: Experimental realization of the quantum van der Pol oscillator (or more accurately, the quantum Stuart Landau oscillator). Figure adapted from [LTP+15].

8.2 Synchronization of spin-1 on IBM-Q

In a recent paper by M. Koppenhofer, C. Bruder and A. Roulet, quantum synchronization by a digital quantum simulation was demostrated experimentally [KBR20]. The quantum limit-cycle oscillator is realized in a single spin-1 system, the smallest possible system that can host a limit-cycle oscillator [RB18]. In this work, two qubits of a quantum processor were used to implement the desired spin-1 system while the remaining qubits play the role of the environment sustaining the oscillation. The advantage of this approach is that the nonlinear dissipation required to study quantum synchronization corresponds to easily engineered single-qubit relaxation.

The spin-1 system is described by a quantum master equation under a rotating wave approximation:

$$\dot{\rho} = -i[\Delta \hat{S}_z + \epsilon \hat{H}_{ext}, \rho] + \Gamma_{-1,0}\mathcal{D}[\hat{S}_+\hat{S}_z]\rho + \Gamma_{1,0}\mathcal{D}[\hat{S}_-\hat{S}_z]\rho, \tag{8.2}$$

where $\Delta = \omega_0 - \omega_{ext}$ is the detuning between the spin precession frequency and the driving frequency. And external driving Hamiltonian $\hat{H}_{ext}$ describes coherent transition between spin-1 eigenstates:

$$\hat{H}_{ext} = t_{0,1}\hat{S}_z\hat{S}_+ - t_{-1,0}\hat{S}_+\hat{S}_z + t_{-1,1}\hat{S}_+^2 + H.c. \tag{8.3}$$

where $t_{i,j}$ are complex coefficients determine the relative amplitude and phase of the transitions.

To map the dynamics of (8.2) onto a quantum computer, the spin levels are encoded by the product two-qubit states:

$$|+1\rangle \to |1\rangle_{q1} \otimes |0\rangle_{q0}, \tag{8.4}$$

$$|0\rangle \to |0\rangle_{q1} \otimes |0\rangle_{q0}, \tag{8.5}$$

$$|-1\rangle \to |0\rangle_{q1} \otimes |1\rangle_{q0}. \tag{8.6}$$

Note that this encoding gives rise to a redundant state $|X\rangle \to |1\rangle_{q1} \otimes |1\rangle_{q0}$ which needs to be isolated from the subspace.

To simulate the unitary time evolution in a quantum computer, the exact time evolution is approximated by a series of many transformations that propagate the system's state for a small time step dt. This technique is referred to as Trotterization. In this work they chose a symmetric decomposition that is exact up to third-order corrections in

terms of dt [NC10]:

$$e^{i(A+B)dt} = e^{iAdt/2}e^{iBdt}e^{iAdt/2} + \mathcal{O}(dt^3). \tag{8.7}$$

In a final step, these abstract unitary transformations of the two-qubit state must be decomposed in terms of the quantum gates available on the IBM-Q System, namely, a two-qubit CNOT gate and the three single-qubit gates U_1, U_2, and U_3.

Simulating the remaining non-unitary dissipative dynamics can be achieved by simulating discrete-time unitary dynamics on an extended system where ancillary degrees of freedom mimic a dissipative environment. In fact, this environment can be modeled by s single resetable qubit [LV01].

Using a quantum circuit compatible with the current NISQ computers, the authors performed a digital quantum simulation of quantum synchronization dynamics on the IBM Q System and experimentally demonstrate typical features of quantum synchronization, such as observing non-zero phase distribution and coherence dynamics proportional to driving.

8.3 Simulation of driven QHO on IBM-Q

Besides observing quantum synchronization in spin systems, quantum oscillator is another venue where synchronization can occur. However, due to the discrete nature of current quantum computing architecture based on qubits, simulations of quantum harmonic oscillators (QHO) remain challenging. In a recent work [BKBP19], the authors demonstrated a quantum simulation of QHO in the presence of both time-varying and constant force field for both one and two dimensional case. Though this work is not directly related to quantum synchronization, it is an important step towards the possibility of digital simulation of synchronization involving oscillators, especially on NISQ hardwares.

A two-qubit system is implemented to simulate a driven quantum harmonic oscillator with Hamiltonian:

$$\hat{H} = \omega\hat{a}^\dagger\hat{a} + F(t)(\hat{a} + \hat{a}^\dagger), \tag{8.8}$$

where ω_0 is the natural frequency of the oscillator, $F(t) \propto \cos(\Omega t + \phi)$ with driving frequency Ω and phase ϕ. The lowest four energy states of the QHO are encoded into the four two-qubit product states: $|00\rangle, |01\rangle, |10\rangle, |11\rangle$. Under this encoding, the creation operator $\hat{a}^\dagger$ can be mapped to a single qubit rotation, followed by a two-qubit

operation: $(I \otimes X)_{12}(CNOT)_{21}$, and similarly the annihilation operator $\hat{a}$ mapped to $(I \otimes X)_{12}(ACNOT)_{21}$, with $ACNOT$ denotes the anti-controlled-NOT operation.

Such method for simulating a QHO can only be justified under assumption of low excitations. For higher levels of QHO, the requirement for the number of qubits grow dramatically, and the circuit complexity increases as well, which poses another hurdle on quantum error correction. However, with the current NISQ hardware available, the digital simulation of a quantum Stuart-Landau oscillator (in deep quantum limit) could be made possible by combining the techniques demonstrated in 8.2 and 8.3.

Chapter 9

Outlook

The study of quantum synchronization in the context of circuit QED has opened up exciting avenues for both fundamental research and practical applications in the field of quantum information processing. As we conclude this thesis on quantum synchronization in circuit QED, it is crucial to highlight the potential directions for future investigations and developments in this rapidly evolving field.

Experimental Realization and Verification

One important avenue for future research is the experimental realization and verification of the synchronization phenomena explored in this thesis. Advancements in circuit QED technology and experimental techniques offer the potential to implement and observe various synchronization regimes in coupled quantum systems. Experimentalists can explore different physical platforms, optimize parameters, and devise novel measurement schemes to probe and characterize quantum synchronization in circuit QED systems with increasing precision and control.

Many-body Synchronization

Extending the study of quantum synchronization to many-body systems is another promising direction. Investigating the emergence and properties of synchronization in larger networks of coupled qubits can reveal new insights into collective dynamics, quantum correlations, and the interplay between classical and quantum effects. Understanding and harnessing synchronization in multi-qubit systems will have significant implications for quantum computation, communication, and quantum simulation. One interesting top worth investigating is the topological synchronization in large networks, where the power of topology can give rise to non-trival collective behaviours.

Novel oscillator models

The development and exploration of novel oscillator models offer promising advances in our understanding of synchronization phenomena in circuit QED systems. The study of synchronization in these novel oscillator models can unveil new synchronization phenomena, uncover novel types of phase transitions, and shed light on the interplay between different degrees of freedom in complex quantum systems. The insights gained from these investigations can lead to the development of innovative synchronization-based quantum devices and technologies, and further enrich our understanding of quantum dynamics.

Synchronization-based Quantum Information Processing

Quantum synchronization phenomena can be exploited for novel quantum information processing tasks. Exploring the potential applications of synchronization in tasks such as quantum communication, quantum metrology, and quantum sensing can lead to significant advancements in these areas. Developing synchronization-based protocols and algorithms for quantum information processing could enhance the efficiency, robustness, and security of quantum technologies.

Noise and Decoherence Effects

Quantum systems are inevitably subject to noise and decoherence, which can significantly impact synchronization dynamics. Investigating the effects of noise and decoherence on quantum synchronization in circuit QED systems is an important avenue for future research. Understanding how synchronization phenomena are affected by these detrimental factors and developing strategies to mitigate their impact will be crucial for practical implementation and scalability of synchronization-based quantum technologies.

Theoretical Advances and Analytical Tools

Advancing theoretical models, analytical techniques, and numerical simulations will be instrumental in deepening our understanding of quantum synchronization in circuit QED. Developing new theoretical frameworks, investigating novel synchronization measures, and establishing connections with other areas of physics can lead to breakthroughs in our understanding of synchronization phenomena and their broader implications.

In conclusion, the study of quantum synchronization in circuit QED offers immense

potential for advancing our understanding of complex quantum dynamics, as well as for practical applications in quantum information processing. The outlook for future research in this field is bright, with opportunities for experimental advancements, theoretical developments, and interdisciplinary collaborations. By further exploring and harnessing quantum synchronization in circuit QED, we can pave the way for transformative advancements in quantum technologies and unlock new frontiers in quantum information science.

Appendix A

Quantum computing

Quantum computing exploits phenomena of quantum nature, such as superposition, interference, and entanglement, to provide beyond-classical computational resources.

NISQ stands for Noisy Intermediate-Scale Quantum computers. The term "noisy" refers to the fact that current quantum computing technologies are still prone to errors due to various sources of noise, such as decoherence and imperfect control of quantum systems. The term "intermediate-scale" refers to the size of the quantum computers that are currently available, which are larger than the few-qubit devices of the early days of quantum computing, but smaller than the fault-tolerant, error-corrected devices that are predicted to be possible with advances in technology.

The term "NISQ" was coined by John Preskill to describe the era of quantum computing that we are currently in [Pre18]. During this era, quantum computers are expected to have a limited number of qubits and a limited coherence time, but they can still perform useful computations beyond what is possible with classical computers. NISQ devices are expected to be useful for quantum simulation, quantum chemistry, optimization problems, and machine learning.

The NISQ era is characterized by the need for new algorithms and techniques that are specifically designed to work with noisy intermediate-scale quantum devices. These algorithms and techniques often involve a combination of classical and quantum computations, and they take into account the limitations of current quantum hardware. Researchers are actively working to develop new NISQ algorithms and to explore the potential applications of NISQ devices.

A.1 NISQ hardwares

As the circuit QED platform has been discussed extensively in the main text, the other mainstream platforms are described in the following:

Trapped ions

Trapped-ion quantum computing is a type of quantum computing that utilizes ions trapped in an electromagnetic field as qubits [CZ95, BCMS19, BCO23]. This approach to quantum computing offers certain advantages such as long coherence times and high-fidelity quantum gate operations.

In a trapped-ion system, ions are trapped and isolated from their environment using electromagnetic fields generated by specialized devices called ion traps. The most common types are the Paul trap and the Penning trap. The trapped ions are typically held in a vacuum chamber to minimize interactions with other particles and to maintain their quantum states for coherence time. Laser beams are used to manipulate the ions and create entangled states, which are essential for quantum computation. The entangled states are created by applying a sequence of laser pulses to the ions, which causes them to interact with each other and become entangled.

However, they require a complex system of lasers and vacuum chambers to operate, and they are more difficult to scale up than other technologies like superconducting qubits. Their operational speed is also much slower than other quantum computing architectures. Despite these challenges, researchers continue to explore the potential of trapped-ion qubits for building practical quantum computers.

semiconductor spin qubits

Semiconductor spin qubits are another type of quantum computing architecture that utilizes the intrinsic spin of electrons in semiconductor materials to represent and manipulate quantum information [Kan98, LD98]. In this architecture, qubits are encoded in the spin states of individual electrons confined in quantum dots or donor atoms embedded in the semiconductor. Quantum dots are nanoscale structures that can trap single electrons, while donor atoms are impurities in the semiconductor lattice that can bind an extra electron. The electron's spin can be in one of two states, commonly denoted as "spin up" and "spin down," which correspond to the basis states of a qubit.

Semiconductor spin qubits offer several advantages, such as they are compatible with existing semiconductor technology, which makes them easier to integrate and scale with existing electronics. They also have relatively long coherence times, which means that they can maintain quantum states for longer periods of time, allowing for more complex quantum operations.

However, there are also challenges associated with semiconductor spin qubits. For example, manipulating and controlling individual electron spins with high fidelity can be challenging, particularly when qubits are closely spaced. Semiconductor spin qubits can be sensitive to various noise sources, such as electric and magnetic field fluctuations or charge noise from nearby defects, which can limit their coherence times and gate fidelities.

photonic qubits

Photonic qubits are another technology used to build quantum computers [TF19]. Photonic quantum computers leverage the unique properties of photons, such as their weak interaction with the environment and the ability to encode quantum information in various degrees of freedom, to perform quantum operations and store quantum information.

In a photonic quantum computer, quantum information can be encoded in various properties of photons, such as their polarization, path, time-bin, or orbital angular momentum. Single qubit operations can be efficiently achieved using linear optical elements, such as beam splitters, wave plates, and phase shifters. Multi-qubit operations are typically performed using nonlinear interactions, such as Hong-Ou-Mandel interference and nonlinear crystals, which are not idealy deterministic.

The advantages of photonic quantum computers include low decoherence, especially due to the fact that photons only interact very weakly to the environment. Also it operates under room temperature, which make it favorable for large scale on-chip integration.

However, there are also challenges associated with photonic qubits. Apart from the non-deterministic gates mentioned above, due to difficulties in photon detection, performing measurements in photonic regime is problematic and may introduce extra noise into the computation.

quantum error correction

Quantum error correction [Got97, Got09, LB13] is a set of techniques used to protect quantum information from errors caused by the noise and decoherence in quantum systems. Unlike classical information, which can be copied and read without being disturbed, quantum information is inherently fragile and susceptible to errors due to the quantum nature of the system and cannot be copied with unit fidelity (no-cloning theorem).

Quantum error correction is based on the principle of redundancy, where multiple copies of a quantum state are stored and processed in a way that allows errors to be detected and corrected. The basic idea is to encode the quantum information into a larger number of qubits, and to use quantum operations to detect and correct errors that occur during the computation.

The effectiveness of quantum error correction depends on the quality of the quantum codes used, as well as the quality of the quantum operations used for error detection and correction. The development of practical quantum error correction techniques is an active area of research, and is essential for the development of large-scale fault-tolerant quantum computers.

Stablizer codes

The stabilizer formalism is a mathematical framework used in quantum computing to describe and efficiently simulate certain types of quantum states and quantum operations. It is particularly well-suited for representing quantum error-correcting codes and studying fault-tolerant quantum computation.

The surface code [FMMC12, Cle22, AAA+23] is an error-detecting code that embeds some concepts from topology. There are two main parts to the surface code: A geometric layout for the individual physical qubits, and a sequence of operations that are carried out in a continuous cycle with these qubits. The combination of these two parts leads to an error-protected "fabric" in which errors can still occur, but are corrected with exponentially growing probability as the number of physical qubits is increased (as long as the operations that make up the continuous cycle are performed above a certain level of fidelity). Logical qubits can then be defined in this fabric, with size of the logical qubits (the area of the fabric, or equivalently the number of physical qubits involved) determined by the rate at which errors occur in the physical qubits and the rate of errors that can be tolerated at the logical level. The rate at which logical qubit errors can be tolerated depends on the computational problem.

Quantum Low Density Parity Check (QLDPC) [BBA+15], also called a sparse quantum code, is another type of stablizer code. Member of a family of $[n, k, d]$ modular-qudit or Galois-qudit stabilizer codes for which the number of sites participating in each stabilizer generator and the number of stabilizer generators that each site participates in are both bounded by a constant as $n \to \infty$. A geometrically local stabilizer code is a QLDPC code where the sites involved in any syndrome bit are contained in a fixed volume that does not scale with n . As opposed to general stabilizer codes, syndrome

extraction of the constant-weight check operators of a QLDPC codes can be done using a constant-depth circuit.

Bosonic qubits

The cat qubits [LKV+13, MLA+14, OPH+16, Mir16, PGCI+19] uses the infinite dimensional Hilbert space to redundantly encode quantum information. The power of this idea lies in the fact that the dominant decoherence channel in a cavity is photon damping, and no extra decay channels are added if we increase the number of photons we insert in the cavity. Hence, only a single error syndrome needs to be measured to identify if an error has occurred or not. A qubit encoded in a four-component Schrödinger cat state is represented as $|\Phi^0\rangle = c_0|0\rangle_L + c_1|1\rangle_L = c_0|\mathcal{C}_\alpha^{0mod4}\rangle + c_1|\mathcal{C}_\alpha^{2mod4}\rangle$, where

$$
\begin{aligned}
|\mathcal{C}_\alpha^{0mod4}\rangle &\propto |\alpha\rangle + |-\alpha\rangle + |i\alpha\rangle + |-i\alpha\rangle, \\
|\mathcal{C}_\alpha^{1mod4}\rangle &\propto |\alpha\rangle - |-\alpha\rangle - |i\alpha\rangle + |-i\alpha\rangle, \\
|\mathcal{C}_\alpha^{2mod4}\rangle &\propto |\alpha\rangle + |-\alpha\rangle - |i\alpha\rangle - |-i\alpha\rangle, \\
|\mathcal{C}_\alpha^{3mod4}\rangle &\propto |\alpha\rangle - |-\alpha\rangle + |i\alpha\rangle - |-i\alpha\rangle.
\end{aligned} \tag{A.1}
$$

The GKP code [GKP01, CIET+20, GP21] is another QEC code that encodes a qubit in the continuous-variable state of a quantum harmonic oscillator. The idea is to create a "grid" in the phase space (position-momentum space) of the oscillator, where each cell in the grid corresponds to a distinct logical qubit state. The two logical states of the qubit are represented by superpositions of position and momentum eigenstates that are centered on the grid points. The stabilizers of the canonical square grid-state code are $S_a = D(a = 2\sqrt{\pi})$ and $S_b = D(b = 2i\sqrt{\pi})$, and the Pauli operators are $X = D(a/2), Z = D(b/2)$ and $Y = D((a+b)/2)$, where $D(\cdot)$ is the displacement operator. There are other GKP codes with a different grid formation, for example hexgonal code.

A.2 NISQ algorithms

Although a fully universal quantum computer is yet to come, NISQ-level quantum processors already exisit and are available. In the search for achieving quantum advantage with these devices, algorithms have been proposed for applications in various disciplines spanning physics, machine learning, quantum chemistry, and combinatorial optimization [BCLK+22].

Deutsch-Jozsa algorithm

The Deutsch-Jozsa algorithm is a quantum algorithm that solves a special type of problem called the "oracle problem". The oracle problem involves determining whether an unknown function is balanced (i.e., maps half of the possible inputs to 0 and half to 1) or constant (i.e., maps all inputs to either 0 or 1).

The algorithm is named after its inventors, David Deutsch and Richard Jozsa, who developed it in 1992. The algorithm uses a quantum computer to determine the nature of the unknown function with just one query to the function, whereas a classical computer would require two queries in the worst case.

The Deutsch-Jozsa algorithm works by first preparing a quantum register in a superposition of all possible input values. This is done using a series of Hadamard gates. The quantum register is then passed through the unknown function, which is represented by a black box oracle. The oracle maps each input to either 0 or 1, and the output is stored in a separate quantum register.

Next, another series of Hadamard gates is applied to the first quantum register, which allows us to measure the state of the second register and determine whether the unknown function is balanced or constant. If the output of the second register is all 0s, the function is constant, whereas if the output is a non-zero value, the function is balanced.

The Deutsch-Jozsa algorithm provides a quadratic speedup over classical algorithms for solving the oracle problem, which has important implications for cryptography and other areas of computer science.

Grover's algorithm

Grover's algorithm is a quantum algorithm for searching an unsorted database of N items. Grover's algorithm provides a quadratic speedup over classical search algorithms, making it one of the foundational quantum algorithms that demonstrates the potential power of quantum computing. In the context of an unsorted database with N elements, Grover's algorithm can find the target element with a high probability using only $O(\sqrt{N})$ iterations, whereas a classical search algorithm would require $O(N)$ iterations on average to find the target element.

The main steps of Grover's algorithm are as follows:

1. Initialization: Prepare an equal superposition of all possible computational basis states using an n-qubit quantum register, where $N = 2^n$. This can be achieved

by applying a Hadamard gate (H) to each qubit.

2. Oracle operation: Apply an oracle function (a unitary transformation) that flips the sign of the amplitude of the state corresponding to the target element (also known as the marked element). The oracle function encodes the problem-specific information, and its design depends on the problem being solved.

3. Diffusion operation (amplitude amplification): Perform an operation that amplifies the amplitude of the target state while decreasing the amplitudes of the other states. This is achieved using the following steps:

   (a) Apply a Hadamard gate to each qubit.

   (b) Apply a conditional phase shift, which flips the sign of the amplitude of every state except the all-zero state $|0...0\rangle$.

   (c) Apply a Hadamard gate to each qubit again.

4. Iteration: Repeat steps 2 and 3 approximately $\sqrt{N}$ times to maximize the probability of measuring the target state. The exact number of iterations for optimal probability depends on the problem and can be estimated using techniques such as the Grover iterate.

5. Measurement: Measure the quantum register in the computational basis. The measured state with the highest probability will correspond to the target element.

Bernstein-Vazirani algorithm

The Bernstein-Vazirani algorithm is a quantum algorithm that solves a classical problem of determining the hidden bit string in a black box function. The algorithm was developed by Ethan Bernstein and Umesh Vazirani in 1993 and has important implications for cryptography and other areas of computer science.

The problem addressed by the algorithm is as follows: Suppose there is a black box function f(x) that takes as input a binary string x of length n and returns a single bit, either 0 or 1. The function is implemented in such a way that the output is equal to the inner product of x and a hidden binary string s of length n, modulo 2, i.e., f(x) = sx mod 2, where sx represents the inner product of s and x. The goal of the problem is to determine the hidden bit string s using the minimum possible number of queries to the function f(x).

The Bernstein-Vazirani algorithm solves this problem using a quantum computer. It prepares a superposition of all possible input strings using a series of Hadamard gates,

applies the black box function f(x), and measures the output. The algorithm then applies another set of Hadamard gates to the input qubits, which allows it to extract the hidden bit string s with high probability using a single query to the black box function.

The key insight behind the algorithm is that the Hadamard gates create a superposition of all possible input strings, which allows the algorithm to extract information about the hidden bit string s from a single query to the black box function. By contrast, a classical computer would need to query the function multiple times to extract this information.

The Bernstein-Vazirani algorithm has important implications for cryptography, where it can be used to break certain types of classical encryption schemes, such as the one-time pad. It also has implications for optimization and machine learning, where it can be used to speed up certain types of calculations.

Simon's algorithm

Simon's algorithm is a quantum algorithm developed by Daniel Simon in 1994 that solves a classical problem in computational complexity theory known as the Simon problem. The problem involves finding a hidden period of a black box function, which has important implications for cryptography and other areas of computer science.

The Simon problem is as follows: Suppose there is a black box function f(x) that takes as input a binary string x of length n and returns a binary string of length n, such that f(x) = f(y) if and only if $y = x \oplus s$, where s is a fixed, unknown binary string of length n/2, and $\oplus$ denotes bitwise XOR. The goal of the problem is to determine the hidden string s using the minimum possible number of queries to the function f(x).

Simon's algorithm solves this problem using a quantum computer. It prepares a superposition of all possible input strings using a series of Hadamard gates, applies the black box function f(x), and measures the output. The algorithm then applies a quantum Fourier transform to the measured output to extract information about the hidden string s.

The key insight behind the algorithm is that the superposition of all possible input strings can be used to obtain linearly independent equations that involve the hidden string s. By applying the quantum Fourier transform to these equations, the algorithm can extract information about the hidden string s with high probability using a polynomial number of queries to the black box function.

The Simon algorithm has important implications for cryptography, where it can be used to break certain types of classical encryption schemes, such as the ones based on the discrete logarithm problem and the elliptic curve discrete logarithm problem. It also has implications for quantum computing, where it can be used as a subroutine in other quantum algorithms, such as Shor's algorithm for factoring large numbers.

Quantum Fourier transform(QFT)

The Quantum Fourier Transform (QFT) is the quantum analogue of the classical Discrete Fourier Transform (DFT). It is an essential subroutine in many quantum algorithms, such as Shor's algorithm for factoring large numbers and quantum phase estimation. The QFT allows for the efficient transformation of a quantum state from one basis to another, namely from the computational basis to the Fourier basis.

Mathematically, the QFT is defined as a unitary transformation that maps an n-qubit computational basis state $|x\rangle$ to the Fourier basis state as follows:

$$QFT|x\rangle = \frac{1}{\sqrt{N}} \sum_{y=0}^{N-1} e^{2\pi i x y/N} |y\rangle, \tag{A.2}$$

where $N = 2^n$, and x, y are integers between 0 and $N - 1$.

The QFT is performed using a combination of Hadamard gates (H) and controlled phase rotation gates, which are applied to the n qubits in a specific order. The circuit implementation of QFT can be expressed as:

1. Apply a Hadamard gate to the first qubit.
2. Apply controlled phase rotation gates to the first qubit, with each subsequent qubit acting as a control qubit and with phase angles of $\pi/2, \pi/4, \pi/8, ..., \pi/2^{(n-1)}$, respectively.
3. Repeat steps 1-2 for each remaining qubit, but reduce the number of phase rotation gates applied by one for each successive qubit.
4. Perform a swap operation on the qubits at opposite ends of the register and work inwards, swapping qubits until the center of the register is reached (this step is required to reverse the order of the qubits).
5. The QFT circuit has a complexity of $O(n^2)$ quantum gates, which is significantly faster than the classical DFT, which has a complexity of $O(nlogn)$ using the Fast Fourier Transform (FFT) algorithm.

The QFT is a fundamental building block of many quantum algorithms and is an essential tool for quantum computing and quantum information processing. It enables the efficient manipulation of quantum states and has important implications for the development of practical quantum technologies.

Shor's algorithm

Shor's algorithm [Sho94] is a quantum algorithm that is used to factor large numbers efficiently. It was developed by mathematician Peter Shor in 1994 and has important implications for cryptography and other areas of computer science.

The problem of factoring large numbers is considered to be difficult for classical computers, as the time required to factor a number using the best known classical algorithms increases exponentially with the size of the number. Shor's algorithm uses a quantum computer to factor large numbers efficiently in polynomial time.

The algorithm works by first preparing a superposition of all possible values of the number to be factored using quantum parallelism. This is done using a quantum Fourier transform, which is a key component of many quantum algorithms. The algorithm then applies a modular exponentiation function to the superposition state, which is designed to extract information about the factors of the number.

The information obtained from the modular exponentiation is then used to find the factors of the number using a classical algorithm called the continued fractions algorithm. The continued fractions algorithm is used to find the factors by solving a set of linear equations that are derived from the information obtained from the modular exponentiation.

Shor's algorithm has important implications for cryptography, as it can be used to break certain types of classical encryption schemes, such as the ones based on the RSA algorithm. It also has implications for quantum computing, where it can be used as a subroutine in other quantum algorithms, such as quantum simulations and quantum chemistry.

One of the main challenges in implementing Shor's algorithm is the requirement for a large number of qubits and the need for error correction to maintain the coherence of the quantum states. However, advances in quantum hardware and error correction techniques have made it possible to implement the algorithm on small-scale quantum computers.

HHL algorithm

The HHL algorithm [HHL09], named after its creators Harrow, Hassidim, and Lloyd, is a quantum algorithm designed to solve systems of linear equations efficiently. The HHL algorithm can be applied to various problems, such as optimization, machine learning, and data processing, where solving linear systems is a core component.

The problem of solving linear systems of equations is considered to be an important problem in computational science and engineering, with many applications in areas such as signal processing, machine learning, and physics. The traditional classical algorithms for solving linear systems of equations have a runtime that is at least quadratic in the size of the system, which makes them impractical for large-scale problems.

The HHL algorithm is a quantum algorithm that can solve linear systems of equations efficiently using a quantum computer. The algorithm works by encoding the matrix A and the vector b into quantum states and then performing a series of quantum operations to solve for the unknown vector x.

The algorithm works by first preparing a quantum state that encodes the matrix A and the vector b. The quantum state is then manipulated using a set of quantum gates to obtain a state that encodes the solution vector x. The quantum gates used in the algorithm include quantum phase estimation, quantum linear systems solving, and quantum measurements.

The HHL algorithm has important implications for quantum machine learning and quantum optimization, where solving linear systems of equations is a fundamental problem. However, the algorithm is currently limited by the need for a large number of qubits and the need for error correction to maintain the coherence of the quantum states. Nevertheless, the algorithm is an important step towards the development of practical quantum computing technologies.

Variational quantum eigensolver

The Variational Quantum Eigensolver (VQE) is a quantum algorithm that is used to find the ground state energy of a given molecule. The ground state energy is the lowest possible energy state of a molecule, and it is an important quantity in chemistry, as it provides information about the stability and properties of the molecule.

VQE is a hybrid algorithm that combines classical and quantum computing. The algorithm works by first encoding the problem of finding the ground state energy of

a molecule into a quantum circuit. This circuit is then run on a quantum computer, which produces an output state that approximates the ground state of the molecule.

The output state is then measured, and the resulting measurements are used to compute an estimate of the energy of the molecule. This energy estimate is then fed back into the circuit, which is updated to produce a new output state that is closer to the true ground state energy. This process is repeated until the energy estimate converges to a minimum value, which corresponds to the ground state energy of the molecule.

The VQE algorithm is a powerful tool for studying molecular properties because it can be used to find the ground state energy of molecules that are too large to simulate using classical computers. Additionally, VQE can be adapted to solve optimization problems by constructing a Hamiltonian that represents the cost function of the problem. By finding the ground state energy of this Hamiltonian, VQE essentially finds the optimal solution to the optimization problem [MBB+18]. VQE can be used to compute the kernel matrix in quantum machine learning algorithms based on kernel methods, such as support vector machines or kernel ridge regression. By constructing a Hamiltonian that represents the inner products of data points in a high-dimensional feature space, VQE can be used to estimate the kernel matrix elements efficiently. VQE is also proven to be capable of performing quantum search [Liu23].

Quantum approximate optimization algorithm (QAOA)

The Quantum Approximate Optimization Algorithm (QAOA) is a quantum algorithm for solving combinatorial optimization problems. It was introduced by Farhi, Goldstone, and Gutmann in 2014.

Combinatorial optimization problems are those where the objective is to find the optimal combination of variables that satisfy certain constraints. Examples of such problems include the traveling salesman problem and the max-cut problem.

The QAOA algorithm is designed to solve such problems by mapping them to a Hamiltonian, which is a mathematical representation of the energy of a quantum system. The Hamiltonian is constructed using a set of objective and constraint functions that describe the problem.

The algorithm then applies a sequence of quantum gates to the quantum state of the system, which evolves the system towards the ground state of the Hamiltonian. The ground state of the Hamiltonian corresponds to the optimal solution of the original

combinatorial optimization problem.

The QAOA algorithm is a hybrid algorithm, meaning that it combines classical and quantum computations. The classical part of the algorithm involves optimizing the parameters of the quantum gates in order to minimize the energy of the system. This optimization problem can be solved using classical optimization algorithms.

The QAOA algorithm has important implications for a wide range of applications in areas such as finance, logistics, and transportation. However, the algorithm is currently limited by the need for a large number of qubits and the need for error correction to maintain the coherence of the quantum states. Nevertheless, the algorithm is an important step towards the development of practical quantum computing technologies.

References

[AAA+23] Rajeev Acharya, Igor Aleiner, Richard Allen, Trond I. Andersen, Markus Ansmann, Frank Arute, Kunal Arya, Abraham Asfaw, Juan Atalaya, Ryan Babbush, Dave Bacon, Joseph C. Bardin, Joao Basso, Andreas Bengtsson, Sergio Boixo, Gina Bortoli, Alexandre Bourassa, Jenna Bovaird, Leon Brill, Michael Broughton, Bob B. Buckley, David A. Buell, Tim Burger, Brian Burkett, Nicholas Bushnell, Yu Chen, Zijun Chen, Ben Chiaro, Josh Cogan, Roberto Collins, Paul Conner, William Courtney, Alexander L. Crook, Ben Curtin, Dripto M. Debroy, Alexander Del Toro Barba, Sean Demura, Andrew Dunsworth, Daniel Eppens, Catherine Erickson, Lara Faoro, Edward Farhi, Reza Fatemi, Leslie Flores Burgos, Ebrahim Forati, Austin G. Fowler, Brooks Foxen, William Giang, Craig Gidney, Dar Gilboa, Marissa Giustina, Alejandro Grajales Dau, Jonathan A. Gross, Steve Habegger, Michael C. Hamilton, Matthew P. Harrigan, Sean D. Harrington, Oscar Higgott, Jeremy Hilton, Markus Hoffmann, Sabrina Hong, Trent Huang, Ashley Huff, William J. Huggins, Lev B. Ioffe, Sergei V. Isakov, Justin Iveland, Evan Jeffrey, Zhang Jiang, Cody Jones, Pavol Juhas, Dvir Kafri, Kostyantyn Kechedzhi, Julian Kelly, Tanuj Khattar, Mostafa Khezri, Mária Kieferová, Seon Kim, Alexei Kitaev, Paul V. Klimov, Andrey R. Klots, Alexander N. Korotkov, Fedor Kostritsa, John Mark Kreikebaum, David Landhuis, Pavel Laptev, Kim-Ming Lau, Lily Laws, Joonho Lee, Kenny Lee, Brian J. Lester, Alexander Lill, Wayne Liu, Aditya Locharla, Erik Lucero, Fionn D. Malone, Jeffrey Marshall, Orion Martin, Jarrod R. McClean, Trevor McCourt, Matt McEwen, Anthony Megrant, Bernardo Meurer Costa, Xiao Mi, Kevin C. Miao, Masoud Mohseni, Shirin Montazeri, Alexis Morvan, Emily Mount, Wojciech Mruczkiewicz, Ofer Naaman, Matthew Neeley, Charles Neill, Ani Nersisyan, Hartmut Neven, Michael Newman, Jiun How Ng, Anthony Nguyen, Murray Nguyen, Murphy Yuezhen Niu, Thomas E. O'Brien, Alex Opremcak, John Platt, Andre Petukhov, Rebecca Potter, Leonid P. Pryadko, Chris Quintana, Pedram Roushan, Nicholas C. Rubin, Negar Saei, Daniel Sank, Kannan

Sankaragomathi, Kevin J. Satzinger, Henry F. Schurkus, Christopher Schuster, Michael J. Shearn, Aaron Shorter, Vladimir Shvarts, Jindra Skruzny, Vadim Smelyanskiy, W. Clarke Smith, George Sterling, Doug Strain, Marco Szalay, Alfredo Torres, Guifre Vidal, Benjamin Villalonga, Catherine Vollgraff Heidweiller, Theodore White, Cheng Xing, Z. Jamie Yao, Ping Yeh, Juhwan Yoo, Grayson Young, Adam Zalcman, Yaxing Zhang, Ningfeng Zhu, and Google Quantum AI. Suppressing quantum errors by scaling a surface code logical qubit. *Nature*, 614(7949):676–681, Feb 2023.

[ACG+15] Dario Antonio, David A Czaplewski, Jeffrey R Guest, Daniel López, Sebastián I Arroyo, and Damián H Zanette. Nonlinearity-Induced Synchronization Enhancement in Micromechanical Oscillators. *Physical Review Letters*, 114(3):034103, 2015.

[AEAM+15] V Ameri, M Eghbali-Arani, A Mari, A Farace, F Kheirandish, V Giovannetti, and R Fazio. Mutual information as an order parameter for quantum synchronization. *Physical Review A*, 91(1):012301, 2015.

[AEK90] D.G. Aronson, G.B. Ermentrout, and N. Kopell. Amplitude response of coupled oscillators. *Physica D*, 41(3):403–449, 1990.

[AKLB18] Ehud Amitai, Martin Koppenhöfer, Niels Lörch, and Christoph Bruder. Quantum effects in amplitude death of coupled anharmonic self-oscillators. *Phys. Rev. E*, 97:052203, May 2018.

[ANNVLF15] Ulrik L Andersen, Jonas S Neergaard-Nielsen, Peter Van Loock, and Akira Furusawa. Hybrid discrete-and continuous-variable quantum information. *Nat. Phys.*, 11(9):713–719, 2015.

[App22] Edward Victor Appleton. Automatic synchronization of triode oscillators. In *Proc. Cambridge Phil. Soc*, volume 21, page 1923, 1922.

[ARE12] S. Agarwal, S. M. Hashemi Rafsanjani, and J. H. Eberly. Tavis-Cummings model beyond the rotating wave approximation: Quasidegenerate qubits. *Phys. Rev. A*, 85:043815, Apr 2012.

[AVK66] A.A. ANDRONOV, A.A. VITT, and S.E. KHAIKIN. CHAPTER II - NON-LINEAR CONSERVATIVE SYSTEMS. In *Theory of Oscillators*, Adiwes International Series in Physics, pages 74–145. Pergamon, 1966.

[BACL21] Lior Ben Arosh, M. C. Cross, and Ron Lifshitz. Quantum limit cycles and the Rayleigh and van der Pol oscillators. *Phys. Rev. Research*, 3:013130, Feb 2021.

[BB21] Biswabibek Bandyopadhyay and Tanmoy Banerjee. Revival of oscillation and symmetry breaking in coupled quantum oscillators. *Chaos*, 31(6):063109, 2021.

[BBA05] R Barak and Y Ben-Aryeh. Non-orthogonal positive operator valued measure phase distributions of one-and two-mode electromagnetic fields. *Journal of Optics B: Quantum and Semiclassical Optics*, 7(5):123, 2005.

[BBA+15] Zunaira Babar, Panagiotis Botsinis, Dimitrios Alanis, Soon Xin Ng, and Lajos Hanzo. Fifteen years of quantum LDPC coding and improved decoding strategies. *iEEE Access*, 3:2492–2519, 2015.

[BBJ22] Berislav Buča, Cameron Booker, and Dieter Jaksch. Algebraic theory of quantum synchronization and limit cycles under dissipation. *SciPost Phys.*, 12:097, 2022.

[BCBS16] Daniel Braak, Qing-Hu Chen, Murray T Batchelor, and Enrique Solano. Semi-classical and quantum Rabi models: in celebration of 80 years. *J. Phys. A: Math. Theor.*, 49(30):300301, jun 2016.

[BCLK+22] Kishor Bharti, Alba Cervera-Lierta, Thi Ha Kyaw, Tobias Haug, Sumner Alperin-Lea, Abhinav Anand, Matthias Degroote, Hermanni Heimonen, Jakob S. Kottmann, Tim Menke, Wai-Keong Mok, Sukin Sim, Leong-Chuan Kwek, and Alán Aspuru-Guzik. Noisy intermediate-scale quantum algorithms. *Reviews of Modern Physics*, 94(1):015004, 2022.

[BCMS19] Colin D. Bruzewicz, John Chiaverini, Robert McConnell, and Jeremy M. Sage. Trapped-ion quantum computing: Progress and challenges. *Applied Physics Reviews*, 6(2):021314, 2019.

[BCO23] Francesco Bernardini, Abhijit Chakraborty, and Carlos Ordóñez. Quantum computing with trapped ions: a beginner's guide, 2023.

[BGGW21] Alexandre Blais, Arne L. Grimsmo, S. M. Girvin, and Andreas Wallraff. Circuit quantum electrodynamics. *Rev. Mod. Phys.*, 93:025005, May 2021.

[BGO20] Alexandre Blais, Steven M. Girvin, and William D. Oliver. Quantum information processing and quantum optics with circuit quantum electrodynamics. *Nature Physics*, pages 1–10, 2020.

[BGW+07] Alexandre Blais, Jay Gambetta, A. Wallraff, D. I. Schuster, S. M. Girvin, M. H. Devoret, and R. J. Schoelkopf. Quantum-information processing with circuit quantum electrodynamics. *Phys. Rev. A*, 75(3):032329, 3 2007.

[BJPS09] Alexander Balanov, Natalia Janson, Dmitry Postnov, and Olga Sosnovtseva. *From Simple to Complex*. Springer, 2009.

[BKB21] Biswabibek Bandyopadhyay, Taniya Khatun, and Tanmoy Banerjee. Quantum Turing bifurcation: Transition from quantum amplitude death to quantum oscillation death. *Phys. Rev. E*, 104:024214, Aug 2021.

[BKBB20] Biswabibek Bandyopadhyay, Taniya Khatun, Debabrata Biswas, and Tanmoy Banerjee. Quantum manifestations of homogeneous and inhomogeneous oscillation suppression states. *Phys. Rev. E*, 102:062205, Dec 2020.

[BKBP19] Alakesh Baishya, Lingraj Kumar, Bikash K. Behera, and Prasanta K. Panigrahi. Experimental Demonstration of Force Driven Quantum Harmonic Oscillator in IBM Quantum Computer, 2019.

[BMS+17] Jochen Braumüller, Michael Marthaler, Andre Schneider, Alexander Stehli, Hannes Rotzinger, Martin Weides, and Alexey V Ustinov. Analog quantum simulation of the Rabi model in the ultra-strong coupling regime. *Nature communications*, 8(1):779, 2017.

[BOZ+15] V. M. Bastidas, I. Omelchenko, A. Zakharova, E. Schöll, and T. Brandes. Quantum signatures of chimera states. *Phys. Rev. E*, 92:062924, Dec 2015.

[BP02] H.-P. Breuer and F. Petruccione. *The Theory of Open Quantum Systems*. Oxford University Press, 2002.

[Bra01] D. Braun. *Dissipative Quantum Chaos and Decoherence*. (Springer, Berlin, Heidelberg), 2001.

[Bra11] D. Braak. Integrability of the Rabi Model. *Phys. Rev. Lett.*, 107(10):100401, 2011.

[BT11] Hendrik Wolter Broer and Floris Takens. *Dynamical systems and chaos*, volume 172. Springer, 2011.

[CA86] David Ceperley and Berni Alder. Quantum Monte Carlo. *Science*, 231(4738):555–560, 1986.

[Cam87] David K Campbell. Nonlinear science. *Los Alamos Science*, 15:218–262, 1987.

[Car09] Howard Carmichael. *An open systems approach to quantum optics: lectures presented at the Université Libre de Bruxelles, October 28 to November 4, 1991*, volume 18. Springer Science & Business Media, 2009.

[CFWD01] JC Chedjou, HB Fotsin, P Woafo, and S Domngang. Analog simulation of the dynamics of a van der Pol oscillator coupled to a Duffing oscillator. *IEEE Transactions on Circuits and Systems I: Fundamental Theory and Applications*, 48(6):748–757, 2001.

[CIET+20] P. Campagne-Ibarcq, A. Eickbusch, S. Touzard, E. Zalys-Geller, N. E. Frattini, V. V. Sivak, P. Reinhold, S. Puri, S. Shankar, R. J. Schoelkopf, L. Frunzio, M. Mirrahimi, and M. H. Devoret. Quantum error correction of a qubit encoded in grid states of an oscillator. *Nature*, 584(7821):368–372, 2020.

[CIZGN+18] P. Campagne-Ibarcq, E. Zalys-Geller, A. Narla, S. Shankar, P. Reinhold, L. Burkhart, C. Axline, W. Pfaff, L. Frunzio, R. J. Schoelkopf, and M. H. Devoret. Deterministic Remote Entanglement of Superconducting Circuits through Microwave Two-Photon Transitions. *Phys. Rev. Lett.*, 120(20):200501, 2018.

[CKN20] A. Chia, L. C. Kwek, and C. Noh. Relaxation oscillations and frequency entrainment in quantum mechanics. *Physical Review E*, 102(4):042213, 2020.

[CL10] Ping Chen and Shunlong Luo. Clocks and Fisher information. *Theoretical and Mathematical Physics*, 165:1552–1564, 2010.

[Cle22] Andrew N. Cleland. An introduction to the surface code. *SciPost Phys. Lect. Notes*, page 49, 2022.

[CLL+23] Dianzhen Cui, Jianning Li, Fude Li, Zhi-Cheng Shi, and X. X. Yi. Enhancing the sensitivity of nonlinearity sensors through homodyne

detection in dissipatively coupled systems. *Phys. Rev. A*, 107:013709, Jan 2023.

[CMNK22] A. Chia, W. K. Mok, C. Noh, and L. C. Kwek. Pure and truly nonclassical noise-induced transitions at the microscopic scale. *arXiv:2204.03267*, 2022.

[CNAA+22] Christopher Chamberland, Kyungjoo Noh, Patricio Arrangoiz-Arriola, Earl T. Campbell, Connor T. Hann, Joseph Iverson, Harald Putterman, Thomas C. Bohdanowicz, Steven T. Flammia, Andrew Keller, Gil Refael, John Preskill, Liang Jiang, Amir H. Safavi-Naeini, Oskar Painter, and Fernando G.S.L. Brandão. Building a fault-tolerant quantum computer using concatenated cat codes. *PRX Quantum*, 3:010329, Feb 2022.

[CRL13] SA Chilingaryan and BM Rodríguez-Lara. The quantum Rabi model for two qubits. *Journal of Physics A: Mathematical and Theoretical*, 46(33):335301, 2013.

[CTDRG98] Claude Cohen-Tannoudji, Jacques Dupont-Roc, and Gilbert Grynberg. *Atom-photon interactions: basic processes and applications*. Wiley-VCH, 1998.

[CW08] John Clarke and Frank K. Wilhelm. Superconducting quantum bits. *Nature*, 453(7198):1031–1042, 2008.

[CZ95] J. I. Cirac and P. Zoller. Quantum computations with cold trapped ions. *Phys. Rev. Lett.*, 74:4091–4094, May 1995.

[CZG+15] L S Costanzo, A Zavatta, S Grandi, M Bellini, H Jeong, M Kang, S-W Lee, and T C Ralph. Properties of hybrid entanglement between discrete- and continuous-variable states of light. *Phys. Scr.*, 90(7):074045, 2015.

[DBK23] Aaron Daniel, Christoph Bruder, and Martin Koppenhöfer. Geometric phase in quantum synchronization. *arXiv preprint arXiv:2302.08866*, 2023.

[DC19] Shovan Dutta and Nigel R. Cooper. Critical Response of a Quantum van der Pol Oscillator. *Phys. Rev. Lett.*, 123:250401, Dec 2019.

[DD90] Supriyo Datta and Biswajit Das. Electronic analog of the electro-optic modulator. *Appl. Phys. Lett.*, 56(7):665–667, 1990.

[DDI06] Fabio Dell'Anno, Silvio De Siena, and Fabrizio Illuminati. Multiphoton quantum optics and quantum state engineering. *Physics Reports*, 428(2):53–168, 2006.

[Deb12] Lokenath Debnath. *Nonlinear partial differential equations for scientists and engineers,3rd ed.* Springer, 2012.

[DGS07] M.H. Devoret, Steven Girvin, and Robert Schoelkopf. Circuit-QED: How strong can the coupling between a Josephson junction atom and a transmission line resonator be? . *Annalen der Physik*, 16(10-11), 2007.

[DIA12] Benjamin DEVLIN, Makoto IKEDA, and Kunihiro ASADA. Energy minimum operation with self synchronous gate-level autonomous power gating and voltage scaling. *IEICE Transactions on Electronics*, E95.C(4):546–554, 2012.

[DLM+15] Avik Dutt, Kevin Luke, Sasikanth Manipatruni, Alexander L Gaeta, Paulo Nussenzveig, and Michal Lipson. On-chip optical squeezing. *Physical Review Applied*, 3(4):044005, 2015.

[Don16] Kun Dong. Dynamics of two arbitrary qubits strongly coupled to a quantum oscillator. *Chinese Phys. B*, 25(12):124202, nov 2016.

[DPBE23] Federico Dell'Anna, Sunny Pradhan, Cristian Degli Esposti Boschi, and Elisa Ercolessi. Quantum Fisher Information and multipartite entanglement in spin-1 chains. *arXiv:2307.02407*, 2023.

[dSVL21] VB da Silva, JP Vieira, and Edson D Leonel. Fisher information of the Kuramoto model: A geometric reading on synchronization. *Physica D: Nonlinear Phenomena*, 423:132926, 2021.

[DUM+12] Benjamin Devlin, Hiroshi Ueki, Shintaro Mori, Shigenori Miyauchi, Makoto Ikeda, and Kunihiro Asada. Performance and side-channel attack analysis of a self synchronous montgomery multiplier processing element for RSA in 40nm CMOS. In *2012 IEEE Asian Solid State Circuits Conference (A-SSCC)*, pages 385–388, 2012.

[EK05] Leah Edelstein-Keshet. *Mathematical models in biology.* SIAM, 2005.

[ERCL+19] H Eneriz, DZ Rossatto, Francisco A Cárdenas-López, E Solano, and M Sanz. Degree of quantumness in quantum synchronization. *Scientific Reports*, 9(1):19933, 2019.

[FDLR+19] P. Forn-Díaz, L. Lamata, E. Rico, J. Kono, and E. Solano. Ultrastrong coupling regimes of light-matter interaction. *Rev. Mod. Phys.*, 91:025005, Jun 2019.

[FLB+12] T. Frey, P. J. Leek, M. Beck, A. Blais, T. Ihn, K. Ensslin, and A. Wallraff. Dipole Coupling of a Double Quantum Dot to a Microwave Resonator. *Phys. Rev. Lett.*, 108(4):046807, 2012.

[FMMC12] Austin G. Fowler, Matteo Mariantoni, John M. Martinis, and Andrew N. Cleland. Surface codes: Towards practical large-scale quantum computation. 2012.

[Fri90] B Roy Frieden. Fisher information, disorder, and the equilibrium distributions of physics. *Physical Review A*, 41(8):4265, 1990.

[Fri04] B Roy Frieden. *Science from Fisher information: a unification.* Cambridge University Press, 2004.

[FSD16] Florian Fröwis, Pavel Sekatski, and Wolfgang Dür. Detecting Large Quantum Fisher Information with Finite Measurement Precision. *Phys. Rev. Lett.*, 116:090801, Mar 2016.

[GG02] Frédéric Grosshans and Philippe Grangier. Continuous variable quantum cryptography using coherent states. *Phys. Rev. Lett.*, 88:057902, Jan 2002.

[GHJM98] Luca Gammaitoni, Peter Hänggi, Peter Jung, and Fabio Marchesoni. Stochastic resonance. *Rev. Mod. Phys.*, 70:223–287, Jan 1998.

[GHSZ90] Daniel M. Greenberger, Michael A. Horne, Abner Shimony, and Anton Zeilinger. Bell's theorem without inequalities. *Am. J. Phys.*, 58(12):1131–1143, 1990.

[Gir11] Steven M Girvin. Superconducting qubits and circuits: Artificial atoms coupled to microwave photons. *Lectures delivered at Ecole d'Eté Les Houches*, 2011.

[GKP01] Daniel Gottesman, Alexei Kitaev, and John Preskill. Encoding a qubit in an oscillator. *Phys. Rev. A*, 64:012310, Jun 2001.

[GKS76] Vittorio Gorini, Andrzej Kossakowski, and E. C. G. Sudarshan. Completely positive dynamical semigroups of n-level systems. *J. Math. Phys*, 17(5):821–825, 1976.

[GLM11] Vittorio Giovannetti, Seth Lloyd, and Lorenzo Maccone. Advances in quantum metrology. *Nat. Photonics*, 5(4):222, 2011.

[GMK12] Vladimir García-Morales and Katharina Krischer. The complex Ginzburg–Landau equation: an introduction. *Contemporary Physics*, 53(2):79–95, 2012.

[Got97] Daniel Gottesman. *Stabilizer codes and quantum error correction.* California Institute of Technology, 1997.

[Got09] Daniel Gottesman. An introduction to quantum error correction and fault-tolerant quantum computation, 2009.

[GP21] Arne L. Grimsmo and Shruti Puri. Quantum Error Correction with the Gottesman-Kitaev-Preskill Code. *PRX Quantum*, 2:020101, Jun 2021.

[GVAW+03] Frédéric Grosshans, Gilles Van Assche, Jérôme Wenger, Rosa Brouri, Nicolas J. Cerf, and Philippe Grangier. Quantum key distribution using gaussian-modulated coherent states. *Nature*, 421(6920):238–241, Jan 2003.

[Haa91] Fritz Haake. Quantum signatures of chaos. In *Quantum Coherence in Mesoscopic Systems*, pages 583–595. Springer, 1991.

[Haa00] F. Haake. *Quantum Signatures of Chaos 2nd ed.* (Springer, Switzerland), 2000.

[HBR20] S. Haroche, M. Brune, and J. M. Raimond. From cavity to circuit quantum electrodynamics. *Nat. Phys.*, 16(3):1–4, 2020.

[HHL09] Aram W. Harrow, Avinatan Hassidim, and Seth Lloyd. Quantum algorithm for linear systems of equations. *Phys. Rev. Lett.*, 103:150502, Oct 2009.

[HJG+98] R.J Hughes, D.F.V. James, J.J. Gomez, M.S. Gulley, M.H. Holzscheiter, P.G. Kwiat, S.K. Lamoreaux, C.G. Peterson, V.D. Sandberg, M.M. Schauer, C.M. Simmons, C.E. Thorburn, D. Tupa, P.Z. Wang, and A.G. White. The los alamos trapped ion quantum computer experiment. *Fortsch. Phys.*, 46(4-5):329–361, 1998.

[HLG+15] Michael R. Hush, Weibin Li, Sam Genway, Igor Lesanovsky, and Andrew D. Armour. Spin correlations as a probe of quantum synchro-

nization in trapped-ion phonon lasers. *Phys. Rev. A*, 91:061401, Jun 2015.

[HLJM+19] Kun Huang, Hanna Le Jeannic, Olivier Morin, Tom Darras, Giovanni Guccione, Adrien Cavaillès, and Julien Laurat. Engineering optical hybrid entanglement between discrete-and continuous-variable states. *New J. Phys.*, 21(8):083033, 2019.

[HLLMH18] Marcus Huber, Ludovico Lami, Cécilia Lancien, and Alexander Müller-Hermes. High-dimensional entanglement in states with positive partial transposition. *Phys. Rev. Lett.*, 121:200503, Nov 2018.

[HPJ22] Le Hu, Shengshi Pang, and Andrew N. Jordan. Achieving Heisenberg scaling on measurement of a three-qubit system via quantum error correction. *Phys. Rev. A*, 106:052609, Nov 2022.

[HQ22] Timo Hillmann and Fernando Quijandría. Designing Kerr Interactions for Quantum Information Processing via Counterrotating Terms of Asymmetric Josephson-Junction Loops. *Phys. Rev. Appl.*, 17:064018, Jun 2022.

[HQGY21] Yan Hong, Xianfei Qi, Ting Gao, and Fengli Yan. Detection of multipartite entanglement via quantum Fisher information. *Europhysics Letters*, 134(6):60006, sep 2021.

[HSS03] Daihai He, Pengliang Shi, and Lewi Stone. Noise-induced synchronization in realistic models. *Phys. Rev. E*, 67:027201, Feb 2003.

[HWA+08] Max Hofheinz, E. M. Weig, M. Ansmann, Radoslaw C. Bialczak, Erik Lucero, M. Neeley, A. D. O'Connell, H. Wang, John M. Martinis, and A. N. Cleland. Generation of Fock states in a superconducting quantum circuit. *Nature*, 454(7202):310–314, 2008.

[HWA+09] Max Hofheinz, H. Wang, M. Ansmann, Radoslaw C. Bialczak, Erik Lucero, M. Neeley, A. D. O'Connell, D. Sank, J. Wenner, John M. Martinis, and A. N. Cleland. Synthesizing arbitrary quantum states in a superconducting resonator. *Nature*, 459(7246):546–549, 2009.

[IGBMS05] EK Irish, J Gea-Banacloche, I Martin, and KC Schwab. Dynamics of a two-level system strongly coupled to a high-frequency quantum oscillator. *Phys. Rev. B*, 72(19):195410, 2005.

[IK17] Kenta Ishibashi and Rina Kanamoto. Oscillation collapse in coupled quantum van der Pol oscillators. *Phys. Rev. E*, 96:052210, Nov 2017.

[JADW00] Richard Jozsa, Daniel S Abrams, Jonathan P Dowling, and Colin P Williams. Quantum clock synchronization based on shared prior entanglement. *Physical Review Letters*, 85(9):2010, 2000.

[JC63] E. T. Jaynes and F. W. Cummings. Comparison of quantum and semiclassical radiation theories with application to the beam maser. *Proceedings of the IEEE*, 51(1):89–109, 1963.

[JHS+20] Noufal Jaseem, Michal Hajdušek, Parvinder Solanki, Leong-Chuan Kwek, Rosario Fazio, and Sai Vinjanampathy. Generalized measure of quantum synchronization. *Physical Review Research*, 2(4):043287, 2020.

[JKJL+13] Paul Jouguet, Sébastien Kunz-Jacques, Anthony Leverrier, Philippe Grangier, and Eleni Diamanti. Experimental demonstration of long-distance continuous-variable quantum key distribution. *Nature Photonics*, 7(5):378–381, May 2013.

[JS07] Dominic Jordan and Peter Smith. *Nonlinear ordinary differential equations: an introduction for scientists and engineers*. OUP Oxford, 2007.

[JZK+14] Hyunseok Jeong, Alessandro Zavatta, Minsu Kang, Seung-Woo Lee, Luca S. Costanzo, Samuele Grandi, Timothy C. Ralph, and Marco Bellini. Generation of hybrid entanglement of light. *Nat. Photonics*, 8(7):564–569, 2014.

[Kan98] B. E. Kane. A silicon-based nuclear spin quantum computer. *Nature*, 393(6681):133–137, May 1998.

[KBR20] Martin Koppenhofer, Christoph Bruder, and Alexandre Roulet. Quantum synchronization on the IBM Q system. *Physical Review Research*, 2(2):023026, 2020.

[KCK+12] J Kengne, JC Chedjou, G Kenne, K Kyamakya, and GH Kom. Analog circuit implementation and synchronization of a system consisting of a van der Pol oscillator linearly coupled to a Duffing oscillator. *Nonlinear Dynamics*, 70:2163–2173, 2012.

[KFR+15] Thi Ha Kyaw, Simone Felicetti, Guillermo Romero, Enrique Solano, and L-C Kwek. Scalable quantum memory in the ultrastrong coupling regime. *Sci. Rep.*, 5(1):1–5, 2015.

[KML+19] Anton Frisk Kockum, Adam Miranowicz, Simone De Liberato, Salvatore Savasta, and Franco Nori. Ultrastrong coupling between light and matter. *Nature Reviews Physics*, 1(1), 2019.

[KN20] Yuzuru Kato and Hiroya Nakao. Semiclassical optimization of entrainment stability and phase coherence in weakly forced quantum limit-cycle oscillators. *Phys. Rev. E*, 101:012210, Jan 2020.

[KN21a] Yuzuru Kato and Hiroya Nakao. Enhancement of quantum synchronization via continuous measurement and feedback control. *New Journal of Physics*, 23(1):013007, 2021.

[KN21b] Yuzuru Kato and Hiroya Nakao. Quantum coherence resonance. *New J. Phys.*, 23(4):043018, apr 2021.

[Kni05] E. Knill. Quantum computing with realistically noisy devices. *Nature*, 434(7029):39–44, 2005.

[KR19] Martin Koppenhöfer and Alexandre Roulet. Optimal synchronization deep in the quantum regime: Resource and fundamental limit. *Phys. Rev. A*, 99:043804, Apr 2019.

[KST09] AP Kuznetsov, NV Stankevich, and LV Turukina. Coupled van der Pol–Duffing oscillators: Phase dynamics and structure of synchronization tongues. *Physica D: Nonlinear Phenomena*, 238(14):1203–1215, 2009.

[Kur75] Yoshiki Kuramoto. Self-entrainment of a population of coupled nonlinear oscillators. In *International Symposium on Mathematical Problems in Theoretical Physics*, pages 420–422, Berlin, Heidelberg, 1975. Springer Berlin Heidelberg.

[KVK13] Aneta Koseska, Evgeny Volkov, and Jürgen Kurths. Oscillation quenching mechanisms: Amplitude vs. oscillation death. *Phys. Rep.*, 531(4):173–199, 2013.

[KYG+07] Jens Koch, Terri M. Yu, Jay Gambetta, A. A. Houck, D. I. Schuster, J. Majer, Alexandre Blais, M. H. Devoret, S. M. Girvin, and R. J. Schoelkopf. Charge-insensitive qubit design derived from the Cooper pair box. *Physical Review A*, 76(4), 2007.

[KYN19] Yuzuru Kato, Naoki Yamamoto, and Hiroya Nakao. Semiclassical phase reduction theory for quantum synchronization. *Phys. Rev. Research*, 1:033012, Oct 2019.

[KZP18] Alexander C Kalloniatis, Mathew L Zuparic, and Mikhail Prokopenko. Fisher information and criticality in the Kuramoto model of nonidentical oscillators. *Physical Review E*, 98(2):022302, 2018.

[LANB16] Niels Lörch, Ehud Amitai, Andreas Nunnenkamp, and Christoph Bruder. Genuine Quantum Signatures in Synchronization of Anharmonic Self-Oscillators. *Physical Review Letters*, 117(7):073601, 2016.

[LB13] Daniel A Lidar and Todd A Brun. *Quantum error correction*. Cambridge university press, 2013.

[LCW14] Tony E. Lee, Ching-Kit Chan, and Shenshen Wang. Entanglement tongue and quantum synchronization of disordered oscillators. *Phys. Rev. E*, 89:022913, Feb 2014.

[LD98] Daniel Loss and David P. DiVincenzo. Quantum computation with quantum dots. *Phys. Rev. A*, 57:120–126, Jan 1998.

[Lin76] G. Lindblad. On the generators of quantum dynamical semigroups. *Commun. Math. Phys*, 48(2):119–130, Jun 1976.

[Liu23] Chen-Yu Liu. Practical quantum search by variational quantum eigensolver on noisy intermediate-scale quantum hardware. *arXiv:2304.03747*, 2023.

[LKV+13] Zaki Leghtas, Gerhard Kirchmair, Brian Vlastakis, Michel H. Devoret, Robert J. Schoelkopf, and Mazyar Mirrahimi. Deterministic protocol for mapping a qubit to coherent state superpositions in a cavity. *Phys. Rev. A*, 87:042315, Apr 2013.

[LL13] Kelvin MC Lee and CK Law. Ground state of a resonant two-qubit cavity system in the ultrastrong-coupling regime. *Phys. Rev. A*, 88(1):015802, 2013.

[LNN+17] Niels Lörch, Simon E. Nigg, Andreas Nunnenkamp, Rakesh P. Tiwari, and Christoph Bruder. Quantum synchronization blockade: Energy quantization hinders synchronization of identical oscillators. *Phys. Rev. Lett.*, 118:243602, Jun 2017.

[LR12] Muthusamy Lakshmanan and Shanmuganathan Rajaseekar. *Nonlinear dynamics: integrability, chaos and patterns*. Springer Science & Business Media, 2012.

[LS13] Tony E Lee and HR Sadeghpour. Quantum synchronization of quantum van der Pol oscillators with trapped ions. *Physical Review Letters*, 111(23):234101, 2013.

[LTP+15] Z. Leghtas, S. Touzard, I. M. Pop, A. Kou, B. Vlastakis, A. Petrenko, K. M. Sliwa, A. Narla, S. Shankar, M. J. Hatridge, M. Reagor, L. Frunzio, R. J. Schoelkopf, M. Mirrahimi, and M. H. Devoret. Confining the state of light to a quantum manifold by engineered two-photon loss. *Science*, 347(6224):853–857, 2015.

[Lud19] Stefan Ludwig. Noise put to use. *Nat. Phys.*, 15(4):310–311, Apr 2019.

[LV01] Seth Lloyd and Lorenza Viola. Engineering quantum dynamics. *Phys. Rev. A*, 65:010101, Dec 2001.

[LYO15] Xiao-Ming Lu, Sixia Yu, and C. H. Oh. Robust quantum metrological schemes based on protection of quantum Fisher information. *Nature Communications*, 6(1), jun 2015.

[May19] Robert M May. Stability and complexity in model ecosystems. In *Stability and Complexity in Model Ecosystems*. Princeton university press, 2019.

[MBB+18] Nikolaj Moll, Panagiotis Barkoutsos, Lev S Bishop, Jerry M Chow, Andrew Cross, Daniel J Egger, Stefan Filipp, Andreas Fuhrer, Jay M Gambetta, Marc Ganzhorn, Abhinav Kandala, Antonio Mezzacapo, Peter Müller, Walter Riess, Gian Salis, John Smolin, Ivano Tavernelli, and Kristan Temme. Quantum optimization using variational algorithms on near-term quantum devices. *Quantum Science and Technology*, 3(3):030503, jun 2018.

[MCG+07] J. Majer, J. M. Chow, J. M. Gambetta, Jens Koch, B. R. Johnson, J. A. Schreier, L. Frunzio, D. I. Schuster, A. A. Houck, A. Wallraff, A. Blais, M. H. Devoret, S. M. Girvin, and R. J. Schoelkopf. Coupling superconducting qubits via a cavity bus. *Nature*, 449(7161):443–447, 2007.

[MFB14] Víctor Montenegro, Alessandro Ferraro, and Sougato Bose. Nonlinearity-induced entanglement stability in a qubit-oscillator system. *Physical Review A*, 90(1):013829, 2014.

[MH15] Lisa Morgan and Haye Hinrichsen. Oscillation and synchronization of two quantum self-sustained oscillators. *J. Stat. Mech.: Theory Exp.*, 2015(9):P09009, sep 2015.

[Mir16] Mazyar Mirrahimi. Cat-qubits for quantum computation. *Comptes Rendus Physique*, 17(7):778–787, 2016.

[MKH20] W.-K. Mok, L.-C. Kwek, and H. Heimonen. Synchronization boost with single-photon dissipation in the deep quantum regime. *Phys. Rev. Res.*, 2:033422, Sep 2020.

[MLA+14] Mazyar Mirrahimi, Zaki Leghtas, Victor V Albert, Steven Touzard, Robert J Schoelkopf, Liang Jiang, and Michel H Devoret. Dynamically protected cat-qubits: a new paradigm for universal quantum computation. *New Journal of Physics*, 16(4):045014, apr 2014.

[MNAU02] John M. Martinis, S. Nam, J. Aumentado, and C. Urbina. Rabi Oscillations in a Large Josephson-Junction Qubit. *Physical Review Letters*, 89(11):117901, 2002.

[Moo08] Francis C Moon. *Chaotic and fractal dynamics: introduction for applied scientists and engineers*. John Wiley & Sons, 2008.

[MPC+20] Y. Ma, X. Pan, W. Cai, X. Mu, Y. Xu, L. Hu, W. Wang, H. Wang, Y. P. Song, Zhen-Biao Yang, Shi-Biao Zheng, and L. Sun. Manipulating Complex Hybrid Entanglement and Testing Multipartite Bell Inequalities in a Superconducting Circuit. *Phys. Rev. Lett.*, 125(18):180503, 2020.

[MSB01] Laurens W. Molenkamp, Georg Schmidt, and Gerrit E. W. Bauer. Rashba Hamiltonian and electron transport. *Phys. Rev. B*, 64:121202, Sep 2001.

[NC10] Michael A Nielsen and Isaac L Chuang. *Quantum computation and quantum information*. Cambridge university press, 2010.

[NC11] Pierre Nataf and Cristiano Ciuti. Protected Quantum Computation with Multiple Resonators in Ultrastrong Coupling Circuit QED. *Phys. Rev. Lett.*, 107:190402, Nov 2011.

[NDH+10] Thomas Niemczyk, F Deppe, H Huebl, EP Menzel, F Hocke, MJ Schwarz, JJ Garcia-Ripoll, D Zueco, T Hümmer, E Solano, et al.

Circuit quantum electrodynamics in the ultrastrong-coupling regime. *Nat. Phys.*, 6(10):772–776, 2010.

[OPH+16] Nissim Ofek, Andrei Petrenko, Reinier Heeres, Philip Reinhold, Zaki Leghtas, Brian Vlastakis, Yehan Liu, Luigi Frunzio, S. M. Girvin, L. Jiang, Mazyar Mirrahimi, M. H. Devoret, and R. J. Schoelkopf. Extending the lifetime of a quantum bit with error correction in superconducting circuits. *Nature*, 536(7617):441–445, Aug 2016.

[Par09] Matteo G. A. Paris. Quantum Estimation for Quantum Technology. *International Journal of Quantum Information*, 7(supp01):125–137, 2009.

[PFDSGR10] B. Peropadre, P. Forn-Díaz, E. Solano, and J. J. García-Ripoll. Switchable Ultrastrong Coupling in Circuit QED. *Phys. Rev. Lett.*, 105:023601, Jul 2010.

[PGCI+19] Shruti Puri, Alexander Grimm, Philippe Campagne-Ibarcq, Alec Eickbusch, Kyungjoo Noh, Gabrielle Roberts, Liang Jiang, Mazyar Mirrahimi, Michel H. Devoret, and S. M. Girvin. Stabilized cat in a driven nonlinear cavity: A fault-tolerant error syndrome detector. *Phys. Rev. X*, 9:041009, Oct 2019.

[PNR13] Arthur Pewsey, Markus Neuhäuser, and Graeme D Ruxton. *Circular statistics in R*. Oxford University Press, 2013.

[PRB+14] Jie Peng, Zhongzhou Ren, Daniel Braak, Guangjie Guo, Guoxing Ju, Xin Zhang, and Xiaoyong Guo. Solution of the two-qubit quantum Rabi model and its exceptional eigenstates. *Journal of Physics A: Mathematical and Theoretical*, 47(26):265303, 2014.

[Pre18] John Preskill. Quantum Computing in the NISQ era and beyond. *Quantum*, 2:79, August 2018.

[PRK01] A Pikovsky, M Rosenblum, and J Kurths. *Synchronization Cambridge University Press*. 2001.

[PVS+18] Nirmal Punetha, Vaibhav Varshney, Samir Sahoo, Garima Saxena, Awadhesh Prasad, and Ram Ramaswamy. Dynamical effects of breaking rotational symmetry in counter-rotating Stuart-Landau oscillators. *Physical Review E*, 98(2):022212, 2018.

[RB18] Alexandre Roulet and Christoph Bruder. Synchronizing the smallest possible system. *Phys. Rev. Lett.*, 121:053601, Jul 2018.

[RBMV21] Aniket Rath, Cyril Branciard, Anna Minguzzi, and Benoît Vermersch. Quantum Fisher Information from Randomized Measurements. *Phys. Rev. Lett.*, 127:260501, Dec 2021.

[RBW+12] G. Romero, D. Ballester, Y. M. Wang, V. Scarani, and E. Solano. Ultrafast Quantum Gates in Circuit QED. *Physical Review Letters*, 108(12):120501, 2012.

[RFNSG01] Robert Rozenfeld, Jan A. Freund, Alexander Neiman, and Lutz Schimansky-Geier. Noise-induced phase synchronization enhanced by dichotomic noise. *Phys. Rev. E*, 64:051107, Oct 2001.

[RKT+22] Janarthanan Ramadoss, Jacques Kengne, Sosthene Tsamene Tanekou, Karthikeyan Rajagopal, and Germaine Djuidje Kenmoe. Reversal of period doubling, multistability and symmetry breaking aspects for a system composed of a Van der Pol oscillator coupled to a Duffing oscillator. *Chaos, Solitons & Fractals*, 159:112157, 2022.

[RP03] Michael Rosenblum and Arkady Pikovsky. Synchronization: From pendulum clocks to chaotic lasers and chemical oscillators. *Contemp. Phys.*, 44(5):401–416, 2003.

[RVBSS17] Daniel Z. Rossatto, Celso J. Villas-Bôas, Mikel Sanz, and Enrique Solano. Spectral classification of coupling regimes in the quantum Rabi model. *Phys. Rev. A*, 96(1), 2017.

[Sch17] Roman Schnabel. Squeezed states of light and their applications in laser interferometers. *Physics Reports*, 684:1–51, 2017.

[SCN20] Roberto Stassi, Mauro Cirio, and Franco Nori. Scalable quantum computer with superconducting circuits in the ultrastrong coupling regime. *npj Quantum Inf.*, 6(1):67, 2020.

[Sco06] Alwyn Scott. *Encyclopedia of nonlinear science*. Routledge, 2006.

[SCVC15] Tirth Shah, Rohitashwa Chattopadhyay, Kedar Vaidya, and Sagar Chakraborty. Conservative perturbation theory for nonconservative systems. *Phys. Rev. E*, 92:062927, Dec 2015.

[SG64] Leonard Susskind and Jonathan Glogower. Quantum mechanical phase and time operator. *Physics Physique Fizika*, 1:49–61, Jul 1964.

[SHM+18] Sameer Sonar, Michal Hajdušek, Manas Mukherjee, Rosario Fazio, Vlatko Vedral, Sai Vinjanampathy, and Leong-Chuan Kwek. Squeezing Enhances Quantum Synchronization. *Physical Review Letters*, 120(16):163601, 2018.

[Sho94] Peter W Shor. Algorithms for quantum computation: discrete logarithms and factoring. In *Proceedings 35th annual symposium on foundations of computer science*, pages 124–134. Ieee, 1994.

[SK20] Jasminder S. Sidhu and Pieter Kok. Geometric perspective on quantum parameter estimation. *AVS Quantum Science*, 2(1):014701, 02 2020.

[SL22] Finn Schmolke and Eric Lutz. Noise-induced quantum synchronization. *Phys. Rev. Lett.*, 129:250601, Dec 2022.

[SMC+21] Yuan Shen, Giampiero Marchegiani, Gianluigi Catelani, Luigi Amico, Ai Qun Liu, Weijun Fan, and Leong Chuan Kwek. GHZ-like states in the Qubit-Qudit Rabi model. *SciPost Physics*, 11(6):099, 2021.

[SMN+23] Yuan Shen, Wai-Keong Mok, Changsuk Noh, Ai Qun Liu, Leong-Chuan Kwek, Weijun Fan, and Andy Chia. Quantum synchronization effects induced by strong nonlinearities. *Phys. Rev. A*, 107:053713, May 2023.

[SMnFS21] Carlos Sánchez Muñoz, Gaetano Frascella, and Frank Schlawin. Quantum metrology of two-photon absorption. *Phys. Rev. Research*, 3:033250, Sep 2021.

[SPR12] Garima Saxena, Awadhesh Prasad, and Ram Ramaswamy. Amplitude death: The emergence of stationarity in coupled nonlinear systems. *Phys. Rep.*, 521(5):205–228, 2012.

[SSFK23] Yuan Shen, Hong Yi Soh, Weijun Fan, and Leong-Chuan Kwek. Enhancing quantum synchronization through homodyne measurement, noise, and squeezing. *Physical Review E*, 108(2):024204, 2023.

[Ste93] M Kay Steven. Fundamentals of statistical signal processing. *PTR Prentice-Hall, Englewood Cliffs, NJ*, 10:151045, 1993.

[Stö00] Hans-Jürgen Stöckmann. Quantum chaos: an introduction, 2000.

[Str18] Steven H Strogatz. *Nonlinear dynamics and chaos: with applications to physics, biology, chemistry, and engineering*. CRC press, 2018.

[Stu60] FLHM Stumpers. Balth. Van der Pol's Work on Nonlinear Circuits. *IRE Transactions on Circuit Theory*, 7(4):366–367, 1960.

[SVM07] Jan A Sanders, Ferdinand Verhulst, and James Murdock. *Averaging methods in nonlinear dynamical systems*, volume 59. Springer, 2007.

[TF19] S. Takeda and A. Furusawa. Toward large-scale fault-tolerant universal photonic quantum computing. *APL Photonics*, 4(6):060902, 2019.

[TMHGP01] Raúl Toral, Claudio R. Mirasso, Emilio Hernández-Garcıa, and Oreste Piro. Analytical and numerical studies of noise-induced synchronization of chaotic systems. *Chaos: An Interdisciplinary Journal of Nonlinear Science*, 11(3):665–673, 2001.

[TSKO04] DM Tong, Erik Sjöqvist, Leong Chuan Kwek, and Choo Hiap Oh. Kinematic approach to the mixed state geometric phase in nonunitary evolution. *Physical review letters*, 93(8):080405, 2004.

[TV18] Géza Tóth and Tamás Vértesi. Quantum States with a Positive Partial Transpose are Useful for Metrology. *Phys. Rev. Lett.*, 120(2):020506, 2018.

[Tó20] Géza Tóth. Activating Hidden Metrological Usefulness. *Phys. Rev. Lett.*, 125(2):020402, 2020.

[vdP17] Balthasar van der Pol. A note on the relation of the audibility factor of a shunted telephone to the antenna current as used in the reception of wireless signals. *The London, Edinburgh, and Dublin Philosophical Magazine and Journal of Science*, 34(201):184–188, 1917.

[VdP20] Balthasar Van der Pol. Theory of the amplitude of free and forced triode vibrations. *Radio review*, 1:701–710, 1920.

[vdP22] Balthasar van der Pol. On oscillation hysteresis in a triode generator with two degrees of freedom. *The London, Edinburgh, and Dublin Philosophical Magazine and Journal of Science*, 43(256):700–719, 1922.

[VK08] UE Vincent and A Kenfack. Synchronization and bifurcation structures in coupled periodically forced non-identical Duffing oscillators. *Physica Scripta*, 77(4):045005, 2008.

[VW02] G. Vidal and R. F. Werner. Computable measure of entanglement. *Phys. Rev. A*, 65:032314, Feb 2002.

[Wal12] Daniel Waltner. *Semiclassical Approach to Mesoscopic Systems: Classical Trajectory Correlations and Wave Interference*, volume 245. Springer Science & Business Media, 2012.

[WCF96] P Woafo, JC Chedjou, and HB Fotsin. Dynamics of a system consisting of a van der Pol oscillator coupled to a Duffing oscillator. *Physical Review E*, 54(6):5929, 1996.

[Wim14] Sandro Wimberger. *Nonlinear dynamics and quantum chaos*, volume 10. Springer, 2014.

[Win67] Arthur T. Winfree. Biological rhythms and the behavior of populations of coupled oscillators. *Journal of Theoretical Biology*, 16(1):15–42, 1967.

[Win80] Arthur T Winfree. *The geometry of biological time*, volume 2. Springer, 1980.

[WKM16] Talitha Weiss, Andreas Kronwald, and Florian Marquardt. Noise-induced transitions in optomechanical synchronization. *New Journal of Physics*, 18(1):013043, 2016.

[WM93] H. M. Wiseman and G. J. Milburn. Quantum theory of field-quadrature measurements. *Phys. Rev. A*, 47:642–662, Jan 1993.

[WM09] Howard M. Wiseman and Gerard J. Milburn. *Quantum Measurement and Control*. Cambridge University Press, 2009.

[WNB14] Stefan Walter, Andreas Nunnenkamp, and Christoph Bruder. Quantum synchronization of a driven self-sustained oscillator. *Physical Review Letters*, 112(9):094102, 2014.

[WNB15] Stefan Walter, Andreas Nunnenkamp, and Christoph Bruder. Quantum synchronization of two Van der Pol oscillators. *Annalen der Physik*, 527(1-2):131–138, 2015.

[WSB03] Thomas Wellens, Vyacheslav Shatokhin, and Andreas Buchleitner. Stochastic resonance. *Rep. Prog. Phys.*, 67(1):45, dec 2003.

[WTB+19] Timo Wagner, Peter Talkner, Johannes C. Bayer, Eddy P. Rugeramigabo, Peter Hänggi, and Rolf J. Haug. Quantum stochastic resonance in

an A.C.-driven single-electron quantum dot. *Nat. Phys.*, 15(4):330–334, Apr 2019.

[WWM17] Talitha Weiss, Stefan Walter, and Florian Marquardt. Quantum-coherent phase oscillations in synchronization. *Phys. Rev. A*, 95:041802, Apr 2017.

[XAYN13] Ze-Liang Xiang, Sahel Ashhab, J. Q. You, and Franco Nori. Hybrid quantum circuits: Superconducting circuits interacting with other quantum systems. *Rev. Mod. Phys.*, 85:623–653, Apr 2013.

[YFA+17] Fumiki Yoshihara, Tomoko Fuse, Sahel Ashhab, Kosuke Kakuyanagi, Shiro Saito, and Kouichi Semba. Superconducting qubit–oscillator circuit beyond the ultrastrong-coupling regime. *Nat. Phys.*, 13(1):44, 2017.

[YKAD17] Deshui Yu, Leong Chuan Kwek, Luigi Amico, and Rainer Dumke. Theoretical description of a micromaser in the ultrastrong-coupling regime. *Phys. Rev. A*, 95(5):053811, 2017.

[YKAD18] Deshui Yu, Leong Chuan Kwek, Luigi Amico, and Rainer Dumke. Nonlinear circuit quantum electrodynamics based on the charge-qubit–resonator interface. *Phys. Rev. A*, 98:033833, Sep 2018.

[YLK+18] Deshui Yu, Alessandro Landra, Leong Chuan Kwek, Luigi Amico, and Rainer Dumke. Stabilizing Rabi oscillation of a charge qubit via the atomic clock technique. *New J. Phys.*, 20(2):023031, 2018.

[YLV+16] Deshui Yu, Alessandro Landra, María Martínez Valado, Christoph Hufnagel, Leong Chuan Kwek, Luigi Amico, and Rainer Dumke. Superconducting resonator and Rydberg atom hybrid system in the strong coupling regime. *Phys. Rev. A*, 94(6):062301, 2016.

[YLW+21] Min Yu, Dongxiao Li, Jingcheng Wang, Yaoming Chu, Pengcheng Yang, Musang Gong, Nathan Goldman, and Jianming Cai. Experimental estimation of the quantum Fisher information from randomized measurements. *Phys. Rev. Res.*, 3:043122, Nov 2021.

[YVH+16] Deshui Yu, María Martínez Valado, Christoph Hufnagel, Leong Chuan Kwek, Luigi Amico, and Rainer Dumke. Quantum state transmission in a superconducting charge qubit-atom hybrid. *Sci. Rep.*, 6:38356, 2016.

[YZF15] Jie-Dong Yue, Yu-Ran Zhang, and Heng Fan. Operation-triggered quantum clock synchronization. *Physical Review A*, 92(3):032321, 2015.

[ZHC+19] G. Zhang, J. Y. Haw, H. Cai, F. Xu, S. M. Assad, J. F. Fitzsimons, X. Zhou, Y. Zhang, S. Yu, J. Wu, W. Ser, L. C. Kwek, and A. Q. Liu. An integrated silicon photonic chip platform for continuous-variable quantum key distribution. *Nature Photonics*, 13(12):839–842, Dec 2019.

[ZK02] Changsong Zhou and Jürgen Kurths. Noise-induced phase synchronization and synchronization transitions in chaotic oscillators. *Phys. Rev. Lett.*, 88:230602, May 2002.

[ZSZK21] Wei Zou, DV Senthilkumar, Meng Zhan, and Jürgen Kurths. Quenching, aging, and reviving in coupled dynamical networks. *Physics Reports*, 931:1–72, 2021.

[ZZMF13] Yong-Liang Zhang, Yu-Ran Zhang, Liang-Zhu Mu, and Heng Fan. Criterion for remote clock synchronization with Heisenberg-scaling accuracy. *Physical Review A*, 88(5):052314, 2013.

List of publications

1. Y. Shen, L. Cao, X. Y. Wang, J. Zou, W. Luo, Y. X. Wang, H. Cai, B. Dong, X. S. Luo, W. J. Fan, L. C. Kwek, and A. Q. Liu, *On-Chip Continuous-Variable Quantum Key Distribution(CV-QKD) and Homodyne Detection*, Optical Fiber Communication Conference (OFC) 2020, OSA Technical Digest (Optica Publishing Group, 2020), paper W2A.53. doi: 10.1364/OFC.2020.W2A.53

2. Y. Shen, G. Marchegiani, G. Catelani, L. Amico, A. Q. Liu, W. Fan, and L. C. Kwek, *GHZ-like states in the qubit-qudit Rabi model*, SciPost Phys. 11, 099, 2021. doi: 10.21468/SciPostPhys.11.6.099

3. Y. Shen; W.K. Mok; C. Noh; A.Q. Liu; L.C. Kwek; W. Fan; A. Chia. *Quantum synchronization effects induced by strong nonlinearities*. Phys. Rev. A, 107, 053713, 2023. doi: 10.1103/PhysRevA.107.053713

4. Y. Shen, H. Y. Soh, W. Fan, and L.-C. Kwek, *Enhancing quantum synchronization through homodyne measurement, noise and squeezing*, Phys. Rev. E 108, 024204, 2023. doi: 10.1103/PhysRevE.108.024204

5. Y. Shen, H. Y. Soh, L.-C. Kwek, and W. Fan, *Fisher information as general metrics of quantum synchronization*, Entropy 25(8), 1116, 2023. doi: 10.3390/e25081116